Advanced Machine Learning Algorithms for Canadian Wetland Mapping using Polarimetric Synthetic Aperture Radar (PolSAR) and Optical Imagery

by

© Masoud Mahdianpari

A thesis submitted to the

School of Graduate Studies

in partial fulfilment of the requirements for the degree of

Doctor of Philosophy

Faculty of Engineering and Applied Science

Memorial University of Newfoundland

October 2019

St. John's, Newfoundland and Labrador

Dedicated to my family

Abstract

Wetlands are complex land cover ecosystems that represent a wide range of biophysical conditions. They are one of the most productive ecosystems and provide several important environmental functionalities. As such, wetland mapping and monitoring using cost- and time-efficient approaches are of great interest for sustainable management and resource assessment. In this regard, satellite remote sensing data are greatly beneficial, as they capture a synoptic and multi-temporal view of landscapes. The ability to extract useful information from satellite imagery greatly affects the accuracy and reliability of the final products. This is of particular concern for mapping complex land cover ecosystems, such as wetlands, where complex, heterogeneous, and fragmented landscape results in similar backscatter/spectral signatures of land cover classes in satellite images. Accordingly, the overarching purpose of this thesis is to contribute to existing methodologies of wetland classification by proposing and developing several new techniques based on advanced remote sensing tools and optical and Synthetic Aperture Radar (SAR) imagery. Specifically, the importance of employing an efficient speckle reduction method for polarimetric SAR (PolSAR) image processing is discussed and a new speckle reduction technique is proposed. Two novel techniques are also introduced for improving the accuracy of wetland classification. In particular, a new hierarchical classification algorithm using multi-frequency SAR data is proposed that discriminates wetland classes in three steps depending on their complexity and similarity. The experimental results reveal that the proposed method is advantageous for mapping complex land cover ecosystems compared to single stream classification approaches, which have been extensively used in the literature. Furthermore, a new feature weighting approach is proposed based on the statistical and physical characteristics of PolSAR data to improve the discrimination capability of input features prior to incorporating them into the classification scheme. This study

also demonstrates the transferability of existing classification algorithms, which have been developed based on RADARSAT-2 imagery, to compact polarimetry SAR data that will be collected by the upcoming RADARSAT Constellation Mission (RCM). The capability of several well-known deep Convolutional Neural Network (CNN) architectures currently employed in computer vision is first introduced in this thesis for classification of wetland complexes using multispectral remote sensing data. Finally, this research results in the first provincial-scale wetland inventory maps of Newfoundland and Labrador using the Google Earth Engine (GEE) cloud computing resources and open access Earth Observation (EO) collected by the Copernicus Sentinel missions. Overall, the methodologies proposed in this thesis address fundamental limitations/challenges of wetland mapping using remote sensing data, which have been ignored in the literature. These challenges include the backscattering/spectrally similar signature of wetland classes, insufficient classification accuracy of wetland classes, and limitations of wetland mapping on large scales. In addition to the capabilities of the proposed methods for mapping wetland complexes, the use of these developed techniques for classifying other complex land cover types beyond wetlands, such as sea ice and crop ecosystems, offers a potential avenue for further research.

Keywords: Wetland, remote sensing, Synthetic Aperture Radar (SAR), polarimetric SAR (PolSAR), compact polarimetry, RADARSAT Constellation Mission (RCM), deep convolutional neural network (CNN), Google Earth Engine (GEE), Earth Observation (EO), Sentinel missions.

Acknowledgement

Table of Contents

List of Tables

List of Figures

List of Abbreviations and Symbols

Acronyms	Description
A	Anisotropy
API	Application Programming Interface
ASF	Alaska Satellite Facility
BOA	Bottom-Of-Atmosphere
CART	Classification And Regression Trees
CC	Circularly transmitted Circularly received
CNN	Convolutional Neural Network
CP	Compact Polarimetry
CPD	Co-polarized Phase Difference
CRF	Conditional Random Field
CSA	Canadian Space Agency
CWCS	Canadian Wetland Classification System
DBN	Deep Belief Net
DEM	Digital Elevation Model
DL	Deep Learning
DP	Dual Polarimetry
DT	Decision Tree
EMMS	Wetland Mapping and Monitoring System
ENL	Equivalent Number of Look
EO	Earth Observation
EPD-ROA	Edge-Preservation Degree based on the Ratio of Average

FLDA	Fisher Linear Discriminant Analysis
FP	Full Polarimetry
FQ	Fine Quad
FR	Faraday Rotation
GEE	Google Earth Engine
GMRF	Gaussian Markov Random Field
GPS	Global Positioning System
GRD	Ground Range Detected
H	Entropy
HH	Horizontal transmit and Horizontal receive
HP	Hybrid Polarimetry
HV	Horizontal transmit and Vertical receive
IDAN	Intensity-Driven Adaptive Neighborhood
IW	Interferometric Wide
JM	Jeffries–Matusita
K	Kappa coefficients
LAE	Line-And-Edge
LIDAR	Light Detection and Ranging
LSE	Least Square Estimator
MAP	Maximum A Posterior
ML	Maximum Likelihood
MLC	Maximum Likelihood Classification
MMSE	Minimum Mean-Square Error

MRF	Markov Random Field
MRS	Multi-Resolution Segmentation
MVRI	Mean and Variance of Ratio Image
NDVI	Normalized Difference Vegetation Index
NDWI	Normalized Difference Water Index
NL	Newfoundland and Labrador
NL-SAR	Non-Local SAR
OA	Overall Accuracy
OBIA	Object-Based Image Analysis
PA	Producer Accuracy
PDF	Probability Distribution Function
PolSAR	Polarimetric Synthetic Aperture Radar
PRF	Pulse Repetition Frequency
RCM	RADARSAT Constellation Mission
RELU	Rectified Linear Unit
RF	Random Forest
RS	Remote Sensing
SA	Simulated Annealing
SAE	Stacked Auto-Encoder
SAR	Synthetic Aperture Radar
SGD	Stochastic Gradient Descent
SMBF	Scattering Model-Based Filter
SNIC	Simple Non-Iterative Clustering

SVM	Support Vector Machine
SWIR	Shortwave Infrared
TOA	Top-Of-Atmosphere
TV	Total Variation
UA	User Accuracy
VH	Vertical transmit and Horizontal receive
VV	Vertical transmit and Vertical receive
α	Alpha angle

Letters in equations	Description
S	Scattering matrix
S_{HV}	Scattering coefficient of horizontal receiving and vertical transmitting
K	Pauli complex vector
T	Coherency matrix
A_k	Amplitude
φ_k	Phase
$E(\hat{I})$	Mean
$Var(\hat{I})$	Variance
y_i	Observed value
x_i	Noise-free signal
n_i	Speckle noise
$\hat{x}$	De-speckled value

θ	Model parameter
B	Inverse of coherency matrix
z	Normalization constant
$U(x)$	Energy function
$\hat{x}_{MAP}$	Maximum a posteriori (MAP)
$T_{11}{}', T_{22}{}',$ and $T_{33}{}'$	De-speckled diagonal elements of the coherency matrix
K	Normalized Kennaugh
P_G	Polarization content
T_m	Modified coherency matrix
F_t	Final weighting matrix
C	Coherency matrix
JM	JM distance
B	Bhattacharyya distance
χ^2	chi-square

Chapter 1. Introduction

1.1. Overview

A simple, straightforward definition for wetlands is that " wetlands are environments subject to permanent or periodic inundation or prolonged soil saturation sufficient for the establishment of hydrophytes and/or the development of hydric soils or substrates unless environmental conditions are such that they prevent them from forming" [1]. Another definition based on the Ramsar Convention on wetlands is that "wetlands are areas of marsh, fen, peatland, or water, whether natural or artificial, permanent or temporary, with water that is static or flowing, fresh, brackish, or salt, including areas of marine water the depth of which at low tide does not exceed six meters". This disparity in terms of wetland definition is because they are being subjected to both spatial and temporal hydrological variations, surrounded by upland and open water, as well as the variability of their spatial distribution and extent, thus making a concise definition of wetlands difficult [2]. Despite this, there is consensus that wetlands support hydrology and vegetation [3].

Wetlands provide several key roles in maintaining ecosystem functions globally. They play an important role in hydrological and biogeochemical cycles, significantly contribute to wildlife habitat, and offer several services to humankind [4]. For example, according to the Millennium Ecosystem Assessment Report on Wetlands and Water, the annual combined global value of wetlands, tidal marshes and swamp ecosystem services is US$ 44,355 ha^{-1} year^{-1}[5] , which is significantly higher than that of forest ecosystems (US$ 3,278) [6]. Despite these benefits, wetlands have degraded by 64% to 71 % due to land reclamation, hydrological changes, and extensive agricultural and industrial activities, as well as pollution during the twentieth century [7], [8].

Traditional approaches for wetland mapping, such as point-based measurements of biochemical, ecological, and hydrological variables through ground surveying techniques, are laborious and costly, especially on large scales [4]. In this regard, remote sensing (RS) is a key tool, which is of great benefit for mapping and monitoring different aspects of wetland ecosystems, as it captures a synoptic and multi-temporal view of landscapes [9], [10]. There are varieties of Earth Observation (EO) data that may be useful to aid in our understanding of spatial and temporal variability of wetlands [11]. These include data collected by airborne and spaceborne (satellites) missions, as well as unmanned aerial vehicles. These data may be also a high resolution single scene or a medium to high resolution time series of imagery collected by optical or Synthetic Aperture RADAR (SAR) sensors [7]. Accordingly, the selection of the most appropriate EO data for wetland studies depends on several factors. This is because wetlands represent diversity according to their geographic location, dominant vegetation types, hydrology, and soil and sediment types [3].

1.2. Background

The application of aerial photography was among the earliest attempts for wetland mapping and characterization [11]. Having high spatial resolution, cost- and time-efficiency made aerial photographs an important source of information for wetland mapping, especially in early developmental stages of satellite RS sensors. Prior to the availability of satellite imagery, aerial photography techniques were primarily employed for wetland mapping through visual interpretation [12]. This was a challenging task, given the complexity of wetland ecosystems and the variation of biophysical parameters, such as water level, phenological cycle, and vegetation biomass and density [13]. Despite these challenges, several studies reported the success of wetland characterization using aerial photography in the United States [14], [15], Austria [16], and Canada

2

[17]. One of the main challenges of wetland mapping using aerial photography is its inability to map wetlands on large scales. As such, after the launch of satellites (particularly Landsat), aerial photography has been mainly used for the preparation of the training data and the classification accuracy assessment [11].

Multispectral satellite imagery is the most common type of EO data used for wetland classification. These data include coarse (>100m: e.g., MODIS and AVHRR), medium (>10m; Landsat, ASTER, SPOT), and high (<5; IKONOS, Quickbird, and WorldView) spatial resolution imagery. Among coarse spatial resolution optical data, MODIS images have been extensively used in several studies of wetland [18], [19] and water body mapping [20], [21] due to their spectral, temporal, and spatial resolution relative to other global sensors. Because of its lower spectral and coarse spatial resolution, sparse studies reported the capability of AVHRR imagery for wetland characterization [22]. Medium resolution multispectral images have also been widely used for wetland mapping. In particular, data collected by Landsat sensors were used for mapping wetland extent [23], discriminating various wetland vegetation classes [24], and change detection [25] due to their relatively adequate temporal and spatial resolution and, importantly, free availability.

High spatial resolution multispectral data are advantageous for the determination of wetland boundaries and identification of small-sized wetland classes. These data significantly improved the accuracy of wetland classification. High spatial resolution data collected by IKONOS and WorldView-2, for example, were used in various wetland studies, including the production of a coastal wetland map [26], shoreline change detection [27], and mangrove mapping [28], [29]. Despite the benefit of these data for wetland studies, very detailed information within imagery causes challenges in pixel-based classification approaches. Accordingly, advanced image analysis techniques, such as object-based image analysis (OBIA), have been developed to address the

limitations of pixel-based classifications using high spatial resolution images [30], [31]. As such, several studies reported the success of wetland mapping using the object-based approach using high spatial resolution data collected by WorldView-2 [32] and IKONOS [33].

Hyperspectral sensors contain tens to hundreds of narrow bands, thus improving the discrimination of wetland vegetation types [34]. Hyperspectral images collected by hand-held, airborne, and satellite instrumentation have been used in various wetland studies, such as wetland classification, wetland species identification, plant leaf chemistry studies, and in wetland soil analysis [11]. These data are advantageous for mapping complex and similar wetland classes due to the availability of various bands and continuous reflectance values relative to multispectral imagery. The success of mapping tidal marshes [35], salt marshes [36], and marsh habitats [37] using hyperspectral imagery has been reported in the literature. Other studies also reported promising results for identification of mangrove species using various hyperspectral data [38].

The advent of Synthetic Aperture RADAR (SAR) imagery has significantly altered wetland mapping and monitoring using EO data. This is because spaceborne SAR sensors are capable of acquiring EO data independent of solar radiations and day/night conditions, thus addressing the main limitations of optical imagery [39]. Furthermore, SAR signals have the capability of penetrating through soil and vegetation, which make them advantageous for wetland studies [10]. As such, several studies reported the success of wetland classification using SAR imagery collected from various sensors, such as ERS-1/2 [40], JERS-1 [41], ALOS PALSAR-1 [42], RADARSAT-1 [43], RADARSAT-2 [44], TerraSAR-X [45], and Sentinel-1 [46].

The capability of SAR signals for mapping various wetland classes depends on SAR operating parameters and the type of wetland classes [47]. For example, longer wavelengths are advantageous for monitoring forested wetland, given their deeper penetration capability.

Furthermore, SAR signals with steep incidence angles and HH polarization have a superior capability to monitor flooded vegetation [48]. Notably, polarimetric SAR (PolSAR) and, in particular, full polarimetric SAR data are advantageous relative to SAR imagery for wetland class characterization. This is because the various backscattering mechanisms of ground targets are collected by PolSAR data[10]. Furthermore, full polarimetric data allow the application of advanced polarimetric decomposition techniques that discriminate ground targets according to their types of scattering mechanisms. This is of great benefit for characterizing ground targets with similar backscattering mechanisms, such as wetland complexes. The details of the capability of various polarimetric data are presented in Chapters 3, 4, and 5.

Despite the great capability of SAR and PolSAR images for wetland and land cover mapping, the radiometric quality of both data is hindered by speckle noise caused by the coherent interference of waves reflected from many elementary scatterers [39]. The presence of speckle complicates radar image interpretation, degrades the image segmentation performance, and reduces the detectability of targets in the images [49]. This highlights the significance of employing an efficient speckle reduction as a mandatory pre-processing step in studies based on SAR imagery. As such, several speckle reduction methods have been introduced for SAR and PolSAR imagery [50]–[52]. A detailed description of various speckle reduction methods along with the introduction of a new speckle reduction technique are presented in Chapter 2.

In addition to the type of data, the accuracy of wetland classification depends on the classification algorithms. Generally, non-parametric classification algorithms are advantageous relative to the parametric approaches, particularly for classification of SAR and PolSAR data [53]. This is because the former techniques are independent of input data distribution and they have the capability of handling a large volume of multi-temporal imagery during the classification scheme

[4]. Accordingly, several studies reported the success of wetland classification using non-parametric classification algorithms, such as decision trees (DT) [43], support vector machine (SVM) [54], and random forest (RF) [55]. The details of the advantages and disadvantages of different machine learning tools is provided in Chapters 3, 4, and 5.

Despite the great capability of conventional machine learning tools for land cover and wetland classification, the accuracy of pixel-based classification algorithms may be insufficient. This is because these approaches are based only on the statistical distribution of pixels and ignore the contextual and neighbouring information of a given pixel [30]. As such, object-based classification approaches yield better results than the former, as they take into account both the spectral and spatial information of a given pixel [31]. These advanced tools allow the integration of various EO data with different spectral and spatial resolutions, which is beneficial for wetland mapping.

Due to the advantages mentioned above, several studies demonstrated the capability of conventional machine learning tools (e.g., SVM and RF) for the classification of wetland complexes using object-based image analysis techniques [56], [57]. However, the accuracy of wetland classification using the aforementioned tools depends on the number of input features incorporated into the classification scheme. The process of extracting amenable features, also known as feature engineering design, is laborious and requires profound knowledge [58]. Therefore, deep learning (DL) methods have recently drawn attention for several computer vision and remote sensing applications [59]. Deep Belief Net (DBN), Stacked Auto-Encoder (SAE), and deep Convolutional Neural Network (CNN) are current deep learning models, of which the latter is most well-known [60]. CNNs are characterized by multi-layered interconnected channels, with a high capacity for learning the features and classifiers from data spontaneously given their deep architecture, their capacity to adjust parameters jointly, and to classify simultaneously [26]. One

of the ubiquitous characteristics of such a configuration is its potential to encode both spectral and spatial information into the classification scheme in a completely automated workflow [61]. Accordingly, several studies investigated the capability of CNNs for a variety of remote sensing applications, such as scene classification [62], semantic segmentation [63], and object detection [64]. The details of the capability of deep CNNs and their application are presented in Chapter 6.

Although the methodologies and results for wetland mapping using the above-mentioned techniques were sound, wetland classification on large scales remains challenging. In particular, precise, consistent, and comprehensive wetland inventories are lacking on large scales [4]. This is attributed to the low availability of powerful processing systems, which are capable of handling a large volume of remote sensing data, and unavailability of EO data with a sufficient spatial and temporal resolution on large scale [65]. Most recently, the increasing availability of large-volume open-access EO data, such as Sentinel-1 and Sentinel-2 data [66], and the development of powerful cloud computing resources, such as Google Earth Engine (GEE), offer new opportunities for monitoring ecosystems on large scales [67]. Several recent studies highlighted the capability of GEE and open access EO data (e.g., Landsat, Sentinel-1, and Sentinel-2) for a variety of large-scale applications, such as global surface water mapping [68], global forest-cover change mapping [69], and large-scale cropland mapping [70]. Chapter 7 provides the details of recent advances of cloud computing resources and open access data for land cover and wetland mapping on large scales.

1.3. Research motivations

Despite several wetland research studies that have used optical and SAR imagery worldwide (e.g., [42], [55], [71]), the accuracy of wetland classification is still less than adequate. Although some

research reported an acceptable result by integrating various sources of EO data (e.g., optical, SAR, and high resolution digital elevation model (DEM)), many others found insufficient semantic information obtained from single-source EO data [11]. Accordingly, this PhD thesis bridges the main technological gaps in the existing techniques by introducing several innovative classification schemes. In particular, a comprehensive literature review of existing techniques revealed the following technological gaps:

i. The importance of the pre-processing step for classification of SAR and PolSAR imagery is not taken into account. However, an efficient speckle reduction of SAR imagery can significantly affect the accuracy of further image processing.

ii. The complexity and similarity of various wetland classes are ignored. Many developed techniques are based on a single stream classification algorithm rather than hierarchical approaches.

iii. In several wetland studies using PolSAR imagery, the typical PolSAR features were only incorporated into the classification scheme. As such, the statistical and physical characteristics of PolSAR imagery are not considered for enhancing the capability of such data for land cover and, in particular, wetland mapping.

iv. The effect of employing highly correlated features is ignored in almost all existing developed methods for land cover and wetland classification.

v. Despite the great potential of deep CNNs for various remote sensing applications, little to no research has examined the capability of state-of-art classification algorithms for mapping complex land cover ecosystems.

vi. Existing wetland inventory maps are fragmented, incomplete, inconsistent, and incomparable with each other globally. This highlights the significance of developing

provincial- and national-scale wetland inventory maps using advanced remote sensing tools and data.

In addition to identifying technological gaps in the existing literature and mitigating these limitations, another strong motivation behind conducting this research is to map and monitor Newfoundland and Labrador (NL), which is one of the richest Canadian provinces in terms of wetlands and biodiversity. In particular, despite vast expanses of wetland classes across NL, less research has been conducted for monitoring wetlands across NL and, importantly, mapping wetland on provincial-scale is completely ignored. Having identified challenges in the literature, this thesis improves and fills the technical gaps for mapping wetlands in NL and beyond using advanced remote sensing tools and data by introducing markedly novel techniques.

1.4. Scope and objectives

The scope of this study is to map wetlands using both optical and PolSAR imagery using advanced remote sensing tools. Much effort is devoted to take into account various aspects of wetland mapping using EO data. For example, this research investigates the importance of employing pre-processing steps on the accuracy of further image analysis. This study also addresses the issue of backscattering/spectrally similar wetland classes by proposing or employing several novel classification schemes using either conventional machine learning tools or state-of-the-art deep learning methods. The developed classification tools in this work are best suited for discriminating land cover classes with similar spectral or backscatter signatures, such as sea ice, where heterogeneous and fragmented landscape hinder the effectiveness of conventional remote sensing tools.

Six papers compose the main contribution of this thesis, and the main objectives are to:

i.   investigate the importance of an efficient speckle reduction method on the accuracy of wetland classification (Paper 1);

ii.   propose a new hierarchical classification scheme, specifically designed for distinguishing similar wetland classes (Paper 2);

iii.   introduce a new PolSAR feature, known as the modified coherency matrix, that considers both statistical and physical characteristics of PolSAR data (Paper 3);

iv.   examine the capability of simulated compact polarimetry (CP) SAR data for mapping wetlands (Paper 4);

v.   develop a deep learning framework compatible with optical remote sensing data for mapping wetlands (Paper 5);

vi.   leverage the capability of cloud computing resources and open access EO data for mapping wetlands on a provincial scale (Paper 6).

All of these methodologies were applied to case studies in NL and they have the potential to be applied elsewhere.

1.5. Contribution and novelty

This section provides an overview of the contributions of this doctoral dissertation and its significance in improving the existing methodologies for mapping complex land cover ecosystems, particularly in effectively classifying wetlands. In this regard, a comprehensive literature review of wetland mapping using remote sensing data and techniques was carried out to identify potential methodologies and mathematical tools, which are beneficial for addressing identified challenges in the existing literature. A brief description of the main methodological contributions and

novelties of this PhD thesis are described below, the details of which are presented in relevant chapters of this study.

1.5.1. PolSAR pre-processing: a novel speckle reduction method

Since the introduction of SAR imagery in the early 1980s, several speckle reduction methods have been proposed to address this common drawback of SAR imagery (e.g., [50]–[52]). The continued development of new speckle reduction methods in SAR and PolSAR image applications highlights that existing techniques are yet far from what is required for practical applications. Therefore, this work provides an improvement to the current techniques by introducing a new speckle reduction method based on an adaptive Gaussian Markov Random Field model [72]. Notably, one of the most innovative aspects of this proposed method is its application in a practical case study to map wetlands in NL. The details of the proposed method and its comparison with well-known de-speckling methods are presented in Chapter 2.

1.5.2. A novel hierarchical framework for wetland classification

Most techniques developed for land cover mapping consider the classification problem as a single stream image processing chain [55], [57]. While this may be a good, straightforward approch for distinguishing typical land cover classes, it is not optimal for discriminating land cover classes with similar backscattering/spectral signatures. Therefore, this study introduces a novel hierarchical classification scheme to discriminate wetland classes depending on their degree of complexity [73]. Some classes, such as shallow- and deep-water, are much easier to distinguish compared to other wetland classes (e.g., bog and fen), as they are characterized by a single dominant scattering mechanism. Additionally, the capability of various EO data collected from multi-frequency SAR sensors, namely ALOS PALSAR-2 L-band, RADARSAT-2 C-band, and

11

TerraSAR-X, was examined for wetland mapping. To the best of the author's knowledge, this study is the first to discriminate Canadian wetland classes using this new hierarchical classification scheme and such enhanced SAR observations. Chapter 3 presents a detailed description of the proposed method along with the classification results.

1.5.3. Fisher Linear Discriminant Analysis of PolSAR data

Full polarimetric SAR imagery contains full scattering information from ground targets and such data are advantageous compared to dual- and single-polarimetric SAR data in terms of information content [74]. Despite these benefits, the classification accuracy using such data may be less than adequate, as the accuracy greatly depends on the polarimetric features that are incorporated into the classification scheme. To address this limitation, a novel feature weighting approach for PolSAR imagery is proposed based on the integration of Fisher Linear Discriminant Analysis (FLDA) and the physical interpretation of PolSAR data. The obtained feature from the proposed method was found to be advantageous compared to several well-known PolSAR features [44]. The details of the proposed algorithm and its experimental results are presented in Chapter 4.

1.5.4. Wetland classification using simulated compact Polarimetric SAR data

The upcoming RADARSAT Constellation Mission (RCM) will continue the Canadian Space Agency's (CSA) program for acquiring SAR data through its scheduled launch in 2019 [74]. RCM contains three C-band satellites and will collect Compact Polarimetric (CP) SAR data with enhanced temporal resolution compared to RADARSAT-2 [75]. The investment in this advanced SAR mission indicates that SAR will continue to be one of the most important mapping tools in Canada. This also highlights that developed methods using RADARSAT-2 will need to be evaluated for their transferability to the new RCM data format. Accordingly, this study assesses

the capability of simulated CP SAR data for classification of wetland complexes. Furthermore, the classification results obtained from simulated CP SAR data are compared with those of full- and dual-pol SAR data [76]. Chapter 5 represents a detailed description of the methodology adopted in this study.

1.5.5. Deep learning models for wetland classification using satellite data

Most recently, deep CNNs have gained increasing interest for a variety of computer vision and, subsequently, remote sensing tasks [59]. While several studies have employed high and very high-resolution aerial imagery for classification of typical land cover classes (e.g., water, vegetation, and built-up) using state-of-the-art deep CNNs [63], [77], little to no research has examined the capability of multi-spectral satellite data for the classification of land cover classes with similar spectral signatures (e.g., wetlands). Most developed techniques use only three input bands (i.e., red, green, and blue), as this is compatible with the intrinsic structure of these deep CNNs [77]. Furthermore, several studies only introduced or adopted relatively shallow-structured CNNs for their classification tasks [78], [79]. Accordingly, we develop a framework in Python for classification of multi-spectral remote sensing data with five input bands using several well-known deep CNNs currently employed in computer vision, including DenseNet121 [80], InceptionV3 [81], VGG16, VGG19 [82], Xception [83], ResNet50 [84], and InceptionResNetV2. A detailed description of these advanced tools for wetland classification is presented in Chapter 6.

1.5.6. Large-scale wetland mapping using fusion of PolSAR and optical imagery

Although wetland classification using EO data has been a popular topic over the last two decades [42], [47], [85]–[87], given the cost and infeasibility of wetland mapping on large scales (e.g., provincial- or national-scale), many studies have focused only on small scales (e.g.,[88]). This has

resulted in the production of partial, incomplete, and fragmented wetland inventories globally [4]. For example, although Canada contains 24% of world's wetlands [89], comprehensive wetland inventory maps are lacking in most provinces. Several studies have classified various wetland classes in different Canadian provinces, such as Manitoba [90], Ontario [91], and Nova Scotia [92], yet all on small scales. Leveraging the capability of advanced cloud computing resources and availability of open access EO data, this thesis produces the first provincial scale wetland inventory map of NL. In particular, more than 3000 images collected by Sentinel-1 and Sentinel-2 sensors are used to produce the ever-in-demand inventory map of NL using GEE [93]. Chapter 7 provides a detailed description of the proposed methodology for generating the first provincial-scale wetland inventory map.

1.6. Organization of this doctoral dissertation

This PhD thesis is manuscript-based, comprising six published peer-reviewed journal articles described in Table 1.1.

Table 1.1. Organization of the thesis

Chapter title	Paper title
Chapter 1: Introduction	N/A
Chapter 2: PolSAR pre-processing: a novel speckle reduction method	The effect of PolSAR image de-speckling on wetland classification: introducing a new adaptive method. *Canadian Journal of Remote Sensing*, *43*(5), pp.485-503, (2017).
Chapter 3: A novel hierarchical framework for wetland classification	Random forest wetland classification using ALOS-2 L-band, RADARSAT-2 C-band, and TerraSAR-X imagery. *ISPRS Journal of Photogrammetry and Remote Sensing*, *130*, pp.13-31, (2017).
Chapter 4: Fisher Linear Discriminant Analysis of PolSAR data	Fisher Linear Discriminant Analysis of coherency matrix for wetland classification using PolSAR imagery. *Remote Sensing of Environment*, *206*, pp.300-317, (2018).
Chapter 5: Wetland classification using simulated compact Polarimetric SAR data	An assessment of simulated compact polarimetric SAR data for wetland classification using random forest algorithm. *Canadian Journal of Remote Sensing*, *43*(5), pp.468-484, (2017).
Chapter 6: Deep learning models for wetland classification using satellite data	Very deep convolutional neural networks for complex land cover mapping using multispectral remote sensing imagery. *Remote Sensing*, *10*(7), p.1119, (2018).
Chapter 7: Large-scale wetland mapping using fusion of PolSAR and optical imagery	The first wetland inventory map of Newfoundland at a spatial resolution of 10 m using Sentinel-1 and Sentinel-2 data on the Google Earth Engine cloud computing platform. *Remote Sensing*, *11*(1), p.43, (2019).
Chapter 8: Summary, conclusions, and future outlook	N/A
Appendix. Canadian wetland inventory map	Canadian wetland inventory map through the synergistic use of Sentinel-1 and Sentinel-2 data on the Google Earth Engine cloud computing platform (*Submitted*).

The outline of remaining chapters is described below:

A detailed description of the proposed speckle reduction method for PolSAR imagery appears in Chapter 2. The capability of the proposed method was also compared with several well-known speckle reduction methods and was evaluated for a subsequent image processing task (i.e., wetland classification in this case). Next, a new hierarchical wetland classification scheme that uses data collected from various SAR missions, including ALOS PALSAR-2 L-band, RADARSAT-2 C-band, and TerraSAR-X, is presented in Chapter 3.

In Chapter 4, a novel feature weighting method for PolSAR imagery is proposed. The method is based on both the statistical and physical characteristics of PolSAR data as means for improving the discrimination capability of PolSAR features prior to their incorporation into the classification scheme. The capability of simulated CP SAR data for discriminating Canadian wetland classes is then investigated in Chapter 5. The author also compared the potential of CP data with those of FP and DP SAR data for wetland classification in a study area located in NL.

A detailed description of various, well-known deep CNNs architectures (e.g., Inception and ResNet) is presented in Chapter 6. This is followed by the author's experimental design for the exploitation of these deep CNNs for the classification of multi-spectral imagery. The proposed methodology for the production of the first provincial-scale wetland inventory map of NL is then presented in Chapter 7.

The thesis is drawn to a close in Chapter 8, which contains a brief summary, conclusion, and recommendations and directions for future research. Notably, the candidate also extended the wetland classification's study from Newfoundland (Chapter 7) to the entire country (i.e., Canada). In particular, similar methodologies as those described in Chapter 7 were employed to produce the first wetland inventory map of Canada at a spatial resolution of 10-m based on the synergistic use of Sentinel-1 and Sentinel-2 EO data. The results of this part are presented in the appendix.

1.7. Other publications

In addition to the above-mentioned journal papers, the candidate published or contributed to the following peer-reviewed journal papers and book chapter, either as author or co-author, during his PhD program.

- **Mahdianpari, M.,** Salehi, B., Mohammadimanesh, F., Larsen, G. and Peddle, D.R., 2018. Mapping land-based oil spills using high spatial resolution unmanned aerial vehicle imagery and electromagnetic induction survey data. *Journal of Applied Remote Sensing*, *12*(3), p.036015.

- **Mahdianpari, M.,** Motagh, M., Akbari, V., Mohammadimanesh, F. and Salehi, B., 2019. A Gaussian Random Field Model for De-speckling of Multi-polarized Synthetic Aperture Radar Data. *Advances in Space Research*.

- Rezaee, M., **Mahdianpari, M.,** Zhang, Y. and Salehi, B., 2018. Deep convolutional neural network for complex wetland classification using optical remote sensing imagery. *IEEE Journal of Selected Topics in Applied Earth Observations and Remote Sensing*, 11(9), pp.3030-3039.

- Mohammadimanesh, F., Salehi, B., **Mahdianpari, M.,** English, J., Chamberland, J. and Alasset, P.J., 2019. Monitoring surface changes in discontinuous permafrost terrain using small baseline SAR interferometry, object-based classification, and geological features: a case study from Mayo, Yukon Territory, Canada. *GIScience & Remote Sensing*, *56*(4), pp.485-510.

- Mohammadimanesh, F., Salehi, B., **Mahdianpari, M.,** Brisco, B. and Motagh, M., 2018. Wetland water level monitoring using interferometric synthetic aperture radar (InSAR): A review. *Canadian Journal of Remote Sensing*, 44(4), pp.247-262.

- Mohammadimanesh, F., Salehi, B., **Mahdianpari, M.,** Brisco, B. and Motagh, M., 2018. Multi-temporal, multi-frequency, and multi-polarization coherence and SAR backscatter analysis of wetlands. *ISPRS Journal of Photogrammetry and Remote Sensing*, 142, pp.78-93.

- Mohammadimanesh, F., Salehi, B., **Mahdianpari, M.,** Motagh, M. and Brisco, B., 2018. An efficient feature optimization for wetland mapping by synergistic use of SAR intensity, interferometry, and polarimetry data. *International Journal of Applied Earth Observation and Geoinformation*, *73*, pp.450-462.

- Mohammadimanesh, F., Salehi, B., **Mahdianpari, M.,** Brisco, B. and Gill, E., 2019. Full and Simulated Compact Polarimetry SAR Responses to Canadian Wetlands: Separability Analysis and Classification. *Remote Sensing, 11(5)*, p. 516.

- Mohammadimanesh, F., Salehi, B., **Mahdianpari, M.,** Gill, E. and Molinier, M., 2019. A new fully convolutional neural network for semantic segmentation of polarimetric SAR imagery in complex land cover ecosystem. *ISPRS Journal of Photogrammetry and Remote Sensing*, *151*, pp.223-236.

- **Mahdianpari, M.,** Salehi, B., Mohammadimanesh, F., Brisco, B., Homayouni, S., Gill, E., and Bourgeau-Chavez, L. 2019. Canadian wetland inventory map through the synergistic use of Sentinel-1 and Sentinel-2 data on the Google Earth Engine cloud computing platform. *Submitted*.

- Salehi, B., **Mahdianpari, M.,** Amani, M., Mohammadimanesh, F., Granger, J., Mahdavi, S. and Brisco, B., 2018. A collection of novel algorithms for wetland classification with SAR and optical data. In *Wetlands*. IntechOpen. (Book Chapter)

1.8. References

[1]   R. W. Tiner, *Wetland indicators: A guide to wetland formation, identification, delineation, classification, and mapping*. CRC press, 2016.

[2]   W. J. Mitsch and J. G. Gosselink, "The value of wetlands: importance of scale and landscape setting," *Ecol. Econ.*, vol. 35, no. 1, pp. 25–33, 2000.

[3]   W. Meng *et al.*, "Status of wetlands in China: A review of extent, degradation, issues and recommendations for improvement," *Ocean Coast. Manag.*, vol. 146, pp. 50–59, 2017.

[4]   R. W. Tiner, M. W. Lang, and V. V Klemas, *Remote sensing of wetlands: applications and advances*. CRC press, 2015.

[5]   M. E. Assessment, *Ecosystems and human well-being: wetlands and water*. World Resources Institute, 2005.

[6]   R. Costanza *et al.*, "The value of the world's ecosystem services and natural capital," *Nature*, vol. 387, no. 6630, p. 253, 1997.

[7]   P. Kandus *et al.*, "Remote sensing of wetlands in South America: Status and challenges," *Int. J. Remote Sens.*, vol. 39, no. 4, pp. 993–1016, 2018.

[8]   R. C. Gardner *et al.*, "State of the world's wetlands and their services to people: a compilation of recent analyses," 2015.

[9]   A. L. Gallant, "The challenges of remote monitoring of wetlands." Multidisciplinary Digital Publishing Institute, 2015.

[10]   B. Brisco, "Mapping and monitoring surface water and wetlands with synthetic aperture radar," *Remote Sens. Wetl. Appl. Adv.*, pp. 119–136, 2015.

[11]   M. Guo, J. Li, C. Sheng, J. Xu, and L. Wu, "A review of wetland remote sensing," *Sensors*, vol. 17, no. 4, p. 777, 2017.

[12]   W. Z. Madison, "Wetland mapping from digitized aerial photography," *Photogramm. Eng. Remote Sensing*, vol. 47, no. 6, pp. 829–838, 1981.

[13]   M. D. Cline, R. A. Feagin, K. M. Yeager, and J. M. Van Alstyne, "Fault-induced wetland loss at Matagorda, Texas, USA: land cover changes from 1943 to 2008," *Geocarto Int.*, vol. 26, no. 8, pp. 633–645, 2011.

[14]   R. W. Tiner Jr, "Use of high-altitude aerial photography for inventorying forested wetlands in the United States," *For. Ecol. Manage.*, vol. 33, pp. 593–604, 1990.

[15]   K. Tuxen *et al.*, "Mapping changes in tidal wetland vegetation composition and pattern across a salinity gradient using high spatial resolution imagery," *Wetl. Ecol. Manag.*, vol. 19, no. 2, pp. 141–157, 2011.

[16]   P. E. R. Dale, K. Hulsman, and A. L. Chandica, "Classification of reflectance on colour infrared

aerial photographs and sub-tropical salt-marsh vegetation types," *Int. J. Remote Sens.*, vol. 7, no. 12, pp. 1783–1788, 1986.

[17]   S. B. Matthews, "An assessment of bison habitat in the Mills/Mink Lakes area, Northwest Territories, using LANDSAT thematic mapper data," *Arctic*, pp. 75–80, 1991.

[18]   D. Pflugmacher, O. N. Krankina, and W. B. Cohen, "Satellite-based peatland mapping: Potential of the MODIS sensor," *Glob. Planet. Change*, vol. 56, no. 3–4, pp. 248–257, 2007.

[19]   C. Petus, M. Lewis, and D. White, "Monitoring temporal dynamics of Great Artesian Basin wetland vegetation, Australia, using MODIS NDVI," *Ecol. Indic.*, vol. 34, pp. 41–52, 2013.

[20]   H. Mizuochi, T. Hiyama, T. Ohta, and K. Nasahara, "Evaluation of the surface water distribution in north-central Namibia based on MODIS and AMSR series," *Remote Sens.*, vol. 6, no. 8, pp. 7660–7682, 2014.

[21]   C. Ordoyne and M. A. Friedl, "Using MODIS data to characterize seasonal inundation patterns in the Florida Everglades," *Remote Sens. Environ.*, vol. 112, no. 11, pp. 4107–4119, 2008.

[22]   M. L. Zoffoli, P. Kandus, N. Madanes, and D. H. Calvo, "Seasonal and interannual analysis of wetlands in South America using NOAA-AVHRR NDVI time series: the case of the Parana Delta Region," *Landsc. Ecol.*, vol. 23, no. 7, pp. 833–848, 2008.

[23]   M. Jia *et al.*, "Mapping China's mangroves based on an object-oriented classification of Landsat imagery," *Wetlands*, vol. 34, no. 2, pp. 277–283, 2014.

[24]   S. Rapinel, J.-B. Bouzillé, J. Oszwald, and A. Bonis, "Use of bi-seasonal Landsat-8 imagery for mapping marshland plant community combinations at the regional scale," *Wetlands*, vol. 35, no. 6, pp. 1043–1054, 2015.

[25]   N.-T. Son, C.-F. Chen, N.-B. Chang, C.-R. Chen, L.-Y. Chang, and B.-X. Thanh, "Mangrove mapping and change detection in Ca Mau Peninsula, Vietnam, using Landsat data and object-based image analysis," *IEEE J. Sel. Top. Appl. Earth Obs. Remote Sens.*, vol. 8, no. 2, pp. 503–510, 2015.

[26]   P. Chen, S. C. Liew, R. Lim, and L. K. Kwoh, "Coastal and marine habitat mapping for the straits of Malacca using SPOT and Landsat data," in *2013 IEEE International Geoscience and Remote Sensing Symposium-IGARSS*, 2013, pp. 2431–2434.

[27]   M. S. Zhu, T. Sun, and D. D. Shao, "Impact of land reclamation on the evolution of shoreline change and nearshore vegetation distribution in Yangtze River estuary," *Wetlands*, vol. 36, no. 1, pp. 11–17, 2016.

[28]   B. Satyanarayana *et al.*, "Long-term mangrove forest development in Sri Lanka: early predictions evaluated against outcomes using VHR remote sensing and VHR ground-truth data," *Mar. Ecol. Prog. Ser.*, vol. 443, pp. 51–63, 2011.

[29]   B. W. Heumann, "An object-based classification of mangroves using a hybrid decision tree—Support vector machine approach," *Remote Sens.*, vol. 3, no. 11, pp. 2440–2460, 2011.

[30]   U. C. Benz, P. Hofmann, G. Willhauck, I. Lingenfelder, and M. Heynen, "Multi-resolution, object-

oriented fuzzy analysis of remote sensing data for GIS-ready information," *ISPRS J. Photogramm. Remote Sens.*, vol. 58, no. 3–4, pp. 239–258, 2004.

[31]   T. Blaschke, "Object based image analysis for remote sensing," *ISPRS J. Photogramm. Remote Sens.*, vol. 65, no. 1, pp. 2–16, 2010.

[32]   N. J. Lantz and J. Wang, "Object-based classification of Worldview-2 imagery for mapping invasive common reed, Phragmites australis," *Can. J. Remote Sens.*, vol. 39, no. 4, pp. 328–340, 2013.

[33]   D. Rokitnicki-Wojcik, A. Wei, and P. Chow-Fraser, "Transferability of object-based rule sets for mapping coastal high marsh habitat among different regions in Georgian Bay, Canada," *Wetl. Ecol. Manag.*, vol. 19, no. 3, pp. 223–236, 2011.

[34]   C. Kuenzer, A. Bluemel, S. Gebhardt, T. V Quoc, and S. Dech, "Remote sensing of mangrove ecosystems: a review. Remote Sens. 3, 878–928." 2011.

[35]   E. Belluco *et al.*, "Mapping salt-marsh vegetation by multispectral and hyperspectral remote sensing," *Remote Sens. Environ.*, vol. 105, no. 1, pp. 54–67, 2006.

[36]   L. Kumar and P. Sinha, "Mapping salt-marsh land-cover vegetation using high-spatial and hyperspectral satellite data to assist wetland inventory," *GIScience Remote Sens.*, vol. 51, no. 5, pp. 483–497, 2014.

[37]   P. H. Rosso, S. L. Ustin, and A. Hastings, "Mapping marshland vegetation of San Francisco Bay, California, using hyperspectral data," *Int. J. Remote Sens.*, vol. 26, no. 23, pp. 5169–5191, 2005.

[38]   T. Kumar, S. Panigrahy, P. Kumar, and J. S. Parihar, "Classification of floristic composition of mangrove forests using hyperspectral data: case study of Bhitarkanika National Park, India," *J. Coast. Conserv.*, vol. 17, no. 1, pp. 121–132, 2013.

[39]   J.-S. Lee and E. Pottier, *Polarimetric radar imaging: from basics to applications*. CRC press, 2009.

[40]   E. S. Kasischke, K. B. Smith, L. L. Bourgeau-Chavez, E. A. Romanowicz, S. Brunzell, and C. J. Richardson, "Effects of seasonal hydrologic patterns in south Florida wetlands on radar backscatter measured from ERS-2 SAR imagery," *Remote Sens. Environ.*, vol. 88, no. 4, pp. 423–441, 2003.

[41]   Y. Wang, "Seasonal change in the extent of inundation on floodplains detected by JERS-1 Synthetic Aperture Radar data," *Int. J. Remote Sens.*, vol. 25, no. 13, pp. 2497–2508, 2004.

[42]   T. L. Evans and M. Costa, "Landcover classification of the Lower Nhecolândia subregion of the Brazilian Pantanal Wetlands using ALOS/PALSAR, RADARSAT-2 and ENVISAT/ASAR imagery," *Remote Sens. Environ.*, vol. 128, pp. 118–137, 2013.

[43]   M. G. Parmuchi, H. Karszenbaum, and P. Kandus, "Mapping wetlands using multi-temporal RADARSAT-1 data and a decision-based classifier," *Can. J. Remote Sens.*, vol. 28, no. 2, pp. 175–186, 2002.

[44]   M. Mahdianpari *et al.*, "Fisher Linear Discriminant Analysis of coherency matrix for wetland classification using PolSAR imagery," *Remote Sens. Environ.*, vol. 206, 2018.

[45]   C. Wohlfart, K. Winkler, A. Wendleder, and A. Roth, "TerraSAR-X and Wetlands: A Review,"

Remote Sens., vol. 10, no. 6, p. 916, 2018.

[46]   A. Whyte, K. P. Ferentinos, and G. P. Petropoulos, "A new synergistic approach for monitoring wetlands using Sentinels-1 and 2 data with object-based machine learning algorithms," *Environ. Model. Softw.*, vol. 104, pp. 40–54, 2018.

[47]   F. M. Henderson and A. J. Lewis, "Radar detection of wetland ecosystems: a review," *Int. J. Remote Sens.*, vol. 29, no. 20, pp. 5809–5835, 2008.

[48]   F. Mohammadimanesh, B. Salehi, M. Mahdianpari, B. Brisco, and M. Motagh, "Wetland water level monitoring using interferometric synthetic aperture radar (InSAR): A review," *Can. J. Remote Sens.*, pp. 1–16, 2018.

[49]   X. Ma, P. Wu, Y. Wu, and H. Shen, "A review on recent developments in fully polarimetric SAR image despeckling," *IEEE J. Sel. Top. Appl. Earth Obs. Remote Sens.*, vol. 11, no. 3, pp. 743–758, 2018.

[50]   D. T. Kuan, A. A. Sawchuk, T. C. Strand, and P. Chavel, "Adaptive noise smoothing filter for images with signal-dependent noise," *IEEE Trans. Pattern Anal. Mach. Intell.*, no. 2, pp. 165–177, 1985.

[51]   V. S. Frost, J. A. Stiles, K. S. Shanmugan, and J. C. Holtzman, "A model for radar images and its application to adaptive digital filtering of multiplicative noise," *IEEE Trans. Pattern Anal. Mach. Intell.*, no. 2, pp. 157–166, 1982.

[52]   J.-S. Lee, M. R. Grunes, D. L. Schuler, E. Pottier, and L. Ferro-Famil, "Scattering-model-based speckle filtering of polarimetric SAR data," *IEEE Trans. Geosci. Remote Sens.*, vol. 44, no. 1, pp. 176–187, 2006.

[53]   G. Mountrakis, J. Im, and C. Ogole, "Support vector machines in remote sensing: A review," *ISPRS J. Photogramm. Remote Sens.*, vol. 66, no. 3, pp. 247–259, 2011.

[54]   F. Mohammadimanesh, B. Salehi, M. Mahdianpari, M. Motagh, and B. Brisco, "An efficient feature optimization for wetland mapping by synergistic use of SAR intensity, interferometry, and polarimetry data," *Int. J. Appl. Earth Obs. Geoinf.*, vol. 73, pp. 450–462, 2018.

[55]   S. van Beijma, A. Comber, and A. Lamb, "Random forest classification of salt marsh vegetation habitats using quad-polarimetric airborne SAR, elevation and optical RS data," *Remote Sens. Environ.*, vol. 149, pp. 118–129, 2014.

[56]   I. Dronova, P. Gong, and L. Wang, "Object-based analysis and change detection of major wetland cover types and their classification uncertainty during the low water period at Poyang Lake, China," *Remote Sens. Environ.*, vol. 115, no. 12, pp. 3220–3236, 2011.

[57]   L. Dingle Robertson, D. J. King, and C. Davies, "Object-based image analysis of optical and radar variables for wetland evaluation," *Int. J. Remote Sens.*, vol. 36, no. 23, pp. 5811–5841, 2015.

[58]   F. Chollet, *Deep learning with python*. Manning Publications Co., 2017.

[59]   Y. LeCun, Y. Bengio, and G. Hinton, "Deep learning," *Nature*, vol. 521, no. 7553, pp. 436–444,

2015.

[60]   I. Goodfellow, Y. Bengio, A. Courville, and Y. Bengio, *Deep learning*, vol. 1. MIT press Cambridge, 2016.

[61]   M. Rezaee, M. Mahdianpari, Y. Zhang, and B. Salehi, "Deep Convolutional Neural Network for Complex Wetland Classification Using Optical Remote Sensing Imagery," *IEEE J. Sel. Top. Appl. Earth Obs. Remote Sens.*, no. 99, 2018.

[62]   R. M. Anwer, F. S. Khan, J. van de Weijer, M. Molinier, and J. Laaksonen, "Binary patterns encoded convolutional neural networks for texture recognition and remote sensing scene classification," *ISPRS J. Photogramm. Remote Sens.*, vol. 138, pp. 74–85, 2018.

[63]   M. Volpi and D. Tuia, "Dense semantic labeling of subdecimeter resolution images with convolutional neural networks," *IEEE Trans. Geosci. Remote Sens.*, vol. 55, no. 2, pp. 881–893, 2017.

[64]   X. Chen, S. Xiang, C.-L. Liu, and C.-H. Pan, "Vehicle detection in satellite images by hybrid deep convolutional neural networks," *IEEE Geosci. Remote Sens. Lett.*, vol. 11, no. 10, pp. 1797–1801, 2014.

[65]   N. Gorelick, M. Hancher, M. Dixon, S. Ilyushchenko, D. Thau, and R. Moore, "Google Earth Engine: Planetary-scale geospatial analysis for everyone," *Remote Sens. Environ.*, vol. 202, pp. 18–27, 2017.

[66]   R. Torres *et al.*, "GMES Sentinel-1 mission," *Remote Sens. Environ.*, vol. 120, pp. 9–24, 2012.

[67]   J. N. Hird, E. R. DeLancey, G. J. McDermid, and J. Kariyeva, "Google Earth Engine, open-access satellite data, and machine learning in support of large-area probabilistic wetland mapping," *Remote Sens.*, vol. 9, no. 12, p. 1315, 2017.

[68]   J.-F. Pekel, A. Cottam, N. Gorelick, and A. S. Belward, "High-resolution mapping of global surface water and its long-term changes," *Nature*, vol. 540, no. 7633, p. 418, 2016.

[69]   M. C. Hansen *et al.*, "High-resolution global maps of 21st-century forest cover change," *Science (80-.).*, vol. 342, no. 6160, pp. 850–853, 2013.

[70]   P. Teluguntla *et al.*, "A 30-m landsat-derived cropland extent product of Australia and China using random forest machine learning algorithm on Google Earth Engine cloud computing platform," *ISPRS J. Photogramm. Remote Sens.*, vol. 144, pp. 325–340, 2018.

[71]   X. Zhang, B. Wu, G. Ponce-Campos, M. Zhang, S. Chang, and F. Tian, "Mapping up-to-Date Paddy Rice Extent at 10 M Resolution in China through the Integration of Optical and Synthetic Aperture Radar Images," *Remote Sens.*, vol. 10, no. 8, p. 1200, 2018.

[72]   M. Mahdianpari, B. Salehi, and F. Mohammadimanesh, "The Effect of PolSAR Image De-speckling on Wetland Classification: Introducing a New Adaptive Method," *Can. J. Remote Sens.*, vol. 43, no. 5, 2017.

[73]   M. Mahdianpari, B. Salehi, F. Mohammadimanesh, and M. Motagh, "Random forest wetland

classification using ALOS-2 L-band, RADARSAT-2 C-band, and TerraSAR-X imagery," *ISPRS J. Photogramm. Remote Sens.*, vol. 130, pp. 13–31, 2017.

[74]   F. J. Charbonneau *et al.*, "Compact polarimetry overview and applications assessment," *Can. J. Remote Sens.*, vol. 36, no. sup2, pp. S298–S315, 2010.

[75]   M. Dabboor, B. Montpetit, and S. Howell, "Assessment of the High Resolution SAR Mode of the RADARSAT Constellation Mission for First Year Ice and Multiyear Ice Characterization," *Remote Sens.*, vol. 10, no. 4, p. 594, 2018.

[76]   M. Mahdianpari, B. Salehi, F. Mohammadimanesh, and B. Brisco, "An Assessment of Simulated Compact Polarimetric SAR Data for Wetland Classification Using Random Forest Algorithm," *Can. J. Remote Sens.*, vol. 43, no. 5, 2017.

[77]   K. Nogueira, O. A. B. Penatti, and J. A. dos Santos, "Towards better exploiting convolutional neural networks for remote sensing scene classification," *Pattern Recognit.*, vol. 61, pp. 539–556, 2016.

[78]   Y. Liu, D. Minh Nguyen, N. Deligiannis, W. Ding, and A. Munteanu, "Hourglass-shapenetwork based semantic segmentation for high resolution aerial imagery," *Remote Sens.*, vol. 9, no. 6, p. 522, 2017.

[79]   Y. Wang, C. He, X. Liu, and M. Liao, "A Hierarchical Fully Convolutional Network Integrated with Sparse and Low-Rank Subspace Representations for PolSAR Imagery Classification," *Remote Sens.*, vol. 10, no. 2, p. 342, 2018.

[80]   G. Huang, Z. Liu, L. Van Der Maaten, and K. Q. Weinberger, "Densely Connected Convolutional Networks.," in *CVPR*, 2017, vol. 1, no. 2, p. 3.

[81]   C. Szegedy *et al.*, "Going deeper with convolutions," in *Proceedings of the IEEE conference on computer vision and pattern recognition*, 2015, pp. 1–9.

[82]   K. Simonyan and A. Zisserman, "Very deep convolutional networks for large-scale image recognition," *arXiv Prepr. arXiv1409.1556*, 2014.

[83]   F. Chollet, "Xception: Deep learning with depthwise separable convolutions," *arXiv Prepr.*, pp. 1610–2357, 2017.

[84]   K. He, X. Zhang, S. Ren, and J. Sun, "Deep residual learning for image recognition," in *Proceedings of the IEEE conference on computer vision and pattern recognition*, 2016, pp. 770–778.

[85]   E. S. Kasischke and L. L. Bourgeau-Chavez, "Monitoring South Florida wetlands using ERS-1 SAR imagery," *Photogramm. Eng. Remote Sensing*, vol. 63, no. 3, pp. 281–291, 1997.

[86]   M. W. Lang, E. S. Kasischke, S. D. Prince, and K. W. Pittman, "Assessment of C-band synthetic aperture radar data for mapping and monitoring Coastal Plain forested wetlands in the Mid-Atlantic Region, USA," *Remote Sens. Environ.*, vol. 112, no. 11, pp. 4120–4130, 2008.

[87]   L. F. de Almeida Furtado, T. S. F. Silva, and E. M. L. de Moraes Novo, "Dual-season and full-polarimetric C band SAR assessment for vegetation mapping in the Amazon várzea wetlands," *Remote Sens. Environ.*, vol. 174, pp. 212–222, 2016.

[88]   L. White, K. Millard, S. Banks, M. Richardson, J. Pasher, and J. Duffe, "Moving to the RADARSAT constellation mission: Comparing synthesized compact polarimetry and dual polarimetry data with fully polarimetric RADARSAT-2 data for image classification of peatlands," *Remote Sens.*, vol. 9, no. 6, p. 573, 2017.

[89]   E. S. W. G. (Canada), C. for Land, B. R. R. (Canada), and C. S. of the E. Directorate, *A national ecological framework for Canada*. Centre for Land and Biological Resources Research; Hull, Quebec: State of …, 1996.

[90]   B. Brisco, K. Li, B. Tedford, F. Charbonneau, S. Yun, and K. Murnaghan, "Compact polarimetry assessment for rice and wetland mapping," *Int. J. Remote Sens.*, vol. 34, no. 6, pp. 1949–1964, 2013.

[91]   K. Millard and M. Richardson, "On the importance of training data sample selection in random forest image classification: A case study in peatland ecosystem mapping," *Remote Sens.*, vol. 7, no. 7, pp. 8489–8515, 2015.

[92]   R. Jahncke, B. Leblon, P. Bush, and A. LaRocque, "Mapping wetlands in Nova Scotia with multi-beam RADARSAT-2 Polarimetric SAR, optical satellite imagery, and Lidar data," *Int. J. Appl. earth Obs. Geoinf.*, vol. 68, pp. 139–156, 2018.

[93]   M. Mahdianpari, B. Salehi, F. Mohammadimanesh, S. Homayouni, and E. Gill, "The First Wetland Inventory Map of Newfoundland at a Spatial Resolution of 10 m Using Sentinel-1 and Sentinel-2 Data on the Google Earth Engine Cloud Computing Platform," *Remote Sens.*, vol. 11, no. 1, p. 43, 2019.

Chapter 2. PolSAR pre-processing: a novel speckle reduction method[1]

Preface

A version of this manuscript has been published in the *Canadian Journal of Remote Sensing*. I am a primary author of this manuscript along with the co-authors, Bahram Salehi and Fariba Mohammadimanesh. I conceptualized and designed the study. I developed the model and performed all experiments and tests. I wrote the paper and revised it based on comments from all co-authors. I also revised the paper according to the reviewers' comments. The co-author, Fariba Mohammadimanesh, helped in performing the experiments and analyzing the results and contributed to revising the manuscript. All co-authors provided editorial input and scientific insights to further improve the paper. They also reviewed and commented on the manuscript.

---

[1] Mahdianpari, M., Salehi, B. and Mohammadimanesh, F., 2017. The effect of PolSAR image de-speckling on wetland classification: introducing a new adaptive method. *Canadian Journal of Remote Sensing*, *43*(5), pp.485-503.

Abstract

Speckle noise significantly degrades the radiometric quality of PolSAR image and, consequently, decreases the classification accuracy. This paper proposes a new speckle reduction method for PolSAR imagery based on an adaptive Gaussian Markov Random Field model. We also introduce a new span image, called pseudo-span, obtained by the diagonal elements of the coherency matrix based on the least square analysis. The proposed de-speckling method was applied to full polarimetric C-band RADARSAT-2 data from the Avalon area, Newfoundland, Canada. The efficiency of the proposed method was evaluated in two different levels: de-speckled images and classified maps obtained by the Random Forest classifier. In terms of de-speckling, the proposed method illustrated approximately of 19%, 43%, 46%, and 50% improvements in Equivalent Number of Looks (ENL) values, in comparison with SARBM3D, Enhanced Lee, Frost, and Kuan filter, respectively. Also, improvements of approximately 19%, 9%, 55%, and 32% were obtained in the overall classification accuracy using de-speckled PolSAR image by the proposed method compared with SARBM3D, Enhanced Lee, Frost, and Kuan filter, respectively. This new adaptive de-speckling method illustrates to be an efficient approach in terms of both speckle noise suppression and details/edges preservation, while has a great influence on the overall wetland classification accuracy.

2.1. Introduction

Wetlands are transitional lands between terrestrial areas and aquatic systems, which regulate local climate and prevent accelerated rates of climate change. This productive ecosystem provides several advantages, such as filtering contamination, sequestering carbon, supporting wildlife habitat, and several recreational activities [1]. In the recent years, wetland monitoring has gained increasing attention, thanks to the advancement in remote sensing technologies [2]–[4]. Most of these studies highlighted the importance of a wetland inventory map, which distinguishes different wetland classes and is essential for sustainable preservation of this productive ecosystem [5]–[7].

Remote sensing offers both cost- and time-efficient tools for wetland mapping and monitoring by providing data from inaccessible geographic regions [8]. The capability of optical satellite imagery for wetland mapping has been documented in several studies [9]–[14]. However, the main hindrances to optical sensors are cloud coverage and dependency on solar illumination. Synthetic Aperture Radar (SAR) sensors address these limitations, since they are sun-independent, all-weather condition sensors [15]. Furthermore, SAR penetration capability, depending on SAR wavelength, through cloud, soil, and vegetation makes SAR image an ideal tool for land cover classification [16]–[21].

The advent of Polarimetric SAR data greatly enhanced the capability of remote sensing images for land cover classification by providing different characteristics of land surface in different polarizations [22], [23]. A full polarimetric SAR (PolSAR) image has the highest discriminating capability due to multiple polarizations, which make it more efficient in classification of complex land cover such as wetland and sea ice. This is because different scattering mechanisms of ground targets, including surface, double-bounce, and volume scattering are obtainable using PolSAR imagery. Each ground target has a distinct scattering mechanism, which is useful for discrimination

28

of various land cover types. Polarimetric decomposition is a typical technique to extract PolSAR data information [24]–[26].

The main drawback of PolSAR images is the presence of speckle. Speckle is a signal-dependent granular disturbance, which degrades the radiometric quality of PolSAR imagery [27]. Moreover, speckle severely affects the accuracy of further PolSAR image analysis [28]. Thus, applying an efficient speckle reduction method is a necessary pre-processing step in PolSAR image processing [29]. This is because the accuracy of end-user products of SAR images, such as image classification, segmentation, and target detection greatly depends on the quality and reliability of the input data [30].

Over the past decades, several studies have proposed different speckle reduction algorithms for SAR and PolSAR images [31]–[37]. These algorithms are generally divided into four main categories, including filters based on (1) homogeneity criteria [30], [38], [39], (2) a probability distribution assumption [40], [41], (3) patch matching [37], and (4) other techniques [42]–[44]. A brief introduction of some well-known de-speckling methods is presented below.

One of the simplest and commonly used methods is the boxcar filter, wherein the center pixel is replaced with the average of its neighboring pixels [41]. Other commonly-used traditional filters are the Lee, Kuan, and Frost filters, which use a weighted averaging to estimate the statistical parameters over different windows [27], [45], [46]. These traditional approaches are widely used because they can be easily applied; however, they degrade the spatial resolution of images and blur edges and strong targets [41]. To address the limitations associated with traditional approaches, Lee proposed two other de-speckling filters [32], [43]. Specifically, Lee et al. (2006) proposed a scattering model-based filter (SMBF), wherein neighboring pixels with the same

scattering characteristics are selected based on the Freeman-Durden decomposition [43]. Furthermore, Lee et al. (2009) introduced the refined Lee filter. This filter uses the minimum mean-square error (MMSE) technique and edge-aligned non-squared windows to preserve the edges of ground targets as well as image details [32]. Also, Vasile et al. (2006) proposed the intensity-driven adaptive neighborhood (IDAN) filter based on a region-growing technique, which utilized all intensity images [40]. This filter defines an adaptive neighborhood for each pixel and then employs simple averaging. Later, a modified version of the IDAN filter was proposed in order to mitigate the limitations of the original one, which was bias in the radiometric information of the images [47]. Deledalle et al. (2015) suggested a novel patch-wise non-local SAR (NL-SAR) method that smooths images by determining data-driven weights from the similarities between small patches [37]. Lang et al. (2015) proposed an adaptive-window PolSAR de-speckling method based on a line-and-edge (LAE) detector and homogeneity measurement [48]. In particular, a LAE detector algorithm identifies image details (i.e., lines and edges). Next, the Equivalent Number of Looks (ENL) and the LAE maps are integrated to determine polarimetric homogeneity. Then, an adaptive filtering is applied that uses small and non-square windows in heterogeneous areas to preserve detail, and large and square windows in homogeneous regions to maximize suppression of speckle noise. Another speckle filters are knowns as variational methods, which work based on a total variation (TV) regularization, and were first applied for speckle reduction of single SAR images [49], [50]. These methods were later developed for PolSAR image filtering. In particular, Nie et al. (2015) proposed a PolSAR de-speckling based on the complex Wishart distribution of the covariance or coherency matrix and multichannel total variation (TV) regularization [51]. This algorithm was the first de-speckling method based on the TV-based variational model that can be applied to a whole PolSAR coherency or covariance matrix. Most recently, Nie et al. (2016)

proposed a non-local TV-based variational model that has been applied to the covariance or coherency matrix of PolSAR data [52].

Another important criterion in the case of speckle reduction is to evaluate the performance of the de-speckling method. In particular, the effectiveness of a given de-noising method must be assessed based on the success of the subsequent processing tasks (e.g., classification). For this purpose, in addition to well-known de-speckling performance criteria such as ENL, Edge-Preservation Degree based on the Ratio of Average (EPD-ROA), and Mean and Variance of Ratio Image (MVRI), we evaluated the effectiveness of the proposed method on subsequent wetland classification. In particular, the performance of the proposed method was evaluated in terms of wetland classification accuracy and compared with the results of other well-known speckle filter methods. In this paper, a brief review of the theoretical concepts of speckle and polarimetric SAR image formation is first provided. Then, our proposed method for speckle reduction of PolSAR data is explained. Finally, the experimental results, the arguments, and a conclusion are presented.

2.2. PolSAR image and speckle noise characteristics

2.2.1. Polarimetric SAR images

In the last two decades, Synthetic Aperture Radar (SAR) sensors have been established as an important remote sensing tool for environmental and natural resource monitoring, as well as for planetary exploration [53]. SAR, as an active sensor, illuminates targets with electromagnetic pulses that are able to penetrate cloud cover. A full PolSAR sensor measures the amplitude and phase of returned electromagnetic waves in the four combinations of the linear receiving and transmitting polarizations (HH, HV, VH, and VV) [54]. A common representation of PolSAR measurement is a 2x2 complex scattering matrix, $[\boldsymbol{S}]$, and in the case of linear polarization is expressed as follows:

$$S = \begin{bmatrix} S_{HH} & S_{HV} \\ S_{VH} & S_{VV} \end{bmatrix} \quad\quad (2.1)$$

where S_{HV} is the scattering coefficient of horizontal receiving and vertical transmitting. The coherency matrix is another representation of PolSAR data with more physical meaning, and formulated based on the Pauli complex vector as:

$$K = \frac{1}{\sqrt{2}} [S_{HH} + S_{VV} \quad S_{HH} - S_{VV} \quad 2S_{HV}]^T \quad\quad (2.2)$$

The coherency matrix from a single-look image is determined as follows [41]:

$$(2.3)$$

$$T = < K.K^{*T} > = \begin{bmatrix} T_{11} & T_{12} & T_{13} \\ T_{21} & T_{22} & T_{23} \\ T_{31} & T_{32} & T_{33} \end{bmatrix}$$

$$= \begin{bmatrix} \frac{1}{2}\langle |S_{HH} + S_{VV}|^2 \rangle & \frac{1}{2}\langle (S_{HH} + S_{VV})(S_{HH} - S_{VV})^* \rangle & (S_{HH} + S_{VV})S_{HV}^* \\ \frac{1}{2}\langle (S_{HH} - S_{VV})(S_{HH} + S_{VV})^* \rangle & \frac{1}{2}\langle |S_{HH} - S_{VV}|^2 \rangle & \langle (S_{HH} - S_{VV})S_{HV}^* \rangle \\ \langle S_{HV}(S_{HH} + S_{VV})^* \rangle & \langle S_{HV}(S_{HH} - S_{VV})^* \rangle & \langle 2|S_{HV}|^2 \rangle \end{bmatrix}$$

Finally, the span image, which indicates the total received power, is formulated based on diagonal elements of the coherency matrix as:

$$Span = T_{11} + T_{22} + T_{33} \quad\quad (2.4)$$

The following section describes the characteristics of speckle in PolSAR images.

2.2.2. Speckle noise

Speckle is defined as a scattering phenomenon due to the complex nature of scattered waves from observed terrain elements in each resolution cell. The overall objective of de-speckling filters is to estimate the noise-free radar reflectivity of a noisy image for each resolution cell [55]. More precisely, an incident radar pulse interacts with each element of the surface and, depending on the

surface characteristics, the backscatter signals propagate in different directions [56]. Accordingly, the SAR focusing procedure coherently combines all backscatters to produce a SAR image.
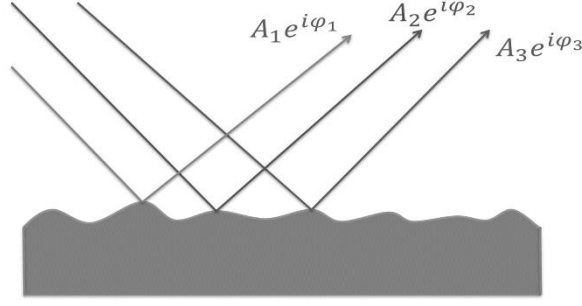
Figure 2.1. Scattering model addressing fully developed speckle.

Given the distributed target assumption [57] (see also Figure 2.1), each resolution cell consists of several scatterers, all of which have equal strength [34]. As a result, the received signal in the sensor is the sum of all backscattered rays in different directions from the target and is presented as follows:

$$A_t \, e^{\, i\varphi_t} = \sum_k A_k \, e^{\, i\varphi_k} \qquad\qquad (2.5)$$

where amplitudes, A_k, and phases, φ_k, are functions of several factors, such as propagation attenuation, scattering of the illuminated targets, and the antenna directivity [58]. Maxwell's equations, which are typically used to model the received signal, were developed based on both propagation geometry and scattering medium [59]. The basic information about the observation scene is obtained by interfering of each propagation path. The amplitude of the received signal changes randomly, since the phases of each path are very different from each other. The scattered wave phase results in both constructive and destructive interference of individual scattered returns, and randomly modulates the strength of the signal in each resolution cell. The received signal is strong if the waves are relatively constructive and weak if the waves are out of phase. Constructive

interference increases mean intensity and produces bright pixels. In contrast, destructive interference decreases mean intensity and produces dark pixels. Both situations are illustrated in Figure 2.2.
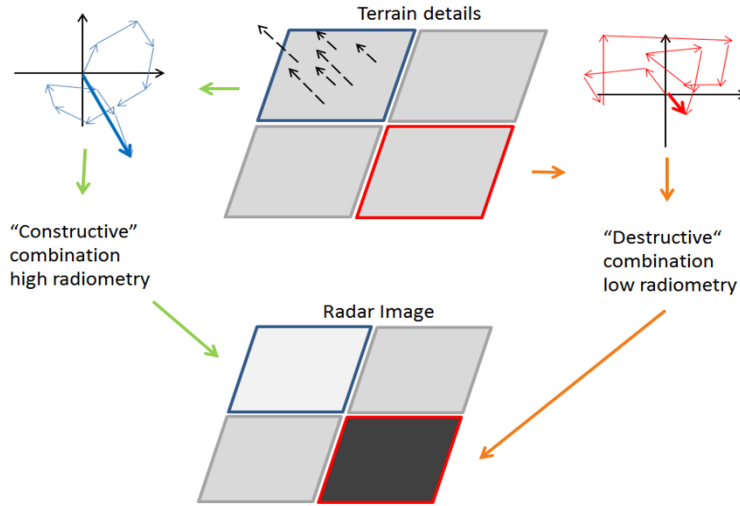
Figure 2.2. Constructive and destructive interference.

In the case of a distributed target, it is demonstrated that intensity measurement comprises information about the average backscattering coefficients. As a result, even in homogeneous areas, SAR images are affected by a "salt and pepper" noise, known as speckle, in a SAR imaging system [60].

As previously mentioned, a full PolSAR image has four polarimetric channels and is represented using a scattering matrix. Given the same statistic for all polarization channel, the statistics of a fully polarized image is described by extending the statistical model of single SAR image [61]. The statistical models of a SAR image defined in three categories in terms of scattering: homogeneous, heterogeneous, and highly heterogeneous. Homogenous area represents an area with low (e.g., slack water and roads) or moderate backscattering (e.g., crops). A heterogeneous

area represents targets with diffusing backscattering towards the sensor (e.g., forests). Finally, a highly heterogeneous area represents targets with strong backscattering (e.g., man-made objects).

2.3. Accuracy assessment parameters

In this paper, we evaluate our proposed de-speckling method in two different steps, a pre-processing and a post-processing step. In the pre-processing step, different de-speckling metrics are used to evaluate the performance of the proposed method in comparison with other well-known de-speckling methods. Since the main purpose of this study is to improve classification accuracy, the capability of the proposed method is further evaluated in terms of classification results. Therefore, assessment of classification accuracy is performed based on the confusion matrix.

2.3.1. Speckle reduction evaluation metrics

The main objectives of PolSAR image filtering are to reduce the speckle noise and to maintain spatial resolution and polarimetric information. In order to evaluate the strength of different de-speckling methods, a number of indices, including ENL, EPD-ROA, and MVRI were employed in this study. These indices are briefly introduced below.

2.3.1.1. Equivalent Number of Looks (ENL)

A common metric to evaluate the de-speckling performance and the degree of speckle suppression in a PolSAR image is ENL, which is calculated over a homogeneous area of the image. The ENL parameter is used to determine algorithm validity in speckle reduction, and is defined as follows:

$$ENL = \frac{E(\hat{I})}{Var(\hat{I})}$$

(2.6)

where $E(\hat{I})$ and $Var(\hat{I})$ are the mean and variance of the de-speckled image. A higher value of ENL corresponds to a better performance of de-speckling method [62].

2.3.1.2. Edge-Preservation Degree based on the Ratio of Average (EPD-ROA)

Another index used in this study for evaluation of the proposed method is EPD-ROA [63], which

is formulated as follows:

$$EPD - ROA = \frac{\sum_{i=1}^{m} |I_{D1}(i)/I_{D2}(i)|}{\sum_{i=1}^{m} |I_{O1}(i)/I_{O2}(i)|} \tag{2.7}$$

where, m is the pixel number of the selected area. $I_{D1}(i)$ and $I_{D2}(i)$ denote the adjacent pixel values

of the de-speckled image along the vertical and horizontal directions, respectively. Also, $I_{O1}(i)$

and $I_{O2}(i)$ illustrate the adjacent pixel values of the original image. The EPD-ROA values closer

to one illustrate the high efficiency of the de-speckling method for edge preservation.

2.3.1.3. Mean and Variance of Ratio Image (MVRI)

To evaluate the capability of the de-speckling method for preservation of polarimetric information,

the two parameters, mean and variance of ratio image are extracted as follows:

$$\mu_r = E(r), \qquad \sigma^2 = Var(r) \tag{2.8}$$

where r denotes the ratio image that is a point-by-point ratio between the original and de-speckled

images and is extracted by:

$$r(i) = \frac{I(i)}{\hat{I}(i)} , i = 1,2,\dots,n \tag{2.9}$$

where I and $\hat{I}$ are the original and de-speckled image, respectively, and n denotes the number of

pixels in the image. This ratio image can be used in a fully developed speckle model, contains

useful information for both the homogeneous and heterogeneous areas, and also represents the

noise pattern removal.

2.3.2. Classification accuracy assessment

For evaluation of classification results, we used Overall Accuracy (OA), commission and omission errors obtained by the classification confusion matrix. The confusion matrix compares the classification results with reference data collected in the field (ground truth). Overall accuracy is calculated by dividing the total number of correctly classified pixels (diagonal elements of confusion matrix) to the total number of pixels [64]. Commission error for class A shows pixels that belong to another class, but are mislabeled to class A. In contrast, omission error represents those pixels that belong to a specific class according to the ground truth data, but the classifier has failed to classify them into the proper class [65].

2.4. Proposed GMRF-based de-speckling method

In this section, we describe our proposed method for speckle reduction of PolSAR imagery. Generally, de-speckling methods are applied to a single intensity channel [66], or the covariance and coherency matrix [36], [67]. In this study, we proposed a new de-speckling approach applied to the coherency matrix that carries the full polarimetric information. One of the advantages of the coherency matrix compared to the covariance matrix is that its diagonal elements are directly related to the physical characteristics (i.e., scattering mechanism) of the ground targets. The three diagonal elements of the coherency matrix T_{11}, T_{22}, and T_{33} are related to the surface, double-bounce, and volume scattering mechanism, respectively. Strong targets, which are not affected by speckle noise, are determined based on the first two elements (T_{11} and T_{22}) [68]. Thus, excluding the strong targets from the de-speckling procedure improves speckle reduction performance and, subsequently, classification results. Most of the standard speckle reduction methods are applied to the entire polarimetric information carried by the coherency and covariance matrix [43], [69].

However, in our new proposed method, strong targets are excluded in order to both reduce the blurring effects and preserve polarimetric information.

In this study, the proposed speckle reduction method consists of 4 main steps. First, the coherency matrix is extracted from the PolSAR imagery. Second, strong point targets are determined using the first two diagonal elements of the coherency matrix (i.e., T_{11} and T_{22}), and excluded from the subsequent processing step. This is because maintaining the signature from strong point targets and man-made objects is desirable for further PolSAR image processing and interpretation. Both double-bounce and direct specular scattering mechanisms generate a strong point target in a SAR image. These two components are found within the T_{11} and T_{22} elements of the coherency matrix, and not found in the T_{33} element. Thus, we used the 98th percentile for detection of strong targets in a small 3x3 window [36]. In the next step, for better preservation of textural and contextual information, the de-speckling filter is applied using a Gaussian Markov Random Field (GMRF) based on a Bayesian framework. Finally, a pseudo-span image is produced using the diagonal elements of the de-speckled coherency matrix. Based on the Bayesian framework, the image can be modelled as a random field, and the de-speckling problem is expressed as an estimation problem. Since each pixel value is generally dependent on the neighboring pixels in the image, the ability of MRF to model spatial dependency is used. Thus, the de-speckling problem is converted to an optimization problem in which the minimization of the Gaussian energy function is solved based on simulated annealing (SA) [70]. Figure 2.3 summarizes the main steps of the proposed method.
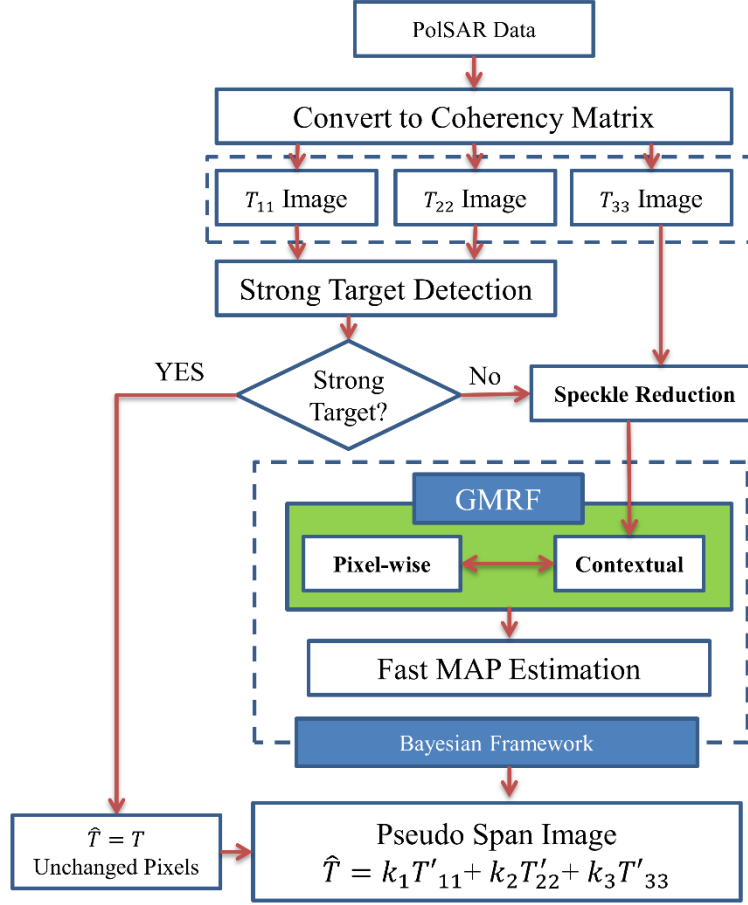
Figure 2.3. The flowchart of the proposed method.

2.4.1. Bayesian framework

Over the last few decades, model-based image techniques are widely applied to solve inverse problems in the field of image processing [71]–[73]. More specifically, the unknown image value x is determined based on the measured value of y in the image de-noising procedure. This is called an inverse problem because x is not directly observed and is determined based on the observed y. This is the main objective of all inversion approaches to estimate $\hat{x}$ of the unknown image value x, from the observation y.

Speckle is considered as a multiplicative noise in the intensity images. Assuming speckle has an individual mean and is independent of the signal, the multiplicative model can be represented as follows [34]:

$$y_i = x_i \times n_i \tag{2.10}$$

where y_i denotes the observed value of the SAR image, x_i represents a noise-free signal response to scatterer, and n_i is the speckle noise. For convenience, the multiplicative noise is rewritten as an additive noise:

$$y_i = x_i + x_i(n_i - 1) \tag{2.11}$$

$$y_i = x_i + N_i \tag{2.12}$$

where in Equation 2.11, $x_i(n_i - 1)$ term is considered as an additive noise (N_i). For simplicity, several studies have established a logarithmic transformation to convert multiplicative noise to additive noise [42], [74]. However, the main drawback of applying logarithmic transformation is that the dynamic range of the original signals is compressed by the logarithm operation.

As shown in Figure 2.3, our proposed speckle reduction method is based on the Bayesian framework. In pixel-wise analysis, prior knowledge can be combined with observations to obtain a logical derivation of the optimal decision for speckle reduction in a Bayesian scheme. The Bayesian framework is used to determine the likelihood model for estimation of speckle and texture in a PolSAR image. The Bayesian rule is defined as follows [35]:

$$\hat{x} = y_{PCM}(y|\theta) \rightarrow P(\hat{x}|y, \theta) = \frac{P(y|\hat{x}, \theta)P(\hat{x}|\theta)}{P(y|\theta)} \propto P(y|\hat{x}, \theta)P(\hat{x}|\theta) \tag{2.13}$$

where y refers to the noisy image, $\hat{x}$ shows the de-speckled image and θ is the model parameters. In the conditional probability distribution function (PDF), the prior probability and the observation are represented by $P(y|\hat{x}, \theta)$, $P(\hat{x}|\theta)$ and $P(y|\theta)$, respectively [75]. Therefore, likelihood and prior PDFs are determined from Equation 2.13. The accomplishment of a Maximum A Posterior (MAP) method requires statistical knowledge of a prior distribution of PolSAR images.

2.4.2. Markov Random Field

Preservation of textural information is important in PolSAR image de-speckling. Notably, textural features should be accurately reconstructed in the de-speckled image. For this purpose, Gaussian Markov Random Fields (GMRFs) were applied as texture models in this study, which used Bayesian inference to gain a maximum a posteriori (MAP) estimate of the de-speckled image. Since Markov Random Field (MRF) models allow integration of prior knowledge of the images, they are commonly applied for regularization. MRFs are known as undirected graphical models and also defined in terms of the conditional independence characteristics of the random variables. More specifically, in a pairwise MRF model, each pixel of an image corresponds to a node. In a first-order neighboring system, the simplest way to define a pairwise MRF is to connect each pixel to its horizontal and vertical neighbors. However, in a second-order neighboring system, each pixel is connected to its eight neighbors. Figure 2.4 illustrates first and second order neighboring systems [76]:
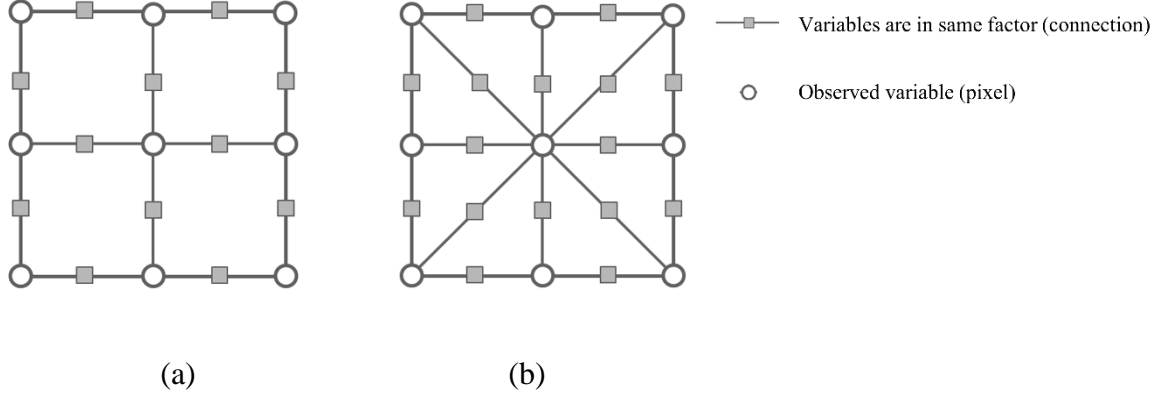
Figure 2.4. (a) First-order neighborhood system (4 connections), (b) Second-order neighborhood system (8 connections).

Prediction is a primary tool in modelling; also, the result of an accurate model is an accurate prediction. Generally, two different orders are used for modelling data based on prediction: casual and non-casual. In casual order, which is the simplest way to predict values, the procedure starts in the past and continues toward the future. Unfortunately, casual order is not an efficient model in the context of visual problems and image de-noising, since it often causes artifacts in the results. Therefore, in the field of image processing, approaches that remove causality from modelling are required. Thus, image models are used to determine the probability distribution for an image based on the differences between neighboring pixels. For this purpose, a GMRF model is used as an image model in this study. Given ∂s as a neighborhood system, wherein $\partial s \in S$ is the set of neighboring pixels to s, in this system if s is a neighbor of t, then t is a neighbor of s ($s \in \partial t$ if only if $t \in \partial s$). Thus, a set of pair-wise cliques is defined as follows [77]:

$$P = \{\{s, t\} | s \in \partial t\} \tag{2.14}$$

where P is the set of all unordered neighboring pixel pairs $\{s, t\}$, in which $t \in \partial s$. The distribution of a zero-mean GMRF is formulated based on this convention given by:

$$p(x) = \frac{1}{z} \exp\{-\frac{1}{2} x^T B x\} \tag{2.15}$$

where B is the inverse of coherency matrix, z represents the normalization constant and $B_{t,s} = 0$ when $t \notin \partial s$. Also, x is a random vector with Gaussian distribution and denstiy $N(0, B^{-1})$. In order to hilight the difference between neighboring pixels, a pairwise quadratic form identity, which converts matrix to vector, is used [78]. Therefore, $x^T B x$ term for image pixels is presented as follows:

$$x^T B x = \sum_{s \in S} a_s x_s^2 + \sum_{\{s,t\} \in P} b_{s,t} |x_s - x_t|^2 \tag{2.16}$$

where $a_s = \sum_{t \in s} B_{s,t}$, $b_{s,t} = -B_{s,t}$ and in the case of image modelling, the coefficients a_s are most often chosen to be zero in order to guarantee that the prior probability of an image x is invariant to additive constant shifts in the pixel values [79]. Therefore, by dropping first term, the pair-wised GMRF distribution is defined as follows:

$$p(x) = \frac{1}{z} exp \left\{ - \sum_{\{s,t\} \in P} b_{s,t} \frac{|x_s - x_t|^2}{2} \right\} \tag{2.17}$$

It is worth noting that this concept is originated from statistical thermodynamics, in which the energy function is formulated as follows:

$$p(x) = \frac{1}{z} exp \{-U(x)\} \tag{2.18}$$

Therefore, in this study, the energy function of the pair-wise Gaussian distribution is defined as [78]:

$$U(x) = \sum_{\{s,t\} \in P} b_{s,t} \frac{|x_s - x_t|^2}{2} \tag{2.19}$$

in which the optimization algorithm is used to find the global maximum of a posteriori distribution in Equation 2.17, and is equivalent to the global minimum of the energy function. In this study, the stochastic optimization method, Simulated Annealing (SA), is used to detect the global minimum of the energy function [80].

2.4.3. Fast MAP estimation

The MAP estimator provides a framework for solving problems that require estimation of an unknown parameter x from observation y. The likelihood function together with the chosen prior probability is used to calculate a MAP estimate of the noise-free scene x. Given a known model parameter, the optimal estimator for this problem is determined by maximum a posteriori (MAP) estimate [81]:

$$\hat{x}_{MAP} = \arg\max_{x \in \Omega} p(x|y) \tag{2.20}$$

where Ω is the set of feasible values for x and the conditional distribution $p(x|y)$ is the posterior distribution. For estimating $\hat{x}_{MAP}$, the first derivative of the logarithm of the posterior is set to zero. In summary, a GMRF is used to model the contextual relationships among pixel labels given the Hammersley-Clifford theorem [78]. Also, the de-speckling problem is formulated as an optimization process with a well-defined cost function using the Fast MAP estimation criterion. More specifically, given the observed image random field $Y = y$, the MAP criterion looks for a labeling $X = x$ which maximizes the conditional probability function $P_{X|Y}(x|y)$ for all possible realizations x of X. In the case of discrete problems such as SAR image de-speckling, this corresponds to maximizing the probability $p(x|y)$ and minimizing the probability of an error.

2.4.4. Pseudo-span image formation

As illustrated in Figure 2.3, a by-product of the proposed de-speckling method is the pseudo-span image, which is explained with more detailed in this section. A span image is the sum of the diagonal elements of the coherency matrix (Equation 2.4). Thus, in the de-speckled image, the span image is formed as follows:

$$\text{De-speckled span image} = T_{11}' + T_{22}' + T_{33}' \tag{2.21}$$

where T_{11}', T_{22}', and T_{33}' are de-speckled diagonal elements of the coherency matrix. In Equation 2.4, the coefficients of these three elements are one. The pseudo-span image of the original image is defined as follows:

$$\text{Pseudo-span image} = k_1 T_{11} + k_2 T_{22} + k_3 T_{33} \tag{2.22}$$

wherein the three coefficients k_1, k_2 and k_3 are unknown and should be determined. Since the span image value represents the total power of the coherency matrix (Equation 2.4), it is approximately equal before and after de-speckling. Given this hypothesis, the optimum weights of pseudo-span image are determined using the following equation in this study:

$$T_{11}' + T_{22}' + T_{33}' = k_1 T_{11} + k_2 T_{22} + k_3 T_{33} \tag{2.23}$$

where the left and right sides of Equation 2.23 are the span of de-speckled and the pseudo-span of the original images, respectively. In this equation, the three unknown coefficients should be determined. In particular, each imaging pixel is an independent observation within each ground target, which is used to determine these coefficients using a least square estimator (LSE) [82]. Furthermore, the k_1, k_2, and k_3 elements illustrate the best linear combination of the diagonal elements of the coherency matrix, which is the nearest representation to the de-speckled span image. Moreover, by solving Equation 2.23, the effect of the de-speckling is inserted into the k_1,

k_2, and k_3 parameters. Next, these parameters are integrated with the de-speckled diagonal elements of the coherency matrix (T_{11}', T_{22}', and T_{33}') to generate the de-speckled pseudo-span image, which is formulated as follows:

$$\text{De-speckled pseudo-span image} = k_1 T_{11}' + k_2 T_{22}' + k_3 T_{33}' \tag{24}$$

Using these weights for the de-speckled diagonal elements of the coherency matrix produces a more accurate feature, which is called the de-speckled pseudo-span image in this study. Accordingly, using the more reliable noise-free feature should improve the classification accuracy of the PolSAR data in further analysis. Next, the de-speckled PolSAR image based on the proposed method is used for wetland classification. Furthermore, the effect of different de-speckling methods on the PolSAR image is compared in terms of wetland classification accuracy.

2.5. Experimental results

2.5.1. Study area and data description

The study area is about 700 km^2 and is located in the northeastern portion of the Avalon Peninsula, Newfoundland and Labrador, Canada (Figure 2.5). The area is mostly covered by boreal wetlands of different types (i.e., bog, fen, swamp, marsh, and shallow-water).
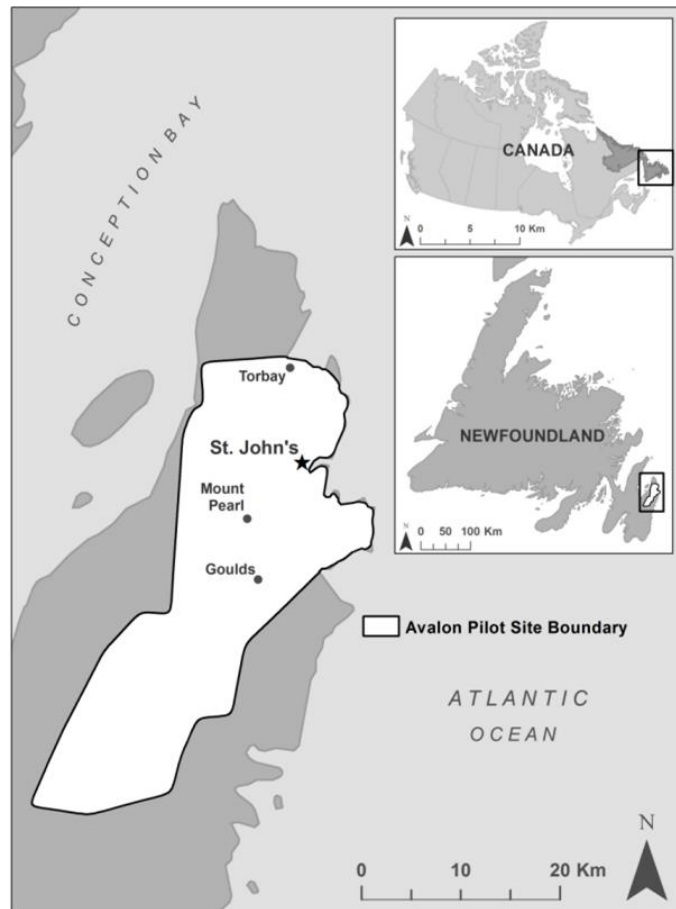
Figure 2.5. The geographic location of the study area, the Avalon Peninsula, Newfoundland and Labrador, Canada.

Eight land cover classes including bog, fen, built-up, marsh, open-water, shallow-water, swamp, and upland are found within this pilot site. For the classified maps, a confusion matrix was calculated for these eight classes. For each class, reference polygons, manually digitized on high-resolution aerial photographs using GPS points collected on the field, and were sorted by size and alternatingly assigned to testing and training groups. Due to the limited amount of data (58 ground-referenced wetlands) and the wide variation of size within each wetland class (some small, some large), random assignment to the testing and training group could result in the testing and training groups having highly uneven pixel counts. However, the random procedure ensured that both the testing and the training groups had equal assignment of small and large wetlands polygons to allow

for comparable pixel counts and to account for the high variation in intra-wetland size. Table 2.1 shows land cover classes and their respective pixel counts.

Table 2.1. Testing and training pixel counts for reference data.

Class	Class Description	Training Pixels	Testing Pixels	Total
Bog	Peatland dominated by *Spahgnum* species*	2523	3536	6059
Fen	Peatland dominated by graminoid species*	1202	2215	3417
Swamp	Mineral wetland dominated by woody vegetation*	458	796	1254
Marsh	Mineral wetland dominated by graminoids and emergent plants*	1096	1246	2342
Shallow-water	Mineral wetland with standing water at most 2m deep*	1007	267	1274
Built-Up	Human-made structures	3938	3491	7429
Open-water	Deep water areas	9352	10804	20156
Upland	Forested dry upland	5973	4551	10524
Total		25549	26906	52455

*(National Wetlands Working Group, 1997)

Two descending RADARSAT-2 images in Fine Quad (FQ) beam mode acquired on June 10th, 2015 were used. Due to the small swath width of FQ mode imagery, more than one image was used to cover the whole study area. In the first step, the scattering matrix was converted to a coherency matrix. The diagonal elements of the coherency matrix are illustrated in Figure 2.6.
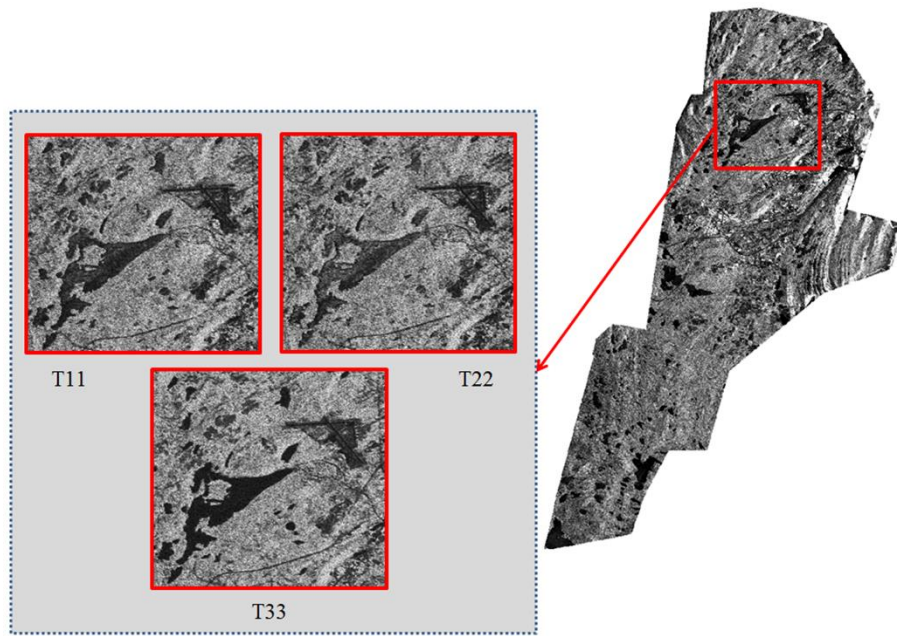
Figure 2.6. Original coherency matrix of RADARSAT-2 image in Fine Quad (FQ) beam mode.

Different speckle reduction methods were applied to the coherency matrix elements. Also, for better evaluation of the de-speckling results, three areas with different land cover types representing a homogeneous area, a linear feature, and edge were selected (see Figure 2.7).
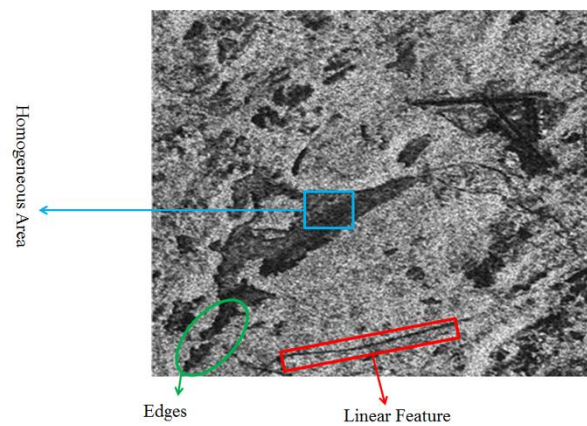
Figure 2.7. A sub-region of the study area and three small areas used for evaluating the performance of the proposed method.

2.5.2. Results of the proposed de-speckling method

The results of our proposed de-speckling method, applied to the PolSAR data, are presented in this section. We also compare the strength of the proposed method, visually and quantitatively, with a number of well-known de-speckling methods listed in Table 2.2. Importantly, the size of the filtering window was set to 5×5 for the Kuan, Frost and Refined Lee filters. These three filters were implemented using the PCI Geomatica 2015 software. For the SARBM3D filter, maximum size of the 3rd dimension of a stack, the diameter of search area, the dimension of step in sliding, and the parameter of the 2-D Kaiser window are set to 16, 39, 3, and 2, respectively. This filter was implemented using Matlab toolbox, provide by [83]. In the proposed method, second order MRF neighboring system was used. Figure 2.8 shows the results of different speckle reduction methods on the span image of RADARSAT-2 PolSAR image.
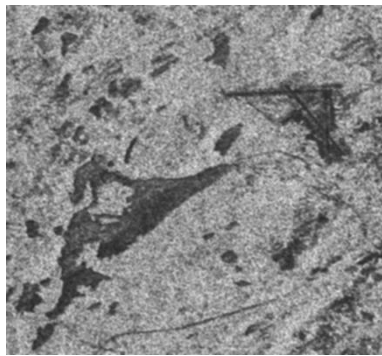
(a)
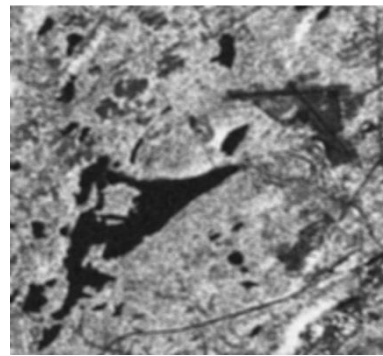
(b)
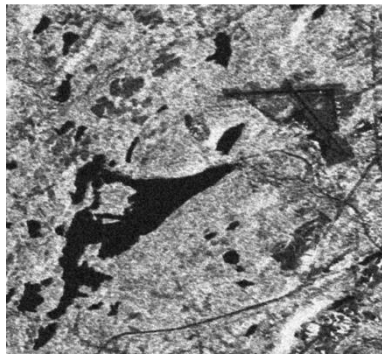
(c)
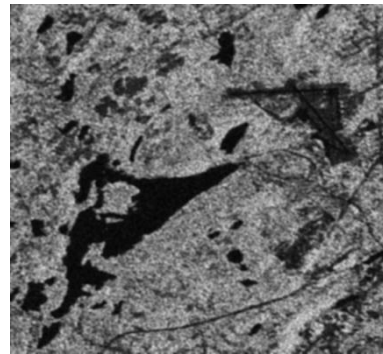
(d)
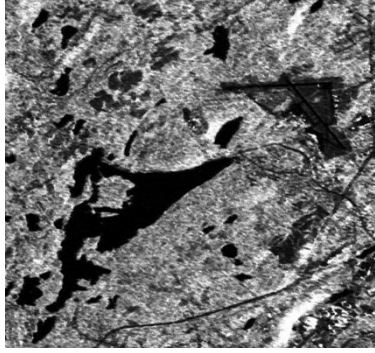
(e)

Figure 2.8. Comparison of the de-speckled span images using different filtering techniques (a) Frost, (b) Kuan, (c) Enhanced Lee, (d) SARBM3D, and (e) the proposed method (Pseudo-span).

Table 2.2 summarizes the interpretation of the obtained results using different de-specking methods in Figure 2.8.

Table 2.2. Properties of different de-speckling methods.

De-speckling method	Properties
Frost	• High speckle level. • Maintains the mean value of the original image in the homogenous areas.
Kuan	• Low speckle level. • High blurring effect. • Loses the mean value of the original image.
Enhanced Lee	• Moderate speckle level. • Maintains the mean value of the original image in the homogenous areas. • Preserves the edges.
SARBM3D	• Moderate speckle level. • Loses the mean value of the original image in the homogenous areas. • Better preservation of the edges and linear features.
The proposed method	• Low speckle level. • Maintains the mean value of the original image in the homogenous and heterogonous areas. • Preserves the edges. • Better preservation of the edges and linear features.

Figure 2.9 represents the results of the proposed method on the diagonal elements of the coherency matrix.
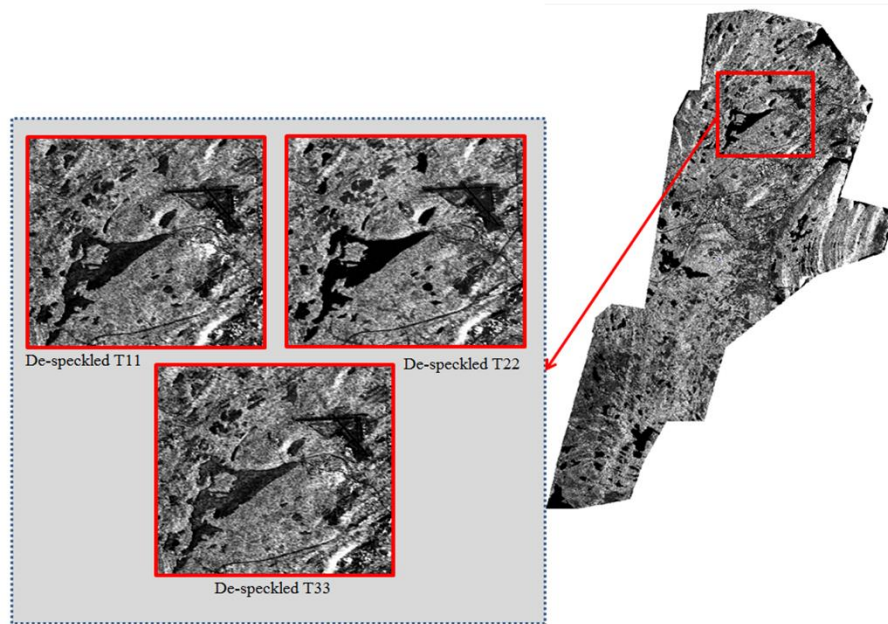
Figure 2.9. De-speckled diagonal elements of the coherency matrix.

Comparing visual appearance (Figure 2.6 versus Figure 2.9), it can be observed that by applying the proposed filtering method speckle noise is removed, while edges, detail, and texture information are well preserved. Also, Figure 2.10 illustrates a visual comparison between the de-speckled image obtained by the proposed method and the optical image.
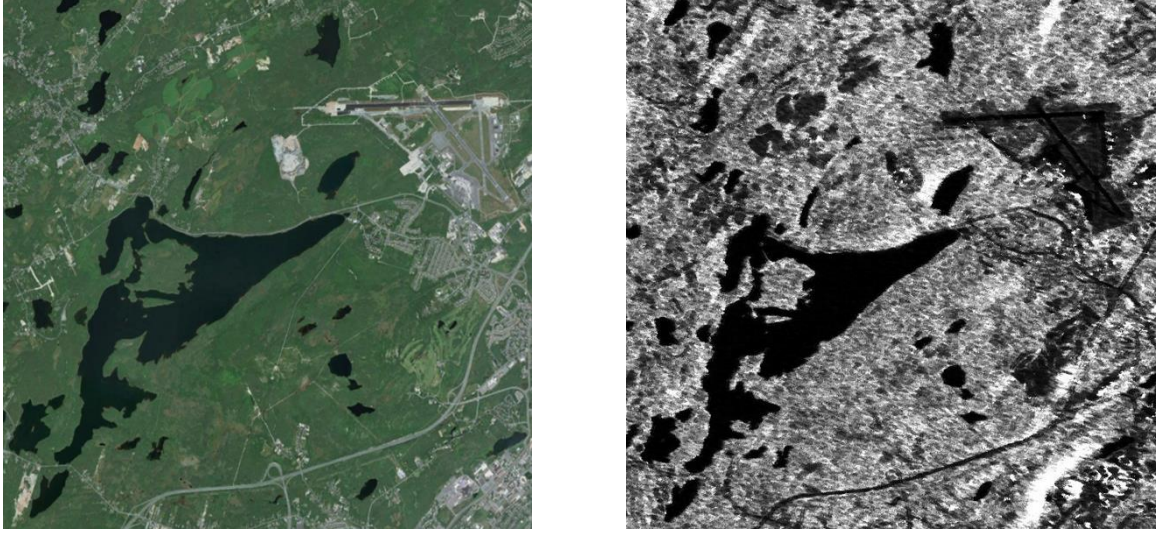
Figure 2.10. Visual comparison of the de-speckled image obtained by the proposed method and the optical imagery.

As seen in Figure 2.10, the linear features and edges (e.g., roads and man-made structures) are preserved representing the efficiency of the proposed method in de-speckling. Furthermore, the quantitative comparisons between the proposed method and other well-known methods are presented in Figure 2.11, Table 2.3, and Table 2.4 using different quantitative indices. Figure 2.11 demonstrates the ENL values for different de-speckling methods. The ENL determines the degree of speckle reduction and was computed in the selected sub-region as marked in Figure 2.7.
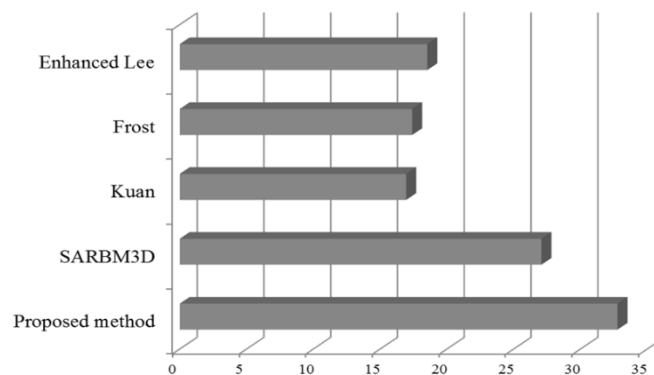
Figure 2.11. Equivalent Number of Looks (ENL) for different de-speckling methods.

As seen, the proposed method shows approximately 19%, 43%, 46%, and 50% improvements in term of ENL values, compared to SARBM3D, Enhanced Lee, Frost, and Kuan, respectively. Another index used to evaluate the strength of the de-speckling is EPD-ROA criterion, which illustrates the efficiency of different filters in term of edge preservation. Table 2.3 represent EPD-ROA values, in both horizontal and vertical direction, for three diagonal elements of the coherency matrix obtained from different de-speckling methods.

Table 2.3. Evaluation of edge preservation based on EPD-ROA index for different de-speckling methods.

De-speckling method	EPD-ROA					
	T_{11}-HD	T_{11}-VD	T_{22}-HD	T_{22}-VD	T_{33}-HD	T_{33}-VD
Kuan	0.5699	0.552	0.572	0.563	0.544	0.538
Frost	0.583	0.566	0.608	0.579	0.561	0.547
Enhanced Lee	0.729	0.698	0.645	0.619	0.594	0.567
SARBM3D	0.709	0.687	0.720	0.706	**0.731**	**0.699**
The proposed method	**0.741**	**0.702**	**0.783**	**0.721**	0.719	0.685

From Table 2.3, it can be observed that the proposed method has a better performance in edge preservation in most cases compared with other well-known filters, which resulted in higher EPD-ROA values. However, there is an exception, wherein the larger EPD-ROA value is obtained from SARBM3D filter in T_{33} element of the coherency matrix in both horizontal and vertical direction. Notably, the proposed method illustrates to be more efficient for speckle reduction of T_{22} element of the coherency matrix resulting in higher EPD-ROA values for this element compared to T_{11} and T_{33} elements. For instance, an improvement of approximately 27%, 22%, 18%, and 8% was observed for T_{22} element of the coherency matrix in horizontal direction in term of edge preservation by the proposed method compared to Kuan, Frost, Enhanced Lee, and SARBM3D,

respectively. In addition to the ENL and EPD-ROA, the mean and variance of the ratio image were determined for various de-speckling methods used in this study and represented in Table 2.4. This index was used in order to determine the amount of bias introduced by each de-speckling method.

Table 2.4. Quantitative comparison of de-speckling algorithms.

Parameters	Mean(r)	Var(r)
Original Image	1.0000	0.0000
Kuan	0.7905	0.5793
Frost	0.7166	0.6309
Enhanced Lee	0.9014	0.3955
SARBM3D	0.8931	0.4380
Proposed method	**0.9386**	**0.3164**

As seen, the proposed method has the highest mean and lowest variance of the ratio image. In particular, the proposed method has mean ratio that is close to one, implying better preservation of mean value. Furthermore, the mean of the ratio image illustrates improvements approximately of 5%, 4%, 31%, and 19% by the proposed method compared to SARBM3D, Enhanced Lee, Frost, and Kuan filter, respectively. Furthermore, the variance of the ratio image is improved using the proposed method approximately of 27%, 20%, 49%, and 45% in comparison with SARBM3D, Enhanced Lee, Frost, and Kuan filter, respectively. Next, we used de-speckled PolSAR images obtained by different filters for classification. We also evaluated the performance of different de-speckling methods on the overall classification results.

2.5.3. Random Forest classification results

The Random Forest (RF) classifier is one of the most effective approaches for classification [84]. In this study, RF is used to evaluate the effects of different de-speckling methods on classification results.

Figure 2.12, 2.13, and 2.14 illustrate the accuracy assessment, including omission error, commission error, and overall accuracy (OA) of classified maps obtained by PolSAR images, which were filtered using different de-speckling methods. Particularly, Figure 2.12 and 2.13 show omission and commission errors, which are calculated from marginal proportions of the row and column of the confusion matrix.
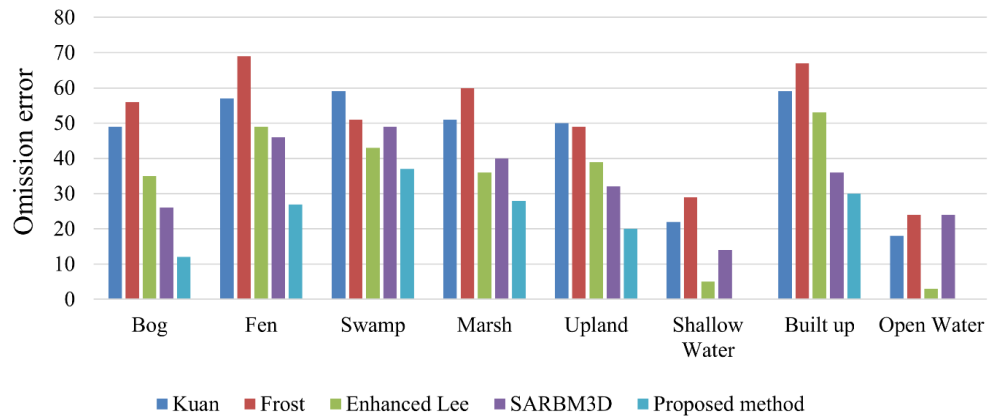
Figure 2.12. Comparison of the omission error in different land cover types for classified maps obtained by different de-speckling methods.
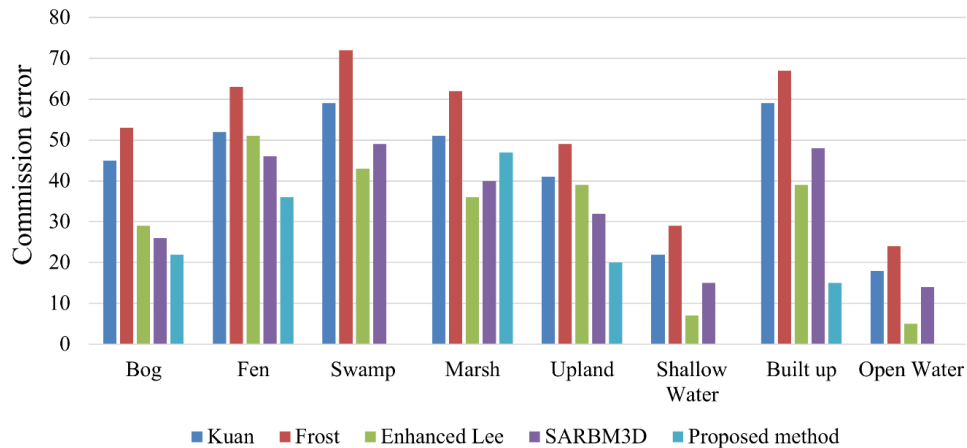
Figure 2.13. Comparison of the commission error in different land cover types for classified maps obtained by different de-speckling methods.

These results confirm the outperformance of the proposed de-speckling method over other methods in terms of classification results. As seen in Figure 2.12 and 2.13, omission and commission errors of both the shallow-water and open-water class and also, commission error of swamp class are zero. Particularly, the average omission and commission errors are significantly lower using the proposed method than using other methods. For example, the omission errors for the marsh class illustrate a reduction of 43%, 51%, 23%, and 27% using the proposed method compared to Kuan, Frost, Enhanced Lee, and SARBM3D, respectively. Figure 2.14 compares the overall accuracies for classified maps obtained by PolSAR images based on different de-speckling methods.
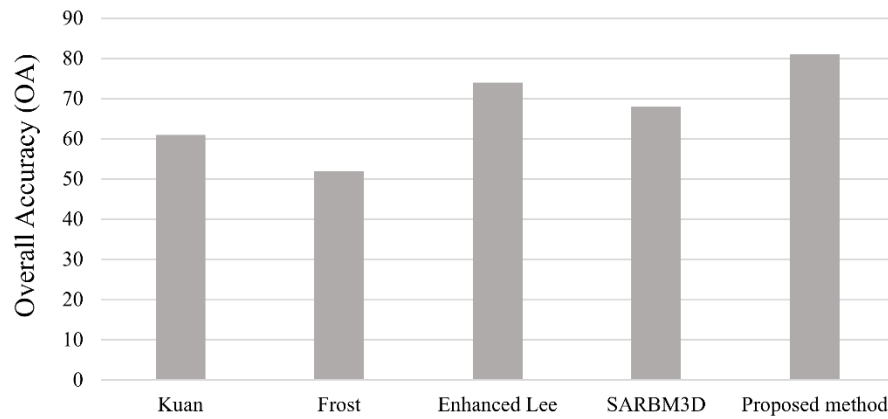
Figure 2.14. Overall accuracies for classified maps obtained by applying different de-speckling methods. Notably, the proposed method shows the highest OA of about 81%, followed by 74% achieved by Enhanced Lee. Furthermore, the classified map obtained by de-speckled PolSAR image (the proposed method) illustrates improvements of about 19%, 9%, 55%, and 32% compared to SARBM3D, Enhanced Lee, Frost, and Kuan filter, respectively.

2.6. Conclusion

PolSAR images are widely used for land cover classification. However, the presence of speckle noise hinders the radiometric quality of the PolSAR images and, subsequently, further PolSAR image analysis (e.g., segmentation and classification). Thus, speckle reduction is a necessary pre-processing step in most of PolSAR image analysis, which has a great influence on the accuracy of end-user products. In this paper, a novel speckle reduction method based on a GMRF model was proposed. We compared the efficiency of the proposed method in term of different quantitative indices with other well-known de-speckling filters. The results demonstrated the superior performance of the proposed method in edges and detailed preservation as well as speckle suppression compared to other methods. Another purpose behind this study was to assess the effect of the proposed speckle reduction method, along with four other well-known de-speckling methods, on the accuracy of wetland classification. The experimental results demonstrated that the overall accuracy of wetland classification was improved by about 19%, 9%, 55%, and 32% using the de-speckled PolSAR image obtained by the proposed method compared to SARBM3D, Enhanced Lee, Frost, and Kuan filter, respectively.

Furthermore, the proposed method outperformed other methods in terms of class-based accuracies (i.e., omission and commission errors). Importantly, the proposed method was demonstrated to be more effective in terms of maintaining polarimetric properties and backscattering mechanisms. This conclusion is based on demonstrably better performance of the proposed method in discriminating between wetland classes with similar spectral signature (e.g., bog and fen, shallow- and open-water). This promises a great potential for operational wetland inventory generation for Canadian north, and elsewhere particularly with Canada's upcoming RADARSAT Constellation Mission (RCM).

2.7. References

[1] D. A. Hammer and R. K. Bastian, "Wetlands ecosystems: natural water purifiers," *Constr. Wetl. wastewater Treat. Munic. Ind. Agric.*, vol. 5, 1989.

[2] N. Torbick and W. Salas, "Mapping agricultural wetlands in the Sacramento Valley, USA with satellite remote sensing," *Wetl. Ecol. Manag.*, vol. 23, no. 1, pp. 79–94, 2015.

[3] I. Dronova, P. Gong, L. Wang, and L. Zhong, "Mapping dynamic cover types in a large seasonally flooded wetland using extended principal component analysis and object-based classification," *Remote Sens. Environ.*, vol. 158, pp. 193–206, 2015.

[4] M. Halabisky, L. M. Moskal, A. Gillespie, and M. Hannam, "Reconstructing semi-arid wetland surface water dynamics through spectral mixture analysis of a time series of Landsat satellite images (1984–2011)," *Remote Sens. Environ.*, vol. 177, pp. 171–183, 2016.

[5] S. L. Ozesmi and M. E. Bauer, "Satellite remote sensing of wetlands," *Wetl. Ecol. Manag.*, vol. 10, no. 5, pp. 381–402, 2002.

[6] M. Kelly and K. Tuxen, "Remote sensing support for tidal wetland vegetation research and management," in *Remote sensing and geospatial technologies for coastal ecosystem assessment and management*, Springer, 2009, pp. 341–363.

[7] F. Mohammadimanesh, B. Salehi, M. Mahdianpari, and S. Homayouni, "Unsupervised wishart classfication of wetlands in Newfoundland, Canada using polsar data based on fisher linear discriminant analysis," in *International Archives of the Photogrammetry, Remote Sensing and Spatial Information Sciences - ISPRS Archives*, 2016, vol. 41.

[8] C. Prigent, E. Matthews, F. Aires, and W. B. Rossow, "Remote sensing of global wetland dynamics with multiple satellite data sets," *Geophys. Res. Lett.*, vol. 28, no. 24, pp. 4631–4634, 2001.

[9] P. A. Townsend and S. J. Walsh, "Modeling floodplain inundation using an integrated GIS with radar and optical remote sensing," *Geomorphology*, vol. 21, no. 3–4, pp. 295–312, 1998.

[10] G. M. Smith, T. Spencer, A. L. Murray, and J. R. French, "Assessing seasonal vegetation change in coastal wetlands with airborne remote sensing: an outline methodology," *Mangroves Salt Marshes*, vol. 2, no. 1, pp. 15–28, 1998.

[11] J. Li and W. Chen, "A rule-based method for mapping Canada's wetlands using optical, radar and DEM data," *Int. J. Remote Sens.*, vol. 26, no. 22, pp. 5051–5069, 2005.

[12] V. Klemas, "Remote sensing techniques for studying coastal ecosystems: An overview," *J. Coast. Res.*, vol. 27, no. 1, pp. 2–17, 2010.

[13] D. P. Ward *et al.*, "Assessing the seasonal dynamics of inundation, turbidity, and aquatic vegetation in the Australian wet–dry tropics using optical remote sensing," *Ecohydrology*, vol. 6, no. 2, pp. 312–323, 2013.

[14] P. Teluguntla *et al.*, "A 30-m landsat-derived cropland extent product of Australia and China using random forest machine learning algorithm on Google Earth Engine cloud computing platform,"

ISPRS J. Photogramm. Remote Sens., vol. 144, pp. 325–340, 2018.

[15] K. O. Pope, J. M. Rey-Benayas, and J. F. Paris, "Radar remote sensing of forest and wetland ecosystems in the Central American tropics," *Remote Sens. Environ.*, vol. 48, no. 2, pp. 205–219, 1994.

[16] E. S. Kasischke, J. M. Melack, and M. C. Dobson, "The use of imaging radars for ecological applications—a review," *Remote Sens. Environ.*, vol. 59, no. 2, pp. 141–156, 1997.

[17] C. M. Birkett, "Contribution of the TOPEX NASA radar altimeter to the global monitoring of large rivers and wetlands," *Water Resour. Res.*, vol. 34, no. 5, pp. 1223–1239, 1998.

[18] F. M. Henderson and A. J. Lewis, "Radar detection of wetland ecosystems: a review," *Int. J. Remote Sens.*, vol. 29, no. 20, pp. 5809–5835, 2008.

[19] T. L. Evans and M. Costa, "Landcover classification of the Lower Nhecolândia subregion of the Brazilian Pantanal Wetlands using ALOS/PALSAR, RADARSAT-2 and ENVISAT/ASAR imagery," *Remote Sens. Environ.*, vol. 128, pp. 118–137, 2013.

[20] B. Brisco, A. Schmitt, K. Murnaghan, S. Kaya, and A. Roth, "SAR polarimetric change detection for flooded vegetation," *Int. J. Digit. Earth*, vol. 6, no. 2, pp. 103–114, 2013.

[21] M. Mahdianpari, B. Salehi, F. Mohammadimanesh, and M. Motagh, "Random forest wetland classification using ALOS-2 L-band, RADARSAT-2 C-band, and TerraSAR-X imagery," *ISPRS J. Photogramm. Remote Sens.*, vol. 130, 2017.

[22] K. C. Slatton, M. M. Crawford, and L.-D. Chang, "Modeling temporal variations in multipolarized radar scattering from intertidal coastal wetlands," *ISPRS J. Photogramm. Remote Sens.*, vol. 63, no. 5, pp. 559–577, 2008.

[23] K. Dabrowska-Zielinska, M. Gruszczynska, S. Lewinski, A. Hoscilo, and J. Bojanowski, "Application of remote and in situ information to the management of wetlands in Poland," *J. Environ. Manage.*, vol. 90, no. 7, pp. 2261–2269, 2009.

[24] S. R. Cloude and E. Pottier, "A review of target decomposition theorems in radar polarimetry," *IEEE Trans. Geosci. Remote Sens.*, vol. 34, no. 2, pp. 498–518, 1996.

[25] Y. Yamaguchi, T. Moriyama, M. Ishido, and H. Yamada, "Four-component scattering model for polarimetric SAR image decomposition," *IEEE Trans. Geosci. Remote Sens.*, vol. 43, no. 8, pp. 1699–1706, 2005.

[26] R. Touzi, "Target scattering decomposition in terms of roll-invariant target parameters," *IEEE Trans. Geosci. Remote Sens.*, vol. 45, no. 1, pp. 73–84, 2007.

[27] J.-S. Lee, "Speckle analysis and smoothing of synthetic aperture radar images," *Comput. Graph. image Process.*, vol. 17, no. 1, pp. 24–32, 1981.

[28] M. Mahdian, S. Homayouni, M. A. Fazel, and F. Mohammadimanesh, "Agricultural land classification based on statistical analysis of full polarimetric SAR data," *Int. Arch. Photogramm. Remote Sens. Spat. Inf. Sci.*, vol. 1, p. W3, 2013.

[29]   F. Argenti and L. Alparone, "Speckle removal from SAR images in the undecimated wavelet domain," *IEEE Trans. Geosci. Remote Sens.*, vol. 40, no. 11, pp. 2363–2374, 2002.

[30]   A. Lopes, E. Nezry, R. Touzi, and H. Laur, "Structure detection and statistical adaptive speckle filtering in SAR images," *Int. J. Remote Sens.*, vol. 14, no. 9, pp. 1735–1758, 1993.

[31]   M. Mansourpour, M. A. Rajabi, and J. A. R. Blais, "Effects and performance of speckle noise reduction filters on active radar and SAR images," in *Proc. ISPRS*, 2006, vol. 36, no. 1, p. W41.

[32]   J.-S. Lee, J.-H. Wen, T. L. Ainsworth, K.-S. Chen, and A. J. Chen, "Improved sigma filter for speckle filtering of SAR imagery," *IEEE Trans. Geosci. Remote Sens.*, vol. 47, no. 1, pp. 202–213, 2009.

[33]   B. Hou, X. Zhang, X. Bu, and H. Feng, "SAR image despeckling based on nonsubsampled shearlet transform," *IEEE J. Sel. Top. Appl. earth Obs. Remote Sens.*, vol. 5, no. 3, pp. 809–823, 2012.

[34]   F. Argenti, A. Lapini, T. Bianchi, and L. Alparone, "A tutorial on speckle reduction in synthetic aperture radar images," *IEEE Geosci. Remote Sens. Mag.*, vol. 1, no. 3, pp. 6–35, 2013.

[35]   L. Torres, S. J. S. Sant'Anna, C. da Costa Freitas, and A. C. Frery, "Speckle reduction in polarimetric SAR imagery with stochastic distances and nonlocal means," *Pattern Recognit.*, vol. 47, no. 1, pp. 141–157, 2014.

[36]   J.-S. Lee, T. L. Ainsworth, Y. Wang, and K.-S. Chen, "Polarimetric SAR speckle filtering and the extended sigma filter," *IEEE Trans. Geosci. Remote Sens.*, vol. 53, no. 3, pp. 1150–1160, 2015.

[37]   C.-A. Deledalle, L. Denis, F. Tupin, A. Reigber, and M. Jäger, "NL-SAR: A unified nonlocal framework for resolution-preserving (Pol)(In) SAR denoising," *IEEE Trans. Geosci. Remote Sens.*, vol. 53, no. 4, pp. 2021–2038, 2015.

[38]   A. Lopes, R. Touzi, and E. Nezry, "Adaptive speckle filters and scene heterogeneity," *IEEE Trans. Geosci. Remote Sens.*, vol. 28, no. 6, pp. 992–1000, 1990.

[39]   R. Touzi, "A review of speckle filtering in the context of estimation theory," *IEEE Trans. Geosci. Remote Sens.*, vol. 40, no. 11, pp. 2392–2404, 2002.

[40]   G. Vasile, E. Trouvé, J.-S. Lee, and V. Buzuloiu, "Intensity-driven adaptive-neighborhood technique for polarimetric and interferometric SAR parameters estimation," *IEEE Trans. Geosci. Remote Sens.*, vol. 44, no. 6, pp. 1609–1621, 2006.

[41]   J.-S. Lee and E. Pottier, *Polarimetric radar imaging: from basics to applications*. CRC press, 2009.

[42]   H. Xie, L. E. Pierce, and F. T. Ulaby, "SAR speckle reduction using wavelet denoising and Markov random field modeling," *IEEE Trans. Geosci. Remote Sens.*, vol. 40, no. 10, pp. 2196–2212, 2002.

[43]   J.-S. Lee, M. R. Grunes, D. L. Schuler, E. Pottier, and L. Ferro-Famil, "Scattering-model-based speckle filtering of polarimetric SAR data," *IEEE Trans. Geosci. Remote Sens.*, vol. 44, no. 1, pp. 176–187, 2006.

[44]   M. Datcu, "Wavelet-based despeckling of SAR images using Gauss–Markov random fields," *IEEE Trans. Geosci. Remote Sens.*, vol. 45, no. 12, pp. 4127–4143, 2007.

[45] V. S. Frost, J. A. Stiles, K. S. Shanmugan, and J. C. Holtzman, "A model for radar images and its application to adaptive digital filtering of multiplicative noise," *IEEE Trans. Pattern Anal. Mach. Intell.*, no. 2, pp. 157–166, 1982.

[46] D. Kuan, A. Sawchuk, T. Strand, and P. Chavel, "Adaptive restoration of images with speckle," *IEEE Trans. Acoust.*, vol. 35, no. 3, pp. 373–383, 1987.

[47] G. Vasile *et al.*, "Normalized coherency matrix estimation under the SIRV model. Alpine glacier POLSAR data analysis," in *IGARSS 2008-2008 IEEE International Geoscience and Remote Sensing Symposium*, 2008, vol. 1, p. I-74.

[48] F. Lang, J. Yang, and D. Li, "Adaptive-window polarimetric SAR image speckle filtering based on a homogeneity measurement," *IEEE Trans. Geosci. Remote Sens.*, vol. 53, no. 10, pp. 5435–5446, 2015.

[49] J. M. Bioucas-Dias and M. A. T. Figueiredo, "Multiplicative noise removal using variable splitting and constrained optimization," *IEEE Trans. Image Process.*, vol. 19, no. 7, pp. 1720–1730, 2010.

[50] H. Woo and S. Yun, "Alternating minimization algorithm for speckle reduction with a shifting technique," *IEEE Trans. Image Process.*, vol. 21, no. 4, pp. 1701–1714, 2012.

[51] X. Nie, H. Qiao, and B. Zhang, "A variational model for PolSAR data speckle reduction based on the Wishart distribution," *IEEE Trans. Image Process.*, vol. 24, no. 4, pp. 1209–1222, 2015.

[52] X. Nie, H. Qiao, B. Zhang, and X. Huang, "A nonlocal TV-based variational method for PolSAR data speckle reduction," *IEEE Trans. Image Process.*, vol. 25, no. 6, pp. 2620–2634, 2016.

[53] B. Brisco, "Mapping and monitoring surface water and wetlands with synthetic aperture radar," *Remote Sens. Wetl. Appl. Adv.*, pp. 119–136, 2015.

[54] W.-M. Boerner, H. Mott, and E. Luneburg, "Polarimetry in remote sensing: basic and applied concepts," in *IGARSS'97. 1997 IEEE International Geoscience and Remote Sensing Symposium Proceedings. Remote Sensing-A Scientific Vision for Sustainable Development*, 1997, vol. 3, pp. 1401–1403.

[55] H. Guo, J. E. Odegard, M. Lang, R. A. Gopinath, I. W. Selesnick, and C. S. Burrus, "Wavelet based speckle reduction with application to SAR based ATD/R," in *Image Processing, 1994. Proceedings. ICIP-94., IEEE International Conference*, 1994, vol. 1, pp. 75–79.

[56] E. F. Knott, *Radar cross section measurements*. Springer Science & Business Media, 2012.

[57] R. Touzi and F. Charbonneau, "Characterization of target symmetric scattering using polarimetric SARs," *IEEE Trans. Geosci. Remote Sens.*, vol. 40, no. 11, pp. 2507–2516, 2002.

[58] A. Freeman, "SAR calibration: An overview," *IEEE Trans. Geosci. Remote Sens.*, vol. 30, no. 6, pp. 1107–1121, 1992.

[59] C. Oliver and S. Quegan, *Understanding synthetic aperture radar images*. SciTech Publishing, 2004.

[60] R. Touzi, W. M. Boerner, J. S. Lee, and E. Lueneburg, "A review of polarimetry in the context of

synthetic aperture radar: concepts and information extraction," *Can. J. Remote Sens.*, vol. 30, no. 3, pp. 380–407, 2004.

[61] S. Benedetto and P. Poggiolini, "Theory of polarization shift keying modulation," *IEEE Trans. Commun.*, vol. 40, no. 4, pp. 708–721, 1992.

[62] J. Bruniquel and A. Lopes, "Multi-variate optimal speckle reduction in SAR imagery," *Int. J. Remote Sens.*, vol. 18, no. 3, pp. 603–627, 1997.

[63] H. Feng, B. Hou, and M. Gong, "SAR image despeckling based on local homogeneous-region segmentation by using pixel-relativity measurement," *IEEE Trans. Geosci. Remote Sens.*, vol. 49, no. 7, pp. 2724–2737, 2011.

[64] G. M. Foody, "Status of land cover classification accuracy assessment," *Remote Sens. Environ.*, vol. 80, no. 1, pp. 185–201, 2002.

[65] R. G. Congalton and K. Green, "A practical look at the sources of confusion in error matrix generation," *Photogramm. Eng. Remote Sens.*, 1993.

[66] L. M. Novak and M. C. Burl, "Optimal speckle reduction in polarimetric SAR imagery," *IEEE Trans. Aerosp. Electron. Syst.*, vol. 26, no. 2, pp. 293–305, 1990.

[67] G. Liu, S. Huang, A. Torre, and F. Rubertone, "The multilook polarimetric whitening filter (MPWF) for intensity speckle reduction in polarimetric SAR images," *IEEE Trans. Geosci. Remote Sens.*, vol. 36, no. 3, pp. 1016–1020, 1998.

[68] A. Freeman and S. L. Durden, "A three-component scattering model for polarimetric SAR data," *IEEE Trans. Geosci. Remote Sens.*, vol. 36, no. 3, pp. 963–973, 1998.

[69] G. Vasile, J.-P. Ovarlez, F. Pascal, and C. Tison, "Coherency matrix estimation of heterogeneous clutter in high-resolution polarimetric SAR images," *IEEE Trans. Geosci. Remote Sens.*, vol. 48, no. 4, pp. 1809–1826, 2010.

[70] M. A. Fischler and O. Firschein, *Readings in computer vision: issues, problem, principles, and paradigms*. Elsevier, 2014.

[71] R. R. Schultz and R. L. Stevenson, "A Bayesian approach to image expansion for improved definition," *IEEE Trans. Image Process.*, vol. 3, no. 3, pp. 233–242, 1994.

[72] Y. Zhang, M. Brady, and S. Smith, "Segmentation of brain MR images through a hidden Markov random field model and the expectation-maximization algorithm," *IEEE Trans. Med. Imaging*, vol. 20, no. 1, pp. 45–57, 2001.

[73] W. R. Crum, T. Hartkens, and D. L. G. Hill, "Non-rigid image registration: theory and practice," *Br. J. Radiol.*, vol. 77, no. suppl_2, pp. S140–S153, 2004.

[74] Y. Lu, Q. Gao, D. Sun, Y. Xia, and D. Zhang, "SAR speckle reduction using Laplace mixture model and spatial mutual information in the directionlet domain," *Neurocomputing*, vol. 173, pp. 633–644, 2016.

[75] G. Liu and H. Zhong, "Nonlocal means filter for polarimetric SAR data despeckling based on

discriminative similarity measure," *IEEE Geosci. Remote Sens. Lett.*, vol. 11, no. 2, pp. 514–518, 2014.

[76]   M. Mahdianpari, M. Motagh, and V. Akbari, "Speckle reduction and restoration of synthetic aperture radar data with an adoptive markov random field model," in *Geoscience and Remote Sensing Symposium (IGARSS), 2012 IEEE International*, 2012, pp. 1–4.

[77]   S. Geman and D. Geman, "Stochastic relaxation, Gibbs distributions, and the Bayesian restoration of images," in *Readings in computer vision*, Elsevier, 1987, pp. 564–584.

[78]   H. Rue and L. Held, *Gaussian Markov random fields: theory and applications*. Chapman and Hall/CRC, 2005.

[79]   G. R. Cross and A. K. Jain, "Markov random field texture models," *IEEE Trans. Pattern Anal. Mach. Intell.*, no. 1, pp. 25–39, 1983.

[80]   D. Bertsimas and J. Tsitsiklis, "Simulated annealing," *Stat. Sci.*, vol. 8, no. 1, pp. 10–15, 1993.

[81]   C. A. Bouman, "Model based image processing," *Purdue Univ.*, 2013.

[82]   D. C. Heinz, "Fully constrained least squares linear spectral mixture analysis method for material quantification in hyperspectral imagery," *IEEE Trans. Geosci. Remote Sens.*, vol. 39, no. 3, pp. 529–545, 2001.

[83]   S. Parrilli, M. Poderico, C. V. Angelino, and L. Verdoliva, "A nonlocal SAR image denoising algorithm based on LLMMSE wavelet shrinkage," *IEEE Trans. Geosci. Remote Sens.*, vol. 50, no. 2, pp. 606–616, 2012.

[84]   L. Breiman, "Random forests," *Mach. Learn.*, vol. 45, no. 1, pp. 5–32, 2001.

Chapter 3. A novel hierarchical framework for wetland classification[2]

Preface

A version of this manuscript has been published in the *ISPRS Journal of Photogrammetry and Remote Sensing*. I am a primary author of this manuscript along with the co-authors, Bahram Salehi, Fariba Mohammadimanesh, and Mahdi Motagh. I designed and conceptualized the study. I developed the model and performed all experiments and tests. I wrote the paper and revised it based on comments from all co-authors. I also revised the paper according to the reviewers' comments. The co-author, Fariba Mohammadimanesh, helped in performing the experiments and analyzing the results and contributed to revising the manuscript. All co-authors provided editorial input and scientific insights to further improve the paper. They also reviewed and commented on the manuscript.

---

[2] Mahdianpari, M., Salehi, B., Mohammadimanesh, F. and Motagh, M., 2017. Random forest wetland classification using ALOS-2 L-band, RADARSAT-2 C-band, and TerraSAR-X imagery. *ISPRS Journal of Photogrammetry and Remote Sensing*, *130*, pp.13-31.

Abstract

Wetlands are important ecosystems around the world, although they are degraded due both to anthropogenic and natural process. Newfoundland is among the richest Canadian province in terms of different wetland classes. Herbaceous wetlands cover extensive areas of the Avalon Peninsula, which are the habitat of a number of animal and plant species. In this study, a novel hierarchical object-based Random Forest (RF) classification approach is proposed for discriminating between different wetland classes in a sub-region located in the north-eastern portion of the Avalon Peninsula. Particularly, multi-polarization and multi-frequency SAR data, including X-band TerraSAR-X single polarized (HH), L-band ALOS-2 dual polarized (HH/HV), and C-band RADARSAT-2 fully polarized images, were applied in different classification levels. First, a SAR backscatter analysis of different land cover types was performed by training data and used in Level-I classification to separate water from non-water classes. This was followed by Level-II classification, wherein the water class was further divided into shallow- and deep-water classes, and the non-water class was partitioned into herbaceous and non-herbaceous classes. In Level-III classification, the herbaceous class was further divided into bog, fen, and marsh classes, while the non-herbaceous class was subsequently partitioned into urban, upland, and swamp classes. In Level-II and -III classifications, different polarimetric decomposition approaches, including Cloude-Pottier, Freeman-Durden, Yamaguchi decompositions, and Kennaugh matrix elements were extracted to aid the RF classifier. The overall accuracy and kappa coefficient were determined in each classification level for evaluating the classification results. The importance of input features was also determined using the variable importance obtained by RF. It was found that the Kennaugh matrix elements, Yamaguchi, and Freeman-Durden decompositions were the most important parameters for wetland classification in this study. Using this new hierarchical RF

classification approach, an overall accuracy of up to 94% was obtained for classifying different land cover types in the study area.

3.1. Introduction

Wetlands are soil saturated areas with water long enough to provide suitable ecosystems for hydrophytic vegetation and various kinds of biological activity, which are associated with a wet environment [1]. Wetlands are important ecosystems with a variety of environmental services, including flood storage, shoreline stabilization, carbon sequestration, water-quality renovation, and, more important, a desirable habitat for both animal and plant species [2]. Despite the benefits, wetlands are being destroyed at increasing rates due both to natural processes, such as climate change, coastal processes, erosion and human interferences, such as road construction, installation of water-control structures, and oil spills [3].

Traditional approaches for wetland mapping and monitoring have been mainly based on ground surveys of water and vegetation patterns to gather information about wetland ecosystems, which are time and cost consuming techniques. These traditional approaches have been gradually replaced with aerial photography and, later, with satellite remote sensing tools [4]. The advent of remote sensing technology has greatly changed applied techniques for wetland monitoring by providing data for inaccessible wetland ecosystems in multi-temporal dimensions that facilitated long term monitoring of wetland complex. The use of remote sensing approaches for wetland monitoring have been well demonstrated in different applications such as classification [5], change detection [6], and water level monitoring [7].

Optical satellite images have been demonstrated to be useful for wetland classification if free cloud cover images are available [8], [9]. However, optical images are less-useful in tropical, subtropical, and northern latitudes regions due to near permanent cloud cover [10]. In contrast, Synthetic Aperture Radar (SAR) images are the preferred alternative for wetland monitoring when the capability of optical remote sensing imagery is hampered by either cloud cover or sun illumination

[11], [12]. In addition to being an independent of weather and day-night time conditions, the capability of SAR images to penetrate to soil, water, and vegetation canopies has caused them to gain increasing attention for wetland monitoring during the past two decades [12]–[15].

Though single SAR polarized data have been less investigated for wetland classification, they represented great potential for monitoring open water surfaces in different applications, including waterbody extraction [16], [17], flooding, and inundation mapping [18]. Since satellite SAR sensors have a side-looking geometric data acquisition and transmit signals in off-nadir look angle, most of the signals transmitted to calm water surfaces are scattered away from the SAR sensor. Particularly, open water acts like a mirror and, as a result, open water appears dark in a SAR image with no or an extremely low SAR backscatter making it distinguishable from surrounding land. C- and X-band SAR data have been examined for open water mapping in several studies [19]–[21].

Surface water detection can also be conducted as an initial step for classification of flooded vegetation [10]. Focusing on the suitable SAR polarization for water detection, HH-polarized data have been illustrated to be more useful due to their highest contrast between upland and open water [19]. Furthermore, it is less affected by wind-induced water surface changes than VV-polarization [22], [23]. However, water surfaces affected by wind or current have higher SAR backscatter than calm water and can be challenging to detect using only single SAR polarized data. In the latter case, using the cross-polarization channel that is less sensitive to surface roughness is useful. Particularly, using the HH/HV ratio assures accurate water body delineation [20].

The selection of appropriate SAR wavelength and polarization are two influential factors for land cover classification. Using Polarimetric Synthetic Aperture Radar (PolSAR) images with high capabilities to discriminate between different land cover classes [24] and, particularly, wetland

classes [25] is a more sophisticated approach. A fully polarimetric SAR sensor such as RADARSAT-2 acquires the full polarimetric scattering matrix, which provides comprehensive ground target information for each imaged pixel [26]. Different scattering mechanisms of ground targets can be detected by PolSAR data, including surface scattering (calm water surface), double-bounce scattering (man-made structure and flooded vegetation), and volume scattering (vegetation canopy). Different decomposition approaches of PolSAR data have been shown to be a promising tool for wetland classification [25]. In addition, wetland ecosystems are dominated by several distributed targets and may be better characterized using incoherent polarimetric decomposition techniques, such as Cloude-Pottier [27], Freeman-Durden [28], van Zyl [29], and Kennaugh matrix [30], different polarimetric decomposition techniques have been used for wetland classification based on several classifiers in recent years [31].

In the case of fully polarimetric SAR data, the classification result would be sufficiently robust due to complete polarimetric information. However, recent studies have focused on using a combination of dual polarized SAR data that provides high classification accuracy, as close to that of fully polarimetric data as possible, for wetland classification [31], [32]. Although, the dual polarization mode obtains half the information of a fully polarimetric dataset, they have a wider swath width, and therefore, cover a larger area [26].

While the suitabilitythe suitability of using dual co-polarized (HH/VV) SAR data for monitoring flooded vegetation was demonstrated early in 1997 [33], it has not been further investigated due to a lack of SAR sensors operating in that particular polarization mode [31]. Later studies have demonstrated the sufficiency of information content of co-polarized SAR data for monitoring of flooded vegetation [14], [31], [34]6). Currently, SAR missions primarily operate in either dual (TerraSAR-X, Sentinel-1) or fully polarimetric (RADARSAT-2, ALOS -2) modes.

Another consideration for land cover classification is the fusion of multi-source data. In particular, a fusion of optical and SAR data for classification of flooded vegetation has been extensively examined [35], [36]. The results demonstrated that integration of optical and radar data provides a promising tool in terms of classification accuracy. Furthermore, the combination of different SAR frequency bands has been found to improve the land cover classification accuracy [26], [35], [37], particularly for wetlands [10], [38], [39]. Importantly, each wavelength has its own advantages in the context of land and wetland cover classifications. For example, longer wavelengths, such as L-band (∼24 cm) have higher penetration depths through the vegetation canopy —necessary for discriminating between different wetland classes— while maintaining sensitivity to soil moisture and inundation. Also, a number of studies have demonstrated that longer wavelengths are better suited for forested wetland due to their higher penetration capability [35], [40]. However, shorter wavelengths, such as C-band (∼5.6cm) and X-band (~3.1 cm), are preferred to discriminate non-forested wetland classes (e.g., bog, fen, and marsh) as well as water [19].

Concerning classification algorithms, the availability of high resolution SAR data has been combined with advanced image analysis techniques, such as Object-Based Image Analysis (OBIA), to further improve the accuracy of land cover classification [41], [42]. OBIA has been demonstrated to outperform pixel-based classification approaches because it fuses multiple sources of data with different spatial resolutions. OBIA employs object features as classification inputs, including the spectral, spatial, geometrical, textural, and contextual information of a group of neighboring pixels (objects), in addition to the original pixel values, and enhances input information for the classification procedure. The capability of OBIA for wetland classification has been examined by a number of studies [38], [43]–[45]. OBIA is initiated with a Multi-Resolution Segmentation (MRS) analysis that generates objects of ground targets, which is a more intuitive

71

representation of ground features compared to that of pixel-based classification [46]. Particularly, MRS is developed based on a region-merging algorithm, starting with a pixel as a first-level object followed by the integration of pixels to produce objects, wherein the heterogeneity criteria is minimized [42]. However, segmentation parameters, such as scale, shape, smoothness, and compactness criteria, should be determined by users through a "trial and error" procedure depending on the classification purposes and available dataset [47]. This segmentation process is usually followed by classification to produce a classified map.

The Random Forest (RF) classifier is a powerful ensemble learning technique that has gained increasing attention in land cover classification using satellite images during the last decade [48]–[50]. The Random Forest algorithm is beneficial because: (1) it is less affected by outliers and noisier datasets; (2) it has a great capability to deal with a high dimensional, multi-source dataset while not being over-fitted to that; and (3) it has represented a higher classification accuracy compared to other well-known classifiers, such as Support Vector Machines (SVM) and Maximum Likelihood (ML) [51], [52]. Moreover, RF assesses the variable importance of input features, which is a qualitative analysis of variable contribution to the classification procedure [53]. The RF algorithm is similar to a decision tree algorithm, though it is constructed based on a series of trees, wherein each tree assigns a pixel to a specific class through a single vote [54]. Finally, RF has been demonstrated to be an easy to handle classifier, since only two input parameters should be determined by the user: the number of trees and the number of split variables.

This study aims to integrate multi-polarization and multi-frequency SAR images for classification of wetland complex. Particularly, single polarized TerraSAR-X, dual polarized ALOS-2, and fully polarized RADARSAT-2 SAR data are integrated in a hierarchical OBIA framework to identify different wetland classes. This flexible, hierarchical classification approach allows for

72

incorporating new rules and datasets without compromising predefined rules [55]. In such an approach, the number of input features is adjusted according to the complexity of classes, which are distinguished from each other in each classification level.

Using multiple scenarios in different classification levels, wetland classes are extracted. Therefore, the capability of each SAR polarization corresponding to different SAR wavelengths is evaluated in terms of classification accuracy in different levels and scenarios. For this purpose, different polarimetric features, including covariance, coherency, Kennaugh matrices obtained by dual and fully polarimetric SAR data, Cloude-Pottier, Freeman-Durden, and Yamaguchi decompositions, as well as SAR intensity images corresponding to single polarimetric SAR data, are extracted as input features for object-based RF classification.

The rest of this paper is structured as follows: Section 2 introduces the study area, *in situ* data, and satellite imagery in this research. This will be followed by a description of the methodology in Section 3. Section 4 presents the experimental results and discussion, and, finally, Section 5 draws a conclusion.

3.2. Study area and data

3.2.1. Study area

Within its borders, Canada contains 24% of the world's wetlands, corresponding to approximately 150 million hectares. The extensiveness of these wetlands highlights the importance of wetland management and particularly, wetland classification in this country [56]. Accordingly, Newfoundland and Labrador is among the richest Canadian provinces in terms of different types of wetlands (e.g., bog, fen, swamp, marsh, and shallow-water) and yet, it is the only province in Atlantic Canada that currently does not have a wetland inventory system. This paper addresses the

73

aforementioned issue by proposing a new wetland classification framework with a case study in Newfoundland and Labrador. The study area is located in the Avalon Peninsula (Figure 3.1) with various types of wetland classes and here is referred to the Avalon pilot site. The Avalon pilot site is a 700 square kilometer area located in the north eastern section of the Avalon Peninsula, on the island of Newfoundland, Canada, located in the Maritime Barren ecoregion. This ecoregion is characterized by a typical oceanic climate, experiencing foggy, cool summers and relatively mild winters. Mean annual temperatures are around 5.5°C and mean annual precipitation ranges from 1200 to 1600mm [57]. Land cover within the pilot site is dominated by different wetland types and it includes other classes such as urban, deep-water, and upland. Particularly, an upland may be more clearly defined as a "forested area" or a "forested dry area", and does not include non-forested upland areas, such as dry, non-woody herbaceous areas or heathlands. The majorities of urban regions are centered in the north eastern portion of the study area and includes the city of St. John's, the capital city of Newfoundland, with a population of around 200,000, and the city of Mount Pearl, Torbay and the Goulds.

According to the Canadian Wetland Classification System, wetland can be categorized as bog, fen, marsh, swamp, and shallow-water. All of these classes are found in the Avalon pilot site, though bog and fen are most common relative to the occurrence of swamp, marsh, and shallow-water. Bogs are dominated by *Sphagnum* moss, *Ericaceous* shrub, and sedge species. Fens are dominated by sedges and grasses, and although *Sphagnum* moss species are often present in fens, they do not dominate as they do in bogs [58]. Marshes are dominated by emergent aquatic species of sedges, rushes, and grasses. Swamps are primarily dominated by both tree and shrub Black Spruce (*Picea mariana*) and Tamarack (*Larix laricina*). Characteristic shallow-water vegetation is submerged aquatic macrophytes, especially species belonging to the genus water lilies (*Nymphaecae*).
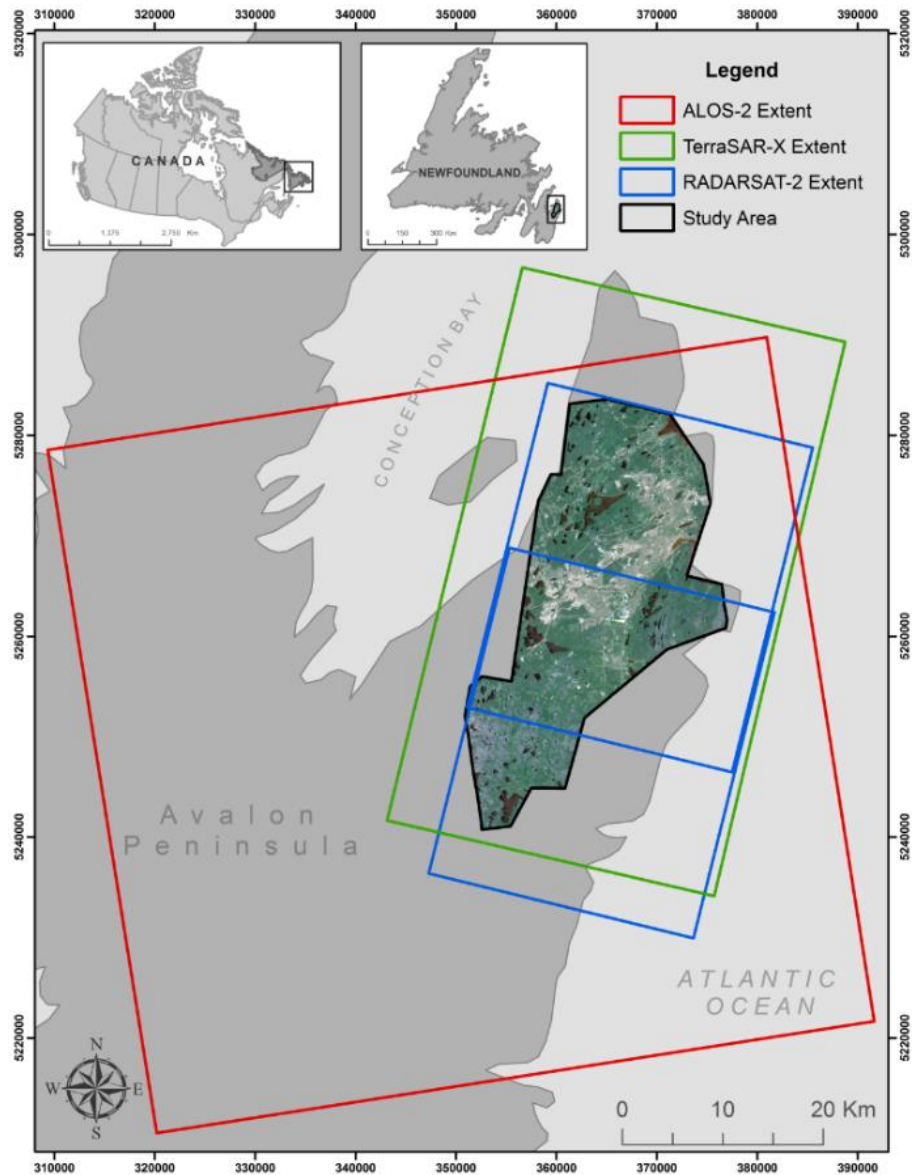
Figure 3.1. Overview of the study area with overlay of SAR images, RADARSAR-2 (blue boxes), TerraSAR-X (green box), and ALOS-2 (red box).

3.2.2. *In situ* data collection

Biologists, as the project team members, collected *in situ* data in the summers and falls of 2015 and 2016 in the Avalon pilot site. Using the visual analysis of high resolution Google Earth imagery and prior knowledge of the area, accessible wetland areas across the Avalon pilot site were flagged for visitation. A total number of 191 wetland sites were visited and categorized as

bog, fen, swamp, marsh, or water, as directed by the Canadian Wetland Classification System. During field work, one or, up to 3 points were taken per wetland site, depending on the size of each wetland. For some wetlands, such as swamp, which are somewhat challenging to delineate using visual methods, a point was taken at the nearest transition to upland. GPS points at each site were collected, along with ancillary data such as notes describing dominant vegetation and hydrology, and photographs, to aid the wetland boundary delineation process. Field delineation was conducted via visual interpretation of aerial photography and satellite images taken at different dates. An effort was made to delineate wetlands conservatively as to avoid including transitional areas within classifications. In particular, the GPS points were imported to ArcMap 10.3.1 to highlight visited wetlands and extract wetland boundary. Using satellite and aerial imagery, including a 50cm resolution orthophotograph and 5m resolution RapidEye imagery, polygons representing classified delineated wetlands were generated.

3.2.3. Reference data

For each class, reference polygons were sorted by size and alternatingly assigned to testing and training groups. Due to the limited amount of data and the wide variation of size within each wetland class (some small, some large), random assignment to testing and training groups could result in these groups having highly uneven pixel counts. However, alternative assignment ensures that both the testing and the training groups had comparable pixel counts for each class. Figure 3.2 illustrates the distribution of the training and the testing polygons for each land cover type across the study area.
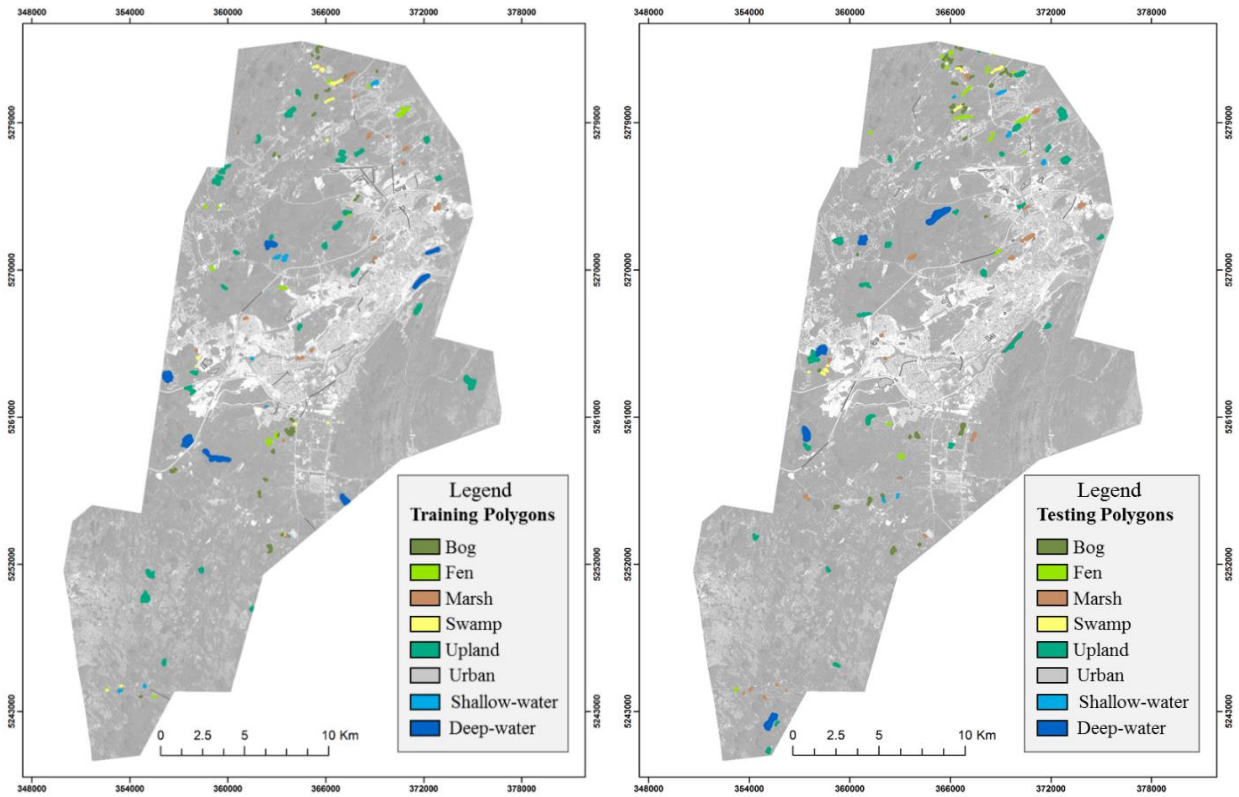
<table>
<tr><td>(a)</td><td>(b)</td></tr>
</table>

Figure 3.2. Distribution of reference data: (a) training and (b) testing polygons used for different classification levels.

Table 3.1 represents land cover classes and their respective pixel counts. As seen, the bog and fen classes have the most associated pixels of the wetland classes. In contrast, shallow-water and swamp classes have the least amount of pixels. The collection of *in situ* data was affected by several factors, including accessibility of wetlands by roadways, the natural ecology and distribution of wetland classes, and availability of biologists for field work. Thus, there is a variation in the quantity and quality of data for each individual class, as seen in Table 3.1. Importantly, the initial goal of the fieldwork component was to provide a minimum mapping unit of one hectare. However, over the course of the field work, many of the accessible wetlands of certain classes frequently occurred in smaller sizes. For example, of the 191 polygons collected in

the Avalon pilot site, 30 of those were swamp wetlands, of which only 7 were greater than 1 hectare in size. Similarly, of the 46 marsh wetlands, only 18 were greater than 1 hectare. These spatially small wetlands were chosen to be included in the study, because, without them, these wetland classes would be represented by a limited amount of field data.

Table 3.1. Testing and training pixel counts for Avalon reference data.

Class	Class Description	#Training Pixels	#Testing Pixels	Total
Bog	Peatland dominated by *Spahgnum* species	20650	17080	37730
Fen	Peatland dominated by graminoid species	11183	11311	22494
Swamp	Mineral wetland dominated by woody vegetation	3197	5161	8358
Marsh	Mineral wetland dominated by graminoids and emergent plants	10869	9685	20554
Shallow-water	Mineral wetland with standing water at most 2m deep	6205	5743	11948
Urban	Human-made structures	66339	67853	134192
Deep-water	Deep water areas	62927	89184	152111
Upland	Forested dry upland	73458	88947	162405
Total		254828	294964	549792

Bog wetlands are often large relative to other wetland classes in the province due both to their natural formation and ecology [58] and the province climate, which facilitates extensive peatland formation [59]. Furthermore, bog wetlands are often easy to access in the pilot site and are better spotted via satellite imagery. As a result, the bog wetland class has a relatively large amount of associated pixels. Conversely, shallow-water and swamps are arduous to flag for visitation and delineate as they may look visually similar to deep-water (>2m deep) and upland forest respectively when looking at aerial or satellite data. Swamps and shallow-water also tend to occur in physically smaller areas compared to other wetlands, such as in transition zones between one

wetland and another or along the edge of a water body. As a result, most swamp and shallow-water polygons will contain fewer pixels when compared to other wetlands types.

3.2.4. Satellite imagery

In this study, we used multi-polarized and multi-frequency SAR images. More specifically, single polarized (HH) TerraSAR-X (TSX), dual polarized (HH/HV) ALOS-2, and full polarized RADARSAT-2 images were acquired from the Avalon pilot site. A summary of data characteristics is presented in Table 3.2. RADARSAT-2 images were acquired in Fine Quad (FQ) mode. Due to small swath of FQ mode, more than one image was used to cover the whole study area. Also, level 3A RapidEye optical imagery with a pixel size of 5m was employed in initial segmentation for object-based classification. An overlay of SAR images on the study area is depicted in Figure 3.1.

Table 3.2. Characteristic of satellite imagery used in this study.

Sensor	Acquisition Date (yyyy/mm/dd)	Number of Images	Image Mode	Polarization	Incidence angle (˚)	Resolution (m) (Range× Azimuth)
TerraSAR-X	2016/08/22	1	StripMap	HH	20-45	3.1 × 3.2
RADARSAT-2	2015/08/21	2	FQ4	Full	22.1-24.1	4.7 × 4.9
ALOS-2	2015/08/02	1	FBD	HH/HV	36	9.1 × 5.3
RapidEye	2015/06/18	1	-	-	-	5

3.3. Methodology

The methodology comprised the four main steps outlined in Figure 3.3, wherein all Levels are classification levels. First, in the pre-processing step (Level-0 classification), image orthorectification and de-speckling were applied and SAR images were prepared for application in the hierarchical classification scheme. A sigma naught backscattering analysis for all land cover classes was then performed and water classes were separated from non-water areas in Level-I classification. This step was followed by Level-II and -III classification wherein: (1) PolSAR features were extracted; (2) MRS with different scale parameters compared to Level-I classification was employed; and (3) the RF classification was applied. This general process is explained in more detail in the following sections.

Secondary Multi-Resolution Segmentation

Ecological Training Data

Polarimetric Feature Extraction:
- Covariance Matrix
- Coherency Matrix
- Cloude-Pottier Decomposition
- Freeman-Durden Decomposition
- Touzi Decomposition

Random Forest Classification

Water

Non-water

Shallow-water

Deep-water

Herbaceous

Non-herbaceous

Ecological Validation Data

Accuracy Assessment

Level-II

Tertiary Multi-Resolution Segmentation

Polarimetric Feature Extraction:
- Covariance Matrix
- Coherency Matrix
- Normalized Kennaugh Matrix
- Cloude-Pottier Decomposition
- Freeman-Durden Decomposition
- Touzi Decomposition
- Yamaguchi Decomposition

Ecological Training Data

Random Forest Classification

Herbaceous

Non-herbaceous

Bog

Fen

Marsh

Urban

Upland

Swamp

Accuracy Assessment

Ecological Validation Data

Level-III

Figure 3.3. Flow diagram of processing and analysis steps employed in this study for wetland classification. The classification is initiated with pre-processing step in Level-0. Next, Level-I classification is at the top of the diagram and its results are water and non-water classes. In the middle of the diagram (Level-II classification), water is classified to shallow- and deep-water and non-water class is distinguished into herbaceous and non-herbaceous classes. In the bottom of the diagram (Level-III classification), herbaceous and non-herbaceous classes are classified to bog, fen, and marsh and urban, upland, and swamp classes, respectively.

3.3.1. Pre-processing step: Level-0 classification

3.3.1.1. Image orthorectification

Aligning the images from different sensors and geo-referencing each pixel is the main objective of orthorectification [60]. In this study, TerraSAR-X level-1 SSC and RADARSAT-2 level 1-SLC images were processed and orthorectified by PCI Orthoengine 2015 SP1 software using a SAR specific satellite orbiting model. ALOS-2 level 1.1 image was geo-referenced through the Gamma Remote Sensing V.4.1 software. An external Digital Elevation Model (DEM) released by Natural Resources Canada, with a resolution of roughly 19 meters, was used for orthorectification (http://geogratis.gc.ca/site/eng/extraction). All images were projected to UTM coordinates (Zone 22, row T) using the WSG84 reference ellipsoid. Also, orthorectified RADARSAT-2 images were mosaicked to produce a cohesive coverage of our case study.

3.3.1.2. Speckle reduction

The enhanced Lee adaptive filter with a 5×5 kernel was applied to reduce the effect of speckle in the images. De Leeuw et al. (2009) have demonstrated that the enhanced Lee adaptive filter outperformed other well-known filters (e.g., Kuan, Frost, Enhanced Frost, and Gamma filters) in terms of both speckle reduction as well as preserving the feature edges [61]. Adaptive filters use the standard deviation of neighboring pixels within a local kernel surrounding each pixel to

calculate a de-noised value [62]. Unlike a traditional filter, they preserve the mean values, image sharpness, pixel value variability, and details while minimizing the loss of radiometric and textural information [62]. More specifically, the enhanced Lee filter has three different solutions according to the level of heterogeneity on the image: (a) a mean filter is applied in homogeneous areas; (b) a Lee filter is applied on heterogeneous areas; and (c) pixel value is preserved in areas with strong heterogeneity [63].

3.3.2. Polarimetric decompositions

In this study, several decomposition features were extracted in OBIA (section 3.3.3). A brief description of these decompositions is presented here. The Cloude-Pottier decomposes information of distributed ground targets into deterministic targets (dominant scattering mechanisms) using a mathematical framework known as eigenvalue and eigenvector decomposition. More precisely, eigenvectors and eigenvalues determine the type and strength of the scattering mechanism, respectively. However, due to the complexity of interpreting scattering vectors in their original representation (eigenvalue/eigenvector), $H/A/\alpha$ parameters are extracted to define the relationship between three scattering mechanisms [31]. Entropy (H) determines the heterogeneity of a single scatter, wherein lower values represent that single scattering mechanism is dominant. On the other hand, higher values illustrate the presence of three equipollent scattering mechanisms. The intermediate values are not, themselves, interpretable and must be considered in relation to the anisotropy (A) values. Thus, anisotropy is a complimentary component to entropy and determines the relative importance of the secondary scattering mechanisms. The alpha angle (α) determines the dominant scattering mechanism and varies between 0-90 degrees. Low alpha angles indicate that the surface scattering mechanism is dominant. Intermediate (~45°) and high

(~90°) alpha angles illustrate that volume scattering and double-bounce are the dominant scattering mechanisms, respectively [64].

The Freeman-Durden decomposition exploits different scattering mechanisms of ground targets using a physical scattering model. Particularly, three polarimetric features from a dihedral corner reflector are extracted to determine the portion of surface, double-bounce, and volume scatterings exhibited in each target [28].

The Touzi decomposition is an eigenvalue/eigenvector-based decomposition like the Cloude-Pottier decomposition. However, in the Touzi decomposition, a roll-invariant coherent scattering model for determination of the coherency eigenvectors is used. The Touzi decomposition has five independent parameters for non-interferometric applications, which are α_s, ϕ_{α_s}, Ψ, τ_m, and m [25]. More specifically, the target scattering types are characterized with a complex entity (α_s) and a symmetric scattering type. The phase ($\emptyset_{\alpha_s}$) of the symmetric scattering represents a high potential for wetland vegetation discrimination, though its magnitude (real part) may not be as useful.

The Yamaguchi decomposition is a four-component scattering model for decomposing PolSAR images and is an extended version of Freeman-Durden decomposition. A helix scattering component is added to separate the co-pol and the cross-pol correlations, which is generally the case of complex urban area [65].

Normalized Kennaugh elements developed by Schmitt and Brisco (2013) were also extracted in this study [31]. It is considered as a complementary feature to typical polarimetric decompositions while may also outperform other decompositions, since the necessity of removing the number of channels, and accordingly, information content is eliminated. More precisely, the elements of

scattering matrix are interpreted without any intermediate tools, and the Kennaugh elements in the case of fully polarimetric data (by considering the reciprocity assumption) are obtained as follows [66]:

$$[\boldsymbol{K}] = \begin{bmatrix} K_0 & K_4 & K_5 & K_6 \\ K_4 & K_1 & K_9 & K_8 \\ K_5 & K_9 & K_2 & K_7 \\ K_6 & K_8 & K_7 & K_3 \end{bmatrix} \qquad (3.1)$$

However, for dual polarimetric data some elements are removed according to the availability of PolSAR data. For instance, Kennaugh elements for cross-pol acquisitions (HH/HV), wherein the transmission is occurred in one while the reception in two linear polarizations, are K_0, K_1, K_5, and K_8. In particular, K_0 denotes the total intensity, K_1 illustrates the difference between co- and cross-polarized intensity (HH and HV), K_5 and K_8 hold the real and imagery part of inter-channel correlation. By dividing the Kennaugh matrix to total intensity (K_0), the normalized Kennaugh matrix is obtained as follows:

$$[\boldsymbol{K}] = K_0 \begin{bmatrix} 1 & k_4 & k_5 & k_6 \\ k_4 & k_1 & k_9 & k_8 \\ k_5 & k_9 & k_2 & k_7 \\ k_6 & k_8 & k_7 & k_3 \end{bmatrix} = I.[\boldsymbol{k}] \qquad (3.2)$$

where each element varies between -1 and 1 and represents in decibel unit. Furthermore, the polarization content is defined as the polarimetric information contribution and obtainable by the sum of the normalized Kennaugh elements as follows:

$$P_G = \sqrt{\frac{1}{n} \sum_{1}^{n} k_i^2} \quad i \in [1,2,\dots,9] \qquad (3.3)$$

3.3.3. Object-Based Image Analysis (OBIA) and classification

Image classification was carried out on the basis of an OBIA framework and executed in the eCognition software package (V.9.0.3). The object oriented classification was preferred over pixel-based classification, since the former incorporates the shape, size and spatial relationship of objects, integrates multi-source data, and significantly increases information content in the classification procedure. Moreover, due to the presence of speckle noise, the object-based classification was demonstrated to be better suited for classification of radar images [41].

OBIA processing generally includes two main steps: segmentation and classification. In this study, the Multi-Resolution Segmentation (MRS) and the Random Forest (RF) were selected as segmentation and classification methods, respectively. The MRS approach is known as a region-merging method, wherein the main objective is to minimize the summed heterogeneity between neighboring pixels [67]. MRS is adjusted in the eCognition software by determining three user-defined factors: shape, compactness, and scale. Particularly, the shape parameter varies between 0-1 and specifies both the level of radiometric homogeneity and object shape simultaneously. Lower and higher shape values produce objects that are optimized for radiometric and shape homogeneity, respectively. The compactness parameter specifies the degree of object smoothing and varies between 0-1. More specifically, the value for compactness determines a relative weighting against smoothness. Finally, the scale parameter specifies the size of the final image object, which corresponds to the maximum acceptable heterogeneity [10]. Higher scale parameter values result in larger image objects and lower values produce smaller image objects.

As mentioned above, the first step in the object-based image classification is to segment the image into different objects, in which the segmentation scale is the most important parameter. This is because different ground targets have different optimal scales that result in the highest

classification accuracy. Thus, three classification levels were defined in this paper and discussed in the following sections.

3.3.3.1. Feature extraction: Level-I classification

The main objective of Level-I classification was to produce image objects that correspond to ground features, particularly lakes. The MRS was employed using an optical image in this study (see Figure 3.3) because unlike segmentation using SAR images, it does not produce meaningless objects. Thus, we extracted objects from optical images (RapidEye) and applied them into SAR images. Furthermore, MRS analysis in this step was carried out using different segmentation parameters. The final parameters for scale, shape, and compactness were obtained 300, 0.05, and 0.5, respectively. These values were chosen since they were well-suited to represent image objects corresponding to ground features and, particularly, for small water bodies.

Level-I classification was performed for the entire Avalon study area. Surface scattering of water body causes low signal return to the SAR sensor and, as a result, calm water appears dark in the SAR image [19]. However, wind and water streams cause water surface disturbance, and the rough water surface appears as different grey levels and can be difficult to distinguish from other land cover types. Thus, to best differentiate water surfaces from other land cover classes, a sigma naught backscattering analysis was performed in this study in multi-polarized, multi-frequency framework to determine the best configuration. Particularly, in Level-I classification, different thresholds in each channel were employed to discriminate water and non-water classes. For this purpose, extracted intensity values from different land cover classes were converted into normalized backscattering coefficients (σ^o) expressed in the logarithmic scaling dB, which is a standard unit to represent SAR backscattering [10]. Accordingly, box-and-whisker plots of the

classes in varying polarizations and SAR wavelengths were exploited to determine the σ^o variability of different training classes.

3.3.3.2. Feature extraction: Level-II classification

The second level of the classification scheme partitioned the water class obtained in Level-I into two possible land covers: shallow- and deep-water. Furthermore, the non-water class obtained in Level-I was further classified into herbaceous and non-herbaceous classes. In this level, a second MRS was performed with a scale parameter set to 50 and other parameters remained the same as in the primary segmentation.

The main objective of Level-II classification was to identify different scattering mechanism of ground target to obtain polarimetric information. For this purpose, SAR intensities, polarimetric decomposition features, as well as covariance and coherency matrices were extracted, and used along with σ^o signatures and the training dataset for object-based image classification obtained in Level-I. Incoherent polarimetric decomposition aids discrimination between several distributed targets of wetland complexes, wherein the measured polarization channels are incorporated in a backscattering matrix [31]. Cloude-Pottier, Freeman-Durden, and Touzi decompositions were applied in different scenarios using varying configuration of input features for wetland classification (scenarios 1-8 in Table 3.3). These decompositions were selected since they represent the basic scattering mechanisms of ground targets and provide the required detail discrimination between land cover types for this classification level. This procedure resulted in four land cover classes, including shallow-water, deep-water, herbaceous, and non-herbaceous.

3.3.3.3. Feature extraction: Level-III classification

Level-III classification considered both herbaceous and non-herbaceous classes while ignoring both shallow- and deep-water classes derived in Level-II classification. In Level-III classification, a third multi-resolution segmentation was performed with a scale parameter set to 10 while other MRS parameters were the same as the primary segmentation.

 In the final classification level, the herbaceous class was further portioned into more detailed wetland classes, including bog, fen, and marsh, and the non-herbaceous class was further classified into swamp, upland, and urban classes. The main reason for this categorization is that the term herbaceous can mean any plant with non-woody stems. In the context of the Canadian Wetland Classification System (CWCS), the marsh and shallow-water classes can be considered to be herbaceous wetlands as they are majorly, if not entirely, dominated by non-woody plant species. Marshes can contain some shrub species (*Myrica gale* for example), but usually contain mostly grasses, sedges, and rushes. Bogs and fens can contain a mix of herbaceous and non-woody plant species, as is reflected by the peatland "types" (a level of the wetland classification hierarchy in the CWCS) of treed bog, shrubby bog, and shrubby fen. However, in the context of Newfoundland and this research, peatlands are majorly treeless on the island, and the majority of bogs and fens sampled during field work were dominated by sphagnum moss species (bogs) and sedges and grasses (fens). Based on this information and for purposes of simplification, bogs and fens can be grouped in the category of herbaceous wetlands. Comparatively, swamps are always dominated by woody vegetation, whether that vegetation is trees, shrubs, or a mixture of both. In this research, upland represents forested dry land which, like swamp, is dominated by woody trees and shrubs. Thus, bog, fen, and marsh are characterized as herbaceous classes, while swamp, upland, and urban are considered as non-herbaceous classes.

The main objective of Level-III classification is to obtain detailed land cover classes. Thus, as seen in Table 3.3, in addition to Level-II features (scenarios 1-7), Yamaguchi decomposition with four elements and Kennaugh matrix with ten elements were added to Level-III classification. More specifically, the classification in this step was followed using the polarimetric features similar to Level-II classification, including covariance and coherency matrices, Cloude-Pottier, Freeman-Durden, and Touzi decompositions (scenarios 1-7 in Table 3.3), as well as other polarimetric decomposition features such as Kennaugh matrix elements, and Yamaguchi components (scenarios 9-13 in Table 3.3). The normalized Kennaugh matrix elements were included since they provided additional information compared to covariance and coherency matrices [31], which may be useful for distinguishing similar herbaceous wetland classes (e.g., bog and fen). Furthermore, by defining different scenarios, the effect of dual polarimetric (HH/HV) versus fully polarimetric images was investigated for wetland classification using different elements of the Kennaugh matrix. The Yamaguchi decomposition was also extracted in this step because the helix term of the Yamaguchi decomposition is suitable for discriminating complex land cover classes [65]. Thus, adding the helix term was beneficial for separating the urban class from other possible land cover types obtained in Level-II.

Table 3.3. Different scenarios employed in Level-II and -III classification. In Level-II classification, scenarios 1 to 7 were defined based on different polarimetric features and scenario 8 was a combination of all seven. In Level-III classification, all scenarios were used excluding scenario 8 (see Figure 3.3).

Scenario	Number of features	Name of features	ALOS-2 Dual (HH/HV)	RADARSAT-2 Dual (HH/HV)	RADARSAT-2 Quad (HH/HV/VV)
1	3	Cov [C_2]	✓		
2	3	Cov [C_2]		✓	
3	6	Cov [C_3]			✓
4	6	Coh [T_3]			✓
5	3	Cloude-Pottier			✓
6	3	Freeman-Durden			✓
7	5	Touzi			✓
8	26	All features in scenarios 1, 3, 4, 5, 6, and 7	✓		✓
9	4	Yamaguchi			✓
10	10	Kennaugh [K_4]			✓
11	4	Kennaugh Elements		✓	
12	4	Kennaugh Elements	✓		
13	44	All features excluding scenario 8	✓		✓

3.3.4. Accuracy assessment

The accuracy assessment was performed for classified maps using the field data held back for validation purposes through: 1) overall accuracy; 2) kappa coefficients; and 3) user's and producer's accuracy. Overall accuracy reflects the correctly classified areas for the whole image and is calculated by the ratio of the correctly classified pixels to the total number of pixels in the confusion matrix. The kappa coefficient determines the degree of matching between reference data and classified map. The other accuracy parameters obtained by confusion matrix are user's and producer's accuracy corresponding to the commission and omission error for each class, respectively [68]. In this study, the first two assessment parameters were extracted for different scenarios. However, the latter one was carried out for the final classified map.

3.4. Results and discussion

3.4.1. Backscatter analysis

Backscattering analysis was performed for all wetland classes as well as other land cover types in the multi-polarization and multi-frequency framework to determine which configuration of wavelength/polarization was better suited for discriminating between different wetland classes. The statistical distribution of backscatter for each class is illustrated using box-and-whisker plots in Figure 3.4. A detailed description of the results of the backscattering analysis in this step is presented in the following sections.
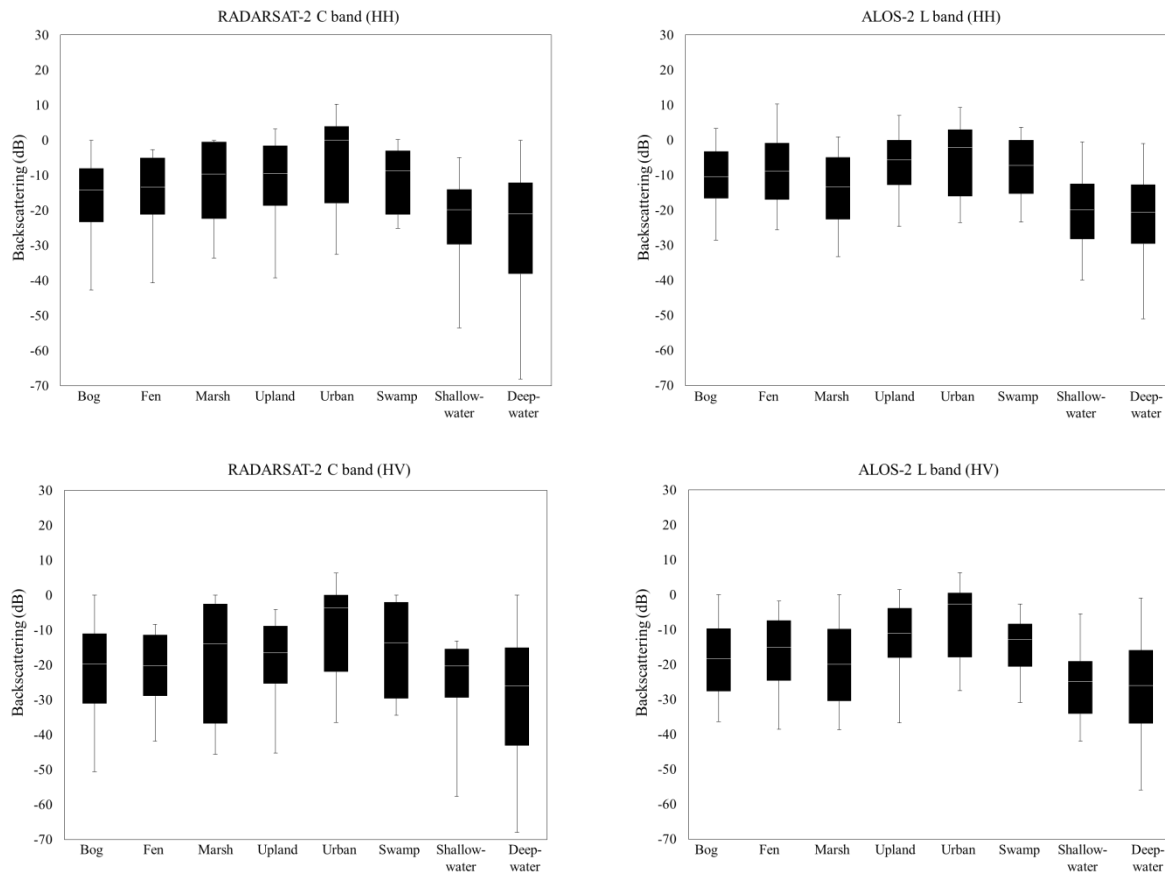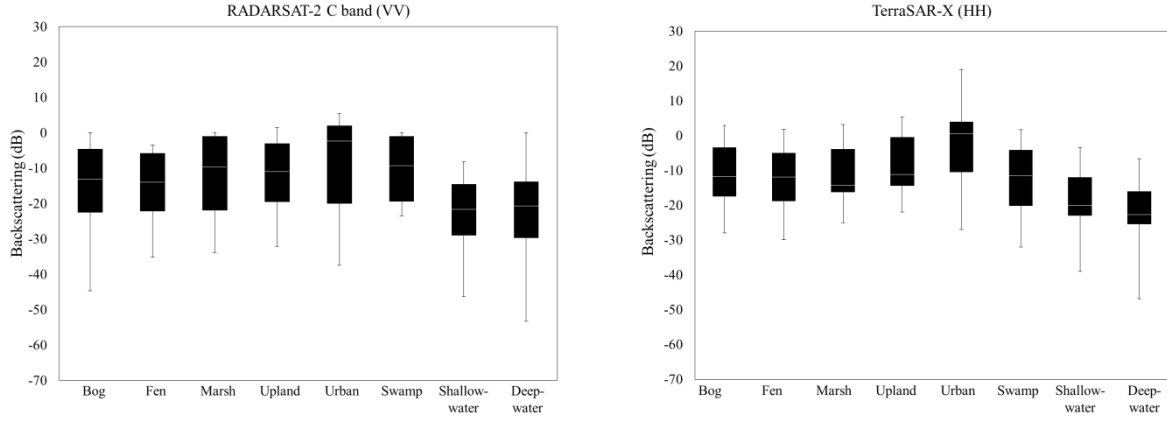
Figure 3.4. Box-and-whisker plots representing the distribution of backscattering coefficients for land cover classes obtained using pixel values extracted from training data sets. The white bars within boxes illustrate the median.

3.4.1.1. Water class

The backscatter analysis demonstrated that water classes, including shallow- and deep-water, have the lowest overall distribution of σ^0 values for all wavelengths and polarizations. The results illustrated that median σ^0 values for shallow-water, which is one of the wetland classes, were approximately -20dB in all HH polarized data as well as in C-band HV, and -22dB, and -23dB for C-band VV and L-band HV, respectively. Furthermore, the σ^0 values represented the lowest and highest variabilities in X-band HH and L-band HV, respectively.

Backscatter analysis of the deep-water class represented the lowest σ^0 values among all classes (water and non-water) and higher variability within water classes. The median σ^0 values for all HH polarized images, regardless of SAR wavelength, as well as C-band VV image were approximately -21dB. However, C- and L-band HV images exhibited lowest median approximately -25dB. The lower median σ^0 in the former values of the deep-water compared to the shallow-water classes could be due to the greater water depth and less emergent vegetation. Thus, the larger water area produces surface scattering and results in a greater decrease in the

median σ^0 values. More precisely, the deep-water class does not have any emergent vegetation and, as such, surface scattering is the only dominant scattering mechanism. In such a class, surface water acts like a mirror and, as a result, most of the transmitted signal is specularly backscattered away from the SAR sensor, causing a negligible σ^0 return [69]. However, shallow-water wetlands generally contain some emergent vegetation. Emergent vegetation can cause both volume- and double-bounce backscatter, depending on vegetation conditions, wavelength, and polarization. Furthermore, though wind roughness has the same effect on both shallow- and deep-water, the magnitude may be different for these two classes. This is because the shallow-water can produce larger waves and generate higher σ^0 compared to the deep-water class.

Overall, the observed median values for the deep-water class illustrated the dominance of the surface scattering mechanism. Furthermore, the results revealed a high degree of σ^0 variabilities at C-band HH and HV images. We speculated that this occurred due to surface roughness caused by wind or water flow at the time of C-band image acquisition [39].

3.4.1.2. Non-water class

The backscatter analysis of non-water class demonstrated that urban class has the highest σ^0 values among all land cover types with a median varied between 0 and -3dB depending on the SAR wavelengths and polarizations. However, HH polarized images had the highest σ^0 median of approximately 0dB. Upland class had the second highest σ^0 values in all HH polarized images with a median about -5dB in L-band and -10dB in C- and X-band images. Among wetland classes (bog, fen, marsh, and swamp within non-water class), swamp class showed the highest overall median σ^0 values in all SAR polarizations and wavelengths images with a few exceptions wherein marsh class had higher median. The overall high σ^0 values for swamp class was an evidence for dominant volume (or multiple) backscattering mechanisms within forest woodland class. In such

an environment, the backscattering is resulted from several sources, including backscattering from upper part of vegetation canopy, volume scattering within the vegetation, and double- or multiple-bounce scattering between water and tree trunk [11]. Furthermore, the longer L-band wavelength has higher penetration depth in comparison with shorter wavelengths such as C- and X-bands. All these mentioned parameters were combined and resulted in higher σ^0 values for L-band in the swamp class. However, for this class, the median σ^0 values were lower in C-band (HH and HV) and X-band (HH) images, which showed the volume scattering was dominant within the canopy in shorter wavelength [70]. A high degree of similarity was observed among non-herbaceous classes especially upland and swamp classes, although HH polarized data, and particularly X-band image, demonstrated to be better able to separate upland and swamp classes.

Focusing on herbaceous wetland classes (bog, fen, and marsh) versus non-herbaceous wetland class (swamp), the backscattering analysis represented that the lower σ^0 values observed in the marsh class compared to the swamp at L-band. This confirmed that herbaceous vegetation is partially transparent at L-band [11], [71]. As also reported by other comparable studies [10], [72] the lower values at L-band in comparison to C-band for marsh class are because of a combined volume and surface scattering mechanisms at L-band. However, the dominant scattering mechanism in marsh class at C-band is expected to be volume scattering, which also caused a relatively higher σ^0 values.

The analysis also revealed a high degree of overlap between herbaceous classes (bog, fen, and marsh) for all imagery especially for bog and fen classes. Particularly, bog and fen classes exhibited close median values regardless of SAR polarizations and wavelengths: both classes are peatland dominated with non-woody structure. The high degree of overlap between herbaceous classes is due both to the similar vegetation cover (*Spahgnum* and *graminoid*) as well as dominant

95

volume scattering mechanism in the herbaceous classes. However, the marsh class represented different median than two other classes although its box plot diagrams still represented a great degree of overlap with these two classes. The backscatter analysis also showed that herbaceous classes overall had the lowest σ^0 values in comparison with non-herbaceous classes due to the heterogeneity of the vegetation canopy compared to the relatively homogeny non-herbaceous classes. Particularly, the mixed vegetation canopy structure in the herbaceous classes caused a relatively higher variability and, as a result, lower median σ^0 values. As it seen in Figure 3.4, marsh class represented a high degree of σ^0 variabilities within non-water class in all imagery.

From the polarization point of view, the backscattering analysis demonstrated that HH and HV polarized images had the highest and lowest backscatter in all classes, respectively. Concerning the SAR wavelength X-band image represented higher backscatter in herbaceous classes while L-band illustrated higher backscatter in the swamp class when comparing only HH polarized images. This is in great consistency with the results of other studies that found shorter wavelengths to be better suited for monitoring of herbaceous classes, while longer wavelengths are preferred for monitoring of woody wetlands [20].

3.4.2. Level-I classification

In this classification level, an initial classified map was obtained using backscattering analysis (Section 3.4.1). More specifically, the mean values of σ^0 were calculated and used along with the median σ^0 values and their variability to separate water and non-water classes. The classified map of Level-I classification is depicted in Figure 3.5 with two water and non-water classes.
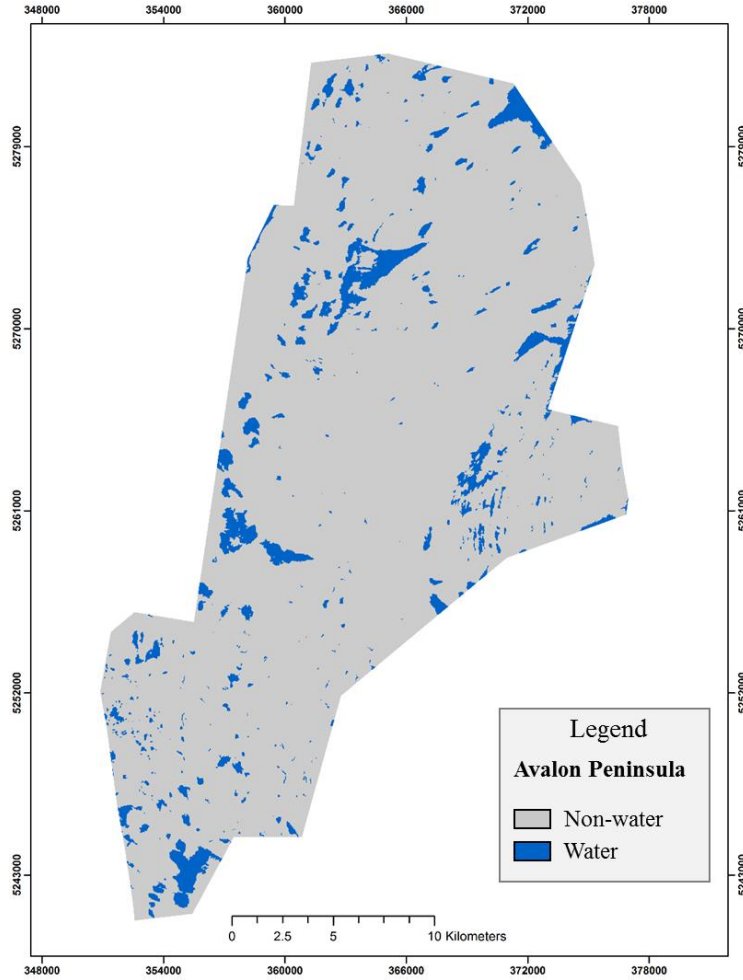
Figure 3.5. Level-I classification, separating water and non-water classes in the study area.

3.4.3. Level-II classification

In Level-II classification, the water and non-water classes obtained from Level-I were further separated into more detail. Particularly, the water class was separated into two classes, shallow- and deep-water, while the non-water class was partitioned into herbaceous and non-herbaceous classes. As discussed earlier, this classification level was performed using different decomposition methods in eight scenarios described in Table 3.3. Table 3.4 represents the overall accuracies and Kappa coefficients of different RF scenarios for Level-II classification.

Table 3.4. Overall accuracy and kappa coefficient for Level-II classification in different scenarios.

Scenarios	Name of features	Kappa Coefficient	OA (%)
1	Cov [C_2]	0.41	41.28
2	Cov [C_2]	0.45	39.79
3	Cov [C_3]	0.52	48.55
4	Coh [T_3]	0.60	52.85
5	Cloude-Pottier	0.63	54.98
6	Freeman-Durden	0.72	73.19
7	Touzi	0.81	76.28
8	All features in scenarios 1, 3, 4, 5, 6, and 7	**0.92**	**96.20**

The effects of dual versus fully polarimetric images, as well as decomposition methods, were investigated in terms of classification accuracies. Focusing on the dual polarimetric images, L-band data (scenario 1) was approximately 1.5% more accurate than C-band (scenario 2). This is in good agreement with backscatter analysis of different wetland classes in Section 3.4.1, wherein overall L-band images exhibited higher σ^0 values in most cases excluding the marsh class. However, using fully polarimetric RADARSAT-2 images significantly improved classification accuracy up to 13% (scenario 4 versus scenario 2). The other remarkable improvement was observed by adding Freeman-Durden decomposition (~20%, scenario 6), while Cloude-Pottier decomposition was less successful for increasing the classification accuracy with only a 2% improvement (scenario 5) compared to the coherency matrix (scenario 4).

The Cloude-Pottier decomposition is usually applied as an initial unsupervised classification to decompose the information of the distributed target into the scattering mechanism of deterministic targets, which may explain its less contribution to increase the classification accuracy [31], [73].

Another reason could be the discrepancy of the phase centers during reflection. In particular, this issue is more severe in the Cloude-Pottier decomposition resulting in a very noisy decomposition parameter and less successful classified map [66]. The anisotropy and entropy layers of the Cloude-Pottier decomposition are characterized by very high noise content over natural scatterer environments such as wetland complexes [31].

In contrast, the Freeman-Durden decomposition (scenario 6) was found to be more successful than covariance and coherency matrices (scenarios 3 and 4, respectively) for improving classification accuracy. This is because Freeman-Durden decomposition incorporates the physical scattering mechanisms of the ground target into the classification scheme, which added more information in this study. Particularly, two steps are involved in the Freeman-Durden decomposition. First, the volume scattering information is exploited and then the remaining scattering content is further divided into dominant double-bounce or dominant surface scattering mechanisms. Although, the classification would be more robust if there was only one dominant scattering mechanism in the second step. The backscatter analysis of wetland vegetation classes represented that the volume scattering was the first dominant scattering mechanism in this study (corresponding to the first step of Freeman-Durden decomposition), followed by double-bounce as the second dominant scattering mechanism (corresponding to the second step of Freeman-Durden decomposition). The above issue demonstrates the reason for significant classification improvement obtained by Freeman-Durden decomposition.

Following the consequent classification scheme in Level-II, the result was further improved by using Touzi decomposition. The best classification result was obtained with scenario 8, which incorporated target decomposition features, covariance and coherency matrices of fully polarimetric RADARSAT-2 image, and covariance matrix of dual polarimetric ALOS-2 image.

An overall accuracy of approximately 96% was obtained using all polarimetric features, which improved the classification accuracy about 20% compared to scenario 7. Figure 3.6 depicts the classified map for scenario 8, which was the most significant result of Level-II classification using the RF classifier.
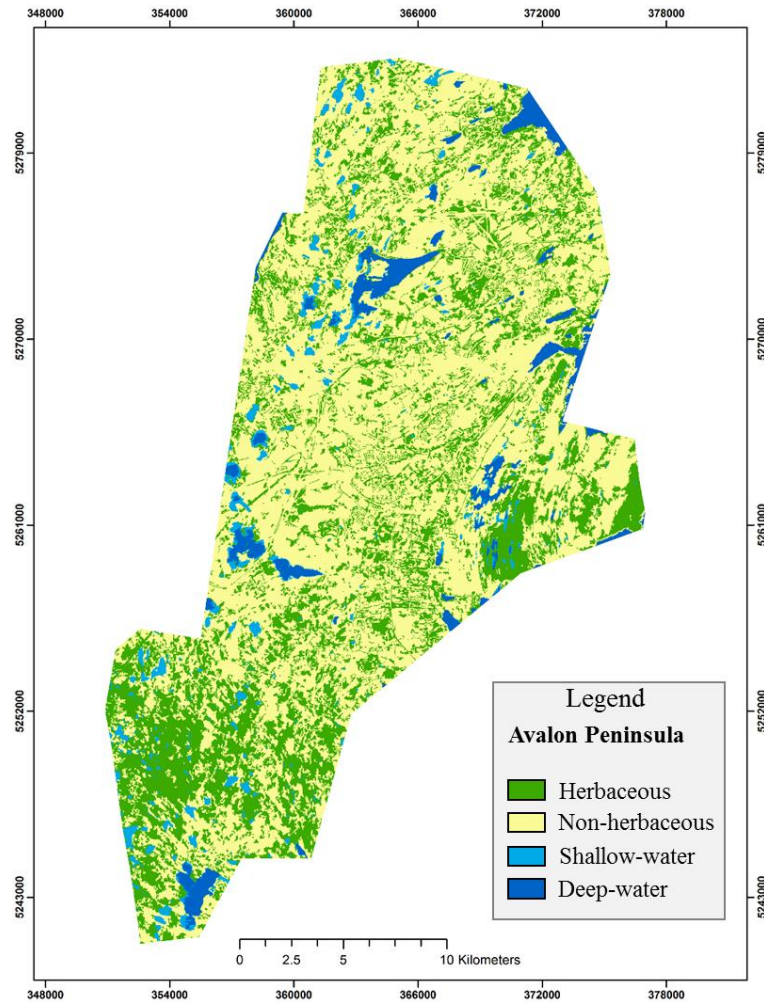
Figure 3.6. The most significant result of RF (scenario 8) in Level-II classification, which divided the water class (from Level-I classification) into shallow- and deep-water, and the non-water class (from Level-I classification) into herbaceous and non-herbaceous classes.

3.4.4. Level-III classification

In Level-III classification, the shallow- and deep-water classes obtained from Level-II classification were removed from further analysis and classification focused on herbaceous and non-herbaceous classes (obtained from Level-II). In this level, the non-herbaceous class was further classified into urban, upland, and swamp classes, while the herbaceous class was divided into bog, fen, and marsh classes. Similar to Level-II classification, different polarimetric features were used for different RF scenarios (see Table 3.3). More precisely, the effect of using polarimetric decompositions (Cloude-Pottier, Freeman-Durden, Touzi, and Yamaguchi decomposition), covariance and coherency matrices, and different elements of the normalized Kennaugh matrix were evaluated in detail to improve the classification accuracy of the wetland complexes. Furthermore, the effect of dual polarimetric images for wetland classification were investigated and compared with fully polarimetric SAR data. Table 3.5 represents the overall accuracies and kappa coefficients obtained in different RF scenarios in Level-III classification.

Table 3.5. Overall accuracy and kappa coefficient for Level-III classification in different scenarios.

Scenarios	Name of features	Kappa coefficient	OA (%)
1	Cov [C_2]	0.33	38.44
2	Cov [C_2]	0.31	37.86
3	Cov [C_3]	0.34	40.07
4	Coh [T_3]	0.42	45.31
5	Cloude-Pottier	0.60	62.39
6	Freeman-Durden	0.64	68.27
7	Touzi	0.66	69.73
9	Yamaguchi	0.67	70.40
10	Kennaugh [K_4]	0.69	71.29
11	Kennaugh Elements (RADARSAT-2)	0.62	63.81
12	Kennaugh Elements (ALOS-2)	0.60	62.07
13	All features excluding scenario 8	**0.88**	**91.83**

In Level-III classification, 12 RF scenarios were considered (scenarios 1-13 in Table 3.3 excluding scenario 8). For the first two scenarios dual polarimetric data were applied. Similar to Level-II classification, L-band dual polarized data (scenario 1) represented higher accuracy than C-band (scenario 2) due to its higher penetration capability. However, using full polarization C-band images (scenarios 3 and 4) illustrated more success than dual polarimetric images (scenario 1 and 2) in comparable cases.

Applying the Cloude-Pottier decomposition was less successful compared to other decompositions as was also the case in Level-II classification. Freeman-Durden, Touzi, and Yamaguchi decompositions demonstrated better results. Yamaguchi decomposition is a modified version of

Freeman-Durden decomposition, wherein the helix scattering term was added to three scattering mechanisms of model-based decomposition. The helix component is particularly important for obtaining scattering information of complex urban structures and may not be as useful for a naturally distributed scatterer (e.g. wetland complex). However, there is a small improvement for Yamaguchi decomposition (scenario 9) in comparison to the Freeman-Durden decomposition (scenario 6), which could be due to its better performance in urban areas.

Following the hierarchical classification procedure using different polarimetric features, the classification accuracy improved by 25% when Kennaugh matrix elements are incorporated (scenarios 10, 11, and 12) compared to scenario 4. The normalized Kennaugh elements are obtained from linear combinations of the correlation between polarization channels, which minimizes noise levels. This contrasts with other common polarimetric approaches, which require classification or eigenvalue decomposition [27]. The results confirm that Kennaugh matrix elements improve the overall classification accuracy [31]. We believe that the normalized Kennaugh elements have the highest polarimetric information content with the least amount of noise compared to other polarimetric features.

The most interesting result was the classification accuracy obtained by Kennaugh elements of dual polarimetric images. Particularly, the classification accuracy of dual polarimetric images (scenarios 1 and 2) was less than 40%. However, incorporating Kennaugh elements, even in dual polarization mode (scenarios 11 and 12), increased the classification accuracy up to 60%. This is of great importance considering the capability of Kennaugh elements for wetland classification, especially when using dual polarized data. As discussed earlier (see section 3.3.2), in the case of cross-pol acquisition (HH/HV), Kennaugh matrix has four elements that breaks down the backscatter signal into the total intensity (K_0), the ratio between intensities (K_1), the ratio between

double-bounce and volume scattering intensity (K_5), as well as the phase shift between double-bounce and volume scattering (K_8). We believe that the most important parameter, which has contributed to improve the classification accuracy in these two scenarios (scenarios 11 and 12), is K_0. This is because Moser et al. (2016) performed a multi-temporal classification using only K_0 data obtained from dual polarimetric (HH/VV) TerraSAR-X data and concluded that K_0 improved classification accuracy [34]. The K_0 element represents total intensity, although it has been formulated differently in the case of co- and cross-polarization imagery. Also, K_1 illustrates the difference between co- and cross-polarized intensities and therefore, might be the second important features to improve the classification accuracy [66]. Finally, K_5 and K_8 are more useful in urban areas with deterministic targets [66], though even those areas are much influenced by intensity information [34]. Fully polarimetric SAR data contain all of the polarimetric scattering information. However, it has been demonstrated that Kennaugh elements $K_0, K_2,$ and K_4 are sufficient for wetland classification since these elements are directly related to land cover scattering mechanisms [31]. In our research, inclusion of all Kennaugh elements further improved the classification accuracy up to 71% (scenario 10), which could be due to incorporating K_2 and K_4 elements into the classification framework [31]. Finally, inclusion of all polarimetric features into the RF classifier significantly improved overall accuracy (scenario 13), up to 91%, in comparison with scenario 10 (see Table 3.5).

3.4.5. Post classification analysis

As mentioned before, a unique advantageous of RF is that it provides information on the importance of input variable to determine the significance of each input feature for increasing classification accuracy. This is particularly important, for PolSAR image classification, wherein several polarimetric decomposition features are incorporated into the classification process. Since

the most significant result was obtained for scenario 13, this classification was selected for further accuracy assessments. Figure 3.7 represents the variable importance of the most significant result in this study.
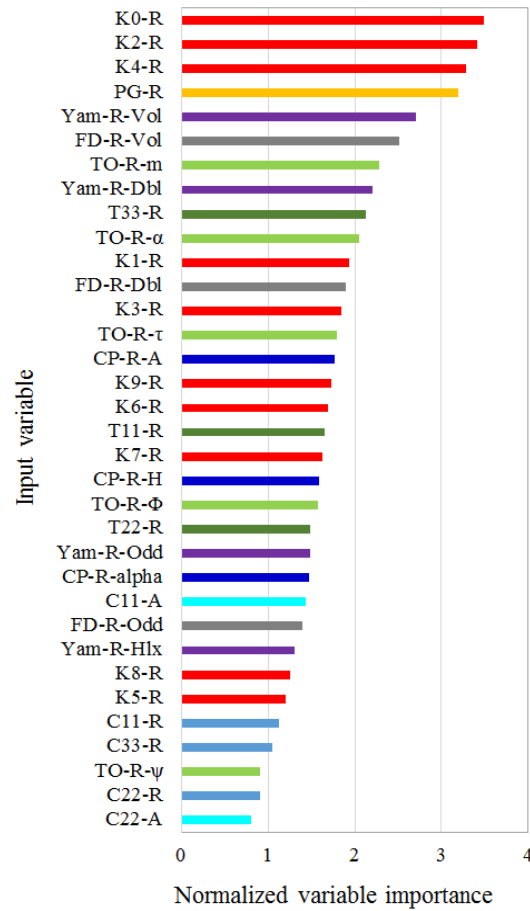
Figure 3.7. Normalized variable importance of RF classification for scenario 13. Different variables are represented as follows: Kennaugh matrix elements (red), polarization content obtained by Kennaugh elements (orange), Yamaguchi decomposition (purple), Freeman-Durden decomposition (gray), Touzi decomposition (light green), diagonal element of coherency matrix (dark green), Cloude-Pottier decomposition (dark blue), diagonal elements of covariance matrix for full polarization data (RADARSAT-2) (light blue), and covariance matrix elements for dual polarization data (ALOS-2) (cyan).

The three most important polarimetric features of scenario 13 are K_0, K_2, and K_4, which are Kennaugh matrix elements. This corresponds to the results of other studies such as [31], which demonstrated that these three input features were the most determining factors for wetland change detection among three decomposition approaches, including Cloude-Pottier, Freeman-Durden, and Kennaugh matrix elements. Polarization content (PG) and Yamaguchi decomposition were the next most important input features (see Figure 3.7).

Another important parameter in the RF classifier is the number of trees, which has a vital role in the classification processing time and final classification accuracy. In this study, the effect of this variable is determined using the user's accuracy for each class. Figure 3.8 depicts the user's accuracy for each class obtained by a different number of trees.
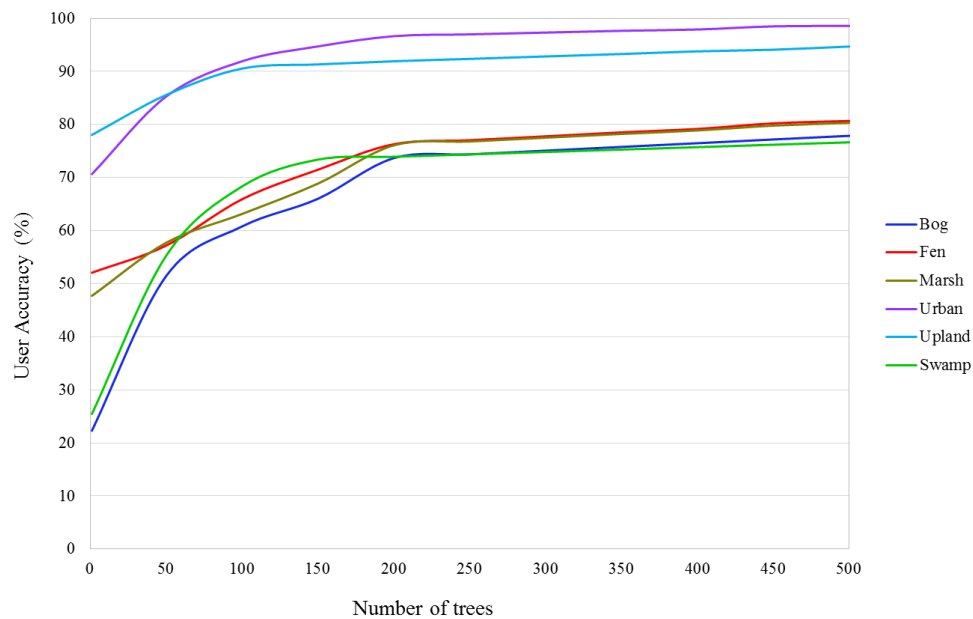
Figure 3.8. User's accuracies for different land cover types based on number of trees in RF classification.

The user's accuracy in classifications with less than 50 trees is low for all classes, excluding upland and urban classes. However, the user's accuracies for all classes improved up to 60% as the number

of trees exceeded approximately 100. Also, this analysis illustrated that the classification user's accuracy tended to be constant as the number of trees reached to 200.

As mentioned earlier, another important parameter is classification processing time. Thus, we evaluated the processing time of the RF classifier by setting varying numbers of trees. The processing time was approximately 14, 39, 68, 127, 191, and 364 minutes, which correspond to 50, 100, 200, 300, 400, and 500 numbers of trees, respectively. Thus, 200 trees were found to be the optimum number, since values beyond 200 did not improve the classification results and would be also computationally extensive.

Figure 3.9 depicts the final classified map, which has been obtained by inclusion of water classes from Level-II classification and the most significant classification result obtained from Level-III classification (scenario 13). An overall accuracy approximately of 94% has been attained for the final classified map, which is for all land cover classes. Furthermore, the overall classification accuracy of approximately 81% was only obtained for wetland classes, including bog, fen, marsh, swamp, and shallow-water. This classification result is comparable with other wetland classification studies [10], [39]. The confusion matrix of the final classified map is represented in Table 3.6.
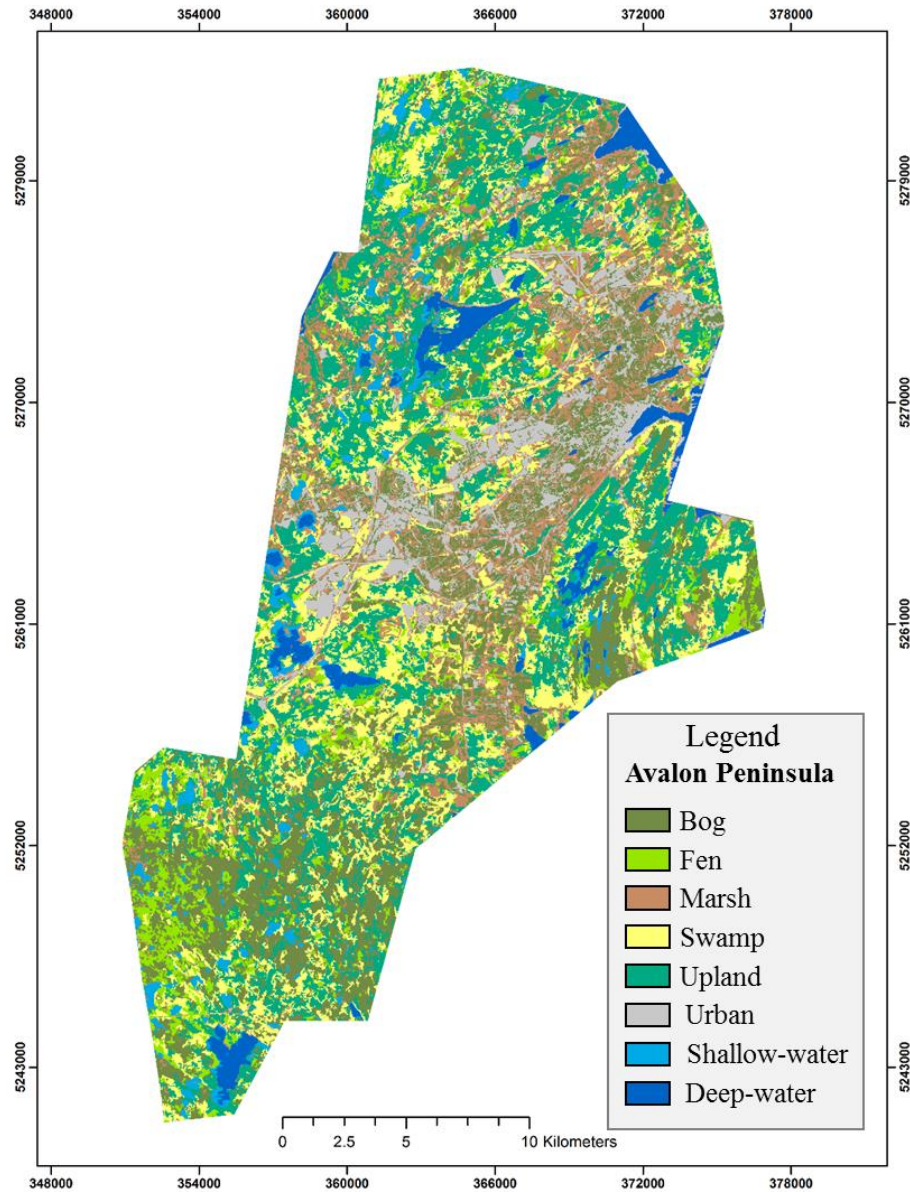
Figure 3.9. The final classified map, which has been obtained by inclusion of water classes from Level-II classification and the most significant classification result obtained from Level-III classification (scenario 13).

Table 3.6. Classification confusion matrix of integrating the most significant results from Level-II and -III classifications. An overall accuracy of 94.82% and kappa coefficient of 0.93 were obtained.

| | Reference Data | | | | | | | | | |
	Bog	Fen	Marsh	Swamp	Upland	Urban	Shallow-water	Deep-water	Tot.	User. Acc.
Bog	**15237**	1810	4	11	1320	1183	0	0	19565	77.88
Fen	256	**7094**	26	920	436	8	54	0	8794	80.67
Marsh	203	128	**7623**	156	978	403	0	0	9491	80.32
Swamp	125	71	773	**4015**	168	86	0	0	5238	76.65
Upland	1259	2187	1259	59	**85114**	0	0	0	89878	94.70
Urban	0	21	0	0	931	**66173**	0	0	67125	98.58
Shallow-water	0	0	0	0	0	0	**5461**	218	5679	96.16
Deep-water	0	0	0	0	0	0	228	**88966**	89194	**99.74**
Tot.	17080	11311	9685	5161	88947	67853	5743	89184	294964	
Prod. Acc.	89.21	62.72	78.71	77.80	95.69	97.52	95.09	**99.76**		

Classified Data (row label, left side)

The deep-water, shallow-water, upland, and urban classes obtained producer's and user's accuracies up to 90%, which represented the smallest omission and commission errors. Among herbaceous classes, fen and marsh had user's accuracy of about 80%; however, for the bog class, the user's accuracy was 77.88%. On the other hand, bog wetland represented the highest producer's accuracy of approximately 89% within the vegetation classes. The fen class represented the smallest producer's accuracy and, as a result, the highest omission error among all land covers classes in this study. This means that a large portion of the fen class was misclassified as bog or upland classes. Swamp wetland was also illustrated to be incorrectly classified due to the smallest user's accuracy of about 76%, which demonstrated the highest commission error. As seen in Table

3.6, the marsh class was particularly misclassified as swamp (commission error). Furthermore, a large percentage of swamp class was also misclassified as fen (omission error). A high commission error was also observed for bog wetland, wherein a large portion of fen and upland were misclassified as bog.

Overall, the greatest confusion error was observed within herbaceous classes, and particularly between bog and fen. The confusion error in herbaceous classes can be due to: (1) the similar backscatter signature of these classes in SAR images as seen in the backscattering analysis performed in this study (see Section 3.4.1); and (2) these classes have high heterogeneous nature in terms of landscape. Furthermore, there is not a straightforward border between these land cover types. As reported by field biologists, these classes were hard to be distinguished during *in-situ* data collection. Particularly, bog and fen wetlands are peatland dominated with very similar vegetation (*Spahgnum* and graminoid species), and no apparent border between the two, contributing to the level of confusion observed between these two classes.

Non-herbaceous classes were found to be better classified, particularly urban and upland classes. However, some degree of mixture was observed between swamp and herbaceous classes (marsh and fen). We speculated that the less accurate result for the swamp class may be due to the smallest portion of *in-situ* data for this class. As mentioned earlier, swamp wetlands tend to occur in physically smaller areas compared to other wetlands, and are found to be arduous to flag for visitation and delineation as they may look visually similar to upland forest. Thus, the limited amount of training data for this class caused the largest portion of errors.

Water classes were found to be the most accurately classified. However, a small level of confusion was observed between the shallow- and deep-water classes. The confusion in these two classes

could be due to similar backscatter signatures in SAR images as seen in the SAR backscatter analysis. Furthermore, a small portion of shallow-water class was misclassified as fen wetland. We speculated this error was likely a result of minimal flooded-vegetation (herbaceous) at the edge of shallow-water, which caused some degree of mixture.

3.5. Conclusion

Newfoundland is among the richest Canadian province in terms of different wetland classes (e.g., bog, fen, marsh, swamp, and shallow-water); however, to date they have not been well mapped or monitored. The results of this study represent the first detailed land cover classification and spatial distribution of wetlands, as well as other land cover classes, in a sub-region of the Avalon Peninsula. A new, advanced hierarchical object-based Random Forest classification was proposed based on a combination of single polarized TerraSAR-X, dual polarized ALOS-2, and fully polarized RADARSAT-2 images.

A detailed backscattering analysis was performed for all land cover classes in both multi-frequency and multi-polarized frameworks. Water classes represented the lowest backscatter, while the highest backscatter was observed in the urban class. Herbaceous classes also represented a lower backscatter than non-herbaceous classes. Overall, HH polarized images illustrated the highest backscatter; in contrast, backscatter was the lowest for HV polarization. Furthermore, by comparing the SAR wavelength (only in HH channels), X-band represents the higher backscatter for herbaceous classes, while L-band represents the higher backscatter in the swamp class.

An overall accuracy of 94.82% was achieved for the final classified map using the 44 PolSAR features assessed in this study. The variable importance analysis of RF has demonstrated that the Kennaugh matrix elements, Yamaguchi, and Freeman-Durden decomposition are the most

important parameters for wetland classification. However, it may not be the same for other land cover classification.

In the classified map, the highest confusion error was observed within the herbaceous vegetation, particularly between the bog and fen classes due to similar SAR backscatter signatures. The swamp class was also misclassified with herbaceous classes in some cases, which could be due to the smallest training data for this specific class. The most accurate results were obtained for the water (shallow- and deep-water), urban and upland classes, respectively.

Overall, the results of this study provide: (1) a detailed spatial distribution map of wetland classes in the Avalon Peninsula; and (2) decisive information for monitoring changes in wetland ecosystems, which is beneficial for conservation efforts to preserve this productive habitat. Thus, the results of this study facilitate and contribute to the sustainable monitoring, management, and conservation of wetlands in Newfoundland, which may be applied in similar conservation efforts elsewhere in the world, especially in Canada. In particular, the RF classifier could be trained using the ecological training datasets from the Avalon pilot site for classification of other wetland sites with similar wetland classes.

3.6. References

[1]   M. A. Hardisky, M. F. Gross, and V. Klemas, "Remote sensing of coastal wetlands," *Bioscience*, vol. 36, no. 7, pp. 453–460, 1986.

[2]   A. L. Gallant, "The challenges of remote monitoring of wetlands." Multidisciplinary Digital Publishing Institute, 2015.

[3]   R. W. Tiner, M. W. Lang, and V. V Klemas, *Remote sensing of wetlands: applications and advances*. CRC Press, 2015.

[4]   D. C. Rundquist, S. Narumalani, and R. M. Narayanan, "A review of wetlands remote sensing and defining new considerations," 2001.

[5]   R. Chopra, V. K. Verma, and P. K. Sharma, "Mapping, monitoring and conservation of Harike wetland ecosystem, Punjab, India, through remote sensing," *Int. J. Remote Sens.*, vol. 22, no. 1, pp. 89–98, 2001.

[6]   C. Munyati, "Wetland change detection on the Kafue Flats, Zambia, by classification of a multitemporal remote sensing image dataset," *Int. J. Remote Sens.*, vol. 21, no. 9, pp. 1787–1806, 2000.

[7]   S. Wdowinski, S.-W. Kim, F. Amelung, T. H. Dixon, F. Miralles-Wilhelm, and R. Sonenshein, "Space-based detection of wetlands' surface water level changes from L-band SAR interferometry," *Remote Sens. Environ.*, vol. 112, no. 3, pp. 681–696, 2008.

[8]   E. Adam, O. Mutanga, and D. Rugege, "Multispectral and hyperspectral remote sensing for identification and mapping of wetland vegetation: a review," *Wetl. Ecol. Manag.*, vol. 18, no. 3, pp. 281–296, 2010.

[9]   X. Li *et al.*, "A hybrid method combining pixel-based and object-oriented methods and its application in Hungary using Chinese HJ-1 satellite images," *Int. J. Remote Sens.*, vol. 34, no. 13, pp. 4655–4668, 2013.

[10]   T. L. Evans and M. Costa, "Landcover classification of the Lower Nhecolândia subregion of the Brazilian Pantanal Wetlands using ALOS/PALSAR, RADARSAT-2 and ENVISAT/ASAR imagery," *Remote Sens. Environ.*, vol. 128, pp. 118–137, 2013.

[11]   M. C. Dobson, L. E. Pierce, and F. T. Ulaby, "Knowledge-based land-cover classification using ERS-1/JERS-1 SAR composites," *IEEE Trans. Geosci. Remote Sens.*, vol. 34, no. 1, pp. 83–99, 1996.

[12]   T. Whiteside and R. Bartolo, "Mapping aquatic vegetation in a tropical wetland using high spatial resolution multispectral satellite imagery," *Remote Sens.*, vol. 7, no. 9, pp. 11664–11694, 2015.

[13]   E. S. Kasischke, J. M. Melack, and M. C. Dobson, "The use of imaging radars for ecological applications—a review," *Remote Sens. Environ.*, vol. 59, no. 2, pp. 141–156, 1997.

[14] B. Brisco, A. Schmitt, K. Murnaghan, S. Kaya, and A. Roth, "SAR polarimetric change detection for flooded vegetation," *Int. J. Digit. Earth*, vol. 6, no. 2, pp. 103–114, 2013.

[15] F. Mohammadimanesh, B. Salehi, M. Mahdianpari, and S. Homayouni, "Unsupervised wishart classfication of wetlands in Newfoundland, Canada using polsar data based on fisher linear discriminant analysis," in *International Archives of the Photogrammetry, Remote Sensing and Spatial Information Sciences - ISPRS Archives*, 2016, vol. 41.

[16] M. Silveira and S. Heleno, "Separation between water and land in SAR images using region-based level sets," *IEEE Geosci. Remote Sens. Lett.*, vol. 6, no. 3, pp. 471–475, 2009.

[17] U. Gessner *et al.*, "Multi-sensor mapping of West African land cover using MODIS, ASAR and TanDEM-X/TerraSAR-X data," *Remote Sens. Environ.*, vol. 164, pp. 282–297, 2015.

[18] S. G. Dellepiane and E. Angiati, "A new method for cross-normalization and multitemporal visualization of SAR images for the detection of flooded areas," *IEEE Trans. Geosci. Remote Sens.*, vol. 50, no. 7, pp. 2765–2779, 2012.

[19] B. Brisco, N. Short, J. van der Sanden, R. Landry, and D. Raymond, "A semi-automated tool for surface water mapping with RADARSAT-1," *Can. J. Remote Sens.*, vol. 35, no. 4, pp. 336–344, 2009.

[20] B. Brisco, M. Kapfer, T. Hirose, B. Tedford, and J. Liu, "Evaluation of C-band polarization diversity and polarimetry for wetland mapping," *Can. J. Remote Sens.*, vol. 37, no. 1, pp. 82–92, 2011.

[21] S. Martinis, J. Kersten, and A. Twele, "A fully automated TerraSAR-X based flood service," *ISPRS J. Photogramm. Remote Sens.*, vol. 104, pp. 203–212, 2015.

[22] V. Gstaiger, J. Huth, S. Gebhardt, T. Wehrmann, and C. Kuenzer, "Multi-sensoral and automated derivation of inundated areas using TerraSAR-X and ENVISAT ASAR data," *Int. J. Remote Sens.*, vol. 33, no. 22, pp. 7291–7304, 2012.

[23] A. Wendleder, B. Wessel, A. Roth, M. Breunig, K. Martin, and S. Wagenbrenner, "TanDEM-X water indication mask: Generation and first evaluation results," *IEEE J. Sel. Top. Appl. Earth Obs. Remote Sens.*, vol. 6, no. 1, pp. 171–179, 2013.

[24] Z. Qi, A. G.-O. Yeh, X. Li, and Z. Lin, "A novel algorithm for land use and land cover classification using RADARSAT-2 polarimetric SAR data," *Remote Sens. Environ.*, vol. 118, pp. 21–39, 2012.

[25] R. Touzi, "Target scattering decomposition in terms of roll-invariant target parameters," *IEEE Trans. Geosci. Remote Sens.*, vol. 45, no. 1, pp. 73–84, 2007.

[26] T. L. Ainsworth, J. P. Kelly, and J.-S. Lee, "Classification comparisons between dual-pol, compact polarimetric and quad-pol SAR imagery," *ISPRS J. Photogramm. Remote Sens.*, vol. 64, no. 5, pp. 464–471, 2009.

[27] S. R. Cloude and E. Pottier, "A review of target decomposition theorems in radar polarimetry," *IEEE Trans. Geosci. Remote Sens.*, vol. 34, no. 2, pp. 498–518, 1996.

[28] A. Freeman and S. L. Durden, "A three-component scattering model for polarimetric SAR data," *IEEE Trans. Geosci. Remote Sens.*, vol. 36, no. 3, pp. 963–973, 1998.

[29] J. J. Van Zyl, M. Arii, and Y. Kim, "Model-based decomposition of polarimetric SAR covariance matrices constrained for nonnegative eigenvalues," *IEEE Trans. Geosci. Remote Sens.*, vol. 49, no. 9, pp. 3452–3459, 2011.

[30] E. M. Kennaugh and R. W. Sloan, "Effects of type of polarization on echo characteristics," OHIO STATE UNIV RESEARCH FOUNDATION COLUMBUS ANTENNA LAB, 1952.

[31] A. Schmitt and B. Brisco, "Wetland monitoring using the curvelet-based change detection method on polarimetric SAR imagery," *Water*, vol. 5, no. 3, pp. 1036–1051, 2013.

[32] M. Dabboor, L. White, B. Brisco, and F. Charbonneau, "Change detection with compact polarimetric SAR for monitoring wetlands," *Can. J. Remote Sens.*, vol. 41, no. 5, pp. 408–417, 2015.

[33] K. O. Pope, E. Rejmankova, J. F. Paris, and R. Woodruff, "Detecting seasonal flooding cycles in marshes of the Yucatan Peninsula with SIR-C polarimetric radar imagery," *Remote Sens. Environ.*, vol. 59, no. 2, pp. 157–166, 1997.

[34] L. Moser, A. Schmitt, A. Wendleder, and A. Roth, "Monitoring of the Lac Bam wetland extent using dual-polarized X-band SAR data," *Remote Sens.*, vol. 8, no. 4, p. 302, 2016.

[35] J. Li and W. Chen, "A rule-based method for mapping Canada's wetlands using optical, radar and DEM data," *Int. J. Remote Sens.*, vol. 26, no. 22, pp. 5051–5069, 2005.

[36] L.-M. Rebelo, "Eco-hydrological characterization of inland wetlands in Africa using L-band SAR," *IEEE J. Sel. Top. Appl. Earth Obs. Remote Sens.*, vol. 3, no. 4, pp. 554–559, 2010.

[37] V. Turkar, R. Deo, Y. S. Rao, S. Mohan, and A. Das, "Classification accuracy of multi-frequency and multi-polarization SAR images for various land covers," *IEEE J. Sel. Top. Appl. Earth Obs. Remote Sens.*, vol. 5, no. 3, pp. 936–941, 2012.

[38] M. P. F. Costa, "Use of SAR satellites for mapping zonation of vegetation communities in the Amazon floodplain," *Int. J. Remote Sens.*, vol. 25, no. 10, pp. 1817–1835, 2004.

[39] M. P. F. Costa and K. H. Telmer, "Utilizing SAR imagery and aquatic vegetation to map fresh and brackish lakes in the Brazilian Pantanal wetland," *Remote Sens. Environ.*, vol. 105, no. 3, pp. 204–213, 2006.

[40] M. W. Lang and E. S. Kasischke, "Using C-band synthetic aperture radar data to monitor forested wetland hydrology in Maryland's coastal plain, USA," *IEEE Trans. Geosci. Remote Sens.*, vol. 46, no. 2, pp. 535–546, 2008.

[41] U. C. Benz, P. Hofmann, G. Willhauck, I. Lingenfelder, and M. Heynen, "Multi-resolution, object-oriented fuzzy analysis of remote sensing data for GIS-ready information," *ISPRS J. Photogramm. Remote Sens.*, vol. 58, no. 3–4, pp. 239–258, 2004.

[42] T. Blaschke, "Object based image analysis for remote sensing," *ISPRS J. Photogramm. Remote*

Sens., vol. 65, no. 1, pp. 2–16, 2010.

[43] L. Durieux, J. Kropáček, G. D. De Grandi, and F. Achard, "Object-oriented and textural image classification of the Siberia GBFM radar mosaic combined with MERIS imagery for continental scale land cover mapping," *Int. J. Remote Sens.*, vol. 28, no. 18, pp. 4175–4182, 2007.

[44] M. Grenier, S. Labrecque, M. Garneau, and A. Tremblay, "Object-based classification of a SPOT-4 image for mapping wetlands in the context of greenhouse gases emissions: the case of the Eastmain region, Québec, Canada," *Can. J. Remote Sens.*, vol. 34, no. sup2, pp. S398–S413, 2008.

[45] W. S. Walker, C. M. Stickler, J. M. Kellndorfer, K. M. Kirsch, and D. C. Nepstad, "Large-area classification and mapping of forest and land cover in the Brazilian Amazon: A comparative analysis of ALOS/PALSAR and Landsat data sources," *IEEE J. Sel. Top. Appl. Earth Obs. Remote Sens.*, vol. 3, no. 4, pp. 594–604, 2010.

[46] A. Comber *et al.*, "Managing uncertainty when aggregating from pixels to objects: habitats, context-sensitive mapping and possibility theory," *Int. J. Remote Sens.*, vol. 31, no. 4, pp. 1061–1068, 2010.

[47] G. J. Hay, T. Blaschke, D. J. Marceau, and A. Bouchard, "A comparison of three image-object methods for the multiscale analysis of landscape structure," *ISPRS J. Photogramm. Remote Sens.*, vol. 57, no. 5–6, pp. 327–345, 2003.

[48] J. C.-W. Chan and D. Paelinckx, "Evaluation of Random Forest and Adaboost tree-based ensemble classification and spectral band selection for ecotope mapping using airborne hyperspectral imagery," *Remote Sens. Environ.*, vol. 112, no. 6, pp. 2999–3011, 2008.

[49] B. Ghimire, J. Rogan, and J. Miller, "Contextual land-cover classification: incorporating spatial dependence in land-cover classification models using random forests and the Getis statistic," *Remote Sens. Lett.*, vol. 1, no. 1, pp. 45–54, 2010.

[50] V. F. Rodriguez-Galiano, B. Ghimire, J. Rogan, M. Chica-Olmo, and J. P. Rigol-Sanchez, "An assessment of the effectiveness of a random forest classifier for land-cover classification," *ISPRS J. Photogramm. Remote Sens.*, vol. 67, pp. 93–104, 2012.

[51] I. Nitze, U. Schulthess, and H. Asche, "Comparison of machine learning algorithms random forest, artificial neural network and support vector machine to maximum likelihood for supervised crop type classification," *Proc. 4th GEOBIA*, pp. 7–9, 2012.

[52] V. F. Rodriguez-Galiano, M. Chica-Olmo, F. Abarca-Hernandez, P. M. Atkinson, and C. Jeganathan, "Random Forest classification of Mediterranean land cover using multi-seasonal imagery and multi-seasonal texture," *Remote Sens. Environ.*, vol. 121, pp. 93–107, 2012.

[53] S. van Beijma, A. Comber, and A. Lamb, "Random forest classification of salt marsh vegetation habitats using quad-polarimetric airborne SAR, elevation and optical RS data," *Remote Sens. Environ.*, vol. 149, pp. 118–129, 2014.

[54] L. Breiman, "Random forests," *Mach. Learn.*, vol. 45, no. 1, pp. 5–32, 2001.

[55]   R. M. Lucas, A. L. Mitchell, A. K. E. Rosenqvist, C. Proisy, A. Melius, and C. Ticehurst, "The potential of L-band SAR for quantifying mangrove characteristics and change: case studies from the tropics," *Aquat. Conserv. Mar. Freshw. Ecosyst.*, vol. 17, no. 3, pp. 245–264, 2007.

[56]   B. G. Warner and C. D. A. Rubec, "The Canadian wetland classification system," *Wetl. Res. Centre, Univ. Waterloo, Waterloo, Ontario*, 1997.

[57]   I. B. Marshall, C. A. S. Smith, and C. J. Selby, "A national framework for monitoring and reporting on environmental sustainability in Canada," in *Global to Local: Ecological Land Classification*, Springer, 1996, pp. 25–38.

[58]   E. S. W. G. (Canada), C. for Land, B. R. R. (Canada), and C. S. of the E. Directorate, *A national ecological framework for Canada*. Centre for Land and Biological Resources Research; Hull, Quebec: State of …, 1996.

[59]   R. South, *Biogeography and Ecology of the Island of Newfoundland*, vol. 48. Springer Science & Business Media, 1983.

[60]   D. Small, "Flattening gamma: Radiometric terrain correction for SAR imagery," *IEEE Trans. Geosci. Remote Sens.*, vol. 49, no. 8, pp. 3081–3093, 2011.

[61]   M. R. de Leeuw and L. M. T. de Carvalho, "Performance evaluation of several adaptive speckle filters for SAR imaging," *An. XIV Simpósio Bras. Sensoriamento Remoto*, pp. 7299–7305, 2009.

[62]   A. Lopes, R. Touzi, and E. Nezry, "Adaptive speckle filters and scene heterogeneity," *IEEE Trans. Geosci. Remote Sens.*, vol. 28, no. 6, pp. 992–1000, 1990.

[63]   J.-S. Lee, J.-H. Wen, T. L. Ainsworth, K.-S. Chen, and A. J. Chen, "Improved sigma filter for speckle filtering of SAR imagery," *IEEE Trans. Geosci. Remote Sens.*, vol. 47, no. 1, pp. 202–213, 2009.

[64]   S. R. Cloude and E. Pottier, "An entropy based classification scheme for land applications of polarimetric SAR," *IEEE Trans. Geosci. Remote Sens.*, vol. 35, no. 1, pp. 68–78, 1997.

[65]   Y. Yamaguchi, T. Moriyama, M. Ishido, and H. Yamada, "Four-component scattering model for polarimetric SAR image decomposition," *IEEE Trans. Geosci. Remote Sens.*, vol. 43, no. 8, pp. 1699–1706, 2005.

[66]   A. Schmitt, A. Wendleder, and S. Hinz, "The Kennaugh element framework for multi-scale, multi-polarized, multi-temporal and multi-frequency SAR image preparation," *ISPRS J. Photogramm. Remote Sens.*, vol. 102, pp. 122–139, 2015.

[67]   U. Benz, M. Baatz, and G. Schreier, "Oscar-object oriented segmentation and classification of advanced radar allow automated information extraction," in *IGARSS 2001. Scanning the Present and Resolving the Future. Proceedings. IEEE 2001 International Geoscience and Remote Sensing Symposium (Cat. No. 01CH37217)*, 2001, vol. 4, pp. 1913–1915.

[68]   R. G. Congalton, "A review of assessing the accuracy of classifications of remotely sensed data,"

Remote Sens. Environ., vol. 37, no. 1, pp. 35–46, 1991.

[69]   M. C. Dobson, F. T. Ulaby, T. LeToan, A. Beaudoin, E. S. Kasischke, and N. Christensen, "Dependence of radar backscatter on coniferous forest biomass," *IEEE Trans. Geosci. Remote Sens.*, vol. 30, no. 2, pp. 412–415, 1992.

[70]   Y. Wang, L. L. Hess, S. Filoso, and J. M. Melack, "Understanding the radar backscattering from flooded and nonflooded Amazonian forests: Results from canopy backscatter modeling," *Remote Sens. Environ.*, vol. 54, no. 3, pp. 324–332, 1995.

[71]   M. P. F. Costa, T. S. F. Silva, and T. L. Evans, "Wetland classification," *Remote Sens. Nat. Resour. CRC Press. Boca Raton-FL*, pp. 461–478, 2013.

[72]   T. S. F. Silva, M. P. F. Costa, J. M. Melack, and E. M. L. M. Novo, "Remote sensing of aquatic vegetation: theory and applications," *Environ. Monit. Assess.*, vol. 140, no. 1–3, pp. 131–145, 2008.

[73]   J.-S. Lee, M. R. Grunes, and G. De Grandi, "Polarimetric SAR speckle filtering and its implication for classification," *IEEE Trans. Geosci. Remote Sens.*, vol. 37, no. 5, pp. 2363–2373, 1999.

Chapter 4. Fisher Linear Discriminant Analysis of PolSAR data[3]

Preface

A version of this manuscript has been published in the *Remote Sensing of Environment Journal*. I am a primary author of this manuscript along with the co-authors, Bahram Salehi, Fariba Mohammadimanesh, Brian Brisco, Sahel Mahdavi, Meisam Amani, and Jean Elizabeth Granger. I designed and conceptualized the study. I developed the model and performed all experiments and tests. I wrote the paper and revised it based on comments from Bahram Salehi, Fariba Mohammadimanesh, and Brian Brisco. I also revised the paper according to the reviewers' comments. Co-authors, Jean Elizabeth Granger, Meisam Amani, and Sahel Mahdavi, helped on collecting in-situ samples and data pre-processing. The co-author, Fariba Mohammadimanesh, helped in performing the experiments and analyzing the results and contributed to revising the manuscript. Bahram Salehi, Fariba Mohammadimanesh, Brian Brisco, and Jean Elizabeth Granger provided editorial input and scientific insights to further improve the paper. They also reviewed and commented on the manuscript.

---

[3] Mahdianpari, M., Salehi, B., Mohammadimanesh, F., Brisco, B., Mahdavi, S., Amani, M. and Granger, J.E., 2018. Fisher Linear Discriminant Analysis of coherency matrix for wetland classification using PolSAR imagery. *Remote Sensing of Environment*, *206*, pp.300-317.

Abstract

Wetlands provide a wide variety of environmental services globally and detailed wetland inventory maps are always necessary to determine the conservation strategies and effectively monitor these productive ecosystems. During the last two decades, satellite remote sensing data have been extensively used for wetland mapping and monitoring worldwide. Polarimetric Synthetic Aperture Radar (PolSAR) imagery is a complex and multi-dimensional data, which has high potential to discriminate different land cover types. However, despite significant improvements to both information content in PolSAR imagery and advanced classification approaches, wetland classification using PolSAR data may not provide acceptable classification accuracy. This is because classification accuracy using PolSAR imagery strongly depends on the polarimetric features that are incorporated into the classification scheme. In this paper, a novel feature weighting method for PolSAR imagery is proposed to increase the classification accuracy of complex land cover. Specifically, a new coefficient is determined for each element of the coherency matrix by integration of Fisher Linear Discriminant Analysis (FLDA) and physical interpretation of the PolSAR data. The proposed methodology was applied to multi-temporal polarimetric C-band RADARSAT-2 data in the Avalon Peninsula, Deer Lake, and Gros Morne pilot sites in Newfoundland and Labrador, Canada. Different combinations of input features, including original PolSAR features, polarimetric decomposition features, and modified coherency matrix were used to evaluate the capacity of the proposed method for improving the classification accuracy using the Random Forest (RF) algorithm. The results demonstrated that the modified coherency matrix obtained by the proposed method, Van Zyl, and Freeman-Durden decomposition features were the most important features for wetland classification. The fine spatial resolution maps obtained in this study illustrate the distribution of terrestrial and aquatic habitats for the three wetland pilot sites in Newfoundland using the modified coherency matrix and other polarimetric

120

features. The classified maps provide valuable baseline data for effectively monitoring climate and land cover changes, and support further scientific research in this area.

4.1. Introduction

Wetlands are important ecosystems that play vital roles in climate change as well as in local and global environmental sustainability [1]. At the microscopic scale, wetlands provide food, carbon storage, filtering contamination, controlling flood, protecting shoreline, and a desirable habitat for a variety of unique plant and animal species [2], [3]. At the macroscopic scale, they influence regional climate by, for example, preventing accelerating rates of climate change. Despite these benefits, population growth and, subsequently, human interferences, such as urbanization, industrial development, and natural resource extractions have significantly contributed to the destruction and degradation of wetland ecosystems. Furthermore, a number of natural processes, such as sea level rise, changing in temperature and precipitation patterns due to climate change, and coastal erosion have further accelerated wetland loss [3].

Given the numerous benefits provided by these ecosystems, the necessity of an all-inclusive, up-to-date inventory map with spatial distribution of different wetland classes is of great importance for the effective monitoring of wetlands over time [3], [4]. The sustainable management of wetland ecosystems is a critical issue for assessing wetland environmental impacts, monitoring land cover changes, and preserving wildlife resources [5]. This is especially important, for countries with large expanses of wetlands, such as Canada and the United States. Traditional approaches (e.g., ground survey) for wetland monitoring are inefficient given the size and inaccessibility of wetland regions worldwide. For example, many wetlands are located in remote areas where vegetation cover, hydrology, and topography make ground surveying challenging and costly. Furthermore, repeated *in-situ* investigations are often required to accurately map wetlands due to their dynamic nature over time [6].

In the past two decades, several studies have demonstrated the efficiency of satellite remote sensing tools for wetland monitoring [1], [7]–[10]. These remote sensing approaches have effectively addressed many difficulties associated with traditional approaches (e.g., accessibility and repeatability). For example, optical satellite images are efficient for wetland classification using spectral signature of different classes although there are some limitations with this approach [11]–[13].The advent of Synthetic Aperture Radar (SAR) images has further facilitated land cover classification and, in particular, wetland mapping and monitoring by addressing the main drawbacks of optical images [14]. Specifically, SAR sensors are independent of solar illumination and have the capability to penetrate through cloud, soil, and vegetation [15]–[17]. With the continuous development of remote sensing sensors, fully Polarimetric SAR (PolSAR) systems have proven to possess great potential for discriminating between similar land cover types such as various wetland complexes [18], [19]. This is because PolSAR images record different backscattering mechanisms of ground targets, which are not obtainable using a single SAR channel [20], [21]. These highly valuable PolSAR data are efficient tools to assess the distribution and dynamics of wetlands at both regional and global scales. Accordingly, the capability of PolSAR images for wetland classification has been investigated by several studies [4], [22]. Moreover, polarimetric decompositions using PolSAR imagery are sophisticated approaches, which hold great promise for wetland classifications [23]–[26]. The main objective of polarimetric decomposition is to determine an average target scattering mechanism as the sum of independent elements and to assign a physical scattering mechanism to each component [27].

Importantly, high resolution satellite images have been integrated with advances in image analysis techniques, such as Object Based Image Analysis (OBIA), to further enhance land cover mapping [28]. The object-based methods exploit several characteristics of optical and SAR imagery,

123

including spectral (or SAR backscatter), geometrical, textural, and contextual information of a group of neighboring pixels (objects or segments) in addition to the original pixel values. Therefore, they employ additional information by incorporating the information of neighboring pixels into the classification scheme, which may be useful in distinguishing between similar land cover classes [4], [29]. Accordingly, a number of studies have successfully used OBIA and SAR imagery for wetland classification [4], [30], [31].

A variety of classification algorithms have been utilized for land cover mapping using satellite imagery. These algorithms can be broadly categorized into unsupervised approaches, such as ISODATA [32] and K-means [33], and supervised approaches, such as Maximum Likelihood Classification (MLC) [34]. Artificial neural network [35], decision tree [36], and Support Vector Machine (SVM) [37] are also non-parametric supervised machine learning techniques commonly used for land cover classification. These algorithms are advantageous compared to parametric approaches because they do not rely on the statistical distribution of input data (e.g., normality) [38]. In the last two decades, ensemble classifiers have gained an increasing attention for land cover mapping [39]–[41]. The Random Forest (RF) classifier is one of the well-known commonly used ensemble classifiers, which utilizes a set of Classification And Regression Trees (CARTs) in the classification scheme [42]. Specifically, the RF classifier is a sophisticated version of the decision tree algorithm for solving classification and regression problems. In this study, RF was selected due to several advantageous compared to other classifiers. First, RF does not require any assumptions for the distribution of the data (e.g., normality) unlike MLC and, thus, it can accommodate polarimetric SAR data with Wishart distributions [43]. Second, it can easily handle large and multi-temporal remote sensing datasets, which is also demanded in this study [38].

124

Finally, it has a flexible and straightforward structure and has shown good results in various remote sensing applications [25], [44].

Despite advanced remote sensing tools (e.g., classification methods and data), thematic mapping of fragmented landscapes, such as wetland complexes, is challenging due to high similarity of some classes, which contribute to confusion in the classification scheme. A practical approach to improve the classifier performance is to increase the class separability of the input data before incorporating them into the classifier. Thus, in this study, a new weighting approach was proposed based on the integration of Fisher Linear Discriminant Analysis (FLDA) [45] and physical characteristic of PolSAR data to increase the separability of input features. In particular, the main objective of this research study was to determine the effect of an optimum feature weighting approach on the classification of heterogeneous landscape using multi-temporal PolSAR data. Our proposed method was applied to full polarimetric RADARSAT-2 data for wetland classification in three different pilot sites in Newfoundland and Labrador province, Canada. We evaluated the efficiency of our proposed method using different combination of input features in three different models in multiple RF scenarios.

The rest of this paper is organized as follows: Section 2 introduces the location of the study areas and provides a description of the data used in this research; Section 3 describes polarimetric features employed in each classification model and represents the proposed methodology in detail; Section 4 presents the experimental results and discussion; and, finally, Section 5 draws the conclusion.

4.2. Study area and data

4.2.1. Study area

Wetland mapping and monitoring in Canada is crucial because 24% of the world's wetlands, corresponding to roughly 150 million hectares are contained within its borders [46]. This indicates the significance of wetland mapping and monitoring in Canada. Accordingly, Newfoundland and Labrador is part of a large Canadian wetland that represents a high biodiversity of different wetland types (e.g., bog, fen, swamp, marsh, and water) as well as many threatened habitats. This study is carried out at three different sites, henceforth referred to as the Avalon, Deer Lake, and Gros Morne pilot sites, distributed across the island of Newfoundland (Figure 4.1).
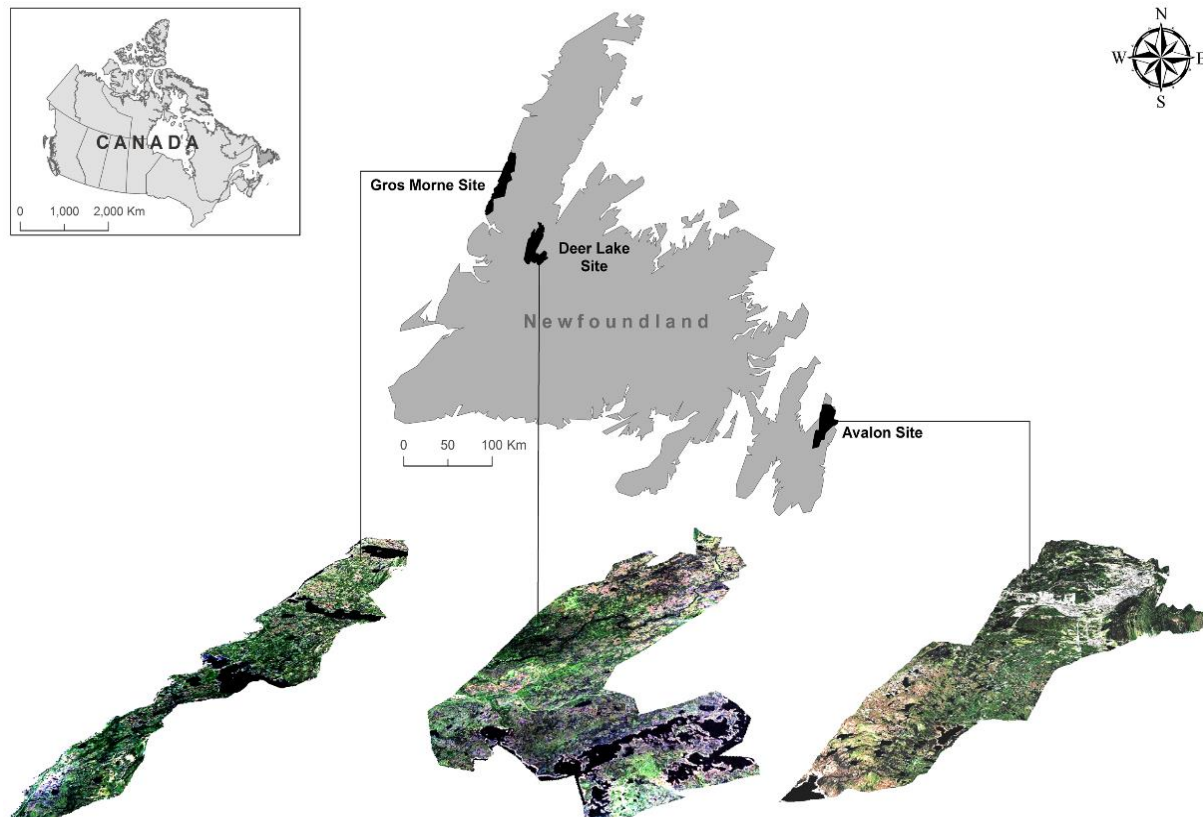
Figure 4.1. General view of the wetland study areas, including the Avalon, Deer Lake, and Gros Morne pilot sites in NL, Canada.

Each pilot site is roughly 700 square kilometers in size, containing various land cover and wetland types. Each site is located within a different ecoregion which, according to the Ecological Stratification Workings Group of Canada, is "a part of a province characterized by distinctive regional ecological factors, including climatic, physiography, vegetation, soil, water, fauna, and land use" [47]. Specific ecoregions relevant to this study are the Maritime Barren ecoregion, the North Central ecoregion, and the Northern Peninsula ecoregion for the Avalon, Deer Lake, and Gros Morne sites, respectively.

4.2.1.1. The Avalon

The Avalon pilot site is located in the North Eastern portion of the Avalon Peninsula, in the Maritime Barren ecoregion. This ecoregion is characterized by a typical oceanic climate, experiencing foggy, cool summers and relatively mild winters [47]. Mean annual temperatures are around 5.5°C and mean annual precipitation ranges from 1200 to 1600mm [47]. Land cover within the pilot site is varied and includes extensive heathland, balsam fir forest, urban, and agriculture. The majority of the urban area is found in the north eastern portion of the pilot site and includes the city of St. John's and the towns of Mount Pearl, Torbay, and the Goulds. Much of the southern portion of the site is generally inaccessible due to the lack of roadways in the area.

4.2.1.2. Deer Lake

The Deer Lake pilot site is located in the North portion of the island, east of the Town of Deer Lake. This pilot site falls within the North Central ecoregion, where summers are hot and winters are cold relative to that of the other pilot sites, and is typical of a more continental climate. Average annual rainfall is close to 1000mm [47]. Land cover includes urban, boreal forest, barrens, and wetlands. Urban land cover is minor and limited to some small settlements including the town of Howely and roads traversing the pilot site. Majority land cover includes balsam and black spruce

forests and peatland formations [48]. The northern portion of the site is largely inaccessible due to limited roadways.

4.2.1.3. Gros Morne

The Gros Morne pilot site can be found on the very west coast of Newfoundland, along the Gulf of St. Lawrence on the Great Northern Peninsula. Located within the Northern Peninsula ecoregion, this area, like the Avalon, has an oceanic climate with average rainfall close to that of 1300mm [47]. This pilot site falls mostly within the low elevation areas along the coast, though as one travels east, elevations increase dramatically above sea level where large mountains dominate. Major land cover includes balsam fir and black spruce forests and low lying peatlands [48].

All five classes of wetlands described by the Canadian Wetland Classification System, including bog, fen, marsh, swamp, and water [46], can be found distributed throughout the three pilot sites, though bog and fen tend to be the most common relative to the occurrence of swamp, marsh, and water. Examples of the five wetland classes and their typical vegetation cover common to the pilot site can be seen in Figure 4.2. Bogs (Figure 4.2a) are dominated by *Sphagnum* moss species. *Ericaceous* shrub species and sedge species are also common. Fens (Figure 4.2b) are dominated by sedges and grasses [48], and although *Sphagnum* moss species are often present in fens, they do not dominate as they do in bogs. Marshes (Figure 4.2c) are dominated by emergent aquatic species of sedges, rushes, and grasses. Swamps (Figure 4.2d) are primarily dominated by both tree and shrub Black Spruce (*Picea mariana*) and Tamarack (*Larix laricina*). Characteristic water (Figure 4.2e) vegetation is submerged aquatic macrophytes, including grasses and species belonging to the genus water lilies (*Nymphaecae*).
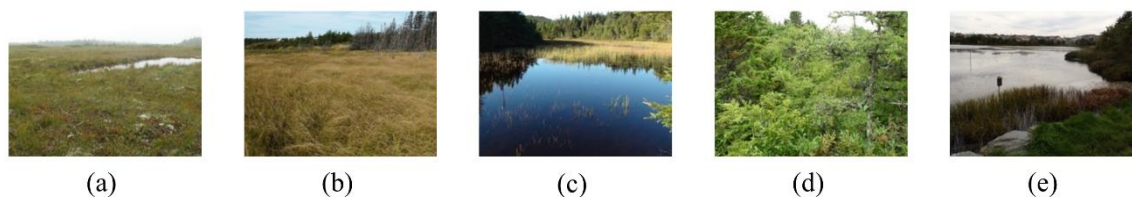
Figure 4.2. Ground reference photos showing the five wetland classes found within the Avalon pilot site: (a) bog, (b) fen, (c) marsh, (d) swamp, and (e) water.

In-situ data were collected by field work biologists in the summers and falls of 2015 and 2016 for the Avalon site, and the summers of 2015 and 2016 for Gros Morne and Deer Lake. Potential wetland areas across the pilot sites were flagged for visitation by field workers via the visual analysis of high resolution Google Earth imagery. Other considerations for site visitation included prior knowledge of the area, accessibility via public roads, and the public or private ownership of lands. A total of 191, 87, and 102 wetland sites in the Avalon, Deer Lake, and Gros Morne sites respectively were visited and classified as bog, fen, swamp, marsh, or water, as directed by the Canadian Wetland Classification System. Global Positioning System (GPS) points at each site were collected, along with ancillary data such as notes describing dominant vegetation and hydrology, and photographs to aid in the wetland boundary delineation process. Wetland boundary delineation was conducted using ArcMap 10.3.1 where the GPS points were imported to highlight visited wetlands. With the aid of satellite and aerial imagery including a 50cm resolution orthophotograph, and 5m resolution, multi-date RapidEye imagery, polygons representing classified delineated wetlands were created.

4.2.2. Reference data

For each class, reference polygons were sorted by size and alternatingly assigned to testing and training groups. This was done to ensure that both the testing and the training groups had roughly comparable pixel counts for each class. Due to the limited amount of data and the wide variation

of size within each wetland class (some small, some large), random assignment could result in the testing and training groups having highly uneven pixel counts. This procedure ensured that both the testing and training groups had equal assignment of small and large wetlands polygons to allow for similar pixel counts and to account for the high variation of intra-wetland size.

Table 4.1. Testing and training pixel counts for Avalon reference data.

Class	Class Description	# Training Pixels	# Testing Pixels	Total
Bog	Peatland dominated by *Spahgnum* species	20650	17080	37730
Fen	Peatland dominated by graminoid species	11183	11311	22494
Swamp	Mineral wetland dominated by woody vegetation	3197	5161	8358
Marsh	Mineral wetland dominated by graminoids and emergent plants	10869	9685	20554
Urban	Human-made structures	66339	67853	134192
Water	Deep water areas	62927	89184	152111
Upland	Forested dry upland	73458	88947	162405
Total		248623	289221	537844

Table 4.2. Testing and training pixel counts for Deer Lake reference data.

Class	Class Description	# Training Pixels	# Testing Pixels	Total
Bog	Peatland dominated by *Spahgnum* species	176626	113857	290483
Fen	Peatland dominated by graminoid species	4645	8840	13485
Swamp	Mineral wetland dominated by woody vegetation	4120	4745	8865
Marsh	Mineral wetland dominated by graminoids and emergent plants	12751	3246	15997
Urban	Human-made structures	11618	15281	26899
Water	Deep water areas	71722	58541	130263
Upland	Forested dry upland	48622	39670	88292
Total		330104	244180	574284

Table 4.3. Testing and training pixel counts for Gros Morne reference data.

Class	Class Description	# Training Pixels	# Testing Pixels	Total
Bog	Peatland dominated by *Spahgnum* species	110743	114018	224761
Fen	Peatland dominated by graminoid species	13153	8812	21965
Swamp	Mineral wetland dominated by woody vegetation	4058	3787	7845
Marsh	Mineral wetland dominated by graminoids and emergent plants	3201	3266	6467
Urban	Human-made structures	12185	14912	27097
Water	Deep water areas	53018	58530	111548
Upland	Forested dry upland	43428	39394	82822
Total		239786	242719	482505

Tables 4.1, 4.2, and 4.3 represent land cover classes and their respective pixel counts for each pilot site. Notably, the marsh and swamp classes tended to have the least amount of associated pixels across pilot sites, particularly in Deer Lake and Gros Morne. This disparity of pixel counts within and across pilot sites and within and across wetland classes is a result of several factors, including the availability of biologists for field work, the accessibility of different wetlands, and the natural ecology and distribution of wetlands in the area. Accordingly, there is variation in the quantity and quality of data for each individual class.

Bog wetlands are particularly easy to spot via satellite imagery and in the field, and are often more expansive relative to other wetlands in Newfoundland and Labrador. This is due both to their natural formation and ecology [49] and due to the provinces climate, which facilitates extensive peatland formation [48]. As a result, the bog class has a larger amount of associated pixels. Conversely, swamps are more difficult to flag for visitation and delineation as they may look visually similar to that of upland forest when looking at aerial or satellite data. This is because swamps are forested wetlands containing substantial tree and shrub vegetation. Additionally, swamps tend to occur in physically smaller areas compared to that of other wetlands, such as in

transition zones between a wetland and other land cover types. As a result, most swamp polygons contained fewer pixels when compared to other wetlands types.

4.2.3. Satellite images

In this study, RADARSAT-2 images in the Fine resolution Quad polarization (FQ) beam mode provided by the Canada Center for Mapping and Earth Observation were used. Due to the small swath of the FQ mode, more than one image was used to cover the entire area in each pilot site. Specifically, three full polarimetric RADARSAT-2 datasets were used for each pilot site in order to examine the temporal variation in wetland ecosystems. However, all of this imagery has been acquired during leaf-on/ice-off season. Additionally, RapidEye optical imagery of level 3A products with a pixel size of 5m was used in initial segmentation [50]. The specifications of these data are provided in Table 4.4.

Table 4.4. The characteristics of satellite images used in this study.

Pilot site	Sensor	Date (yyyy/mm/dd)	Number of Images	Mode	Inc. angle (°)	Nominal Resolution (m) (Range× Azimuth)
Avalon	RADASAT-2	2015/06/10	2	FQ4	22.1-24.1	5.2 × 7.6
		2015/08/21	2	FQ4	22.1-24.1	5.2 × 7.6
		2016/07/25	2	FQ22	41.0-42.4	5.2 × 7.6
	RapidEye	2015/06/18	1	Level 3A	-	5
		2015/10/22	1	Level 3A	-	5
Deer Lake	RADARSAT-2	2015/06/23	2	FQ3	20.9-22.9	5.2 × 7.6
		2015/08/10	2	FQ3	20.9-22.9	5.2 × 7.6
		2015/10/18	2	FQ16	35.4-37.0	5.2 × 7.6
	RapidEye	2015/06/18	1		-	5
Gros Morne	RADARSAT-2	2015/06/16	2	FQ2	19.7-21.7	5.2 × 7.6
		2015/08/03	3	FQ2	19.7-21.7	5.2 × 7.6
		2015/10/14	3	FQ2	19.7-21.7	5.2 × 7.6
	RapidEye	2015/06/18	1	Level 3A	-	5
		2015/09/06	1	Level 3A	-	5

4.3. Methods

Wetland classification using PolSAR imagery has previously been conducted using both SAR backscatter coefficients analysis and physical scattering mechanisms of ground targets [10], [24], [25], [51], [52]. In this study, we proposed a new methodology to determine the appropriate weight for each element of the coherency matrix. The method is based on an integration of Fisher Linear Discriminant analysis and physical interpretation of PolSAR data. To improve the classification accuracy for complex land cover types, such as wetlands, weights for each element of the coherency matrix were determined proportional to the class separability in order to obtain the most discriminant feature space. In particular, three major models were defined for wetland classification using the following polarimetric features: (I) the scattering, covariance, and

coherency matrices (i.e., original features); (II) the polarimetric decomposition features; and (III) the modified coherency matrix obtained by the proposed method. Six, eleven, and seven scenarios were defined and the classification accuracies were compared within the context of Model I, II, and III, respectively. The proposed classification framework has three major steps outlined in Figure 4.3. During the pre-processing step, data conversion into the sinclair scattering matrix, speckle reduction, and terrain correction were applied. Next, the polarimetric features for each model were extracted from the pre-processed PolSAR data. This step was followed by either a pixel- or object-based image analysis after which the RF classifier was applied for classification. Finally, the results were evaluated through the use of ecological validation data. This general process is described in more detailed in the following sections.
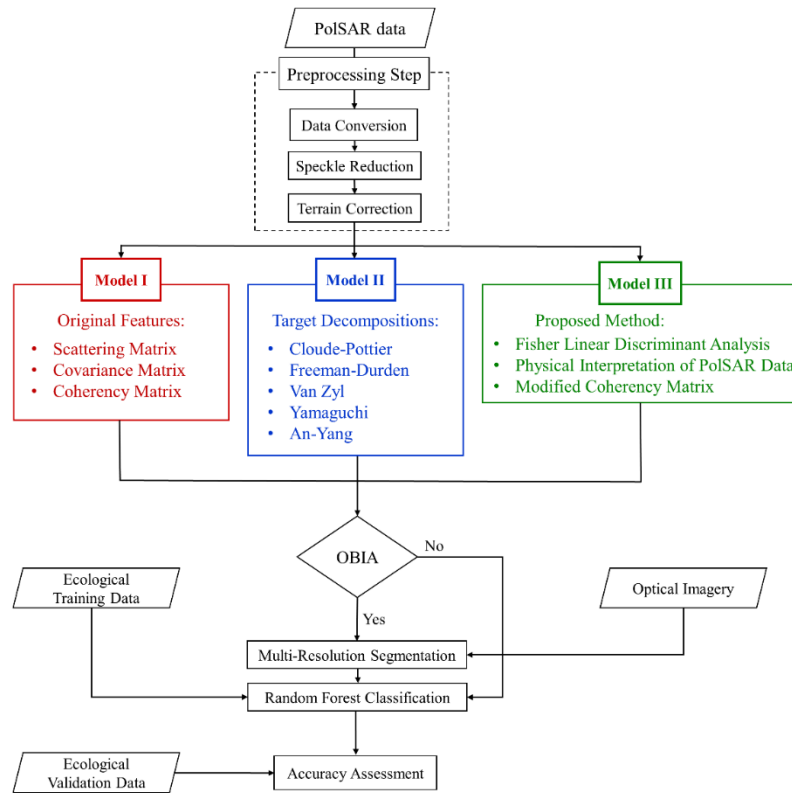
Figure 4.3. The flowchart of the proposed method in this study.

4.3.1. Pre-processing

PolSAR images are presented in radar geometry known as slant range or ground range [53]. However, processing PolSAR images along with other geo-data products, such as ecological field data, often requires conversion to conventional map geometry. Thus, RADARSAT-2 level 1-SLC imagery was pre-processed using MapReady software V3.1 calibration tools provided by the Alaska Satellite Facility (ASF, www.asf.alaska.edu). External Digital Elevation Models (DEMs) released by Natural Resources Canada, with a resolution of roughly 19m, were also used for orthorectification (http://geogratis.gc.ca/site/eng/extraction). For the three pilot sites, all images were projected into UTM coordinate, particularly zone 22/row T for the Avalon area and zone 21/row U for both the Deer Lake and Gros Morne study areas. Next, orthorectified RADARSAT-2 images were mosaicked to generate full coverage of the three pilot sites. RapidEye level 3A images were also obtained terrain corrected with an accuracy of half of a pixel and delivered in this format.

One of the main drawbacks of PolSAR images is the presence of speckle, which degrades the radiometric quality of the images and, consequently, the classification accuracy of further image analysis [54], [55]. Several techniques have been developed to suppress this phenomenon [56], [57]. In this study, an adaptive Lee filter, which has been developed based on Minimum Mean Square Error (MMSE) criteria, was used to suppress the effect of speckle noise. In particular, an adaptive Lee filter of size 9, in both range and azimuth directions, was applied to PolSAR images. The de-speckled PolSAR images illustrated preservation of the mean values and image detail/edges, while reducing the standard deviation of homogeneous targets [58].

4.3.2. Feature extraction

In this study, several polarimetric features were extracted for wetland classification. These features are generally divided into two main categories: the original features and the polarimetric decomposition features.

4.3.2.1. Original features: Model I

A fully polarimetric SAR sensor measures the complex scattering matrix of a medium for all possible combinations of transmitted and received polarization [59]. The reduced scattering vector, $\mathbf{s}_{reduced} = \left[S_{HH} \ \frac{1}{\sqrt{2}} (S_{HV} + S_{VH}) \ S_{VV} \right]^T$, is calculated from the original scattering vector, $\mathbf{s} = [S_{HH} \ S_{HV} \ S_{VH} \ S_{VV}]^T$, by assuming the reciprocity principle ($S_{HV} = S_{VH}$), where $[\ ]^T$ is an ordinary transpose operation. The scattering vector $[\mathbf{s}]$ cannot characterize the distributed targets and is only able to characterize the coherent or pure scatterer. The distributed targets, however, are well characterized by the covariance $[\mathbf{C}]$ or coherency $[\mathbf{T}]$ matrices [60]. Therefore, the scattering, covariance, and coherency matrices with three, six, and six elements, respectively, were extracted in Model I.

4.3.2.2. Target decomposition: Model II

In the decomposition procedure, the backscattered PolSAR signal is deconstructed to determine the scattering mechanisms of the ground targets. Unlike the coherent decompositions (e.g., Krogager decomposition), which are only useful for man-made structures with deterministic targets, the incoherent decompositions determine the relative contributions from different scattering mechanisms. Thus, they may be more efficient for obtaining the information of natural scatterers [61], [62]. Accordingly, five well-known incoherent polarimetric decompositions, including Cloude-Pottier, Freeman-Durden, Yamaguchi, An-Yang, and Van Zyl decomposition

features were used in this study to evaluate the effect of different polarimetric descriptors on wetland classification.

The Cloude-Pottier decomposition [63], the so-called eigenvector/eigenvalue-based decomposition, measures and transforms the information of distributed ground targets into deterministic targets. Due to the complexity of interpreting scattering vectors in their original representation, three secondary parameters, including entropy (H), anisotropy (A), and alpha angle (α), are extracted to determine the relationship between the scattering mechanisms. Entropy measures the randomness of a single scatterer mechanism, wherein dominant scatterers usually have low entropy values. Anisotropy is a complimentary component to entropy and represents the relative importance of the secondary and tertiary scattering mechanisms. The alpha angle indicates type of scattering mechanisms and ranges between 0 and 90 degrees. Alpha angle values around 90 degrees represent dominant double-bounce scattering. By contrast, a low alpha angle represents dominant surface scattering. Also, an alpha angle around 45 degrees denotes dominant volume scattering [63].

The Freeman-Durden decomposition approach determines a three-component scattering mechanisms of ground targets based on a physical model [64]. In this method, double-bounce (Dbl), volume (Vol), and surface (Odd) scattering correspond with the double-bounce scattering from a dihedral corner reflector, randomly oriented thin cylindrical dipoles, and first-order Bragg scattering, respectively [64]. The Freeman-Durden decomposition is useful for decomposing the scattering mechanism from naturally incoherent scatterers such as wetland ecosystems [60]. The Yamaguchi decomposition is a modified version of the Freeman-Durden decomposition, wherein the helix scattering power represents the fourth scattering mechanism. The helix term considers the non-reflection symmetric cases and determines the correlation between the co- and cross-pol

data. The helix term is of great importance for complex urban areas and may be less useful for natural distributed scatterers [65]. The An-Yang decomposition is a modified version of Yamaguchi decomposition in which de-orientation is added for analyzing PolSAR data. In this method, a de-orientation is first performed to the coherency matrix and the de-oriented coherency matrix is then decomposed to four components by the Yamaguchi decomposition [66]. Similar to the Freeman-Durden decomposition, the Yamaguchi and An-Yang decompositions are both efficient for decomposing the polarimetric scattering of natural targets, but are advantageous in urban areas. Thus, we included the Yamaguchi and An-Yang decompositions to better distinguish the urban class from other land cover types in this study.

The Van Zyl decomposition is another modification of the Freeman-Durden decomposition that employs the non-negative eigenvalue decomposition [67]. Additionally, a combination of the non-negative eigenvalue decomposition with the eigenvector decomposition is conducted to remove additional limitations of the model-based decomposition [67]. Although the Van Zyle decomposition is the eigenvector-based decomposition [68], it has descriptors very similar to that of model-based decompositions, including surface, double-bounce, and volume scattering with relatively equal strength to that of model-based decompositions (e.g., FD) [26].

4.3.2.3. Proposed method: Model III

In Model III, we proposed a modified coherency matrix based on statistical and physical analysis of PolSAR data. In the context of polarimetric SAR image classification, each element of the coherency matrix (T11, T12,…, and T33) is considered as a PolSAR feature. In conventional classification methods, these features are equally weighted and then applied to the classification procedure. However, each element of the coherency matrix has a different discriminant capability. Feature selection is a common approach for increasing the classification accuracy of a multi-

dimensional dataset. In most feature selection methods, features with low and moderate between-class discriminant capability are removed and only features providing high class separability are incorporated into the classification [69]. However, classification using a selected number of features may not produce reliable results when there is high within-class diversity, as is the case in wetland complexes. Thus, in this study, a novel method for feature weighting of coherency matrix elements is proposed to increase the classification accuracy of PolSAR data in wetland areas. In this method, rather than selecting and, consequently, ignoring some features, the optimum weight assignment to features is performed according to the class discrimination power of each feature. This adaptive approach enhances the contribution of the most discriminating features and diminishes that of the least discriminating features by assigning them higher and lower weights, respectively. Particularly, each element of the coherency matrix (T11, T12, …, and T33) is weighted based on the integration of FLDA as a statistical approach and the physical interpretation of PolSAR features (number of features: Q=9). The FLDA technique, as a statistical approach, has been widely used in pattern recognition and machine learning [70]. It has been also applied as a feature selection approach for improving classification accuracy [71]. The FLDA reduces the dimension of a given statistical model by defining a new projection that decreases within-class diversity and increases between-class separability. Suppose that P is the number of classes in the image and $\{y_{ik} \mid k=1, 2, …, K\}$ presents a sample of Q dimensional feature vectors in which K is the number of samples and i denotes the ith class. The Fisher criterion of the nth feature is calculated as follows:

$$f(n) = \sum_{i=1}^{P} \sum_{j \neq i}^{P} \frac{\left(\mu_i(n) - \mu_j(n)\right)^2}{\sigma_i^2(n) + \sigma_j^2(n)} \qquad (4.1)$$

where $\mu_i(n)$ and $\sigma_i^2(n)$ are the mean and the variance of the ith class in the nth feature, respectively, and defined as follows:

$$\mu_i(n) = \frac{1}{K} \sum_{k=1}^{K} y_{ik}(n) \qquad (4.2)$$

$$\sigma_i{}^2(n) = \frac{1}{K-1} \sum_{k=1}^{K} \left(y_{ik}(n) - \mu_i(n) \right)^2 \qquad (4.3)$$

$$n = 1, 2, \ldots, Q \;\; \text{and} \;\; i = 1, 2, \ldots, P$$

where Q is the number of features (number of features: Q=9 in this study) and P is the number classes in the image.

Training samples are selected by an unsupervised classification for each class and used as the input for the FLDA processing. More specifically, after PolSAR image pre-processing, the FLDA is used as a feature weighting method by incorporating the scattering models obtained by an initial unsupervised H/α Wishart classification [55]. The Wishart classifier is a supervised Maximum Likelihood Classifier (MLC) that works based on the complex Wishart distribution for PolSAR imagery. Lee et al. (1999) proposed the combination of the H/α decomposition and Wishart classifier, wherein the eight classes resulting from the H/α decomposition were used as training sets for the Wishart classifier (number of classes: P=8) [55]. This automated method is advantageous because it provides information about the inherent scattering properties for terrain identification while maintaining the spatial resolution in the classification procedure [55].

In the PolSAR imagery, one of the important properties for the eigenvalue–eigenvector decomposition is that the parameters are rotation-invariant and remained constant for rotation around the radar line of sight. For a polarimatric image, eight meaningful zones according to the H/α plane are defined. It is worth noting that the class numbers introduced by Lee and Pottier (2009) have been revised in this study as shown in Figure 4.4.
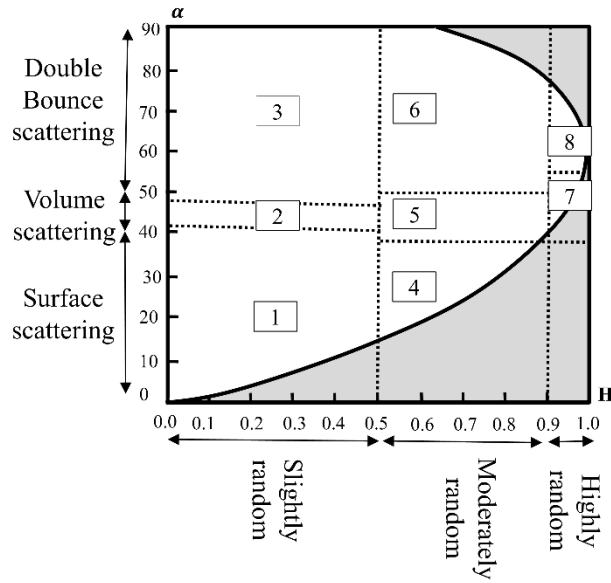
Figure 4.4. Scattering plane of polarimetric entropy and mean scattering alpha angle [58].

Given the eight classes obtained by the initial classification, the Fisher coefficient for the first class is represented as follows:

$$f_1(n) = \left(\frac{(\mu_1(n) - \mu_2(n))^2}{\sigma_1^2(n) + \sigma_2^2(n)} \right) + \left(\frac{(\mu_1(n) - \mu_3(n))^2}{\sigma_1^2(n) + \sigma_3^2(n)} \right) + \cdots + \left(\frac{(\mu_1(n) - \mu_8(n))^2}{\sigma_1^2(n) + \sigma_8^2(n)} \right) \tag{4.4}$$

Accordingly, eight groups of Fisher coefficients are obtained for these eight classes based on the scattering mechanisms of the ground targets that correspond to the H/α plane:

$$\{f_1(1), f_1(2), \dots, f_1(9)\}, \{f_2(1), f_2(2), \dots, f_2(9)\}, \tag{4.5}$$

$$\{f_3(1), f_3(2), \dots, f_3(9)\}, \{f_4(1), f_4(2), \dots, f_4(9)\}, \{f_5(1), f_5(2), \dots, f_5(9)\},$$

$$\{f_6(1), f_6(2), \dots, f_6(9)\}, \{f_7(1), f_7(2), \dots, f_7(9)\}, \{f_8(1), f_8(2), \dots, f_8(9)\}$$

The Fisher coefficient for each element of the coherency matrix is obtained by summing the corresponding Fisher coefficients of the eight classes. For example, the Fisher coefficient that corresponds to the first element of the coherency matrix (T_{11}) is represented as follows:

$$f(1) = f_1(1) + f_2(1) + f_3(1) + \dots + f_8(1) \tag{4.6}$$

The Fisher coefficients for other elements of the coherency matrix can be similarly obtained. Specifically, the relationship between the nine Fisher coefficients and the coherency matrix elements can be better indicated using the following matrix format:

$$F = \begin{bmatrix} f(1) & f(2) & f(3) \\ f(4) & f(5) & f(6) \\ f(7) & f(8) & f(9) \end{bmatrix} = F_1 + F_2 + \dots + F_8 \tag{4.7}$$

where F_i $(i = 1, 2, \dots, 8)$ denotes the weighting matrix for the ith class. In this step, the interpretation of the physical characteristics of scattering mechanisms is incorporated to the weighting procedure to further increase the classification accuracy. In particular, the T_{33} element of the coherency matrix primarily appears in the volumetric scattering information and is less prevalent in the surface and double-bounce scattering. According to the H/α plane (see Figure 4.4), the first, third, fourth, sixth, and eighth classes do not have volumetric scattering information. Thus, in the weighting procedure, the corresponding elements for these classes may be set to zero;

however, an increase in randomness scattering results in higher entropy values, which should be considered in the weighting scheme. Nevertheless, determining the weights for the first and third classes are straightforward and set to zero because of their lower entropy values, as follows:

$$F_1 = \begin{bmatrix} f_1(1) & f_1(2) & f_1(3) \\ f_1(4) & f_1(5) & f_1(6) \\ f_1(7) & f_1(8) & f_1(9) \end{bmatrix} \rightarrow F^*_1 = \begin{bmatrix} f_1(1) & f_1(2) & 0 \\ f_1(4) & f_1(5) & 0 \\ 0 & 0 & 0 \end{bmatrix} \tag{4.8}$$

$$F_3 = \begin{bmatrix} f_3(1) & f_3(2) & f_3(3) \\ f_3(4) & f_3(5) & f_3(6) \\ f_3(7) & f_3(8) & f_3(9) \end{bmatrix} \rightarrow F^*_3 = \begin{bmatrix} f_3(1) & f_3(2) & 0 \\ f_3(4) & f_3(5) & 0 \\ 0 & 0 & 0 \end{bmatrix} \tag{4.9}$$

Assigning the corresponding weights to zero for the fourth, sixth, and eighth classes is not, however, the best scenario, because the entropy values of these classes are moderate to high. The high degree of randomness in the fourth, sixth, and eighth classes may be due to a mixture of different scattering mechanisms. Thus, in order to both decrease the effect of high entropy due to random scattering and maintain the polarimetric information of volume scattering mechanism, which is the dominant scattering type in the wetland complex, an adaptive weighting was employed for the fourth, sixth, and eighth classes. The corresponding weights for the volume scattering component in the aforementioned classes are determined as follows:

$$F_4 = \begin{bmatrix} f_4(1) & f_4(2) & f_4(3) \\ f_4(4) & f_4(5) & f_4(6) \\ f_4(7) & f_4(8) & f_4(9) \end{bmatrix} \rightarrow F^{**}_4 = \begin{bmatrix} f_4(1) & f_4(2) & (1 - \bar{H}_4)f_4(3) \\ f_4(4) & f_4(5) & (1 - \bar{H}_4)f_4(6) \\ (1 - \bar{H}_4)f_4(7) & (1 - \bar{H}_4)f_4(8) & (1 - \bar{H}_4)f_4(9) \end{bmatrix} \tag{4.10}$$

$$F_6 = \begin{bmatrix} f_6(1) & f_6(2) & f_6(3) \\ f_6(4) & f_6(5) & f_6(6) \\ f_6(7) & f_6(8) & f_6(9) \end{bmatrix} \rightarrow F^{**}_6 = \begin{bmatrix} f_6(1) & f_6(2) & (1 - \bar{H}_6)f_6(3) \\ f_6(4) & f_6(5) & (1 - \bar{H}_6)f_6(6) \\ (1 - \bar{H}_6)f_6(7) & (1 - \bar{H}_6)f_6(8) & (1 - \bar{H}_6)f_6(9) \end{bmatrix} \tag{4.11}$$

$$F_8 = \begin{bmatrix} f_8(1) & f_8(2) & f_8(3) \\ f_8(4) & f_8(5) & f_8(6) \\ f_8(7) & f_8(8) & f_8(9) \end{bmatrix} \rightarrow F^{**}{}_8 = \begin{bmatrix} f_8(1) & f_8(2) & (1-\bar{H}_8)f_8(3) \\ f_8(4) & f_8(5) & (1-\bar{H}_8)f_8(6) \\ (1-\bar{H}_8)f_8(7) & (1-\bar{H}_8)f_8(8) & (1-\bar{H}_8)f_8(9) \end{bmatrix} \qquad (4.12)$$

where $\bar{H}_4$, $\bar{H}_6$ and $\bar{H}_8$ are the mean of entropy values in the fourth, sixth, and eighth classes, respectively. As a result, the final weighting matrix is determined as:

$$F_t = F_1{}^* + F_2 + F_3{}^* + F_4{}^{**} + F_5 + F_6{}^{**} + F_7 + F_8{}^{**} \qquad (4.13)$$

The modified coherency matrix ($\mathbf{T}_m$) is then obtained by multiplying of the final weighting matrix (F_t) by the original pixel-wise coherency matrix ($\mathbf{T}$) as follows:

$$\mathbf{T}_m = F_t \cdot \mathbf{T} = \begin{bmatrix} f_t(1)T_{11} & f_t(2)T_{12} & f_t(3)T_{13} \\ f_t(4)T_{21} & f_t(5)T_{22} & f_t(6)T_{23} \\ f_t(7)T_{31} & f_t(8)T_{32} & f_t(9)T_{33} \end{bmatrix} \qquad (4.14)$$

where $\mathbf{T}_m$ is the modified coherency matrix. Notably, both $\mathbf{T}$ and F_t are Hermitian and, therefore, the modified coherency matrix $\mathbf{T}_m$ also remains Hermitian. Since the total scattering power span should remain unchanged, the $\mathbf{T}_m$ matrix can be normalized as follows:

$$\mathbf{T}_{m11} = \frac{f_t(1).T_{11}}{f_t(1).T_{11} + f_t(5).T_{22} + f_t(9).T_{33}} Span \qquad (4.15)$$

$$\mathbf{T}_{m22} = \frac{f_t(5).T_{22}}{f_t(1).T_{11} + f_t(5).T_{22} + f_t(9).T_{33}} Span \qquad (4.16)$$

$$\mathbf{T}_{m33} = \frac{f_t(9).T_{33}}{f_t(1).T_{11} + f_t(5).T_{22} + f_t(9).T_{33}} Span \qquad (4.17)$$

The other elements of the modified coherency matrix may be similarly normalized.

In Model III, the modified coherency matrix and all well-known decomposition features extracted from the modified coherency matrix, including the Cloud-Pottier, Freeman-Durden, Yamaguchi, An-Yang, and Van Zyl were obtained. These features were then incorporated into different scenarios in Model III for wetland classification. A complete list of variable acronyms is provided in Table 4.5.

Table 4.5. Acronyms of features employed in this study.

Prefix	Description	Suffix	Description
CP	Cloude-Pottier decomposition	H	Entropy
		A	Anisotropy
FD	Freeman-Durden decomposition	Alpha	Alpha angle
		Odd	Surface scattering
VZ	Van Zyl decomposition	Dbl	Double-bounce scattering
		Vol	Volume scattering
Yam	Yamaguchi decomposition	Hlx	Helix scattering
		T_{11}	First diagonal element
		T_{22}	Second diagonal element
AnY	An and Yang decomposition	T_{33}	Third diagonal element
		T_{12}	First off-diagonal element
MC	Modified Coherency matrix	T_{13}	Second off-diagonal element
		T_{23}	Third off-diagonal element

4.3.3. Image classification

In this study, 24 different scenarios in three main models were considered for wetland classification using different polarimetric features. Table 4.6 summarizes different combination of input features used for wetland classification.

Table 4.6. Different scenarios employed in this study for wetland classifications. Abbreviation explanations are provided in Table 4.5.

RF model	Scenario	Number of features	Name of features	Pixel-based	Object-based	Single-date	Multi-temporal
I	1	3	Scattering Matrix	✓		✓	
	2	6	Covariance Matrix	✓		✓	
	3	6	Coherency Matrix	✓		✓	
	4	6	Coherency Matrix		✓	✓	
	5	18	Coherency Matrix	✓			✓
	6	18	Coherency Matrix		✓		✓
II	7	3	CP		✓	✓	
	8	3	FD		✓	✓	
	9	3	VZ		✓	✓	
	10	4	Yam		✓	✓	
	11	4	AnY		✓	✓	
	12	9	CP		✓		✓
	13	9	FD		✓		✓
	14	9	VZ		✓		✓
	15	12	Yam		✓		✓
	16	12	AnY		✓		✓
	17	69	Coherency Matrix, CP, FD, VZ, Yam, AnY		✓		✓
III	18	6	MC	✓		✓	
	19	6	MC		✓	✓	
	20	18	MC	✓			✓
	21	18	MC		✓		✓
	22	48	MC , CP, FD, Yam		✓		✓
	23	51	MC , VZ, Yam, AnY		✓		✓
	24	69	MC , CP, FD, VZ, Yam, AnY		✓		✓

4.3.3.1. Object-based Image Analysis

Low spatial resolution satellite images have constrained classification approaches to pixel-based algorithms since the early 1970s [72]. This is because the image pixel size was kept more coarse than, or in the best case, the same size as the ground object. Therefore, per-pixel or sub-pixel image

analysis was the most common approaches in the early stages of land cover classifications using satellite imagery [29]. However, the advent of high spatial resolution satellite imagery has significantly altered the applied methodologies for land cover classification, namely Object-Based Image Analysis (OBIA) techniques [28]. Image segmentation is a first step in OBIA and typically carried out using a Multi-Resolution Segmentation (MRS) algorithm [43], [73]. Segmentation initiates with pixel-sized objects and gradually grows through the pair-wised merging of neighboring objects using pre-defined parameters. This procedure is called bottom-up image segmentation. The pre-defined parameters are determined by users and represent scale, shape, smoothness, and compactness criteria. All these mentioned parameters are combined together to determine a homogeneity factor until convergence criteria are met [28]. The size of image objects is the most important criterion in MRS analysis and determined by the scale parameter [74].

In this study, MRS analysis was performed by eCognition Developer 9 using optical images and its parameters were defined by an iterative trial-and-error approach. An optical image was used in this step because segmentation based on SAR images produces some meaningless objects due to the inherent SAR speckle. Also, Myint et al. (2011) demonstrated the lack of a standard, widely acceptable approach to determine the optimal scale for different segmentation approaches [75]. Therefore, it varies according to different applications as well as the availability of different remote sensing imagery. As such, different scale parameters were examined to provide meaningful ground objects and the optimal values for scale, shape, and compactness parameters were found to be 50, 0.05, and 0.5 in this study, respectively.

4.3.3.2. Random Forest

Random Forest (RF) classification is one of the most well-known ensemble learning algorithms and has recently gained attention for land cover classification using satellite imagery [76]. A non-

parametric RF classifier is comprised of a group of tree classifiers used to make a prediction. The trees are grown through a bagging approach by random selection of training samples that are divided into several bags. Specifically, about two thirds of the samples, known as *in-bags* samples, are randomly selected to train the classifier; however, the remaining one third, known as *out-of-bags* (oob) samples, is applied to a cross-validation procedure to evaluate the classification performance [42]. In this approach, some data may be used several times in the training procedure, while others may not be selected at all. Finally, assigning a pixel to a specific class is determined by the single vote of each tree classifier. The maximum vote for each pixel by tree classifiers specifies its class. However, an appropriate attribute should be assigned to each tree to increase dissimilarity between classes.

The generalization error is defined by dividing the number of misclassified elements by the total number of oob elements [42]. It should be noted that the generalization error or classification accuracy is controlled at two different levels. Firstly, by increasing the number of trees, the generalization error tends to be convergent which in turn prevents the RF classifier from being over-fitted to the data. Secondly, RF employs the best split of a random subset of each node in growing trees, which causes a negligible correlation between trees and, as such, a decrease in the generalization error.

Another advantage of RF is that it provides the relative importance of each variable in the classification scheme and thereby, makes a flexible classification algorithm with the capability to handle high dimensionality datasets. For variable importance determination, RF measures the degradation in the classification accuracy by altering one of the input random features while keeping the rest of input features constant [77]. Specifically, the variable importance determines the influence of each input feature on the classification's overall accuracy. Notably, the two

parameters, which should be adjusted to employ RF, are the number of decision trees (*Ntree*) and the number of variables (*Mtry*) [43]. In this study, a total number of 400 trees were selected in each classification model. Also, the square root of the number of input variables was selected for *Mtry* because it decreased both the computational complexity of the algorithm and the correlation between trees by limiting the number of input variables for a split [39].

4.3.3.3. Accuracy assessment

The accuracy assessments were conducted by comparing the classified maps to the ecological ground truth data using confusion matrices. The common parameters extracted from the confusion matrix for assessing classified maps are: 1) overall accuracy; 2) kappa coefficient; and 3) user's and producer's accuracy. Overall accuracy is determined by dividing the total number of correctly classified pixels (diagonal elements) by the total number of pixels in the confusion matrix. The kappa coefficient measures the level of agreement between the classification map and the reference data. The producer's accuracy illustrates the probability of a reference pixel being correctly classified (omission error), and the user's accuracy indicates the probability that a classified pixel on the map actually illustrates that category on the ground (commission error) [78]. In this study, the first two assessment parameters were extracted for all scenarios in each model; however, the latter one was only presented for the most significant result.

4.4. Results and discussion

4.4.1. Inputs from Model I: original PolSAR feature

In Model I, we investigated the original features in pixel- versus object-based and single- versus multi-date analysis (see Table 4.6). According to Table 4.7, the coherency matrix in the pixel-based and single-date framework, scenario 3, resulted in a higher accuracy than its corresponding scattering and covariance matrices (scenarios 1 and 2). Among the original polarimetric features,

including the scattering, covariance, and coherency matrices, the results illustrated that the coherency matrix in an object-based, multi-temporal framework was superior to all other combinations. This is because the covariance matrix is a second order mathematical representation of the scattering matrix, while the coherency matrix contains physical scattering information of ground targets and, as such, it was found to be more successful than the other two matrices.

Having obtained a higher accuracy via the coherency matrix, it was selected for further analysis in the remaining scenarios of Model I. Following the hierarchical accuracy assessment, the pixel- and object-based classifications were compared. It was observed that applying the object-based approach improved the classification accuracy by about 2% in comparison with the pixel-based classification (scenarios 3 versus 4). Next, two RADARSAT-2 images were added to examine the temporal effect. It was found that the coherency matrix in object-based and multi-temporal framework represented a higher accuracy than pixel-based and single-date case (scenarios 3 versus 6). Furthermore, scenario 6 produced the most powerful combination of features among all of defined scenarios in Model I in terms of classification accuracy.

Table 4.7. Accuracy assessments of RF scenarios for wetland classification. The most accurate results are indicated in bold.

RF model	Scenarios	Avalon		Deer Lake		Gros Morne	
		Kappa Coefficient	OA (%)	Kappa Coefficient	OA (%)	Kappa Coefficient	OA (%)
I	1	0.46	61.08	0.45	59.66	0.58	72.74
	2	0.50	65.91	0.48	62.17	0.64	76.81
	3	0.53	66.20	0.50	63.05	0.65	77.83
	4	0.58	68.43	0.54	65.22	0.68	78.96
	5	0.55	66.87	0.51	64.93	0.67	78.03
	6	0.61	69.54	0.55	66.09	0.70	79.74
II	7	0.41	58.97	0.43	57.91	0.57	69.80
	8	0.63	72.38	0.59	70.46	0.71	81.24
	9	0.66	73.25	0.62	71.05	0.72	82.51
	10	0.62	71.91	0.58	68.88	0.67	79.02
	11	0.63	72.06	0.60	69.14	0.68	80.67
	12	0.46	61.42	0.49	59.85	0.62	73.66
	13	0.65	73.69	0.66	73.71	0.73	82.88
	14	0.66	74.78	0.66	73.96	0.74	83.49
	15	0.64	72.53	0.62	70.00	0.71	81.33
	16	0.65	72.76	0.62	70.29	0.72	81.81
	17	0.79	84.92	0.71	76.90	0.82	88.39
III	18	0.69	73.55	0.59	69.40	0.78	85.92
	19	0.73	76.57	0.65	73.10	0.79	87.14
	20	0.71	74.28	0.62	70.99	0.75	87.05
	21	0.74	77.92	0.69	74.61	0.81	88.52
	22	0.81	85.19	0.73	78.95	0.84	90.31
	23	0.84	86.74	0.75	80.62	0.86	91.09
	24	**0.85**	**87.11**	**0.76**	**81.04**	**0.89**	**92.17**

Note: See Table 4.6 for an overview of the features used to define the scenarios presented in Table 4.7.

Overall, the object-based classification (scenarios 4 and 6) showed a higher accuracy than pixel-based classifications in all scenarios examined in Model I. Additionally, in the temporal context (single- or multi-date), multi-temporal, object-based classification represented a higher accuracy than single-date, object-based classification. Notably, temporal information is generally considered to be an essential factor for reducing possible confusion error when discriminating the main vegetation classes, particularly in the case of adequate temporal image separation [79]. This is due to the highly dynamic nature of wetland ecosystems, wherein the backscattering mechanism of each wetland class in terms of both intensity and type of scattering is strongly affected by both phenology and hydrological conditions [26]. For example, during the high-water season, swamp and marsh classes experience different conditions and, as such, have different signatures in a SAR image. In the swamp class, the double-bounce scattering increases due to the improved chance of double-bounce scattering between the water surface and tree trunks. However, the double-bounce scattering can decrease in the marsh wetland during this time as it is primarily converted to surface scattering due to increasing the water level. Conversely, when the water surface is low, the dominant scattering mechanism is volume scattering from vegetation canopy or upper section of tree for the swamp class [80]. Thus, each wetland classes can be better characterized during the specific time in the growing cycle. Accordingly, using multi-temporal data is helpful for better distinguishing wetland classes with similar structures but different phenology and flooding statuses [26].

It should be noted that multi-temporal, pixel-based classification (scenario 5) was less accurate than single-date, object-based classification (scenario 4). Thus, it was concluded that the objectification factor was more influential for the classification accuracy than the temporal factor in this study. This could be due to that, in the object-based framework, the segmentation analysis

152

was carried out using an optical image, which led to an improvement in the classification accuracy. However, in the case of pixel-based, multi-temporal classification, the inclusion of extra PolSAR images resulted in a lesser degree of improvement in overall accuracy due to speckle noise. These results were also confirmed through the visual comparison of classified maps in pixel- and object-based frameworks (see Figure 4.5). Classification noise was observed in all pixel-based classified maps in Model I.
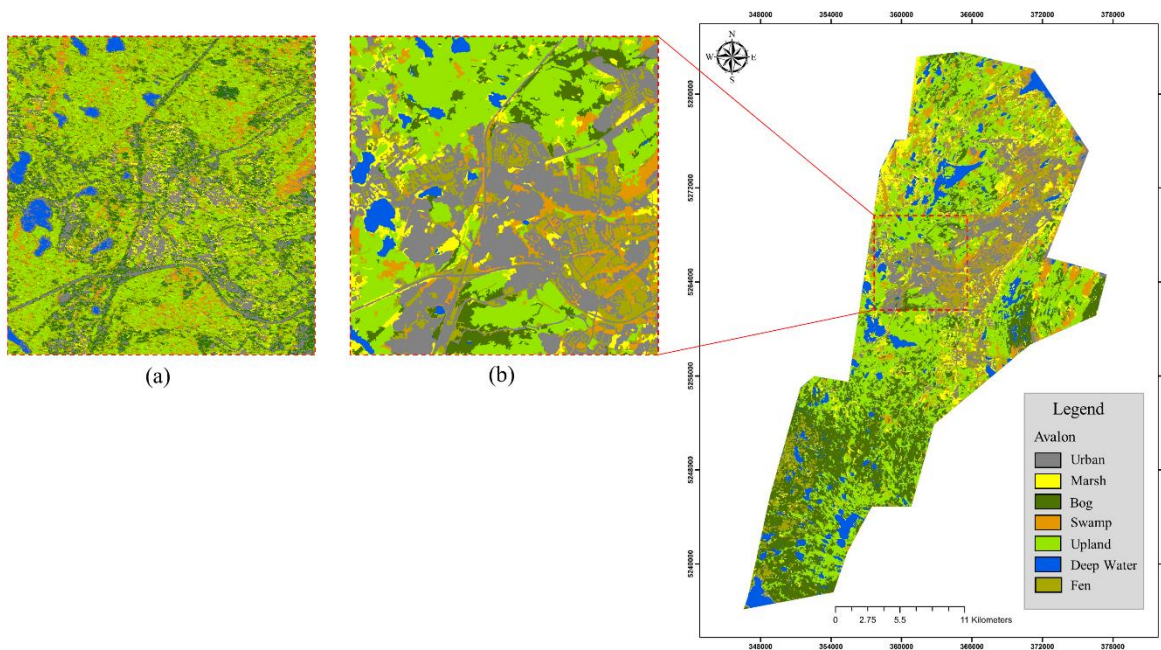
Figure 4.5. A visual comparison between (a) pixel-based and (b) object-based RF classification of a zoomed area in the Avalon pilot site.

As seen, unlike the pixel-based approach, the classes obtained using the object-based method are noiseless and neat and provide a visually appropriate depiction of both wetland and non-wetland classes. This was concluded based on the visual interpretation of the ecological experts familiar with the study areas. For example, the predominance of the urban class in the center of the zoomed area was better illustrated by object-based classification, which indicated less confusion between the urban, swamp, and upland classes.

In summary, using the scattering matrix in the single-date and pixel-based framework provided the least accurate results within all defined scenarios in Model I. In contrast, using the coherency matrix in the multi-temporal, object-based framework presented the most significant results in Model I.

4.4.2. Inputs from Model II: Polarimetric decomposition features

Given the results from Model I, the classification based on the coherency matrix in the context of object-based image analysis was carried out in Model II. Therefore, all target decompositions were exploited based on the coherency matrix during further analysis in Model II. Because the temporal analysis represented variations in the accuracy assessment and a deterministic result was not obtained regarding the influence of adding multi-temporal PolSAR images, we concentrated on different target decomposition algorithms in single- versus multiple-date frameworks in Model II. Particularly, the effect of multi-temporal images was further investigated for wetland classification using polarimetric decomposition features.

Focusing on the target decompositions in the single-date context, VZ and FD decompositions (scenarios 9 and 8) represented the highest accuracies, respectively. The same results were also obtained from the multi-temporal analysis. More specifically, applying multi-temporal data increased the classification accuracy of all scenarios (12 to 16) by about 2%, while VZ and FD had the highest accuracies overall. However, combining the coherency matrix and all decomposition features in the multi-temporal classification analysis (scenario 17) significantly increased the classification accuracy by approximately 3% to 10% (depending on the case studies) compared to the latest most accurate scenario (scenario 14).

Generally, it was found that applying the various target decompositions to the coherency matrix (Model II) was more successful in terms of classification accuracy relative to the original features (Model I). This was the case for all decompositions, excluding CP (scenarios 7 and 12), which was suggestive of two issues. First, polarimetric decompositions have additional information not directly obtainable from the original features. This was also supported by visual comparisons between classified maps of Model I and II, wherein classifications based on polarimetric decompositions were more successful in identifying different vegetation types and discriminating between upland and wetland classes. Thus, it was concluded that incorporating the scattering mechanisms of ground targets, extracted by polarimetric decompositions, into the classification scheme enhanced the discrimination capability of land cover classes and, as a result, improved the classification accuracy. Second, it was found that polarimetric decomposition approaches based on the physical model (e.g., FD) were more successful in terms of improving the classification accuracy than the CP decomposition. This is because these decomposition approaches lie in the real domain and estimate the intensity of each scattering mechanism that occurs in a natural target. In particular, these physical model-based decompositions generate an individual and independent descriptor associated with each backscattering mechanism. For example, in these approaches, the surface scattering contains the information of water, the double-bounce scattering captures the information of flooded-vegetation, and the volume scattering corresponds to the upland and non-flooded vegetation [23]. As such, they effectively determined each wetland class scattering patterns and, thus, yielded higher accuracies in this study [23], [25], [26].

In contrast, the CP decomposition is usually employed as an initial unsupervised classification (as used in this paper) to decompose the information of distributed targets into the scattering of deterministic targets, which may explain why it did not significantly contribute to improving the

155

classification accuracy [51], [55]. In particular, eigenvector-based decompositions (e.g., CP) determine the scattering mechanism of targets as both real and angular values. They usually characterize the main scattering mechanism of ground targets by either a single or several components and then augment this estimate using other real and/or angular descriptors, such as anisotropy. Vegetative density considerably attenuates the shorter wavelengths, such as C-band, leading to similar scattering intensities for vegetation with subtle structural differences, such as bog and fen wetlands [49]. Thus, herbaceous vegetation [22], [81] hinders the ability of CP alpha angle, entropy, and anisotropy to identify subtle differences in backscattering mechanisms when shorter wavelengths are employed [26]. The first, second, and third scattering mechanism for herbaceous vegetation are similar in nature, while they vary in intensity. Thus, the similar nature of scattering mechanisms in herbaceous vegetation (e.g., bog and fen) [82] and the shorter wavelength utilized in this study (i.e., C-band) [83] contributed to less accurate classification results using CP decomposition. The discrepancy of the phase centers during reflection further complicates the matter. This issue is particularly severe in the CP decomposition, which results in very noisy decomposition parameters and a less accurate classified map [84]. Overall, the anisotropy and entropy descriptors of the CP decomposition were less useful for discriminating NL herbaceous vegetation, as they were almost random and characterized by high level of noise content over natural scatterers environments [51]. The decomposition Yam and its modified version, AnY, have been demonstrated to be relatively less accurate compared to FD and VZ. The better performance of these approaches is expected to obtain in urban areas with complex structures. Nevertheless, almost all physical model-based decompositions indicated to be successful, while there was a relatively small difference between the accuracy obtained by those methods.

In conclusion, it was observed that applying polarimetric decompositions (Model II) was more successful than using the original features (Model I) in terms of classification accuracy. Furthermore, the inclusion of all polarimetric decomposition features in the multi-temporal framework provided the highest accuracy thus far (scenario 17).

4.4.3. Inputs from Model III: the proposed method

The objective of this section is to assess the ability of the modified coherency matrix proposed in this study for classification of different wetland classes. First, we evaluated the robustness and reliability of the modified coherency matrix in terms of preserving the polarimetric information. This was done because the Fisher Linear Discriminant analysis is a classical machine learning technique, which mainly uses the statistical information of image pixels while ignoring their scattering characteristics. However, the proposed methodology incorporates the scattering mechanisms of ground targets through the physical interpretation of different elements of the coherency matrix to ensure the preservation of polarimetric information. To investigate this, different polarimetric features of CP and FD decompositions were extracted from the original and modified coherency matrices and are depicted in Figure 4.6.
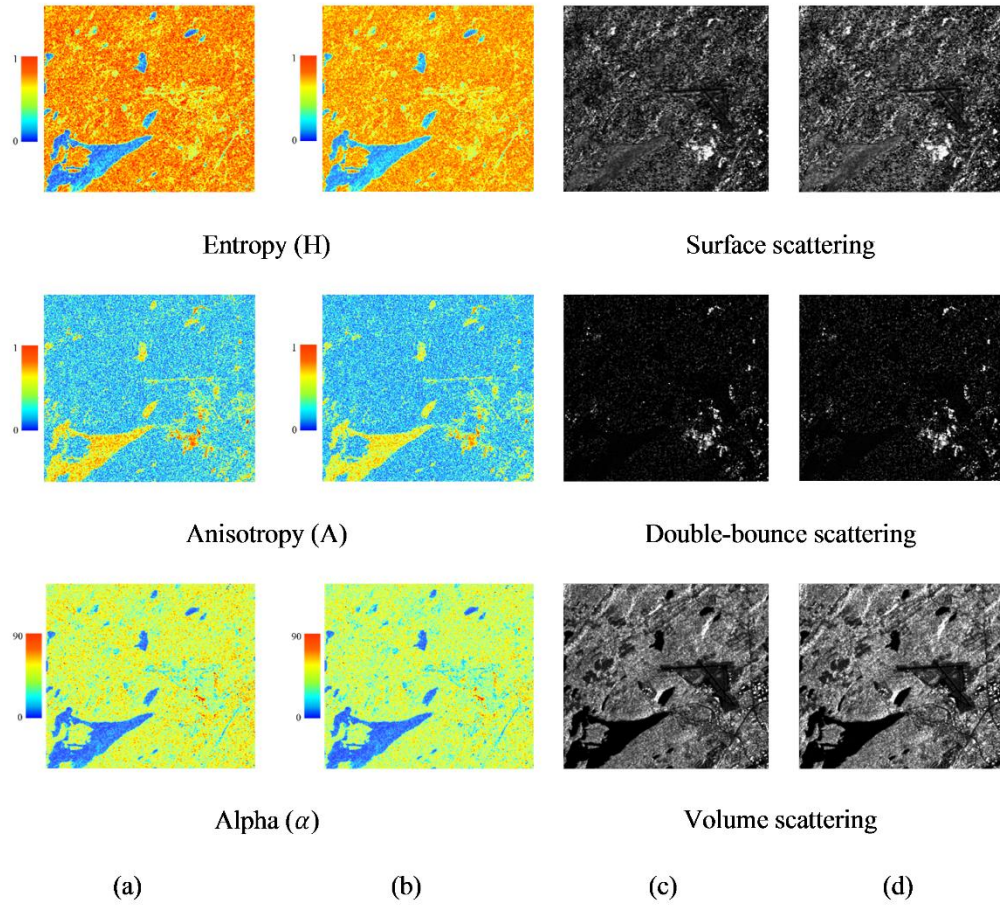
Figure 4.6. Evaluating the polarimetric information preservation by comparing (a) Cloude-Pottier features obtained from the original coherency matrix, (b) Cloude-Pottier features obtained from the modified coherency matrix, (c) Freeman-Durden features obtained from the original coherency matrix, and (d) Freeman-Durden features obtained from the modified coherency matrix.

The polarimetric features obtained from the modified coherency matrix preserved the polarimetric information. For example, the entropy images indicate polarimetric information about the degree of randomness. As illustrated in Figure 4.6, the entropy feature obtained from the modified coherency matrix maintains the distribution of entropy values with the texture in the center of the zoomed area (see Figure 4.6b). Furthermore, the FD polarimetric features obtained from the

modified coherency matrix better distinguish different scattering mechanisms of ground targets relative to the original coherency matrix (Figures 4.6c and 4.6d). Thus, it was concluded that the polarimetric information was well preserved by applying the proposed method. Next, we evaluated the efficiency of the modified coherency matrix for the wetland classification.

For better comparison of the coherency and modified coherency matrices (Model I and III), different scenarios in the context of pixel- versus object-based and single- versus multiple-date were also considered in this section. The modified coherency matrix in the pixel-based and single-date case (scenario 18) increased the classification accuracy above 6% compared to its corresponding case in Model I (scenario 3). Comparatively, applying the modified coherency matrix in the multi-temporal object-based case (scenario 21) represented an approximate 8% improvement over its corresponding case in Model I (scenario 6). Scenario 21 also demonstrated to be more accurate than VZ decomposition (scenario 14), which was the best target decomposition approach determined in Model II. Following the accuracy assessment in Model III, different combinations of polarimetric decompositions and the modified coherency matrix were examined for classification. Overall, adding all polarimetric decomposition features increased the classification accuracy up to 10% (scenario 24 case study 1) relative to scenario 21. However, different combinations of polarimetric decompositions changed the classification accuracy by only about 2% (see scenario 22, 23, and 24).

The classified maps of the 24th scenario for all study sites are depicted in Figure 4.7. They show the distribution of land cover units, wetland and non-wetland classes distinguishable at a 5m spatial resolution. The bog and upland classes are the most dominant wetland and non-wetland classes in all three pilot sites, respectively, while the marsh class is less prevalent. These observations are

consistent with ecological field reports and the visual interpretation of the land cover types using

aerial and optical imagery by ecological experts familiar with the study areas.
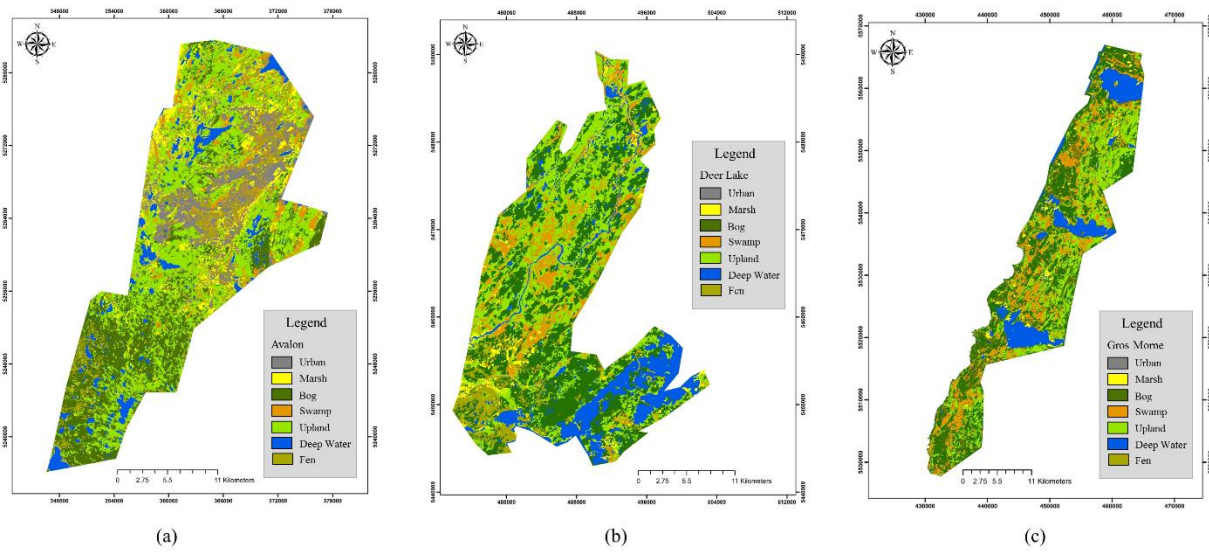
Figure 4.7. The classified maps for the 24th scenario in the three different study areas, including (a)

Avalon, (b) Deer Lake, and (c) Gros Morne.

The 24th scenario in the Gros Morne study area was the most significant result of all the scenarios

for the three pilot sites (see Table 4.7). Therefore, it was selected for the further accuracy analysis.

Figure 4.8 illustrates the relative contributions of the different input variables in the classification

accuracy for the Gros Morne pilot site obtained by RF (scenario 24).
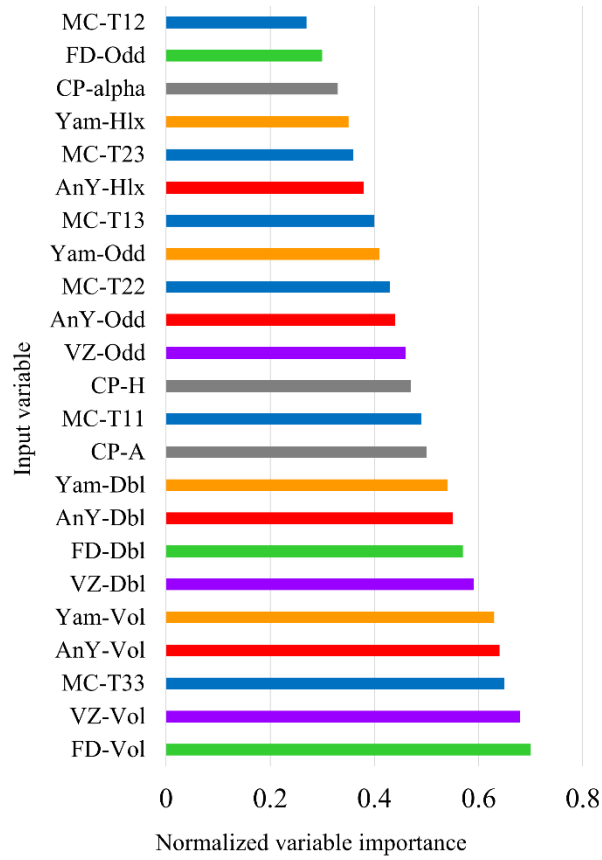
Figure 4.8. Normalized variable importance of RF classification for scenario 24 in the Gros Morne study area. Different variables are represented as follows: MC (blue), FD (green), VZ (purple), AnY (red), Yam (orange), and CP (gray). An explanation of how variables were named can be found in Table 4.5.

FD-Vol, VZ-Vol, and MC-T_{33} were the most important contributing variables. It is worth noting that different polarimetric decomposition features in Model III were also all obtained via the modified coherency matrix. Overall, volumetric components of different polarimetric decompositions, including FD, VZ, AnY, and Yam, as well as the T_{33} element of the modified coherency matrix, were more important variables. These results were consistent with the theory that the volume scattering is the dominant scattering mechanism for vegetation canopies like those found in a wetland complex [3], [85]. Also, the volumetric scattering information is useful to distinguish between woody and the herbaceous wetlands [86]. Double-bounce components of the

161

scattering mechanisms in the polarimetric decompositions were the second most important variables (see Figure 4.8). In this study, FD-Vol was more important than VZ-Vol, while VZ-Dbl was more important than FD-Dbl (see Figure 4.8); overall, the VZ decomposition was the most successful approach amongst all decompositions in this study for differentiating vegetation classes in terms of OA (see Table 4.7). Based on this, it was determined that certain features were more important in the presence of others due to their interdependency [77]. The CP variables were less important, which was consistent with the classification accuracy obtained by the CP decomposition (see Table 4.7).

The confusion matrix for scenario 24 (the Gros Morne case study) is presented in Table 4.8. The results obtained by the accuracy assessment for the wetland classified map were strongly positive, taking into account the complexity of the similar wetland classes, and illustrating the large number of pixels that were correctly classified.

Table 4.8. Classification confusion matrix of the most accurate scenario for the wetland classification (scenario 24, the Gros Morne case study).

		Reference Data								
		Urban	Marsh	Bog	Swamp	Upland	Deep-water	Fen	Tot.	User. Acc.
Classified Data	Urban	14231	43	8	8	19	0	502	14811	96.08
	Marsh	136	2742	50	2	721	0	705	4356	62.95
	Bog	321	14	105431	59	5026	0	545	111396	94.65
	Swamp	13	6	1205	3325	818	0	58	5425	61.29
	Upland	211	412	6498	88	32482	0	29	39720	81.78
	Deep-water	0	0	0	0	0	58530	0	58530	100.00
	Fen	0	49	826	305	328	0	6973	8481	82.22
	Tot.	14912	3266	114018	3787	39394	58530	8812	242719	
	Prod. Acc.	95.43	83.96	92.47	87.80	82.45	100.00	79.13		

The highest user's and producer's accuracies belonged to the deep-water class at 100%. This is because that the dominant scattering mechanism for the deep-water class is usually specular scattering. When the SAR signal hits the surface of calm open water, the most of the transmitted signal is specularly backscattered away from the SAR sensor, resulting in very low SAR backscattering coefficients (σ^0) returns [87]. This makes open water appears dark (black) in SAR images and, accordingly, distinguishable from other land cover types [88]. Although rough and turbulent water surfaces can cause part of the signal to be backscattered to the SAR sensors, this is negligible compared to backscattering responses of other classes. Therefore, the highest user's and producer's accuracies for the water class could be due to the lowest σ^0 value associated to this

class, which effectively contributed to discriminate the water class from other land cover types in this study.

The urban and bog classes were found to be correctly classified with user's accuracies of about 96% and 94%, respectively, which represented the lowest commission error. The fen and upland classes also illustrated relatively high user's accuracies of approximately of 82%. Overall, a confusion error occurred between bog, fen, and upland classes, wherein the bog class was misclassified as upland and, to a lesser degree, the fen class (commission error). The swamp and marsh class had the lowest user's accuracy of about 61% and 63%, respectively, and the highest commission error of about 39% and 37%, respectively. Again, confusion error was found between upland, fen, and marsh classes resulting in a portion of the upland and fen classes to be erroneously classified as marsh. This, too, occurred for the swamp and bog wetland, wherein the bog class was misclassified as the swamp wetland in some cases.

All land cover classes, excluding the fen class, had high producer's accuracies of above 80%, illustrating the relatively small omission error. The producer's accuracy for the fen class was close to 79% indicating slightly higher omission error compared to the other land cover types in this study. In particular, a portion of the fen class was misclassified as other herbaceous vegetation, including the marsh and bog classes.

Overall, the greatest confusion error was observed between herbaceous vegetation (especially between bog and fen classes) as well as other land cover types which may be the result of several phenomena. First, the similar backscattering mechanisms for these classes may have influenced the confusion error. For example, uplands are forested dry lands with a dominant volume scattering mechanism similar to that of swamp wetlands during the low water season, thereby contributing

to the degree of confusion between these classes. Several studies reported that L-band outperformed shorter wavelengths (e.g., C- and X-band imagery) for wetland mapping due to deeper penetration of longer wavelengths [22], [88]. This is particularly true for distinguishing woody wetlands from other classes such as swamp and upland classes.

The heterogeneous mixture of the landscape may also have contributed to the confusion error. Specifically, herbaceous vegetation in the study area is found adjacent to each other without clear cut borders. Also, there is a high degree of similarity between herbaceous vegetation, particularly when shorter wavelengths are applied (e.g., C-band), which are strongly attenuated by vegetative density. For example, the bog and fen classes have ecologically very similar vegetation types and structures; they are peatlands dominated by *Spahgnum* and *graminoid* species, respectively, and as such, are sometimes categorized as the same class (i.e., peatland). Furthermore, as the field notes illustrated, these two classes were found to be hardly distinguished from each other during the *in-situ* field data collection by biologists.

The hydrological variation and phenology of wetland environments may also affect the accuracy of each wetland classes. This is because the backscattering mechanisms of different wetland classes vary in both intensity as well as backscattering types during low and high water seasons. Several studies reported the importance of using multi-temporal satellite imagery for wetland classification to reduce the classification uncertainty due to the highly dynamic nature of wetland environments [1], [26]. Since we used multi-temporal PolSAR images for this study, the classification error due to the hydrological variation and phenology in the wetland ecosystems should be negligible. However, the three PolSAR images, which have been used for each pilot site, may still be insufficient, taking into account the high temporal variation of the wetland ecosystem during the leaf-on season in NL.

Another important consideration when interpreting the above accuracies is the amount of *in-situ* data available for the purpose of applying the supervised classification. Generally, in the case of supervised classification such as RF, larger training sample sizes are recommended for obtaining higher classification accuracies. However, the collection of large amounts of representative ecological field data is often difficult. For example, insufficient amounts of field data for the marsh and swamp class in the Gros Morne pilot site resulted in the lower accuracies for these classes relative to other wetland classes (see Table 4.8). This can be attributed both to the limited time available for field data collection by biologists and to the natural distribution of wetland classes in NL. NL has a generally wet and cool climate, which is particularly suited for extensive peatland (bog and fen) formation. This means that bog and fen are more common than that of other wetland classes and, as a result, were visited more frequently and easily during the field work. Thus, the reason for the lower user's accuracies for swamp and marsh may be attributed to lower amounts of collected *in-situ* data. Accordingly, this may also explain the high accuracy for deep-water, because the high amount of *in-situ* data were available for this class. Hypothetically, the accuracies of all classes except the deep-water class should improve upon the availability and inclusion of greater amounts of *in-situ* data.

The swamp wetlands also tend to occur in physically smaller areas compared to that of other wetlands, such as in transition zones between a wetland and other land cover types. Thus, the swamp wetlands may have been sparse and mixed with other wetland classes reducing the backscattering response significantly; they may have been also too small to be captured as a single object causing the lowest classification accuracy for this class. It is worth noting that the characteristics of wetland classes in other pilot sites (i.e., the Avalon and Deer Lake) are also similar to that of the Gros Morne case study, which is also confirmed by relatively similar

classification accuracies for these pilot sites (see Table 4.7, scenario 24). Thus, in order to reduce the redundancy in the accuracy assessment analysis among three case studies, the results were only interpreted for the Gros Morne study area. The averaged user's and producer's accuracies for wetland classes, including marsh, bog, swamp, deep-water, and fen were equal to 80.2% and 88.6% in the Gros More region, respectively. The classified maps in Figure 4.7 and the high averaged producer's accuracy of about 88% illustrated the fine separation of different wetland classes in the study area.

Another accuracy assessment performed in the Gros Morne case study was backward elimination of the least important features in a consecutive procedure to evaluate the effect of each individual feature on the overall accuracy. It was observed that the overall accuracies were degraded slightly by removing the first 58 least important features (Figure 4.9). Conversely, the overall accuracies significantly decreased when only the last five features remained.
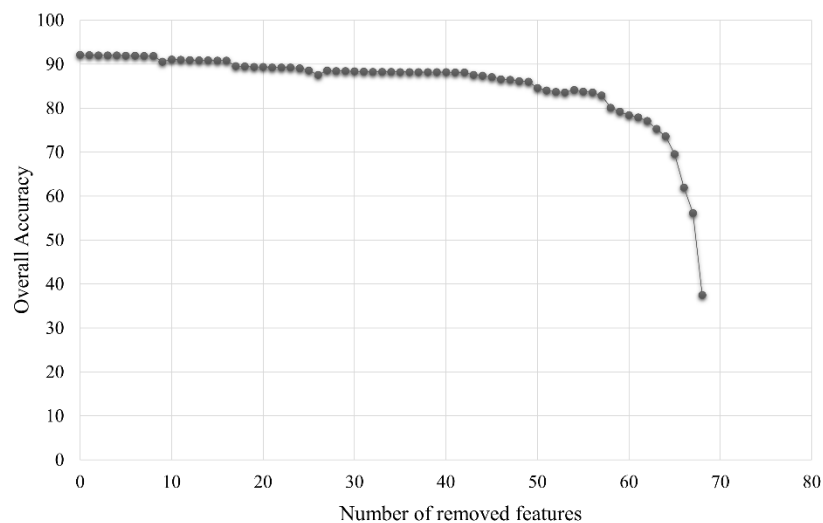
Figure 4.9. Overall classification accuracies based on the number of removed features for the Gros Morne case study.

4.5. Conclusion

Although the Newfoundland wetlands are home to a biologically diverse flora and fauna species, they have not been effectively investigated and monitored to date. Despite the large expanses of different wetland classes, including bog, fen, marsh, swamp, and the large number of diverse lakes, little effort has been carried out to preserve these valuable environmental resources. Therefore, there is an urgent need for (1) a detailed spatial distribution of different wetland classes; and (2) quantitative methods to map and monitor both the naturally and anthropogenic occurring changes in the area for an effective preservation and sustainable management of these productive ecosystems.

The results of this study provide these much needed fine resolution classification maps of the detailed spatial distribution of wetland classes as well as other land cover types for the three pilot sites in Newfoundland. In particular, we proposed a new PolSAR feature, the modified coherency matrix, and used multi-temporal RADARSAT-2 imagery for wetland mapping. We also evaluated the effect of using different combinations of polarimetric features, including well-known polarimetric decompositions, as well as the modified coherency matrix, on the classification accuracy. Specifically, the efficiency of the RF classifier was investigated in 24 different scenarios in single- versus multiple-date and pixel- versus object-based approaches. The results of this study also provide new perspectives into the importance of input variables for the flexible RF classifier.

Object-based classification was found to be better suited for differentiating wetland classes relative to the pixel-based classification. The inclusion of additional PolSAR data increased the overall classification accuracies in all three models when compared to the single-date classifications. It was observed, however, that objectification based on optical images was more influential on the accuracy of wetland classification than increasing the number of PolSAR images.

The main objective of this study was to investigate the efficiency of the modified coherency matrix, which has been established by an integration of Fisher Linear Discriminant analysis and physical interpretation of PolSAR data, in improving the wetland classification accuracy. Our results indicated that the modified coherency matrix in a multi-temporal, object-based framework outperformed all single polarimetric decompositions in different scenarios in terms of classification accuracy. This observation was significant, as it demonstrated the superior performance of the modified coherency matrix over all well-known polarimetric decompositions in terms of wetland classification accuracy. The variable importance analysis illustrated that FD-Vol, VZ-Vol, and MC-T_{33} were the most important features for wetland classification. The analysis of variable importance also revealed that the volumetric component of polarimetric decompositions provided more valuable information than either double- or odd-bounce scattering features in the wetland complex. These results fit well with the theory of scattering mechanism in wetland ecosystems, wherein the volume scattering is the dominant scattering mechanism in vegetation canopies [60]. However, this may not hold true for other classification applications (e.g., urban area classification). The various features from different scenarios all contributed to increase the classification accuracy. Some features contributed less (i.e., CP features), while independent features, such as the modified coherency matrix and volumetric components of the different decompositions, contributed more to improve the wetland classification accuracy. The results of this study confirmed that the synergism of the modified coherency matrix of PolSAR imagery and polarimetric decomposition features in a multi-temporal framework based on the object-based random forest classifier is very efficient for mapping NL wetland classes.

The fine spatial resolution maps produced in this study provide substantial information that will contribute to preserving the wildlife habitat of both terrestrial and aquatic species. Moreover, the

classified maps offer valuable baseline information for effectively understanding and monitoring climate and land cover changes resulting from wetland dynamics, while contributing to conservation plans for wetland habitats in NL.

4.6. References

[1]   J. Li and W. Chen, "A rule-based method for mapping Canada's wetlands using optical, radar and DEM data," *Int. J. Remote Sens.*, vol. 26, no. 22, pp. 5051–5069, 2005.

[2]   L. M. Cowardin, V. Carter, F. C. Golet, and E. T. LaRoe, "Classification of wetlands and deepwater habitats of the United States," US Department of the Interior, US Fish and Wildlife Service, 1979.

[3]   R. W. Tiner, M. W. Lang, and V. V Klemas, *Remote sensing of wetlands: applications and advances*. CRC Press, 2015.

[4]   M. P. F. Costa, T. S. F. Silva, and T. L. Evans, "Wetland classification," *Remote Sens. Nat. Resour. CRC Press. Boca Raton-FL*, pp. 461–478, 2013.

[5]   J. R. Anderson, *A land use and land cover classification system for use with remote sensor data*, vol. 964. US Government Printing Office, 1976.

[6]   I. Dronova, P. Gong, L. Wang, and L. Zhong, "Mapping dynamic cover types in a large seasonally flooded wetland using extended principal component analysis and object-based classification," *Remote Sens. Environ.*, vol. 158, pp. 193–206, 2015.

[7]   S. L. Ozesmi and M. E. Bauer, "Satellite remote sensing of wetlands," *Wetl. Ecol. Manag.*, vol. 10, no. 5, pp. 381–402, 2002.

[8]   J.-R. B. Bwangoy, M. C. Hansen, D. P. Roy, G. De Grandi, and C. O. Justice, "Wetland mapping in the Congo Basin using optical and radar remotely sensed data and derived topographical indices," *Remote Sens. Environ.*, vol. 114, no. 1, pp. 73–86, 2010.

[9]   S. Rapinel, L. Hubert-Moy, and B. Clément, "Combined use of LiDAR data and multispectral earth observation imagery for wetland habitat mapping," *Int. J. Appl. earth Obs. Geoinf.*, vol. 37, pp. 56–64, 2015.

[10]   M. Mahdianpari, B. Salehi, F. Mohammadimanesh, and M. Motagh, "Random forest wetland classification using ALOS-2 L-band, RADARSAT-2 C-band, and TerraSAR-X imagery," *ISPRS J. Photogramm. Remote Sens.*, vol. 130, 2017.

[11]   K. S. Schmidt and A. K. Skidmore, "Spectral discrimination of vegetation types in a coastal wetland," *Remote Sens. Environ.*, vol. 85, no. 1, pp. 92–108, 2003.

[12]   E. Adam, O. Mutanga, and D. Rugege, "Multispectral and hyperspectral remote sensing for identification and mapping of wetland vegetation: a review," *Wetl. Ecol. Manag.*, vol. 18, no. 3, pp. 281–296, 2010.

[13]   X. Li *et al.*, "A hybrid method combining pixel-based and object-oriented methods and its application in Hungary using Chinese HJ-1 satellite images," *Int. J. Remote Sens.*, vol. 34, no. 13, pp. 4655–4668, 2013.

[14]   E. S. Kasischke, K. B. Smith, L. L. Bourgeau-Chavez, E. A. Romanowicz, S. Brunzell, and C. J.

Richardson, "Effects of seasonal hydrologic patterns in south Florida wetlands on radar backscatter measured from ERS-2 SAR imagery," *Remote Sens. Environ.*, vol. 88, no. 4, pp. 423–441, 2003.

[15] K. O. Pope, J. M. Rey-Benayas, and J. F. Paris, "Radar remote sensing of forest and wetland ecosystems in the Central American tropics," *Remote Sens. Environ.*, vol. 48, no. 2, pp. 205–219, 1994.

[16] E. S. Kasischke, J. M. Melack, and M. C. Dobson, "The use of imaging radars for ecological applications—a review," *Remote Sens. Environ.*, vol. 59, no. 2, pp. 141–156, 1997.

[17] F. M. Grings *et al.*, "Monitoring flood condition in marshes using EM models and Envisat ASAR observations," *IEEE Trans. Geosci. Remote Sens.*, vol. 44, no. 4, pp. 936–942, 2006.

[18] T. Ullmann *et al.*, "Land cover characterization and classification of arctic tundra environments by means of polarized synthetic aperture X-and C-Band Radar (PolSAR) and Landsat 8 multispectral imagery—Richards Island, Canada," *Remote Sens.*, vol. 6, no. 9, pp. 8565–8593, 2014.

[19] X. Zhang, W. Dierking, J. Zhang, and J. Meng, "A polarimetric decomposition method for ice in the Bohai Sea using C-band PolSAR data," *IEEE J. Sel. Top. Appl. Earth Obs. Remote Sens.*, vol. 8, no. 1, pp. 47–66, 2015.

[20] T. L. Ainsworth, J. P. Kelly, and J.-S. Lee, "Classification comparisons between dual-pol, compact polarimetric and quad-pol SAR imagery," *ISPRS J. Photogramm. Remote Sens.*, vol. 64, no. 5, pp. 464–471, 2009.

[21] N. Morandeira, F. Grings, C. Facchinetti, and P. Kandus, "Mapping plant functional types in floodplain wetlands: An analysis of C-band polarimetric SAR data from RADARSAT-2," *Remote Sens.*, vol. 8, no. 3, p. 174, 2016.

[22] F. M. Henderson and A. J. Lewis, "Radar detection of wetland ecosystems: a review," *Int. J. Remote Sens.*, vol. 29, no. 20, pp. 5809–5835, 2008.

[23] B. Brisco, M. Kapfer, T. Hirose, B. Tedford, and J. Liu, "Evaluation of C-band polarization diversity and polarimetry for wetland mapping," *Can. J. Remote Sens.*, vol. 37, no. 1, pp. 82–92, 2011.

[24] J. Corcoran, J. Knight, and A. Gallant, "Influence of multi-source and multi-temporal remotely sensed and ancillary data on the accuracy of random forest classification of wetlands in Northern Minnesota," *Remote Sens.*, vol. 5, no. 7, pp. 3212–3238, 2013.

[25] S. van Beijma, A. Comber, and A. Lamb, "Random forest classification of salt marsh vegetation habitats using quad-polarimetric airborne SAR, elevation and optical RS data," *Remote Sens. Environ.*, vol. 149, pp. 118–129, 2014.

[26] L. F. de Almeida Furtado, T. S. F. Silva, and E. M. L. de Moraes Novo, "Dual-season and full-polarimetric C band SAR assessment for vegetation mapping in the Amazon várzea wetlands," *Remote Sens. Environ.*, vol. 174, pp. 212–222, 2016.

[27] Y. Yajima, Y. Yamaguchi, R. Sato, H. Yamada, and W.-M. Boerner, "POLSAR image analysis of

wetlands using a modified four-component scattering power decomposition," *IEEE Trans. Geosci. Remote Sens.*, vol. 46, no. 6, pp. 1667–1673, 2008.

[28]   U. C. Benz, P. Hofmann, G. Willhauck, I. Lingenfelder, and M. Heynen, "Multi-resolution, object-oriented fuzzy analysis of remote sensing data for GIS-ready information," *ISPRS J. Photogramm. Remote Sens.*, vol. 58, no. 3–4, pp. 239–258, 2004.

[29]   T. Blaschke, "Object based image analysis for remote sensing," *ISPRS J. Photogramm. Remote Sens.*, vol. 65, no. 1, pp. 2–16, 2010.

[30]   M. P. F. Costa and K. H. Telmer, "Utilizing SAR imagery and aquatic vegetation to map fresh and brackish lakes in the Brazilian Pantanal wetland," *Remote Sens. Environ.*, vol. 105, no. 3, pp. 204–213, 2006.

[31]   M. Mahdianpari, B. Salehi, and F. Mohammadimanesh, "The Effect of PolSAR Image De-speckling on Wetland Classification: Introducing a New Adaptive Method," *Can. J. Remote Sens.*, vol. 43, no. 5, 2017.

[32]   G. H. Ball and D. J. Hall, "ISODATA, a novel method of data analysis and pattern classification," Stanford research inst Menlo Park CA, 1965.

[33]   S. Lloyd, "Least squares quantization in PCM," *IEEE Trans. Inf. theory*, vol. 28, no. 2, pp. 129–137, 1982.

[34]   J. R. Jensen and K. Lulla, "Introductory digital image processing: a remote sensing perspective," 1987.

[35]   P. Kumar, D. K. Gupta, V. N. Mishra, and R. Prasad, "Comparison of support vector machine, artificial neural network, and spectral angle mapper algorithms for crop classification using LISS IV data," *Int. J. Remote Sens.*, vol. 36, no. 6, pp. 1604–1617, 2015.

[36]   S. R. Safavian and D. Landgrebe, "A survey of decision tree classifier methodology," *IEEE Trans. Syst. Man. Cybern.*, vol. 21, no. 3, pp. 660–674, 1991.

[37]   H. Liu, H. Guo, and L. Zhang, "SVM-based sea ice classification using textural features and concentration from RADARSAT-2 Dual-Pol ScanSAR data," *IEEE J. Sel. Top. Appl. Earth Obs. Remote Sens.*, vol. 8, no. 4, pp. 1601–1613, 2015.

[38]   C. Huang, L. S. Davis, and J. R. G. Townshend, "An assessment of support vector machines for land cover classification," *Int. J. Remote Sens.*, vol. 23, no. 4, pp. 725–749, 2002.

[39]   P. O. Gislason, J. A. Benediktsson, and J. R. Sveinsson, "Random forests for land cover classification," *Pattern Recognit. Lett.*, vol. 27, no. 4, pp. 294–300, 2006.

[40]   S. P. Healey *et al.*, "Mapping forest change using stacked generalization: An ensemble approach," *Remote Sens. Environ.*, vol. 204, pp. 717–728, 2018.

[41]   M. Mahdianpari, B. Salehi, F. Mohammadimanesh, and B. Brisco, "An Assessment of Simulated Compact Polarimetric SAR Data for Wetland Classification Using Random Forest Algorithm," *Can.*

J. Remote Sens., vol. 43, no. 5, 2017.

[42] L. Breiman, "Random forests," *Mach. Learn.*, vol. 45, no. 1, pp. 5–32, 2001.

[43] M. Belgiu and L. Drăguţ, "Random forest in remote sensing: A review of applications and future directions," *ISPRS J. Photogramm. Remote Sens.*, vol. 114, pp. 24–31, 2016.

[44] B. Ghimire, J. Rogan, and J. Miller, "Contextual land-cover classification: incorporating spatial dependence in land-cover classification models using random forests and the Getis statistic," *Remote Sens. Lett.*, vol. 1, no. 1, pp. 45–54, 2010.

[45] J. Gu, J. Yang, H. Zhang, Y. Peng, C. Wang, and H. Zhang, "Speckle filtering in polarimetric SAR data based on the subspace decomposition," *IEEE Trans. Geosci. Remote Sens.*, vol. 42, no. 8, pp. 1635–1641, 2004.

[46] B. G. Warner and C. D. A. Rubec, "The Canadian wetland classification system," *Wetl. Res. Centre, Univ. Waterloo, Waterloo, Ontario*, 1997.

[47] I. B. Marshall, C. A. S. Smith, and C. J. Selby, "A national framework for monitoring and reporting on environmental sustainability in Canada," in *Global to Local: Ecological Land Classification*, Springer, 1996, pp. 25–38.

[48] R. South, *Biogeography and Ecology of the Island of Newfoundland*, vol. 48. Springer Science & Business Media, 1983.

[49] W. J. Mitsch, "GOSSELINK. JG, 2000. Wetlands." John Wiley and Sons, Inc., New York, New York, USA.

[50] M. Krischke, W. Niemeyer, and S. Scherer, "RapidEye satellite based geo-information system," *Acta Astronaut.*, vol. 46, no. 2–6, pp. 307–312, 2000.

[51] A. Schmitt and B. Brisco, "Wetland monitoring using the curvelet-based change detection method on polarimetric SAR imagery," *Water*, vol. 5, no. 3, pp. 1036–1051, 2013.

[52] S. Banks *et al.*, "Contributions of Actual and Simulated Satellite SAR Data for Substrate Type Differentiation and Shoreline Mapping in the Canadian Arctic," *Remote Sens.*, vol. 9, no. 12, p. 1206, 2017.

[53] Y. Wang, T. L. Ainsworth, and J.-S. Lee, "Application of mixture regression for improved polarimetric SAR speckle filtering," *IEEE Trans. Geosci. Remote Sens.*, vol. 55, no. 1, pp. 453–467, 2017.

[54] L. M. Novak and M. C. Burl, "Optimal speckle reduction in polarimetric SAR imagery," *IEEE Trans. Aerosp. Electron. Syst.*, vol. 26, no. 2, pp. 293–305, 1990.

[55] J.-S. Lee, M. R. Grunes, and G. De Grandi, "Polarimetric SAR speckle filtering and its implication for classification," *IEEE Trans. Geosci. Remote Sens.*, vol. 37, no. 5, pp. 2363–2373, 1999.

[56] A. Lopes, E. Nezry, R. Touzi, and H. Laur, "Structure detection and statistical adaptive speckle

filtering in SAR images," *Int. J. Remote Sens.*, vol. 14, no. 9, pp. 1735–1758, 1993.

[57] J.-S. Lee, T. L. Ainsworth, Y. Wang, and K.-S. Chen, "Polarimetric SAR speckle filtering and the extended sigma filter," *IEEE Trans. Geosci. Remote Sens.*, vol. 53, no. 3, pp. 1150–1160, 2015.

[58] J.-S. Lee, J.-H. Wen, T. L. Ainsworth, K.-S. Chen, and A. J. Chen, "Improved sigma filter for speckle filtering of SAR imagery," *IEEE Trans. Geosci. Remote Sens.*, vol. 47, no. 1, pp. 202–213, 2009.

[59] A. Freeman and S. S. Saatchi, "On the detection of Faraday rotation in linearly polarized L-band SAR backscatter signatures," *IEEE Trans. Geosci. Remote Sens.*, vol. 42, no. 8, pp. 1607–1616, 2004.

[60] J.-S. Lee and E. Pottier, *Polarimetric radar imaging: from basics to applications*. CRC press, 2009.

[61] V. Alberga, G. Satalino, and D. K. Staykova, "Comparison of polarimetric SAR observables in terms of classification performance," *Int. J. Remote Sens.*, vol. 29, no. 14, pp. 4129–4150, 2008.

[62] H. McNairn, J. Shang, X. Jiao, and C. Champagne, "The contribution of ALOS PALSAR multipolarization and polarimetric data to crop classification," *IEEE Trans. Geosci. Remote Sens.*, vol. 47, no. 12, pp. 3981–3992, 2009.

[63] S. R. Cloude and E. Pottier, "An entropy based classification scheme for land applications of polarimetric SAR," *IEEE Trans. Geosci. Remote Sens.*, vol. 35, no. 1, pp. 68–78, 1997.

[64] A. Freeman and S. L. Durden, "A three-component scattering model for polarimetric SAR data," *IEEE Trans. Geosci. Remote Sens.*, vol. 36, no. 3, pp. 963–973, 1998.

[65] Y. Yamaguchi, T. Moriyama, M. Ishido, and H. Yamada, "Four-component scattering model for polarimetric SAR image decomposition," *IEEE Trans. Geosci. Remote Sens.*, vol. 43, no. 8, pp. 1699–1706, 2005.

[66] W. An, C. Xie, X. Yuan, Y. Cui, and J. Yang, "Four-component decomposition of polarimetric SAR images with deorientation," *IEEE Geosci. Remote Sens. Lett.*, vol. 8, no. 6, pp. 1090–1094, 2011.

[67] J. J. Van Zyl, M. Arii, and Y. Kim, "Model-based decomposition of polarimetric SAR covariance matrices constrained for nonnegative eigenvalues," *IEEE Trans. Geosci. Remote Sens.*, vol. 49, no. 9, pp. 3452–3459, 2011.

[68] J. J. van Zyl, "Application of Cloude's target decomposition theorem to polarimetric imaging radar data," in *Radar polarimetry*, 1993, vol. 1748, pp. 184–192.

[69] L.-K. Soh, C. Tsatsoulis, D. Gineris, and C. Bertoia, "ARKTOS: An intelligent system for SAR sea ice image classification," *IEEE Trans. Geosci. Remote Sens.*, vol. 42, no. 1, pp. 229–248, 2004.

[70] C. Liu and H. Wechsler, "Gabor feature based classification using the enhanced fisher linear discriminant model for face recognition," *IEEE Trans. Image Process.*, vol. 11, no. 4, pp. 467–476, 2002.

[71] A. Jain and J. Huang, "Integrating independent components and linear discriminant analysis for gender classification," in *Sixth IEEE International Conference on Automatic Face and Gesture Recognition, 2004. Proceedings.*, 2004, pp. 159–163.

[72] R. L. Kettig and D. A. Landgrebe, "Classification of multispectral image data by extraction and classification of homogeneous objects," *IEEE Trans. Geosci. Electron.*, vol. 14, no. 1, pp. 19–26, 1976.

[73] M. Baatz, "Multi resolution Segmentation: an optimum approach for high quality multi scale image segmentation," in *Beutrage zum AGIT-Symposium. Salzburg, Heidelberg, 2000*, 2000, pp. 12–23.

[74] D. C. Duro, S. E. Franklin, and M. G. Dubé, "A comparison of pixel-based and object-based image analysis with selected machine learning algorithms for the classification of agricultural landscapes using SPOT-5 HRG imagery," *Remote Sens. Environ.*, vol. 118, pp. 259–272, 2012.

[75] S. W. Myint, P. Gober, A. Brazel, S. Grossman-Clarke, and Q. Weng, "Per-pixel vs. object-based classification of urban land cover extraction using high spatial resolution imagery," *Remote Sens. Environ.*, vol. 115, no. 5, pp. 1145–1161, 2011.

[76] T. G. Dietterich, "An experimental comparison of three methods for constructing ensembles of decision trees: Bagging, boosting, and randomization," *Mach. Learn.*, vol. 40, no. 2, pp. 139–157, 2000.

[77] V. F. Rodriguez-Galiano, M. Chica-Olmo, F. Abarca-Hernandez, P. M. Atkinson, and C. Jeganathan, "Random Forest classification of Mediterranean land cover using multi-seasonal imagery and multi-seasonal texture," *Remote Sens. Environ.*, vol. 121, pp. 93–107, 2012.

[78] R. G. Congalton, "A review of assessing the accuracy of classifications of remotely sensed data," *Remote Sens. Environ.*, vol. 37, no. 1, pp. 35–46, 1991.

[79] T. S. F. Silva, M. P. F. Costa, and J. M. Melack, "Spatial and temporal variability of macrophyte cover and productivity in the eastern Amazon floodplain: A remote sensing approach," *Remote Sens. Environ.*, vol. 114, no. 9, pp. 1998–2010, 2010.

[80] J.-W. Kim, Z. Lu, J. W. Jones, C. K. Shum, H. Lee, and Y. Jia, "Monitoring Everglades freshwater marsh water level using L-band synthetic aperture radar backscatter," *Remote Sens. Environ.*, vol. 150, pp. 66–81, 2014.

[81] M. P. F. Costa, "Use of SAR satellites for mapping zonation of vegetation communities in the Amazon floodplain," *Int. J. Remote Sens.*, vol. 25, no. 10, pp. 1817–1835, 2004.

[82] K. Millard and M. Richardson, "Wetland mapping with LiDAR derivatives, SAR polarimetric decompositions, and LiDAR–SAR fusion using a random forest classifier," *Can. J. Remote Sens.*, vol. 39, no. 4, pp. 290–307, 2013.

[83] L. R. Sartori, N. N. Imai, J. C. Mura, E. M. L. de Moraes Novo, and T. S. F. Silva, "Mapping macrophyte species in the Amazon floodplain wetlands using fully polarimetric ALOS/PALSAR data," *IEEE Trans. Geosci. Remote Sens.*, vol. 49, no. 12, pp. 4717–4728, 2011.

[84]   A. Schmitt, A. Wendleder, and S. Hinz, "The Kennaugh element framework for multi-scale, multi-polarized, multi-temporal and multi-frequency SAR image preparation," *ISPRS J. Photogramm. Remote Sens.*, vol. 102, pp. 122–139, 2015.

[85]   N. Baghdadi, M. Bernier, R. Gauthier, and I. Neeson, "Evaluation of C-band SAR data for wetlands mapping," *Int. J. Remote Sens.*, vol. 22, no. 1, pp. 71–88, 2001.

[86]   L. L. Bourgeau-Chavez, K. Riordan, R. B. Powell, N. Miller, and M. Nowels, "Improving wetland characterization with multi-sensor, multi-temporal SAR and optical/infrared data fusion," in *Advances in geoscience and remote sensing*, InTech, 2009.

[87]   M. C. Dobson, L. E. Pierce, and F. T. Ulaby, "Knowledge-based land-cover classification using ERS-1/JERS-1 SAR composites," *IEEE Trans. Geosci. Remote Sens.*, vol. 34, no. 1, pp. 83–99, 1996.

[88]   T. L. Evans and M. Costa, "Landcover classification of the Lower Nhecolândia subregion of the Brazilian Pantanal Wetlands using ALOS/PALSAR, RADARSAT-2 and ENVISAT/ASAR imagery," *Remote Sens. Environ.*, vol. 128, pp. 118–137, 2013.

Chapter 5. Wetland classification using simulated compact Polarimetric SAR data[4]

Preface

A version of this manuscript has been published in the *Canadian Journal of Remote Sensing*. I am a primary author of this manuscript along with the co-authors, Bahram Salehi, Fariba Mohammadimanesh, and Brian Brisco. I designed and conceptualized the study and developed the model. I prepared the first draft of the manuscript and revised the manuscript several times according to editorial input and scientific insights from other co-authors. I also revised the manuscript two times based on the comments from the journal's reviewers. The co-author, Fariba Mohammadimanesh, assisted in reviewing and revising the manuscript. All co-authors reviewed and commented on the manuscript.

---

[4] Mahdianpari, M., Salehi, B., Mohammadimanesh, F. and Brisco, B., 2017. An assessment of simulated compact polarimetric SAR data for wetland classification using random forest algorithm. *Canadian Journal of Remote Sensing*, *43*(5), pp.468-484.

Abstract

Synthetic Aperture Radar (SAR) Compact Polarimetry (CP) systems are of great interest for large area monitoring because of their ability to acquire data in a wider swath compared to Full Polarimetry (FP) systems and a significant improvement in information compared to single or Dual Polarimetry (DP) sensors. In this study, we compared the potential of DP, FP, and CP SAR data for wetland classification in a case study located in Newfoundland, Canada. The DP and CP data were simulated using full polarimetric RADARSAT-2 data. We compared the classification results for different input features using an object-based Random Forest classification. The results demonstrated the superiority of FP imagery relative to both DP and CP data. However, CP indicated significant improvements in classification accuracy compared to DP data. An overall classification accuracy of approximately 76% and 84% was achieved with the inclusion of all polarimetric features extracted from CP and FP data, respectively. In summary, although full polarimetric SAR data provide the best classification accuracy, the results demonstrate the potential of RADARSAT Constellation Mission (RCM) for mapping wetlands in a large landscape.

Keywords: Wetland, Synthetic Aperture Radar (SAR), Compact Polarimetric (CP), Object-based classification, Random Forest (RF).

179

5.1. Introduction

Wetlands are areas that experience wet conditions at least periodically during the growing season or permanently in all seasons, often situated between dry land and a water body tiner [1]. Wetlands play a vital role by providing several ecosystem services, including flood control, water balance, as well as food and shelter for a variety of animal and plant species. Despite these benefits, wetlands are poorly understood and maintained globally. For example, although 24% of the world's wetlands are within Canada's borders, an all-inclusive wetland inventory map is lacking in most provinces [2]. Remote sensing, as a time and cost efficient tool, provides unique techniques for wetland mapping and monitoring.

Synthetic Aperture Radar (SAR) sensors are all-weather condition systems and operate independently of solar radiation. Furthermore, SAR penetration depths through cloud, soil, and vegetation make it an ideal tool for land cover mapping [3]. They are considered as a promising alternative to optical sensors, which are less-useful for areas with nearly permanent cloud cover [4]. However, SAR data alone provide less accurate classification results because most wetland classes, especially herbaceous vegetation, have very subtle structural differences not obtainable using only a single SAR channel [5], [6]. Alternatively, Full Polarimetric (FP) SAR imagery has been demonstrated to be useful for several wetland applications, including wetland classification [7]–[11], change detection [12], and water level monitoring [13].

A FP SAR image contains complete scattering information for each resolution cell since a FP SAR sensor acquires data in four channels (HH, VV, HV, and VH) and, also, measures the relative phase between channels. This additional phase information is of great importance for decomposing the SAR backscatter into different scattering types (i.e., surface, double-bounce, and volume scattering), which is useful to distinguish different wetland and land cover classes [15]. Thus, a FP

SAR sensor is constructed based on the standard linear basis (i.e., horizontal (H) and vertical (V)), wherein the sensor interleaves pulses with H and V polarization toward the ground targets and records both received polarizations simultaneously and coherently [16]. As such, the first disadvantage of FP is a time constraint, since two orthogonal polarizations should be transmitted alternately. Furthermore, such a configuration implies complexity due to doubled pulse repetition frequency (PRF), as well as an increase in the data rate by a factor of four compared to a single polarized SAR system [17]. Accordingly, the image swath width of FP SAR images is halved, which results in reduced coverage and an increase in satellite revisit time [16]. Finally, this configuration allows a limited range of incident angles compared to that of single/dual polarization modes [18].

A possible alternative that has addressed some of the limitations of FP SAR imagery, including a reduction of pulse repetition frequency, data volume, and system power is a Dual Polarimetric (DP) SAR configuration. A DP SAR sensor transmits one polarization (either H or V) and receives both H and V polarizations (i.e., HH/HV or VV/VH). This is the typical configuration of several currently operating SAR satellites such as TerraSAR-X. A DP SAR sensor has the same coverage as that of single polarization SAR sensor, while obtains additional information since there are two independent polarization channels on the receiver [16]. However, a DP SAR system is unable to collect full scattering information of the observed scenes relative to FP SAR sensors. Given the reflection symmetry hypothesis, the co- and cross-polarization channels are uncorrelated; therefore, the relative phase between the co- and cross-polarization channels is not available [14], [19]. This drawback has limited the application of DP SAR images in several remote sensing contexts, such as wetland classification [14].

An attractive alternative, which addresses most of the limitations associated with FP and DP SAR mode data, is a Compact Polarimetry (CP) SAR configuration. The CP SAR image is expected to preserve polarimetric information as close as possible to that of FP SAR mode imagery while mitigating the primary limitations of the FP configuration. The CP SAR configuration is similar to DP SAR sensor, wherein one polarization is transmitted and two coherent polarizations are received. Three CP configurations have been proposed in the context of Earth Observation sensors in the literature to date, namely: (1) $\pi/4$; (2) Circularly transmitted Circularly received (CC); and (3) Hybrid Polarimetry (HP) [18]. Souyris et al. (2005) first introduced the $\pi/4$ compact polarimetry mode (H+V), wherein the transmitted polarization is the superposition of linear horizontal and vertical polarization (i.e., at $\pi/4$ degree relative to H or V polarization) and two coherent polarizations (H and V) are received [20]. Given the symmetry properties, the $\pi/4$ SAR configuration has been demonstrated to maintain polarimetric information over natural targets [16]. However, the $\pi/4$ compact SAR configuration does not guarantee orientation invariance for double-bounce scattering [18], [21]. In order to address this issue, a circular polarization should be transmitted, wherein a backscattered field is rotationally robust in relation to the shape of the observed scene [18].

The second typical CP mode is dual-circular polarization (CC) mode, wherein the SAR sensor transmits either a right or left circular polarization (i.e., $H \pm iV$, where i illustrates the complex identity and + and − denote left and right circular polarizations, respectively) and receives both right and left circular polarizations [22]. However, the CC configuration cannot be easily implemented, which is the main drawback of this configuration.

Raney (2007) proposed a third CP configuration, called Hybrid Polarimetry (HP) mode, wherein either a right or left circular polarization is transmitted and both linear polarizations (H and V) are

received, while the relative phase is also retained. This configuration is also called CTLR mode (i.e., Circular Transmitting Linear Receiving) in the literature [21]. The CTLR configuration shares the same advantages as the CC mode but is easier to implement. This is because both CTLR and CC configurations have the same transmitting polarization (circular) and the polarimetric covariance matrix information only depends on the polarization basis of the transmitter. Thus, a circularly transmitted SAR configuration (either left or right) has the same covariance matrix as that of CC mode [18].

All three CP modes are advantageous because they collect a greater amount of scattering information compared to single- and dual-polarization modes while covering twice the swath-width of full polarization SAR systems [23]. Thus, CP SAR configurations reduce the complexity, cost, mass, and data rate of a SAR system, while preserving several advantages of a full polarimetric SAR system [17]. A detailed overview of the applications of CP SAR data with examples of ship detection, sea ice, and crop classification was presented in [24]. The potential of simulated CP images for wetland monitoring [25], [26], sea ice classification [27], crop identification [20], [28], vegetation characterization [29], and maritime applications [19] have been also examined. These studies have outlined the benefits and limitations of the CP SAR data.

The efficiency of the CP configuration has been previously examined in the field of radar astronomy [30], [31], as well as in the Arecibo antenna for imaging the moon's surface [32], wherein the CC mode has been utilized. In the Earth Observation SAR systems, the CP configuration has been (and will be) implemented in a number of SAR systems. Particularly, the Indian Mission Radar Imaging Satellite (RISAT-1) C-band, which was launched in 2012, utilizes the CTLR mode. Advanced Land Observing Satellite (ALOS-2) PALSAR L-band, which was launched in 2014, utilizes both the CTLR and $\pi/4$ compact polarimetry modes. Finally, the future

RADARSAT Constellation Mission (RCM) will operate in the CTLR mode [33]. Specifically, RCM will contain three similar C-band SAR satellites, which are anticipated to be launched simultaneously in 2018 providing a daily coverage over Canada with 350 km imaging swaths [34]. This will offer improved operational capability (e.g., ecosystem monitoring) along with a much shorter satellite revisit cycle, which is of great importance for monitoring highly variable phenomena such as wetlands ecosystem relative to RADARSAT-1 and RADARSAT-2 data [34]. Furthermore, CTLR compact polarimetry mode is the primary polarization option, which will be implemented for all RCM imaging modes [15].

In this study, the Random Forest (RF) [35] algorithm, in an object-based classification scheme [36], was applied to evaluate and compare the potential of DP, CP, and FP SAR images for wetland classification. One of the important characteristics of RF is that it provides a measure of variable importance. In this study, RF variable importance is represented by the mean decrease in accuracy by removing variables from the RF model for input variables extracted from CP SAR data. A higher value for a particular variable indicates that it is a more important parameter for classification. Furthermore, the less important variables may be removed from the RF model, which results in a decrease in processing time and possibly an improvement in model accuracy [15].

Given the need for utilization of the CP data by RCM in the future and Canada's wetland expanses, an assessment of the ability of CTLR SAR data for wetland classification is herein conducted using data simulated by RCM Compact Polarimetry Simulator developed by [24]. Thus, the primarily goal of this research study is to evaluate the trade-off in classification accuracy as a function of polarization diversity and swath width for future RCM SAR system within a wetland classification scheme. In particular, a series of main objectives were defined as follows: (1) determining the

184

sufficiency of detailed scattering power for complex land cover classification provided by the CP data; (2) comparing the classification overall accuracy using different Polarimetric SAR data, including DP, FP, and CP SAR data using an advanced object-based classification scheme; (3) evaluating the influence of incorporating correlated input features into RF as firstly investigated by [37]. Thus, this study provides an insight into applicability of CP SAR data, which is of great value for Canadian wetland classification as well as other wetlands worldwide with similar ecological features and vegetation types.

In the next section, we introduce the methodology employed in this study, including the theoretical background, case study, data, and classification scheme. Next, we present the experimental results and discussion, which is followed by a summary and conclusions.

5.2. Methodology

5.2.1. Theoretical background

5.2.1.1. Dual and full polarimetry

In dual polarization (DP) SAR configuration, one polarization, either H or V, is transmitted and both coherent H and V polarizations are received simultaneously. The main limitation of DP SAR mode data is that they are not subjectable to conventional polarimetric decompositions; therefore DP SAR data are usually analyzed in the form of covariance matrices. In the full polarization SAR imaging mode, both vertically- and horizontally-polarized coherent signals are transmitted and received, thus generating four independent images. A commonly used mathematical representation of scattering information for full polarization is a 3x3 covariance matrix. Unlike dual polarization, polarimetric decompositions can be applied to FP SAR data, making it advantageous. The main purpose of polarimetric decomposition is to characterize the backscatter of distributed targets using

incoherent target decompositions [12]. The Cloude-Pottier, Freeman-Durden, and Yamaguchi decompositions are commonly used PolSAR features for land cover classification [38].

The Cloude-Pottier is an eigenvalue/eigenvector-based decomposition, wherein eigenvectors characterize the scattering mechanism and eigenvalues determine the strength of the scattering mechanism. The Cloude-Pottier method decomposes the coherency matrix into three physically meaningful parameters, derived from its eigenvectors and eigenvalues. These parameters are entropy (H), anisotropy (A), and alpha angle (α). Entropy represents the degree of randomness and is utilized to determine if one or more scattering mechanisms are presented in the pixel. For example, lower entropy corresponds to a dominant single scattering mechanism. Anisotropy is a complementary to entropy and illustrates the relative importance of the secondary scattering mechanism. The alpha angle, which is invariant with rotation around the radar line of sight, varies between 0º and 90º and identifies the type of scattering mechanism. The Cloude-Pottier decomposition is usually applied as an initial, unsupervised classification in order to decompose the information of the distributed target into the scattering mechanism of deterministic targets.

The Freeman-Durden is a physical-based, three-components scattering decomposition that characterizes the scattering information from naturally incoherent scatterers [39]. In particular, it decomposes the backscatter responses of the natural ground targets into three different components, including surface scattering, which is described as the first order Bragg scattering, double-bounce scattering, which is modeled by the scattering from a dihedral corner reflector, and volume scattering, which is defined as canopy scattering [40].

The Yamaguchi decomposition is a physical-based, four-components decomposition and an extended version of the Freeman-Durden decomposition, wherein a helix scattering component is

added to the three components of the Freeman-Durden to separate the co-pol and the cross-pol correlations [41]. In particular, the Freeman-Durden decomposition is based on the reflection symmetry condition, while the helix term in the Yamaguchi decomposition is defined for the non-reflection symmetry cases. The helix term is generally used for scattering information of complex urban areas and is less useful for a naturally distributed target. Furthermore, a different probability distribution function is defined for the volume scattering component, which has better performance in forested areas. Overall, the Yamaguchi decomposition is suitable for both natural and man-made areas [42] and its components were used in this study.

5.2.1.2. Compact Polarimetry

The scattering vector of CTLR mode is given by:

$$\vec{k}_{CTLR} = \frac{1}{\sqrt{2}}[S_{RH} \quad S_{RV}]^T \tag{5.1}$$

where, during the simulation procedure, $S_{RH} = S_{HH} - iS_{HV}$ and $S_{RV} = -iS_{VV} + S_{VH}$ are defined using elements of FP scattering vector [21]. By assuming the reciprocity condition, a 2x2 covariance matrix is calculated by:

$$\boldsymbol{C}_{CTLR} = 2\langle \vec{k}_{CTLR} \vec{k}_{CTLR}^* \rangle \tag{5.2}$$

where * denotes the transpose conjugate [27]. Thus, the covariance matrix is expressed as follows:

$$\boldsymbol{C}_{CTLR} = \frac{1}{2}\begin{bmatrix} |S_{HH}|^2 & i(S_{HH} \cdot S^*_{VV}) \\ -i(S_{VV} \cdot S^*_{HH}) & |S_{VV}|^2 \end{bmatrix} + \frac{1}{2}\begin{bmatrix} |S_{HV}|^2 & -i|S_{HV}|^2 \\ i|S_{HV}|^2 & |S_{HV}|^2 \end{bmatrix} \\ + \frac{1}{2}\begin{bmatrix} -2\Im(S_{HH} \cdot S^*_{HV}) & (S_{HH} \cdot S^*_{HV}) + (S^*_{VV} \cdot S_{HV}) \\ (S^*_{HH} \cdot S_{HV}) + (S_{VV} \cdot S^*_{HV}) & 2\Im(S_{VV} \cdot S^*_{HV}) \end{bmatrix} \tag{5.3}$$

As seen in Equation 5.3, the CTLR covariance matrix is expressed as a sum of three components. The first component has S_{HH} and S_{VV} elements (co-pol), the second component has only the S_{HV} element (cross-pol), while the third component consists of co-pol/cross-pol correlations. Given the reflection symmetry assumption, the co-pol/cross-pol correlations is zero (i.e., $\langle S_{HH}S^*_{HV}\rangle =$

$\langle S_{VV}S_{HV}^* \rangle = 0$). In general, this assumption is true for natural scatterers at different frequencies. The simulated CP data was stored in the Stokes vector form, which characterizes the received scatter wave. The Stokes vector was then utilized to extract the Stokes "child" parameters, including the degree of polarization (m), circular polarization ratio (μ_c), and ellipticity [14]. In addition to CP covariance matrix, a number of decomposition features were also extracted directly from CP SAR mode data in this study and are presented in Table 5.1.

Table 5.1. Polarimetric features extracted from simulated Compact Polarimetry SAR data.

Feature	Description	Symbol	References
Intensity channel	Sigma naught backscatter	$\sigma_{RH}^0, \sigma_{RV}^0, \sigma_{RR}^0, \sigma_{RL}^0$	Charbonneau et al., 2010
Covariance matrix	Covariance matrix elements	C_{11}, C_{12}, C_{22}	Lee and Pottier, 2009
Stokes vector	Stokes vector elements	g_0, g_1, g_2, g_3	Raney et al., 2012
Wave descriptors	Correlation Coefficient of RV and RH	ρ	Charbonneau et al., 2010
	Conformity	μ	Charbonneau et al., 2010
	Relative phase	δ	Charbonneau et al., 2010
	Degree of polarization	m	Raney et al., 2012
	Shannon Entropy Intensity	SE_I	Charbonneau et al., 2010
	Shannon Entropy Polarimetric	SE_P	Charbonneau et al., 2010
	Circular polarization ratio	μ_c	Charbonneau et al., 2010
	Ellipticity of the compact scattered wave	α_s	Cloude et al., 2012
CP decompositions	Surface scattering based on m-delta	m_δ_s	Raney, 2007
	Double bounce scattering based on m-delta	m_δ_db	
	Volume scattering based on m-delta	m_δ_v	
	Odd scattering based on m-chi	m_χ_o	Raney et al., 2012
	Even bounce scattering based on m-chi	m_χ_e	
	Volume scattering based on m-chi	m_χ_v	

Three decomposition approaches that can directly be applied to the CTLR SAR data are $m\text{-}delta$ [21], $m\text{-}chi$ [43], and $m\text{-}alpha$ [44]. In particular, m denotes the degree of polarization, $delta\ (\delta)$ indicates the relative phase between H and V channels, $chi\ (\chi)$ demonstrates the degree of circularity, and $alpha$ denotes the scattering mechanism parameters. Features extracted from m-

delta and *m-chi* decompositions are comparable to those of the Freeman-Durden [24] and Cloude-Pottier decomposition [43], respectively. In particular, these decompositions discriminate backscatter waves into single-bounce scattering, double-bounce scattering, and volume scattering. Cloude et al. (2012) have demonstrated that the alpha parameter can be estimated when there is a dominant eigenvector in the coherency matrix [44]. Thus, the *m-alpha* decomposition is similar to that of Cloude-Pottier decomposition extracted from FP SAR data, which is applicable under specific conditions.

The correlation coefficient is characterized as a measure of the width of the probability density function (PDF) of the Co-polarized Phase Difference (CPD) [19]. The degree of polarization was first utilized in CTLR SAR mode data by Shirvaney et al. (2012) to detect oil spills and man-made objects. Also, the conformity index is Faraday Rotation (FR) independent [45] and is useful for distinguishing different land surface scattering mechanisms [19]. A FR is a rotation of the polarization wave that propagates through the ionosphere. This rotation occurs because of the anisotropy in the ionosphere due to charged particles in the presence of a magnetic field. This index can be used as an indicator of the dominant scattering mechanism (surface, double-bounce, and volume scattering) [45].

5.2.2. Case study

Newfoundland and Labrador has a vast expanse of wetlands and each part of the province is characterized by specific regional ecological factors, such as climate, soil, water, vegetation, fauna, and land use [46]. According to the Canadian wetland classification system, all wetland classes, including bog, fen, marsh, swamp, and shallow-water are present in this province [2]. Wetland ecosystems in Newfoundland are primarily natural and undisturbed by human interferences, although have been little studied or understood to date. This study was carried out within a 700

189

km2 site located in the northeast portion of the Avalon Peninsula, NL, Canada (Figure 5.1). The

Avalon area has an oceanic climate, characterized by cool, foggy summers and mild winters [47].
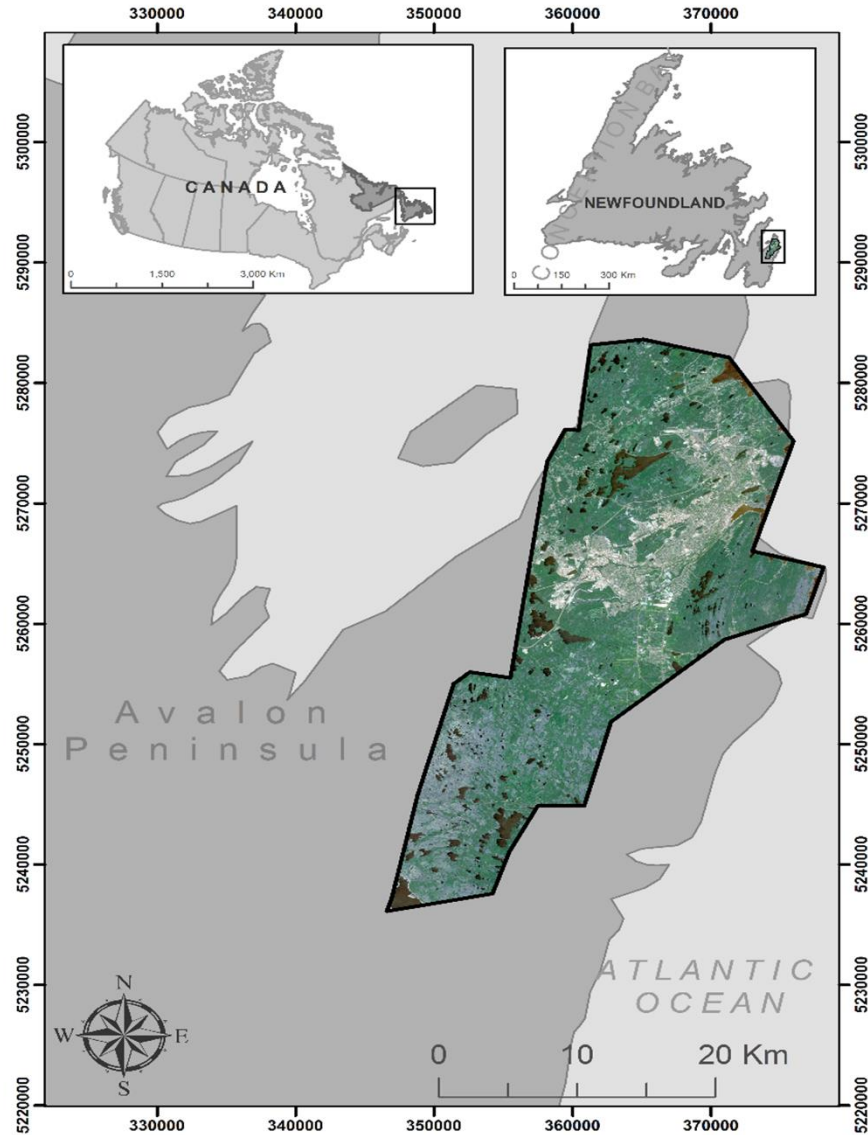
Figure 5.1. RapidEye image, acquired on June 2015, displaying the location of the study area: Avalon

Peninsula, Newfoundland and Labrador, Canada.

5.2.3. Reference data

In-situ data were collected in the summer and fall of 2015 and 2016 to both train the RF classifier

and evaluate the accuracy of the classified maps. A total of 191 sample sites were visited over

multiple times during the leaf-on season and categorized as bog, fen, swamp, marsh, or shallow-water, as directed by the Canadian Wetland Classification System. During in situ data collection, one or, up to three GPS points were taken per wetland site, depending on the size of each wetland, and stored, along with ancillary data such as notes describing dominant vegetation and hydrology, and photographs, to aid the wetland boundary delineation process. Next, the GPS points were imported to ArcMap 10.3.1 to depict visited wetlands and extract the wetland boundary. Using satellite and aerial imagery, including 5m resolution RapidEye imagery and a 50cm resolution orthophotograph, polygons indicating delineated classified wetlands were generated. For each class, reference polygons were sorted by size and alternatingly assigned to training and testing groups. We did not randomly assign the polygons to testing and training groups because of the limited amount of reference data. The alternative assignment procedure resulted in both groups having comparable pixel counts for each class and no overlap between training and testing groups ensured a robust accuracy assessment. Specifically, 50% of the reference data were considered for training the classifier and the other half was used for testing the classification performance.

Table 5.2 represents land cover classes and their respective pixel counts. As seen, the bog class has the most associated pixels of the wetland classes due both to the natural formation and ecology [47] as well as the province climate, which facilitates extensive peatland formation [48]. In contrast, the swamp class has the least amount of pixels. The wetland accessibility by roadways, the natural ecology and distribution of wetland classes, and availability of biologists for field work affected the collection of in situ data for different wetland classes. Therefore, there is a variation in both quantity and quality of data for each individual class (see Table 5.2). Notably, the initial goal of the fieldwork component was to obtain a minimum mapping unit of one hectare. However, many of the accessible wetlands of a certain class were frequently smaller size. For example, of

the 191 polygons collected in the Avalon pilot site, 30 of those were swamp wetlands, of which

only 7 were greater than 1 hectare in size. Likewise, of the 46 marsh wetlands, only 18 were greater

than 1 hectare. These spatially small wetlands were also included in the study because, without

them, these wetland classes would be demonstrated by a limited amount of data.

Table 5.2. Testing and training pixel counts for Avalon reference data.

Class	Class Description	#Training Pixels	#Testing Pixels	Total
Bog	Peatland dominated by *Spahgnum* species	20401	21466	41867
Fen	Peatland dominated by graminoid species	10972	9346	20318
Swamp	Mineral wetland dominated by woody vegetation	2517	1480	3997
Marsh	Mineral wetland dominated by graminoids and emergent plants	9263	7012	16275
Shallow-water	Mineral wetland with standing water at most 2m deep	2418	1645	4063
Urban	Human-made structures	19881	18211	38092
Deep-water	Deep water areas	32609	35490	68099
Upland	Forested dry upland	22356	23562	45918
Total		120417	118212	238629

5.2.4. Satellite Data

RADARSAT-2 images were acquired in Fine beam Quad (FQ) polarization mode. This imagery

is characterized by a small swath width and thus, more than one image was needed to cover the

entire Avalon pilot site. The images with approximately 4.7m range and 4.8m azimuth resolution

were acquired in a descending orbit on August 21, 2015 (ice-off season). This implied that both

the satellite imagery and field data were synchronized in this study.

The Canada Centre for Remote Sensing RCM Compact Polarimetry Simulator was utilized to simulate the CP and DP SAR data at their respective resolutions and noise floors [24]. Specifically, the full polarimetric RADARSAT-2 images were applied to simulate the high resolution 5 m CP mode with the -19 dB NESZ using a 7x7 pixel processing window.

5.2.5. Image Classification and Accuracy Assessment

The object-based classification was selected due to several advantages compared to the pixel-based approach. Particularly, an object-based approach incorporates the shape, size, and the spatial relationship of image objects into the classification procedure [3]. Also, it easily fuses multiple sources of data, regardless of the spatial and spectral resolution of different satellite imagery. The object-based classification procedure applied in this study has two main steps: Multi Resolution Segmentation (MRS) and Random Forest (RF) image classification.

MRS analysis is a region-merging process with the main objective of minimizing the summed heterogeneity between neighboring pixels [36]. MRS is usually controlled by three user-defined parameters, including shape, compactness, and scale [4]. More specifically, the shape and compactness parameters both range from 0 to 1, although the former determines both the degree of radiometric homogeneity and object shapes while the latter determines the degree of object smoothing. The scale parameter is the most important parameter in MRS analysis indicating the maximum acceptable heterogeneity and determines the size of the final image object [49]. These parameters, which are obtainable using a "trial and error" procedure, vary depending on the classification purpose and have great influence on the final classification results. In this study, 0.1, 0.5, and 300 were obtained as the final parameters for shape, compactness, and scale, respectively.

Random Forest (RF) is one of the most powerful non-parametric classifiers for classification of heterogeneous areas, such as crop types and wetlands [6], [9], [10], [37], [50]. In this study, RF was selected for three reasons. First, it is less affected by outliers and noisy data sets, which is of great importance for SAR image processing, wherein the radiometric quality of images has been degraded by speckle [51]. Second, RF is capable of dealing with several input features, while not being over-fitted to the dataset. This is also demanded in this study, given several PolSAR and CP features, which were extracted and incorporated into the classification procedure. Finally, the most significant aspect of RF is that it determines the importance of each input variable. For this purpose, RF measures the degradation in the classification accuracy by randomly altering one of the input features while keeping the rest of input features constant [50]. Thus, the importance of each CP feature in the overall classification accuracy can be determined using the RF classifier. Table 5.3 represents the defined scenarios for wetland classification for FP and CP SAR data.

Table 5.3. The defined scenarios for FP and CP SAR data in this study.

Data	Scenario	Features
Full polarimetric SAR	S1	Covariance matrix
	S2	Cloude-Pottier decomposition
	S3	Freeman-Durden decomposition
	S4	Yamaguchi decomposition
	S5	Covariance matrix, Cloude-Pottier, Freeman-Durden, and Yamaguchi decompositions
Compact polarimetric SAR	S1	Covariance matrix
	S2	Stokes vector
	S3	m-delta decomposition
	S4	m-chi decomposition
	S5	Intensity channel, Stokes vector, Wave descriptors, CP decompositions

The eCognition software package (V.9.0.3) was used for object-based RF classification. A total number of 500 trees (*Ntree*) were selected in each classification model and the square root of the number of input variables was selected for the number of variables (*Mtry*). The same training and testing points were applied to all RF models to allow for direct comparison between different models using varying input variables. Milard and Richardson (2015) reported that despite RF ability to handle high dimensional input variables, the classification accuracy remained constant by only applying the most important variables [37]. Thus, we evaluated the effect of using only important variables into the RF model for variables extracted from simulated CP data. For this purpose, RF classification was carried out 30 times for input variables extracted from simulated CP data (S5 in Table 5.3) and the variable ranking was recorded (see Table 5.4).

Table 5.4. The number of times each variable was determined to be among the top five most important variables for 30 classification models using the same input variables and training data.

Features	Removed Features	# Most Important	# 2nd Most Important	# 3rd Most Important	# 4th Most Important	# 5 Most Important
g0		27	3	0	0	0
m-delta-v		2	18	1	7	1
RR		1	2	14	3	2
m-chi-v	✓	0	6	7	11	5
RL		0	1	2	5	10
m-delta-s	✓	0	0	0	0	3
RH	✓	0	0	1	1	1
RV	✓	0	0	1	0	3
g3		0	0	1	2	1
SE i		0	0	0	1	1
m-chi-o	✓	0	0	0	0	2
m-chi-e	✓	0	0	2	0	0
SE p		0	0	0	0	1
m-delta-db	✓	0	0	1	0	0

The correlation between pair-wise input variables was also determined using Spearman's rank-order correlation [52] (see Table 5.5). As seen, a number of most important variables exhibited a high correlation. As reported by Millard and Richardson (2015), the classification accuracy was unaffected and, also, could be increased in some cases when only uncorrelated important variables were incorporated into the RF classification scheme [37]. This also resulted in a more time efficient and stable classification relative to applying all input variables into the classification model. Thus, two additional classifications were employed using only important variables (number of variables = 14) and uncorrelated important variables (number of variables = 7) extracted from simulated CP data.

Table 5.5. The correlation between pair-wise variables determined by Spearmans rank-order correlation.

	f1	f2	f3	f4	f5	f6	f7	f8	f9	f10	f11	f12	f13	f14	f15	f16	f17	f18	f19	f20	f21	f22
f1		0.14	0.02	0.14	0.24	0.07	0.05	**0.93**	**0.92**	0.79	0.84	0.10	-0.07	0.73	0.60	0.77	0.69	0.60	0.76	0.03	0.55	-0.09
f2	0.14		-0.01	-0.08	0.07	-0.01	0.03	0.48	-0.26	0.17	0.06	0.08	-0.08	0.17	0.09	0.04	0.20	0.09	0.02	0.01	0.11	-0.12
f3	0.02	-0.01		-0.12	0.01	0.01	0.11	0.01	0.02	0.09	-0.05	0.01	-0.01	0.10	-0.01	-0.06	0.11	-0.01	-0.06	0.01	0.02	-0.01
f4	0.14	-0.08	-0.12		-0.49	0.28	-0.21	0.09	0.17	-0.50	0.65	-0.31	0.37	-0.55	-0.07	0.72	-0.57	-0.07	0.72	0.27	0.22	0.25
f5	0.24	0.07	0.01	-0.49		-0.40	0.44	0.23	0.21	0.51	-0.08	0.64	-0.66	0.50	0.28	-0.15	0.50	0.27	-0.16	-0.42	0.10	-0.42
f6	0.07	-0.01	0.01	0.28	-0.40		-0.26	0.06	0.07	-0.11	-0.20	-0.59	0.81	-0.01	-0.45	-0.32	-0.01	-0.45	-0.31	**0.92**	0.14	0.66
f7	0.05	0.03	0.11	-0.21	0.44	-0.26		0.05	0.03	0.17	-0.08	0.62	-0.52	0.14	0.17	-0.12	0.16	0.17	-0.14	-0.30	-0.04	-0.28
f8	**0.93**	0.48	0.01	0.09	0.23	0.06	0.05		0.72	0.76	0.77	0.12	-0.08	0.70	0.56	0.70	0.68	0.56	0.67	0.01	0.53	-0.12
f9	**0.92**	-0.26	0.02	0.17	0.21	0.07	0.03	0.72		0.70	0.80	0.07	-0.03	0.64	0.54	0.73	0.59	0.54	0.73	0.05	0.49	-0.03
f10	0.79	0.17	0.09	-0.50	0.51	-0.11	0.17	0.76	0.70		0.33	0.28	-0.29	**0.97**	0.56	0.23	**0.96**	0.56	0.21	-0.14	0.34	-0.23
f11	0.84	0.06	-0.05	0.65	-0.08	-0.20	-0.08	0.77	0.80	0.33		-0.09	0.15	0.25	0.42	**0.98**	0.21	0.42	**0.97**	0.17	0.55	0.07
f12	0.10	0.08	0.01	-0.31	0.64	-0.59	0.62	0.12	0.07	0.28	-0.09		-0.89	0.21	0.40	-0.19	0.20	0.40	-0.19	-0.67	0.16	-0.76
f13	-0.07	-0.08	-0.01	0.37	-0.66	0.81	-0.52	-0.09	-0.03	-0.29	0.15	-0.89		-0.20	-0.47	0.27	-0.20	-0.47	0.26	0.84	0.06	0.85
f14	0.73	0.17	0.10	-0.55	0.50	-0.01	0.14	0.70	0.64	**0.97**	0.25	0.21	-0.20		0.36	0.20	**0.99**	0.36	0.18	-0.04	0.23	-0.15
f15	0.60	0.09	-0.01	-0.07	0.28	-0.45	0.17	0.56	0.54	0.56	0.42	0.40	-0.47	0.36		0.22	0.33	**0.99**	0.23	-0.44	0.57	-0.43

197

	f1	f2	f3	f4	f5	f6	f7	f8	f9	f10	f11	f12	f13	f14	f15	f16	f17	f18	f19	f20	f21	f22
f16	0.77	0.04	-0.06	0.72	-0.15	-0.32	-0.12	0.70	0.73	0.23	**0.98**	-0.19	0.27	0.20	0.22		0.15	0.22	**0.99**	0.28	0.46	0.18
f17	0.69	0.20	0.11	-0.57	0.50	-0.01	0.16	0.68	0.59	**0.96**	0.21	0.20	-0.20	**0.99**	0.33	0.15		0.33	0.11	-0.03	0.21	-0.13
f18	0.60	0.09	-0.01	-0.07	0.28	-0.45	0.17	0.56	0.54	0.56	0.42	0.40	0.47	0.36	**0.99**	0.22	0.33		0.23	-0.44	0.57	-0.43
f19	0.76	0.02	-0.06	0.72	-0.16	-0.31	-0.14	0.67	0.73	0.21	**0.97**	-0.19	0.26	0.18	0.23	**0.99**	0.11	0.23		0.26	0.45	0.16
f20	0.03	0.01	0.01	0.27	-0.42	**0.92**	-0.30	0.01	0.05	-0.14	0.17	-0.67	0.84	-0.04	-0.44	0.28	-0.03	-0.44	0.26		0.07	0.74
f21	0.55	0.11	0.02	0.22	0.10	0.14	-0.04	0.53	0.49	0.34	0.55	0.16	0.06	0.23	0.57	0.46	0.21	0.57	0.45	0.07		-0.13
f22	-0.09	-.012	-0.01	0.25	-0.42	0.66	-0.28	-0.12	-0.03	-0.23	0.07	-0.76	0.85	-0.15	-0.43	0.18	-0.13	-0.43	0.16	0.74	-0.13	

Note: f1: g0, f2: g1, f3: g2, f4: g3, f5: Circular polarization ratio, f6: Degree of polarization, f7: Relative phase, f8: RH, f9: RV, f10: RR, f11: RL, f12: Ellipticity, f13: Conformity, f14: m-chi-e, f15: m-chi-v, f16: m-chi-o, f17: m-delta-db, f18: m-delta-v, f19: m-delta-s, f20: Correlation coefficient, f21: SEi, f22: SEp.

Kappa statistic and overall accuracy quantify the magnitude of difference between classification maps, however, in order to evaluate the statistical significance difference between pair-wise classifications, the McNemar test can be employed [53], [54]. The input parameters for the McNemar test are the number of grid cells that are, correctly classified by both classifications, incorrectly classified by both classifications, and correctly classified by the first classification but not the second one and vice versa [55].

Although RF provides out of bag error for validation of classification results, we used different parameters for validation purposes. Particularly, Overall Accuracy (OA), Kappa coefficients (K), and User's and Producer's Accuracy (UA and PA) were measured using the testing polygons, which were independent of the training polygons, to ensure a robust classification accuracy assessment. Furthermore, the statistical difference between pair-wise classifications was also determined using the McNemar test.

5.3. Results and Discussion

In this section, the classification results obtained from DP, FP, and simulated CP SAR data are presented and evaluated. Table 5.6 presents the overall classification accuracies and Kappa coefficients for the different SAR configuration modes, which were obtained from the corresponding covariance matrices.

Table 5.6. Accuracy assessment of different PolSAR imaging mode using only covariance matrix for wetland classification.

Mode	Feature	Overall Accuracy	Kappa coefficient
DP	$[\mathbf{C}_2]$	45.69	0.36
CP	$[\mathbf{C}_2]$	56.94	0.51
FP	$[\mathbf{C}_3]$	62.81	0.56

The same training and testing polygons were used for all wetland classification scenarios. As seen, FP and DP covariance matrix produced the highest and lowest classification accuracies, respectively. This is because FP uses all scattering information from the observed scene, while DP recorded the least amount of information among the three aforementioned modes. Importantly, the OA obtained using CP was higher than that of the DP (~11%) and only 6% less than that of FP. Since both DP and CP receive the same polarizations (i.e., linear), it was concluded that the transmitted polarization of the SAR signal (i.e., linear for DP and circular for CP) impacts the extractable information of DP and CP data. This is consistent with the results of other studies such as [28]. Furthermore, the McNemar test was found that the different between classified maps obtained by DP and CP covariance matrices were statistically significant since the $p\ value$ was equal to 0.0455 at the 95% confidence level. However, the different between classified maps obtained by CP and FP data were not quite statistically significance with a $p\ value$ of 0.0662.

Given the highest classification results obtained from FP and CP SAR data, FP and CP were selected for further polarimetric decomposition analysis. Table 5.7 represents overall accuracies and Kappa coefficients for defined scenarios in Table 5.3.

Table 5.7. Overall accuracies and Kappa coefficients for features extracted from FP and CP SAR data (see Table 5.3 for defined scenarios).

Data	Scenarios	Overall Accuracy	Kappa coefficient
Full Polarimetry	S1	62.81	0.56
	S2	67.92	0.62
	S3	70.16	0.64
	S4	72.35	0.69
	S5	84.70	0.81
Compact Polarimetry	S1	56.94	0.51
	S2	68.42	0.62
	S3	61.33	0.58
	S4	62.95	0.59
	S5	76.78	0.71

All polarimetric decompositions (S2, S3, S4, and S5) demonstrated higher overall accuracies compared to the original covariance matrix (S1). This is because polarimetric decompositions incorporate the scattering mechanisms of the distributed ground targets into the classification procedure, which improves the discrimination capability of land cover classes [12]. Among the three polarimetric decomposition techniques, it was observed that model-based polarimetric decompositions, such as Freeman-Durden and Yamaguchi (S3 and S4), were more successful in term of classification accuracy relative to eigenvector-based decompositions such as Cloude-Pottier (S2). This is because the former approaches produce a single and independent descriptor for each backscattering mechanism, which is found to be more useful to discriminate each wetland scattering mechanism. For example, in the Freeman-Durden decomposition, all scattering information from the ground targets is captured by the three independent elements, wherein the surface scattering represents the intensity of open water, the double-bounce scattering represents

the intensity of flooded vegetation and urban areas, and finally the volume scattering represents the intensity of upland and non-flooded vegetation. Furthermore, the Yamaguchi decomposition also obtained a slightly better OA than Freeman-Durden, since it performed better in both urban areas and forests relative to Freeman-Durden. Conversely, the scattering mechanisms of ground targets are determined using both real and angular values in the eigenvector-based decompositions (e.g., Cloude-Pottier). Specifically, in the eigenvector-based decompositions, the main scattering mechanism of ground targets is determined by single or a few components and later may be augmented by other real/angular components. Herbaceous vegetation, as a dominant wetland type in the study area, considerably attenuates the shorter wavelength (e.g., C-band) producing similar scattering intensity for vegetation with subtle structural differences and accordingly, hampers the ability of Cloude-Pottier descriptors to differentiate subtle differences between herbaceous vegetation. Furthermore, the entropy and anisotropy layers of the Cloude-Pottier decomposition are characterized by very high levels of noise content over the natural scatterers such as wetland ecosystems [56]. This may explain the lesser success of Cloude-Pottier decomposition compared to the model-based decompositions in terms of classification accuracy. Nevertheless, the inclusion of all polarimetric features (S5) further improved the classification result up to 85%.

As seen in Table 5.7, the classification accuracies of different scenarios for CP data were generally lower than the FP data; although the difference was not significant. The Stokes vector parameters (S2) attained the highest overall accuracy compared to all other independent scenarios of CP data (S1, S3, and S4). It also resulted in an improved accuracy compared to the Cloude-Pottier method of FP. One possible reason could be that the Stokes vector parameters are directly obtained from the linear combination of the polarization channels [57], which minimizes noise levels. This contrasts with other common polarimetric approaches, which require classification or eigenvalue

decomposition (e.g., Cloude-Pottier). This observation is also consistent with the results of other studies for crop identification [24]. For example, Charbonneau et al. (2010) reported that the Stokes vector parameters extracted from CP mode data attained the highest early season classification accuracy for crop identification [24]. They also pointed out that the classification accuracy for the Stoke vector parameters was even higher than that of Freeman-Durden decomposition in the early season and similar to the Freeman-Durden decomposition at the end of growing season. We believe that the Stokes vector elements have the highest polarimetric information content with the least amount of noise compared to other CP features. This may explain the highest classification accuracy obtained by Stokes vectors relative to other CP features in this study. Thus, the Stokes vector parameters extracted from CP data are promising features for wetland classification. Finally, similar to what was observed in the classification using FP data, the inclusion of all features extracted from the CP data (S5) improved the classification accuracy up to 77%. The classification maps obtained from the CP and FP SAR data (S5 for both) are depicted in Figure 5.2.
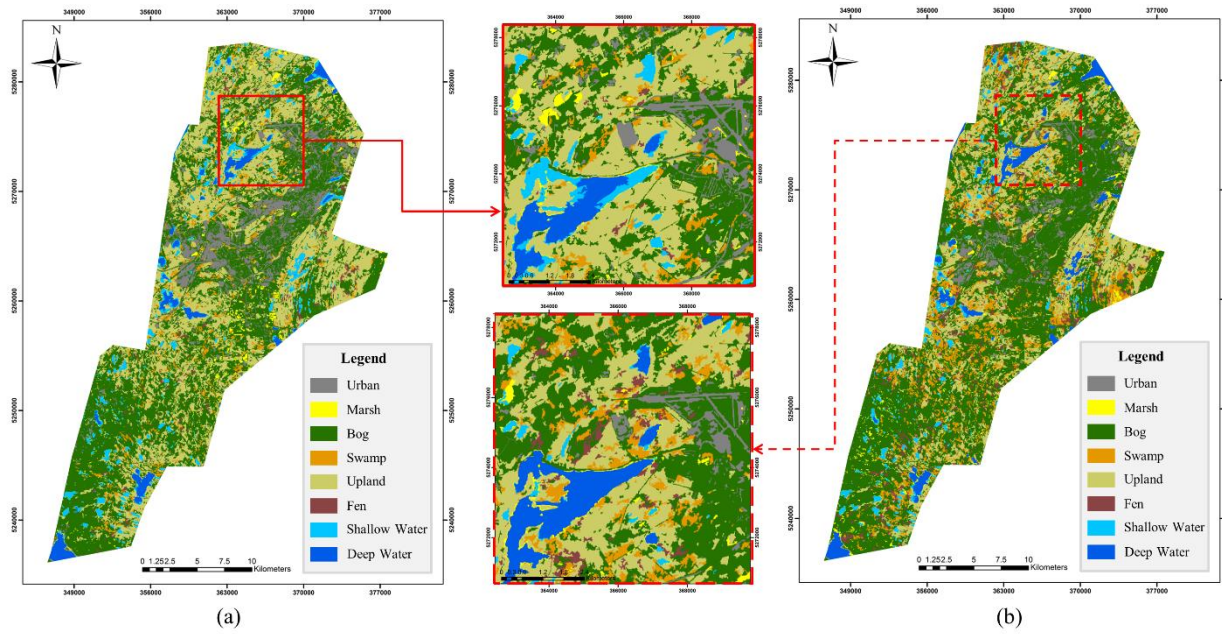
Figure 5.2. The classification maps of the Avalon study area obtained from (a) FP SAR data and (b) CP SAR data.

A visual comparison between the two classified maps illustrates that both have a relatively acceptable detailed spatial distribution of wetland classes with a considerable agreement in most classes (e.g., deep-water, upland, and bog). For quantitative comparison of two classified maps (Figure 5.2), the confusion matrices are presented in Tables 5.8 and 5.9 for FP and CP data (S5 for both), respectively.

Table 5.8. FP confusion matrix for S5 in Table 5.3: Overall accuracy: 84.70%, Kappa coefficient: 0.81.

		Reference Data									
		Upland	Deep-water	Fen	Bog	Swamp	Shallow-water	Marsh	Urban	Tot.	User. Acc.
Classified Data	Upland	20014	0	611	3728	69	0	17	3119	27558	72.63
	Deep-water	0	35372	0	0	0	29	0	0	35401	99.92
	Fen	145	0	7940	2301	171	0	141	53	10751	73.85
	Bog	2070	0	761	14106	108	0	710	621	18376	76.76
	Swamp	92	0	23	208	1109	0	25	8	1465	75.70
	Shallow-water	0	118	0	366	0	1616	559	0	2659	60.77
	Marsh	659	0	11	757	23	0	5560	0	7010	79.32
	Urban	582	0	0	0	0	0	0	14410	14992	96.12
	Tot.	23562	35490	9346	21466	1480	1645	7012	18211	118212	
	Prod. Acc.	84.94	99.67	84.96	65.71	74.93	98.24	79.29	79.13		

As seen in Table 5.8, deep-water was found to have the highest user's accuracy (UA) (~100%). The urban class also obtained a high UA, which was approximately 96%. All wetland classes attained UAs above 70%, excluding shallow-water. The UAs for swamp and fen were relatively low, which reflects the highest commission error. However, the UA for shallow-water was found to be the lowest representing a high degree of commission error. In particular, herbaceous vegetation (i.e., bog and marsh) and deep-water were erroneously classified as shallow-water in some cases. This could be due to a heterogeneous mixture of these classes in the study area, which resulted in a confusion between these classes.

The producer's accuracy (PA) for all classes was higher than 75%, excluding the bog wetland. The PA for the bog class was approximately 66% indicating a high degree of omission error. Particularly, a large portion of bog was misclassified as other herbaceous vegetation as well as the upland class. Overall, a confusion error between herbaceous wetland classes (bog, fen, and marsh) occurred.

Table 5.9. CP confusion matrix for S5 in Table 5.3: Overall accuracy: 76.78%, Kappa coefficient: 0.71.

| | | Reference Data | | | | | | | | | |
		Upland	Deep-water	Fen	Bog	Swamp	Shallow-water	Marsh	Urban	Tot.	User. Acc.
Classified Data	Upland	16109	0	730	2433	11	0	174	2549	22006	73.20
	Deep-water	0	34794	0	0	0	257	0	0	35051	99.27
	Fen	711	0	5689	1539	28	0	1155	31	9153	62.15
	Bog	2719	0	2584	15093	54	0	1349	3129	24928	60.55
	Swamp	26	0	161	509	1103	0	25	0	1824	60.47
	Shallow-water	0	696	0	0	0	1267	88	0	2051	61.77
	Marsh	238	0	182	1892	284	121	4221	9	6947	60.76
	Urban	3759	0	0	0	0	0	0	12493	16252	76.87
	Tot.	23562	35490	9346	21466	1480	1645	7012	18211	118212	
	Prod. Acc.	68.37	98.04	60.87	70.31	74.53	77.02	60.20	68.60		

Generally, the UAs and PAs for the most classes were lower for CP data relative to those of FP data; however, the decrease was more significant for some classes. More specifically, the UAs were degraded by approximately of 18%, 16%, 15%, and 11% for marsh, bog, swamp, and fen, respectively; when CP features were included into the RF classification relative to FP features. The UA for shallow-water was improved of about 1% for CP compared to FP. Similar to FP SAR data, a high degree of confusion error was observed between herbaceous vegetation, namely bog, fen, and marsh.

PAs were also reduced in most classes when CP data were used in comparison to FP data. The highest drop in PAs of the wetland classes was observed for fen (~24%) and shallow-water (~21%), while the lowest PAs occurred for the marsh and fen class. Accordingly, the high omission errors were observed for these two, wherein fen and marsh were largely misclassified as other herbaceous vegetation. Notably, the PA was improved for the bog wetland by approximately 5% when CP features were employed relative to FP features. For non-wetland classes, a degradation of up to 15% was observed in PAs, excluding the deep-water class (less than 2%).

Overall, the greatest confusion error was found within herbaceous wetlands, especially the bog and fen classes. This is due to the highly heterogeneous nature of these classes in the field. As reported by field biologists during ecological field data collection, these classes were found adjacent to each other and identifying a clear-cut border between them was difficult. Furthermore, they have relatively similar backscattering mechanisms and, therefore, there is a high degree of similarity between these classes, especially when shorter wavelength such as C-band applied, which is highly attenuated by herbaceous vegetation. Moreover, some of these classes have very similar ecological vegetation types contributing to the degree of confusion between these classes. For example, bog and fen are peatlands dominated by *Spahgnum* and *graminoid* species, respectively, and thereby, are sometimes categorized as the same class (i.e., peatland).

Phenology and hydrological variation of wetland ecosystems have great influence on discriminating different wetland classes. This is true since different wetland classes exhibit varying scattering mechanisms as well as intensity during low and high water seasons. For example, increasing the water level enhances the chance of double-bounce scattering for the swamp class. In contrast, increasing the water level for the marsh wetland decreases the chance of double-bounce scattering, wherein the double-bounce is mainly converted into the surface scattering [58]. The classification accuracy for all wetland classes can be increased by inclusion of multi-temporal SAR imagery, which reduces the confusion error due to the hydrological variation of wetland complexes [6].

Another consideration in interpretation of the accuracies for wetland classes is the amount of ecological field data available for supervised classification. Generally, the larger training samples are recommended for applying a supervised classification. As seen in Table 5.2, all non-wetland classes (i.e., upland, urban, and deep-water) have a high amount of field data, which resulted in

207

the highest UAs and PAs for both FP and CP data. Among wetland classes, swamp and shallow-water have the least amount of *in situ* data, which may explain the low accuracies for these classes in some cases. The least amount of ecological data for the swamp wetland is because swamps tend to occur in physically smaller areas compared to that of other wetlands, such as in transition zones between a wetland and other land cover types. As a result, most swamp polygons contained fewer pixels when compared to other wetlands types. Conversely, bog wetlands are more expansive relative to other wetland classes in the study area. This could be due to province climate, which facilitates extensive peatland formation [48]. Thus, the bog wetlands were more frequently visited during field data collection and, as such, have a larger number of associated pixels.

As discussed earlier, one of the advantages of the RF classifier is that it provides the variable importance for a set of input features. Figure 5.3 depicts the variable importance of input features utilized for wetland classification in case of using CP SAR data. This figure was obtained by running the RF classification for 30 times using the same CP input features as well as the same training samples (see Table 5.4).
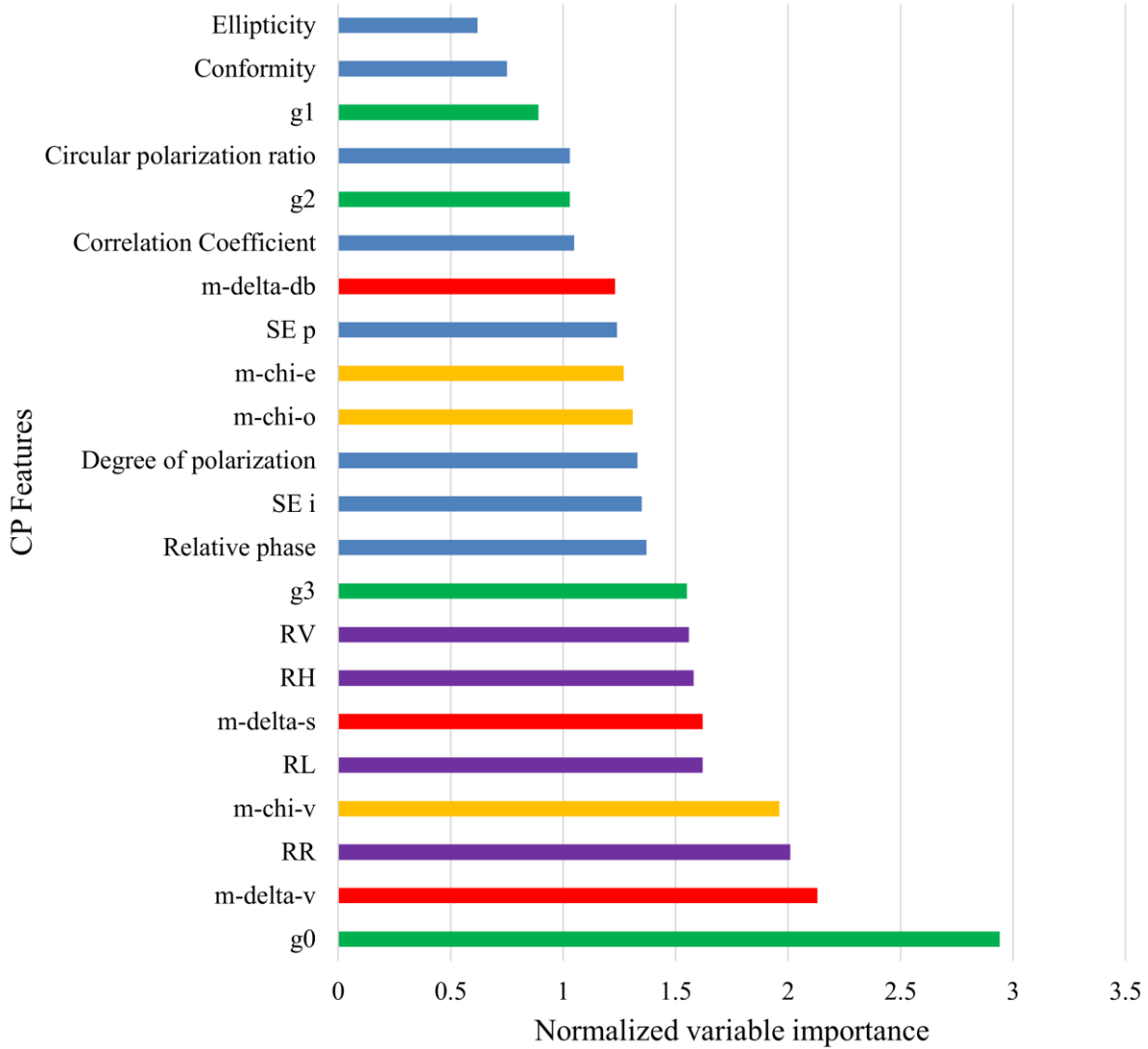
Figure 5.3. Normalized variable importance for the RF classification map obtained from CP SAR features (see Table 3, S5). Different variables are represented as follows: Stokes vector elements (green), m-delta decomposition (red), intensity channels (purple), m-chi decomposition (orange), and wave descriptors (blue).

Analysis of variable importance for the RF classification using CP SAR features indicated that g_0 was the most important CP features for wetland classification in this study. g_0 is the first element of Stokes vector representing the total power or intensity [43]. Other wetland classification studies reported the great importance of the intensity layer for discriminating different wetland classes.

For example, Moser et al. (2016) performed a multi-temporal classification using only the K_0 parameter (the first element of the Kennaugh matrix) obtained from dual polarimetric (HH/VV) TerraSAR-X data and reported the significance of the K_0 parameter relative to other elements of Kennaugh matrix [59]. The K_0 element indicates the total intensity in the Kennaugh matrix, which is similar to the g_0 parameter in the Stokes vector.

Charbonneau et al. (2010), also, have reported that Stokes vector parameters extracted from CP data provided high early-season classification accuracy for crop identification [24]. The volumetric component of the m-delta decomposition was the next most important variable for wetland mapping. The results are consistent with the theoretical concepts of scattering mechanisms, wherein volumetric scattering is the dominant scattering mechanism for vegetation canopies like those found in a wetland complex [1]. Particularly, the m-delta decomposition has relatively the same potential for land cover classification as the Freeman-Durden decomposition [24]. For example, Charbonneau et al. (2010) reported a great capacity of m-delta decomposition for crop identification with relatively comparable strength as Freeman-Durden [24]. Overall, the circular polarizations, including RR, RV, RH, and RL were found to be important features for wetland classification. In particular, the RR polarization is suitable for extracting information from flooded vegetation, which produces the highest double-bounce scattering. This is because, in the case of double-bounce scattering, the returned wave maintains its ellipticity, which results in the highest RR. In contrast, in the case of "pure surface", the ellipticity of the return wave is inverse, which results in the highest RL [14]. White et al. (2017) also reported the importance of RV intensity feature for peatland classification during the summer time [15]. The m-chi-v feature was also found to be useful for wetland classification for the same reason as the m-delta-v feature. Finally, m-delta-s was found to be important, which was also consistent with the results of other studies [8],

[15]. For example, White et al. (2017) reported that the surface scattering was useful for detection and classification of bog and fen since the canopy interference was negligible at low SAR incidence angles, resulted in an increase in surface scattering, which was mainly produced by bogs [15]. Particularly, they reported that the m-delta-s was the most important CP features when spring data were employed, which was not similar to what found in this study. Specifically, the surface scattering was dominant for the spring SAR observation (i.e., April) when the vegetative density was not developed and plants were short. We believe that the main difference between these two results could be due to time difference between satellite imageries.

The variable importance analysis of the remaining CP features indicated the relatively similar contribution of other features. In particular, the wave descriptor parameters contributed slightly less to wetland classification than other CP features. However, some of these wave descriptors (e.g., the degree of polarization and conformity) were found to be important features in maritime applications such as oil spills detection [19].

Previous studies reported that when RF was used for land and wetland classification repeatedly, the most important variables varied among different RF classifications [37]. By applying the RF classification 30 times, the most important variables were obtained. It was observed that the most important variables changed among different classification models by using same input variables (see Table 5.4). Next, the correlation between input variables was determined and important variables with a high degree of correlation were removed (r > 0.9). This allowed us to run two additional classifications using only the important variables (number of variables = 14) and the uncorrelated important variables (number of variables = 7). The overall accuracies for classifications obtained from all variables and important variables were 76.78% and 76.17%, respectively. Thus, the classification accuracy remained unchanged when only important variables

were applied to the classification scheme. This was significant since the variable reduction did not affect the classification accuracy, while resulted in obtaining an optimal classification. Millard and Richardson (2015), also, reported that incorporating high dimensional correlated input variables into the RF classification resulted in a noisy classification [37]. Surprisingly, the overall accuracy for classified map obtained from the uncorrelated important variable was 78.22% representing approximately 2% improvement relative to other classified maps. Figure 5.4 depicts the UAs and PAs for different land cover types obtained from different CP features, including all variables, the important variables, and the uncorrelated important variables.

(a)

Producer's Accuracy
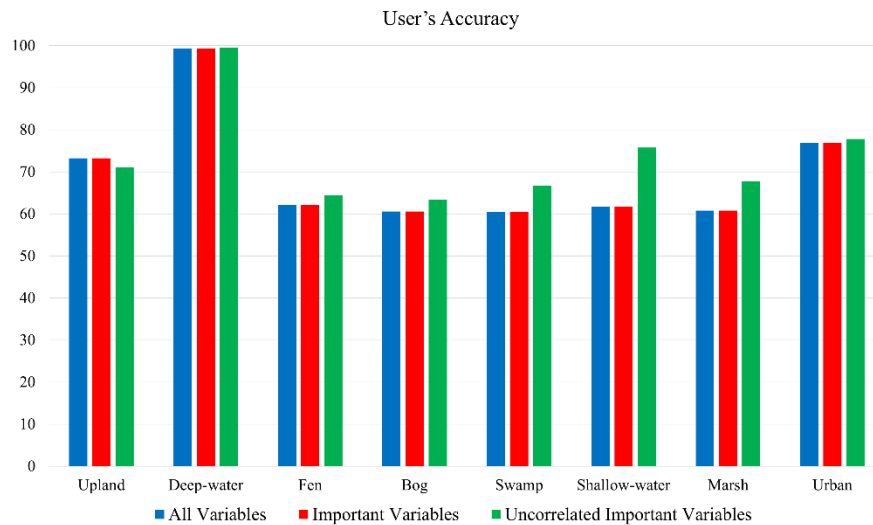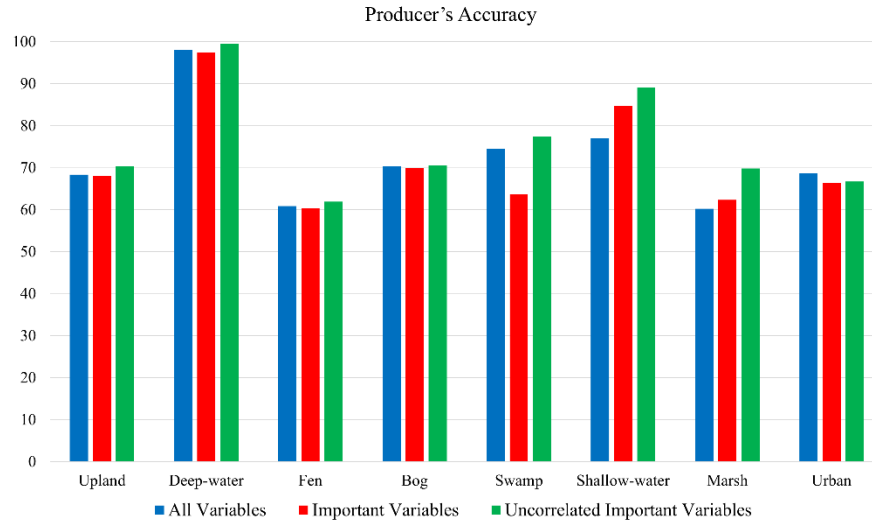
(b)

Figure 5.4. (a) UAs and (b) PAs for different land cover types obtained from different CP features, including all variables, the important variables, and the uncorrelated important variables.

As seen, UAs and PAs were relatively similar in RF classifications for inputs from all variables and the important variables. However, when only the uncorrelated important variables incorporated into the classification scheme, UAs and PAs improved for some classes.

As mentioned earlier, the McNemar test was also applied in order to quantitatively determine the statistical difference between a pair of classifications. The McNemar test illustrated that there was no statistically significant difference between classified maps obtained from all variables versus important variables since the $p\ value$ was equal to 0.4237 at the 95% confidence level. However, the McNemar test illustrated a significant statistical difference between classified maps obtained from the important variables versus the uncorrelated important variables. Specifically, the $p\ value$ for these classification pairs was 0.0139 at the 95% confidence level indicating the statistical difference between the two classified maps.

5.4. Summary and conclusion

This research study evaluated the potential of simulated compact polarimetric SAR data for wetland classification in a study area located on the Avalon Peninsula, Newfoundland, Canada. Different PolSAR features were extracted from dual, full, and compact polarimetric SAR data and incorporated into an object-based RF classification. The overall classification accuracies demonstrated the superiority of the FP data for wetland classification compared to all other data types. However, the classification accuracy obtained from the CP features was higher than DP data and comparable with the results of the FP data in a few cases. More specifically, an overall classification accuracy of approximately 76% was achieved by including all features extracted from the CP data, while incorporating all features from the FP data into the classification scheme produced an overall accuracy of approximately 85%. However, there is a trade-off between CP and FP, wherein the former offers a larger swath width, shorter revisit time, less complexity, and acceptable information content while the latter contains all scattering information of ground targets and, accordingly, results in a higher classification accuracy.

A great advantage of the RF classifier is that it determines the variable importance of input features. The variable importance analysis of CP features found that the first component of the Stokes vector (total power), circular polarizations, and the volumetric component of both m-delta and m-chi decompositions were the most important features for wetland classification. Millard and Richardson (2015) reported a variation among the important variables determined by RF even by using the same training data and input variables [37]. This study, also, reconfirmed the alteration of variable importance, thus, illustrating the significance of more elaborated analysis when RF is employed for the land cover classification using a large number of input features. Iterative RF classifications may reduce the uncertainty in predicted classes by RF. We also found the

importance of removing uncorrelated important variables for classification similar to Millard and Richardson (2015), which, surprisingly, improved the classification accuracy by about 2%.

In summary, the FP SAR imagery provided the best classification accuracy among all SAR data utilized in this study. The CP outperformed DP SAR data in terms of classification accuracy while was less successful relative to FP for classification of most land cover types in this study. Nonetheless, it offers wider swath coverage and, accordingly, an improved temporal resolution, which, in turns, makes it an ideal tool for several remote sensing applications requiring more frequent observations over a larger scale such as wetland and sea ice mapping.

5.5. References

[1] R. W. Tiner, M. W. Lang, and V. V Klemas, *Remote sensing of wetlands: applications and advances*. CRC Press, 2015.

[2] B. G. Warner and C. D. A. Rubec, "The Canadian wetland classification system," *Wetl. Res. Centre, Univ. Waterloo, Waterloo, Ontario*, 1997.

[3] T. L. Evans, M. Costa, K. Telmer, and T. S. F. Silva, "Using ALOS/PALSAR and RADARSAT-2 to map land cover and seasonal inundation in the Brazilian Pantanal," *IEEE J. Sel. Top. Appl. Earth Obs. Remote Sens.*, vol. 3, no. 4, pp. 560–575, 2010.

[4] T. L. Evans and M. Costa, "Landcover classification of the Lower Nhecolândia subregion of the Brazilian Pantanal Wetlands using ALOS/PALSAR, RADARSAT-2 and ENVISAT/ASAR imagery," *Remote Sens. Environ.*, vol. 128, pp. 118–137, 2013.

[5] T. S. F. Silva, M. P. F. Costa, and J. M. Melack, "Spatial and temporal variability of macrophyte cover and productivity in the eastern Amazon floodplain: A remote sensing approach," *Remote Sens. Environ.*, vol. 114, no. 9, pp. 1998–2010, 2010.

[6] L. F. de Almeida Furtado, T. S. F. Silva, and E. M. L. de Moraes Novo, "Dual-season and full-polarimetric C band SAR assessment for vegetation mapping in the Amazon várzea wetlands," *Remote Sens. Environ.*, vol. 174, pp. 212–222, 2016.

[7] K. Millard and M. Richardson, "Wetland mapping with LiDAR derivatives, SAR polarimetric decompositions, and LiDAR–SAR fusion using a random forest classifier," *Can. J. Remote Sens.*, vol. 39, no. 4, pp. 290–307, 2013.

[8] L. Dingle Robertson, D. J. King, and C. Davies, "Object-based image analysis of optical and radar variables for wetland evaluation," *Int. J. Remote Sens.*, vol. 36, no. 23, pp. 5811–5841, 2015.

[9] M. Mahdianpari, B. Salehi, F. Mohammadimanesh, and M. Motagh, "Random forest wetland classification using ALOS-2 L-band, RADARSAT-2 C-band, and TerraSAR-X imagery," *ISPRS J. Photogramm. Remote Sens.*, vol. 130, 2017.

[10] M. Mahdianpari *et al.*, "Fisher Linear Discriminant Analysis of coherency matrix for wetland classification using PolSAR imagery," *Remote Sens. Environ.*, vol. 206, 2018.

[11] M. Mahdianpari, B. Salehi, and F. Mohammadimanesh, "A novel contextual speckle reduction method of PolSAR images: Evaluation of speckle reduction effects on sea ice classification," in *IGTF 2017 - Imaging and Geospatial Technology Forum 2017, ASPRS Annual Conference*, 2017.

[12] A. Schmitt and B. Brisco, "Wetland monitoring using the curvelet-based change detection method on polarimetric SAR imagery," *Water*, vol. 5, no. 3, pp. 1036–1051, 2013.

[13] S. Wdowinski, S.-W. Kim, F. Amelung, T. H. Dixon, F. Miralles-Wilhelm, and R. Sonenshein, "Space-based detection of wetlands' surface water level changes from L-band SAR interferometry," *Remote Sens. Environ.*, vol. 112, no. 3, pp. 681–696, 2008.

[14] B. Brisco, A. Schmitt, K. Murnaghan, S. Kaya, and A. Roth, "SAR polarimetric change detection for flooded vegetation," *Int. J. Digit. Earth*, vol. 6, no. 2, pp. 103–114, 2013.

[15] L. White, K. Millard, S. Banks, M. Richardson, J. Pasher, and J. Duffe, "Moving to the RADARSAT constellation mission: Comparing synthesized compact polarimetry and dual polarimetry data with fully polarimetric RADARSAT-2 data for image classification of peatlands," *Remote Sens.*, vol. 9, no. 6, p. 573, 2017.

[16] P. C. Dubois-Fernandez, J.-C. Souyris, S. Angelliaume, and F. Garestier, "The compact polarimetry alternative for spaceborne SAR at low frequency," *IEEE Trans. Geosci. Remote Sens.*, vol. 46, no. 10, pp. 3208–3222, 2008.

[17] M. E. Nord, T. L. Ainsworth, J.-S. Lee, and N. J. S. Stacy, "Comparison of compact polarimetric synthetic aperture radar modes," *IEEE Trans. Geosci. Remote Sens.*, vol. 47, no. 1, pp. 174–188, 2009.

[18] F. Nunziata, M. Migliaccio, and X. Li, "Sea oil slick observation using hybrid-polarity SAR architecture," *IEEE J. Ocean. Eng.*, vol. 40, no. 2, pp. 426–440, 2015.

[19] A.-B. Salberg, Ø. Rudjord, and A. H. S. Solberg, "Oil spill detection in hybrid-polarimetric SAR images," *IEEE Trans. Geosci. Remote Sens.*, vol. 52, no. 10, pp. 6521–6533, 2014.

[20] J.-C. Souyris, P. Imbo, R. Fjortoft, S. Mingot, and J.-S. Lee, "Compact polarimetry based on symmetry properties of geophysical media: The/spl pi//4 mode," *IEEE Trans. Geosci. Remote Sens.*, vol. 43, no. 3, pp. 634–646, 2005.

[21] R. K. Raney, "Hybrid-polarity SAR architecture," *IEEE Trans. Geosci. Remote Sens.*, vol. 45, no. 11, pp. 3397–3404, 2007.

[22] R. K. Raney, "A perspective on compact polarimetry," *IEEE Geosci. Remote Sens. Newslett*, vol. 160, no. 160, pp. 12–18, 2011.

[23] M. J. Collins, M. Denbina, and G. Atteia, "On the reconstruction of quad-pol SAR data from compact polarimetry data for ocean target detection," *IEEE Trans. Geosci. Remote Sens.*, vol. 51, no. 1, pp. 591–600, 2013.

[24] F. J. Charbonneau *et al.*, "Compact polarimetry overview and applications assessment," *Can. J. Remote Sens.*, vol. 36, no. sup2, pp. S298–S315, 2010.

[25] B. Brisco, K. Li, B. Tedford, F. Charbonneau, S. Yun, and K. Murnaghan, "Compact polarimetry assessment for rice and wetland mapping," *Int. J. Remote Sens.*, vol. 34, no. 6, pp. 1949–1964, 2013.

[26] M. Dabboor, L. White, B. Brisco, and F. Charbonneau, "Change detection with compact polarimetric SAR for monitoring wetlands," *Can. J. Remote Sens.*, vol. 41, no. 5, pp. 408–417, 2015.

[27] M. Dabboor and T. Geldsetzer, "Towards sea ice classification using simulated RADARSAT Constellation Mission compact polarimetric SAR imagery," *Remote Sens. Environ.*, vol. 140, pp. 189–195, 2014.

[28] T. L. Ainsworth, J. P. Kelly, and J.-S. Lee, "Classification comparisons between dual-pol, compact polarimetric and quad-pol SAR imagery," *ISPRS J. Photogramm. Remote Sens.*, vol. 64, no. 5, pp. 464–471, 2009.

[29] C. Lardeux *et al.*, "Classification of tropical vegetation using multifrequency partial SAR polarimetry," *IEEE Geosci. Remote Sens. Lett.*, vol. 8, no. 1, pp. 133–137, 2011.

[30] P. E. Green, "Radar measurements of target scattering properties," *Radar Astron.*, pp. 1–78, 1968.

[31] L. M. Carter, D. B. Campbell, and B. A. Campbell, "Impact crater related surficial deposits on Venus: Multipolarization radar observations with Arecibo," *J. Geophys. Res. Planets*, vol. 109, no. E6, 2004.

[32] D. B. Campbell, B. A. Campbell, L. M. Carter, J.-L. Margot, and N. J. S. Stacy, "No evidence for thick deposits of ice at the lunar south pole," *Nature*, vol. 443, no. 7113, p. 835, 2006.

[33] W. Zhang *et al.*, "Compact Polarimetric Response of Rape (Brassica napus L.) at C-Band: Analysis and Growth Parameters Inversion," *Remote Sens.*, vol. 9, no. 6, p. 591, 2017.

[34] A. A. Thompson*, "Overview of the RADARSAT constellation mission," *Can. J. Remote Sens.*, vol. 41, no. 5, pp. 401–407, 2015.

[35] L. Breiman, "Random forests," *Mach. Learn.*, vol. 45, no. 1, pp. 5–32, 2001.

[36] U. C. Benz, P. Hofmann, G. Willhauck, I. Lingenfelder, and M. Heynen, "Multi-resolution, object-oriented fuzzy analysis of remote sensing data for GIS-ready information," *ISPRS J. Photogramm. Remote Sens.*, vol. 58, no. 3–4, pp. 239–258, 2004.

[37] K. Millard and M. Richardson, "On the importance of training data sample selection in random forest image classification: A case study in peatland ecosystem mapping," *Remote Sens.*, vol. 7, no. 7, pp. 8489–8515, 2015.

[38] B. Brisco, K. Murnaghan, S. Wdowinski, and S.-H. Hong, "Evaluation of RADARSAT-2 acquisition modes for wetland monitoring applications," *Can. J. Remote Sens.*, vol. 41, no. 5, pp. 431–439, 2015.

[39] A. Freeman and S. L. Durden, "A three-component scattering model for polarimetric SAR data," *IEEE Trans. Geosci. Remote Sens.*, vol. 36, no. 3, pp. 963–973, 1998.

[40] J.-S. Lee and E. Pottier, *Polarimetric radar imaging: from basics to applications*. CRC press, 2009.

[41] Y. Yamaguchi, T. Moriyama, M. Ishido, and H. Yamada, "Four-component scattering model for polarimetric SAR image decomposition," *IEEE Trans. Geosci. Remote Sens.*, vol. 43, no. 8, pp. 1699–1706, 2005.

[42] L. Zhang, J. Zhang, B. Zou, and Y. Zhang, "Comparison of methods for target detection and applications using polarimetric SAR image," *Piers online*, vol. 4, no. 1, pp. 140–145, 2008.

[43] R. K. Raney, J. T. S. Cahill, G. W. Patterson, and D. B. J. Bussey, "The m-chi decomposition of

hybrid dual-polarimetric radar data," in *Geoscience and Remote Sensing Symposium (IGARSS), 2012 IEEE International*, 2012, pp. 5093–5096.

[44] S. R. Cloude, D. G. Goodenough, and H. Chen, "Compact decomposition theory," *IEEE Geosci. Remote Sens. Lett.*, vol. 9, no. 1, pp. 28–32, 2012.

[45] M.-L. Truong-Loi, A. Freeman, P. C. Dubois-Fernandez, and E. Pottier, "Estimation of soil moisture and Faraday rotation from bare surfaces using compact polarimetry," *IEEE Trans. Geosci. Remote Sens.*, vol. 47, no. 11, pp. 3608–3615, 2009.

[46] I. B. Marshall, C. A. S. Smith, and C. J. Selby, "A national framework for monitoring and reporting on environmental sustainability in Canada," in *Global to Local: Ecological Land Classification*, Springer, 1996, pp. 25–38.

[47] E. S. W. G. (Canada), C. for Land, B. R. R. (Canada), and C. S. of the E. Directorate, *A national ecological framework for Canada*. Centre for Land and Biological Resources Research; Hull, Quebec: State of …, 1996.

[48] R. South, *Biogeography and Ecology of the Island of Newfoundland*, vol. 48. Springer Science & Business Media, 1983.

[49] L. Dingle Robertson and D. J. King, "Comparison of pixel-and object-based classification in land cover change mapping," *Int. J. Remote Sens.*, vol. 32, no. 6, pp. 1505–1529, 2011.

[50] V. F. Rodriguez-Galiano, M. Chica-Olmo, F. Abarca-Hernandez, P. M. Atkinson, and C. Jeganathan, "Random Forest classification of Mediterranean land cover using multi-seasonal imagery and multi-seasonal texture," *Remote Sens. Environ.*, vol. 121, pp. 93–107, 2012.

[51] M. Mahdianpari, B. Salehi, and F. Mohammadimanesh, "The Effect of PolSAR Image De-speckling on Wetland Classification: Introducing a New Adaptive Method," *Can. J. Remote Sens.*, vol. 43, no. 5, 2017.

[52] E. W. RAMSEY III, "Radar remote sensing of wetlands," *Remote Sens. Chang. Detect.*, 1999.

[53] T. G. Dietterich, "An experimental comparison of three methods for constructing ensembles of decision trees: Bagging, boosting, and randomization," *Mach. Learn.*, vol. 40, no. 2, pp. 139–157, 2000.

[54] Q. McNemar, "Note on the sampling error of the difference between correlated proportions or percentages," *Psychometrika*, vol. 12, no. 2, pp. 153–157, 1947.

[55] G. M. Foody, "Supervised image classification by MLP and RBF neural networks with and without an exhaustively defined set of classes," *Int. J. Remote Sens.*, vol. 25, no. 15, pp. 3091–3104, Aug. 2004.

[56] A. Schmitt, A. Wendleder, and S. Hinz, "The Kennaugh element framework for multi-scale, multi-polarized, multi-temporal and multi-frequency SAR image preparation," *ISPRS J. Photogramm. Remote Sens.*, vol. 102, pp. 122–139, 2015.

[57] R. Raney, "Hybrid-polarity SAR architecture," in *Geoscience and Remote Sensing Symposium, 2006. IGARSS 2006. IEEE International Conference on*, 2006, pp. 3846–3848.

[58] J.-W. Kim, Z. Lu, J. W. Jones, C. K. Shum, H. Lee, and Y. Jia, "Monitoring Everglades freshwater marsh water level using L-band synthetic aperture radar backscatter," *Remote Sens. Environ.*, vol. 150, pp. 66–81, 2014.

[59] L. Moser, A. Schmitt, A. Wendleder, and A. Roth, "Monitoring of the Lac Bam wetland extent using dual-polarized X-band SAR data," *Remote Sens.*, vol. 8, no. 4, p. 302, 2016.

Chapter 6. Deep learning models for wetland classification using satellite data[5]

Preface

A version of this manuscript has been published in the *Remote Sensing Journal*. I am a primary author of this manuscript along with the co-authors, Bahram Salehi, Mohammad Rezaee, Fariba Mohammadimanesh, and Yun Zhang. I designed and conceptualized the study. I developed a pipeline in Python compatible with satellite data. I wrote the paper and revised it based on comments from all co-authors. I also revised the paper according to the reviewers' comments. The co-authors, Mohammad Rezaee and Fariba Mohammadimanesh, helped in performing the experiments and analyzing the results and contributed to revising the manuscript. All co-authors provided editorial input and scientific insights to further improve the paper. They also reviewed and commented on the manuscript.

---

[5] Mahdianpari, M., Salehi, B., Rezaee, M., Mohammadimanesh, F. and Zhang, Y., 2018. Very deep convolutional neural networks for complex land cover mapping using multispectral remote sensing imagery. *Remote Sensing*, *10*(7), p.1119.

Abstract

Despite recent advances of deep Convolutional Neural Networks (CNNs) in various computer vision tasks, their potential for classification of multispectral remote sensing images has not been thoroughly explored. In particular, the applications of deep CNNs using optical remote sensing data have focused on the classification of very high-resolution aerial and satellite data, owing to the similarity of these data to the large datasets in computer vision. Accordingly, this study presents a detailed investigation of state-of-the-art deep learning tools for classification of complex wetland classes using multispectral RapidEye optical imagery. Specifically, we examine the capacity of seven well-known deep convnets, namely DenseNet121, InceptionV3, VGG16, VGG19, Xception, ResNet50, and InceptionResNetV2, for wetland mapping in Canada. In addition, the classification results obtained from deep CNNs are compared with those based on conventional machine learning tools, including Random Forest and Support Vector Machine, to further evaluate the efficiency of the former to classify wetlands. The results illustrate that the full-training of convnets using five spectral bands outperforms the other strategies for all convnets. InceptionResNetV2, ResNet50, and Xception are distinguished as the top three convnets, providing state-of-the-art classification accuracies of 96.17%, 94.81%, and 93.57%, respectively. The classification accuracies obtained using Support Vector Machine (SVM) and Random Forest (RF) are 74.89% and 76.08%, respectively, considerably inferior relative to CNNs. Importantly, InceptionResNetV2 is consistently found to be superior compared to all other convnets, suggesting the integration of Inception and ResNet modules is an efficient architecture for classifying complex remote sensing scenes such as wetlands.

Keywords: Deep learning, Convolutional Neural Network, Machine learning, Multispectral images, Land cover classification, Wetland, RapidEye, Full-training, Fine-tuning.

6.1. Introduction

Wetlands are transitional zones between terrestrial and aquatic systems that support a natural ecosystem of a variety of plant and animal species, adapted to wet conditions [1]. Flood- and storm-damage protection, water quality improvement and renovation, greenhouse gas reduction, shoreline stabilization, and aquatic productivity are only a handful of the advantages associated with wetlands. Unfortunately, wetlands have undergone variations due to natural processes, such as changes in temperature and precipitation caused by climate change, coastal plain subsidence and erosion, as well as human-induced disturbances such as industrial and residential development, agricultural activities, and runoff from lawns and farms [1].

Knowledge of the spatial distribution of these valuable ecosystems is crucial in order to characterize ecosystem processes and to monitor the subsequent changes over time [2]. However, the remoteness, vastness, and seasonally dynamic nature of most wetland ecosystems make conventional methods of data acquisition (e.g., surveying) labor-intensive and costly [3]. Fortunately, remote sensing, as a cost- and time-efficient tool, addresses the limitations of conventional techniques by providing valuable ecological data to characterize wetland ecosystems and to monitor land cover changes [4]. Optical remote sensing data have shown to be promising tools for wetland mapping and monitoring. This is because biomass concentration, leaf water content, and vegetation chlorophyll—all important characteristics of wetland vegetation—can be determined using optical satellite images [5]. In particular, optical remote sensing sensors collect spectral information of ground targets at various points of the electromagnetic spectrum, such as visible and infrared, which is of great benefit for wetland vegetation mapping [5]. Therefore, several studies reported the success of wetland mapping using optical satellite imagery [6], [7].

Despite the latest advances in remote sensing tools, such as the availability of high spatial and temporal resolution satellite data and object-based image analysis tools [8], the classification accuracy of complex land cover, such as wetland ecosystems, is insufficient. This could be attributed to the spectral similarity of wetland vegetation types, making the exclusive use of spectral information insufficient for the classification of heterogeneous land cover classes. In addition, several studies reported the significance of incorporating both spectral and spatial information for land cover mapping [9]. Thus, spatial features may augment spectral information and thereby contribute to the success of complex land cover mapping. Accordingly, several experiments were carried out to incorporate both spectral and spatial features into a classification scheme. These studies were based on the Markov Random Field (MRF) model [10], the Conditional Random Field (CRF) model [11], and Composite Kernel (CK) methods [12]. However, in most cases, the process of extracting a large number of features, the feature engineering process [13], for the purpose of supervised classification is time intensive, and requires broad and profound knowledge to extract amenable features. Furthermore, classification based on hand-crafted spatial features primarily relies on low-level features, resulting in insufficient classification results in most cases and a poor capacity for generalization [9].

Most recently, Deep Learning (DL), a state-of-the-art machine learning tool, has been placed in the spotlight in the field of computer vision and, subsequently, in remote sensing [14]. This is because these advanced machine learning algorithms address the primary limitations of the conventional shallow-structured machine learning tools, such as Support Vector Machine (SVM) and Random Forest (RF) [15]. Deep Belief Net (DBN) [16], Stacked Auto-Encoder (SAE) [17], and deep Convolutional Neural Network (CNN) [18], [19] are current deep learning models, of which the latter is most well-known. Importantly, CNN has led to a series of breakthroughs in

several remote sensing applications, such as classification [6], segmentation [20], and object detection [21], due to its superior performance in a variety of applications relative to shallow-structured machine learning tools. CNNs are characterized by multi-layered interconnected channels, with a high capacity for learning the features and classifiers from data spontaneously given their deep architecture, their capacity to adjust parameters jointly, and to classify simultaneously [22]. One of the ubiquitous characteristics of such a configuration is its potential to encode both spectral and spatial information into the classification scheme in a completely automated workflow [22]. Accordingly, the complicated, brittle, and multistage feature engineering procedure is replaced with a simple end-to-end deep learning workflow [13].

Notably, there is a different degree of abstraction for the data within multiple convolutional layers, wherein low-, mid-, and high-level information is extracted in a hierarchical learning framework at the initial, intermediate, and final layers, respectively [22]. This configuration omits the training process from scratch in several applications since the features in the initial layers are generic filters (e.g., edge) and, accordingly, are less dependent on the application. However, the latest layers are related to the final application and should be trained according to the given data and classification problem. This also addresses the poor generalization capacity of shallow-structured machine learning tools, which are site- and data-dependent, suggesting the versatility of CNNs [13].

Although the advent of CNN dates back to as early as the 1980s, when LeCun designed a primary convolutional neural network known as LeNet to classify handwritten digits, it gained recognition and was increasingly applied around 2010 [23]. This is attributable to the advent of more powerful hardware, larger datasets (e.g., ImageNet) [24], and new ideas, which consequently improved network architecture [19]. The original idea of deep CNNs [23] has been further developed by Krizhevsky and his colleagues, who designed a breakthrough CNN, known as AlexNet, a pioneer

of modern deep CNNs, with multiple convolutional and max-pooling layers that provide deeper feature-learning at different spatial scales [18]. Subsequent successes have been achieved since 2014, when VGG [25], GoogLeNet (i.e., Inception network) [19], ResNet [26], and Xception [27] were introduced in the ImageNet Large-Scale Visual Recognition Challenge (ILSVRC).

The intricate tuning process, heavy computational burden, high tendency of overfitting, and the empirical nature of model establishment are the main limitations associated with deep CNNs [22]. Although some studies have argued that all deep learning methods have a black-box nature, it is not completely true for CNN [13]. This is because the features learned by CNNs can be visualized and, in particular, they are an illustration of visual concepts. There are three different strategies for employing current CNNs: A full-training network, a pre-trained network as a feature extractor, and fine-tuning of a pre-trained network. In the first case, a network is trained from scratch with random weights and biases to extract particular features for the dataset of interest. However, the limited number of training samples constrains the efficiency of this technique due to the overfitting problem. The other two strategies are more useful when a limited amount of training samples is available [28].

In cases of limited training data, a stacked auto-encoder (SAE) is also useful to learn the features from a given dataset using an unsupervised learning network [29]. In such a network, the deconstruction error between the input data at the encoding layer and its reconstruction at the decoding layer is minimized [15]. SAE networks are characterized by a relatively simple structure relative to deep CNNs and they have a great capacity for fast image interpretation. In particular, they convert raw data to an abstract representation using a simple non-linear model and they integrate features using an optimization algorithm. This results in a substantial decrease of redundant information between the features while achieving a strong generalization capacity.

Despite recent advances in deep CNNs, their applications in remote sensing have been substantially limited to the classification of very high spatial resolution aerial and satellite imagery from a limited number of well-known datasets, owing to the similar characteristics of these data to object recognition in computer vision. However, acquiring high spatial resolution imagery may be difficult, especially on a large scale. Accordingly, less research has been carried out on the classification of medium and high spatial resolution satellite imagery in different study areas. Furthermore, the capacity of CNNs has been primarily investigated for the classification of urban areas, whereas there is limited research examining the potential of state-of-the-art classification tools for complex land cover mapping. Complex land cover units, such as wetland vegetation, are characterized by high intra- and low inter-class variance, resulting in difficulties in their discrimination relative to typical land cover classes. Thus, an environment with such highly heterogeneous land cover is beneficial for evaluating the capacity of CNNs for the classification of remote sensing data. Finally, the minimal application of well-known deep CNNs in remote sensing may be due to the limitation of input bands. Specifically, these convnets are designed to work with three input bands (e.g., Red, Green, and Blue), making them inappropriate for most remote sensing data. This indicates the significance of developing a pipeline compatible with multi-channel satellite imagery.

The main goals of this study were, therefore, to: (1) Eliminate the limitation of the number of input bands by developing a pipeline in Python with the capacity to operate with multi-layer remote sensing imagery; (2) examine the power of deep CNNs for the classification of spectrally similar wetland classes; (3) investigate the generalization capacity of existing CNNs for the classification of multispectral satellite imagery (i.e., a different dataset than those they were trained for); (4) explore whether full-training or fine-tuning is the optimal strategy for exploiting the pre-existing

227

convnets for wetland mapping; and (5) compare the efficiency of the most well-known deep CNNs, including DenseNet121, InceptionV3, VGG16, VGG19, Xception, ResNet50, and InceptionResNetV2, for wetland mapping in a comprehensive and elaborate analysis. Thus, this study contributes to the use of the state-of-the-art classification tools for complex land cover mapping using multispectral remote sensing data.

6.2. Materials and Methods

6.2.1. Deep Convolutional Neural Network

CNNs are constructed by multi-layer interconnected neural networks, wherein powerful low-, intermediate-, and high-level features are hierarchically extracted. A typical CNN framework has two main layers—the convolutional and pooling layers—that, together, are called the convolutional base of the network [13]. Some networks, such as AlexNet and VGG, also have fully connected layers. The convolutional layer has a filtering function and extracts spatial features from the images. Generally, the first convolutional layers extract low-level features or small local patterns, such as edges and corners, while the last convolutional layers extract high-level features, such as image structures. This suggests the high efficiency of CNNs for learning spatial hierarchical patterns. Convolutional layers are usually defined using two components: The convolution patch size (e.g., 3×3 or 5×5) and the depth of the output feature map, which is the number of filters (e.g., 32 filters). In particular, a rectangular sliding window with a fixed-size and a pre-defined stride is employed to produce convoluted feature maps using a dot product between the weights of the kernel and a small region of the input volume (i.e., the receptive field). A stride is defined as a distance between two consecutive convolutional windows. A stride of one is usually applied in convolutional layers since larger stride values result in down-sampling in feature maps [13]. A feature map is a new image generated by this simple convolution operation and is a visual

228

illustration of the extracted features. Given the weight-sharing property of CNNs, the number of parameters is significantly reduced compared to fully connected layer, since all the neurons across a particular feature map share the same parameters (i.e., weights and biases).

A non-linearity function, such as the Rectified Linear Unit (ReLU) [30], is usually applied as an elementwise nonlinear activation function to each component in the feature map. The ReLU function is advantageous relative to conventional activation functions used in traditional neural networks, such as the hyperbolic tangent or sigmoid functions, for adding non-linearity to the network [30]. The ReLU significantly accelerates the training phase relative to the conventional functions with gradient descent. This is because of the so-called vanishing gradient problem, wherein the derivatives of earlier functions (e.g., sigmoid) are extremely low in the saturating region and, accordingly, the updates for the weights nearly vanish.

Due to the presence of common pixels in each window, several feature maps may be produced that are very similar, suggesting redundant information. Therefore, pooling layers are used after each convolutional layer to decrease the variance of the extracted features using simple operations such as the maximizing or averaging operations. The max- and average-pooling layers determine the maximum and mean values, respectively, using a fixed-size sliding window and a pre-defined stride over the feature maps and, thereby, are conceptually similar to the convolutional layer. In contrast to convolutional layers, a stride of two or larger is applied in the pooling layers to down-sample the feature maps. Notably, the pooling layer, or the sub-sampling layer, generalizes the output of the convolutional layer into a higher level and selects the more robust and abstract features for the next layers. Thus, the pooling layer decreases computational complexity during the training stage by shrinking the feature maps.

As mentioned, some networks may have fully connected layers before the classifier layer that connect the output of several stacked convolutional and pooling layers to the classifier layer. Overfitting may arise in the fully connected layer because it occupies a large number of parameters. Thus, the dropout technique, an efficient regularization technique, is useful to mitigate or decrease problems associated with overfitting. During training, this technique randomly drops some neurons and their connections across the network, which prevents neurons from excess co-adaptation and contributes to developing more meaningful independent features [18]. The last layer is a classification layer, which determines the posterior probabilities for each category. A softmax classifier, also known as a normalized exponential, is the most commonly used classifier layer among the deep learning community in the image field. Stochastic Gradient Descent (SGD) optimization in a backpropagation workflow is usually used to train CNNs and to compute adjusting weights. This is an end-to-end learning process, from the raw data (i.e., original pixels) to the final label, using a deep CNN.

6.2.1.1. VGG

VGG network [25], the runner-up of the localization and classification tracks of the ILSVRC-2014 competition, is characterized by a deep network structure with a small convolutional filter of 3×3 compared to its predecessor, AlexNet [18]. VGG-VD group introduced six deep CNNs in the competition, among which two of them were more successful than the others, namely VGG16 and VGG19. The VGG16 consists of 13 convolutional layers and three fully connected layers, while the VGG19 has 16 convolutional layers and three fully connected layers. Both networks use a stack of small convolutional filters of 3×3 with stride 1, which are followed by multiple non-linearity layers (see Figure 6.1). This increases the depth of the network and contributes to learning

more complex features. The impressive results of VGG revealed that the network depth is an important factor in obtaining high classification accuracy [28].

(a)

(b)
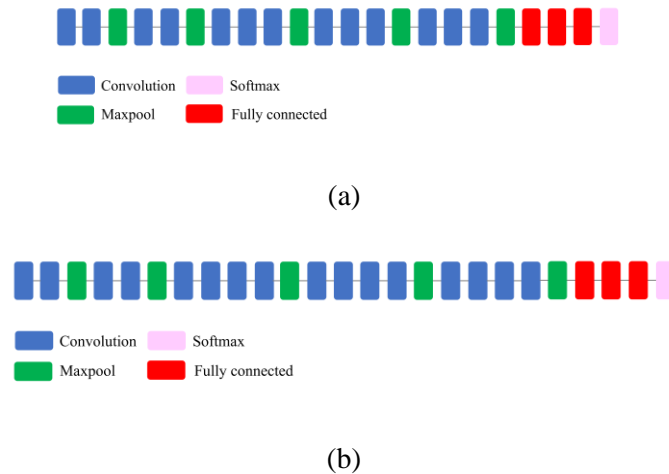
Figure 6.1. Schematic diagram of (a) VGG16 and (b) VGG19 models.

6.2.1.2. Inception

GoogLeNet, the winner of the classification and detection tracks of the ILSVRC-2014 competition, is among the first generation of non-sequential CNNs. In this network, both depth (i.e., the number of levels) and width (i.e., the number of units at each level), were increased without causing computational strain [19]. GoogLeNet is developed based on the idea that several connections between layers are ineffective and have redundant information due to the correlation between them. Accordingly, it uses an "Inception module", a sparse CNN, with 22 layers in a parallel processing workflow, and benefits from several auxiliary classifiers within the intermediate layers to improve the discrimination capacity in the lower layers. In contrast to conventional CNNs such as AlexNet and VGG, wherein either a convolutional or a pooling operation can be used at each level, the Inception module could benefit from both at each layer. Furthermore, filters (convolutions) with varying sizes are used at the same layer, providing more detailed information and extracting patterns with different sizes. Importantly, a 1×1 convolutional

layer, the so-called bottleneck layer, was employed to decrease both the computational complexity and the number of parameters. To be more precise, 1×1 convolutional layers were used just before a larger kernel convolutional filter (e.g., 3×3 and 5×5 convolutional layers) to decrease the number of parameters to be determined at each level (i.e., the pooling feature process). In addition, 1×1 convolutional layers make the network deeper and add more non-linearity by using ReLU after each 1×1 convolutional layer. In this network, the fully connected layers are replaced with an average pooling layer. This significantly decreases the number of parameters since the fully connected layers include a large number of parameters. Thus, this network is able to learn deeper representations of features with fewer parameters relative to AlexNet while it is much faster than VGG [27]. Figure 6.2 illustrates a compressed view of InceptionV3 employed in this study.
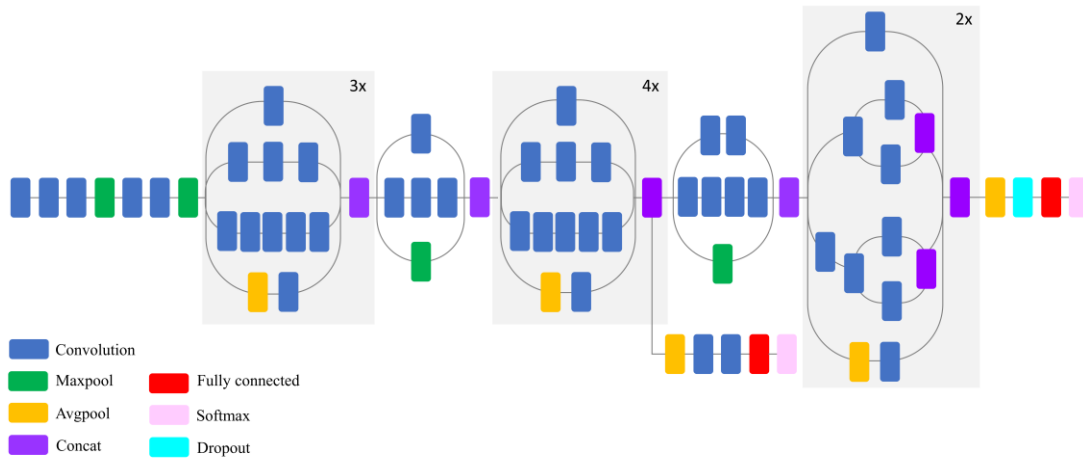
Figure 6.2. Schematic diagram of InceptionV3 model (compressed view).

6.2.1.3. ResNet

ResNet, the winner of the classification task in the ILSVRC-2015 competition, is characterized by a very deep network with 152 layers [26]. However, the main problems associated with the deep network are difficulty in training, high training error, and the vanishing gradient that causes learning to be negligible at the initial layers in the backpropagation step. The deep ResNet

configuration addresses the vanishing gradient problem by employing a deep residual learning module via additive identity transformations. Specifically, the residual module uses a direct path between the input and output and each stacked layer fits a residual mapping rather than directly fitting a desired underlying mapping [26]. Notably, the optimization is much easier on the residual map relative to the original, unreferenced map. Similar to VGG, 3×3 filters were mostly employed in this network; however, ResNet has fewer filters and less complexity relative to the VGG network [26]. Figure 6.3 illustrates a compressed view of ResNet, which was used in this study.
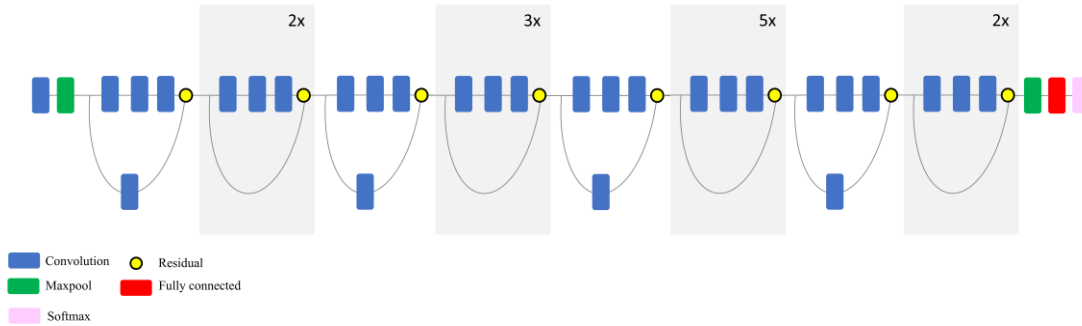
Figure 6.3. Schematic diagram of ResNet model (compressed view).

6.2.1.4. Xception

Xception network is similar to inception (GoogLeNet), wherein the inception module has been substituted with depth-wise separable convolutional layers [27]. Specifically, Xception's architecture is constructed based on a linear stack of a depth-wise separable convolution layer (i.e., 36 convolutional layers) with linear residual connections (see Figure 6.4). There are two important convolutional layers in this configuration: A depth-wise convolutional layer [31], where a spatial convolution is carried out independently in each channel of input data, and a pointwise convolutional layer, where a 1×1 convolutional layer maps the output channels to a new channel space using a depth-wise convolution.
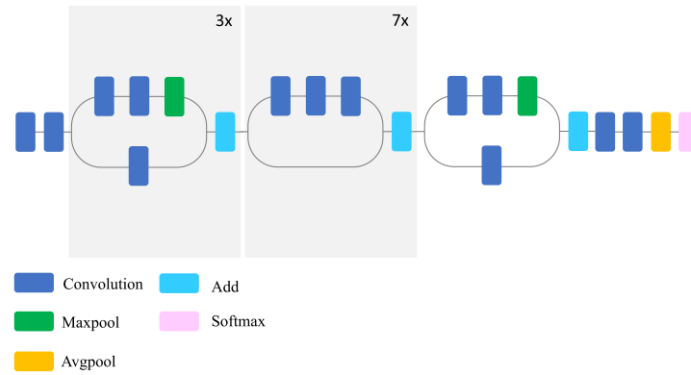
Figure 6.4. Schematic diagram of Xception model (compressed view).

6.2.1.5. InceptionResNetV2

This network is constructed by integrating the two most successful deep CNNs, ResNet [26] and Inception [19], wherein batch-normalization is used only on top of the traditional layers, rather than on top of the summations. In particular, the residual modules are employed in order to allow an increase in the number of Inception blocks and, accordingly, an increase in network depth. As mentioned earlier, the most pronounced problem associated with very deep networks is the training phase, which can be addressed using the residual connections [26]. The network scales down the residual as an efficient approach to address the training problem when a large number of filters (greater than 1,000 filters) is used in the network. Specifically, the residual variants experience instabilities and the network cannot be trained when the number of filters exceeds 1,000. Therefore, scaling the residual contributes to stabilizing network training [32]. Figure 6.5 illustrates a compressed view of InceptionResNetV2 used in this study.
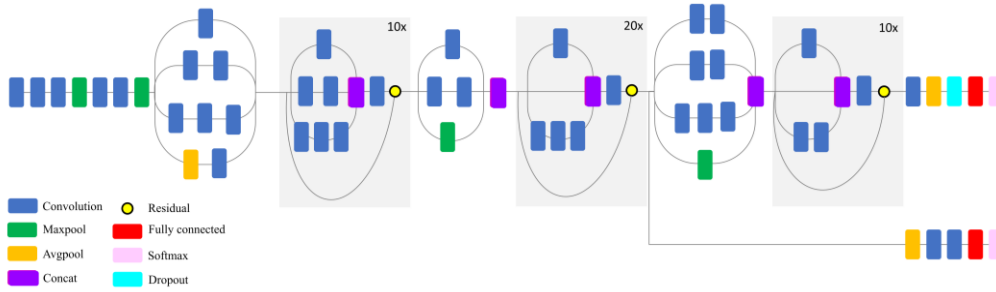
Figure 6.5. Schematic diagram of InceptionResNetV2 model (compressed view).

6.2.1.6. DenseNet

This network is also designed to address the vanishing gradient problem arising from the network depth. Specifically, all layers' connection architectures are employed to ensure maximum flow of information between layers [33]. In this configuration, each layer acquires inputs from all previous layers and conveys its own feature-maps to all subsequent layers. The feature maps are concatenated at each layer to pass information from preceding layers to the subsequent layers. This network architecture removes the necessity to learn redundant information and accordingly, the number of parameters is significantly reduced (i.e., parameter efficiency). It is also efficient for preserving information owing to its all layers connection property. Huang et al. (2017) reported that the network performed very well for classifications with a small training data set and the overfitting is not a problem when DenseNet121 is employed [33]. Figure 6.6 illustrates a compressed view of DenseNet employed in this study.
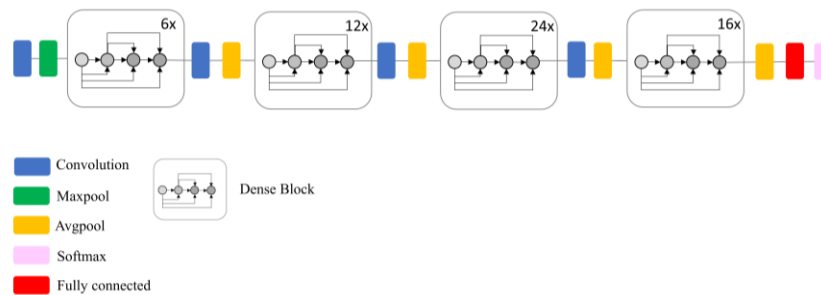
Figure 6.6. Schematic diagram of DenseNet model (compressed view).

235

6.2.2. Training

6.2.2.1. Fine-Tuning of a Pre-Trained Network

Fine-tuning of a pre-trained network is an optimal solution when a limited number of training samples are available. In this case, a fine adjustment is performed on the parameters of the top layers in a pre-trained network, while the first layers, representing general features, are frozen. Freezing is when weights for a layer or a set of layers are not updated during the training stage. Importantly, this approach benefits from the parameters learned from a network that has been previously trained using a specific dataset and, subsequently, adjusts the parameters for the dataset of interest. Accordingly, fine-tuning adjusts the parameters of the reused model, making it more relevant to the dataset of interest. Fine-tuning can be performed for either all layers or the top layers of a pre-trained network; however, the latter approach is preferred [13]. This is because the first layers in convnets encode generic, reusable features, whereas the last layers encode more specific features. Thus, it is more efficient to fine-tune those specific features. Furthermore, fine-tuning of all layers causes overfitting due to the large number of parameters, which should be determined during this process [13]. As such, in this study, fine-tuning of pre-existing convnets was carried out only on the top three layers. These may be either the fully connected layers alone (e.g., VGG) or both the fully connected and convolutional layers (e.g., Xception). Accordingly, the fine-tuning of the top three layers allowed us to compare the efficiency of fine-tuning for both fully connected and convolutional layers.

Notably, the number of input bands for these CNNs is limited to three because they have been trained using the ImageNet dataset; however, RapidEye imagery has five bands. Therefore, a band selection technique was pursued to determine three uncorrelated bands of RapidEye imagery most appropriate for use in CNNs. The results of this analysis demonstrated that green, red, and near-

infrared bands contain the least redundant information and thus, they were selected for fine-tuning of CNNs in this study.

6.2.2.2. Full-Training

Full-training is feasible when a large number of training samples is available to aid in converging the network [22]. In this case, there is a full control on the network parameters and, additionally, more relevant features are produced since the network is specifically tuned with the dataset of interest. However, the full-training of a network from scratch is challenging due to computational and data strains, leading to overfitting problems. Some techniques, such as dropout layers and data augmentation and normalization, are useful for mitigating the problems that arise from overfitting. In particular, data augmentation, introduced by Krizhevsky in 2012, is a process that produces more training samples from existing training data using a number of random transformations (e.g., image translation and horizontal reflection) [18]. The main goal is that the model will never look at the same image twice. In particular, the model explores more aspects of the data, which contributes to a better generalization [13].

Notably, there are two different categories in the case of full-training of convnets. In the first category, a new CNN architecture is fully designed and trained from scratch. In this case, the number of convolutional, and pooling layers, neurons, the type of activation function, the learning rate, and the number of iterations should be determined. Conversely, the second strategy benefits from a pre-existing architecture and full-training is only employed using a given dataset. In the latter case, the network architecture and the number of parameters remain unchanged.

In this study, the second strategy was employed. In particular, we examined the potential of a number of pre-existing networks (e.g., VGG, Inception, and etc.,) for classification of complex

land cover when they are trained from scratch using a new dataset substantially different from those (e.g., ImageNet) for which it was originally trained. Notably, full-training was employed for both three and five bands of RapidEye imagery. The full-training of three bands was performed to make the results comparable with those of the fine-tuning strategy.

6.2.3. Study Area and Satellite Data

The study area is located in the northeast portion of the Avalon Peninsula, Newfoundland and Labrador, Canada. Figure 6.7 shows the geographic location of the study area.
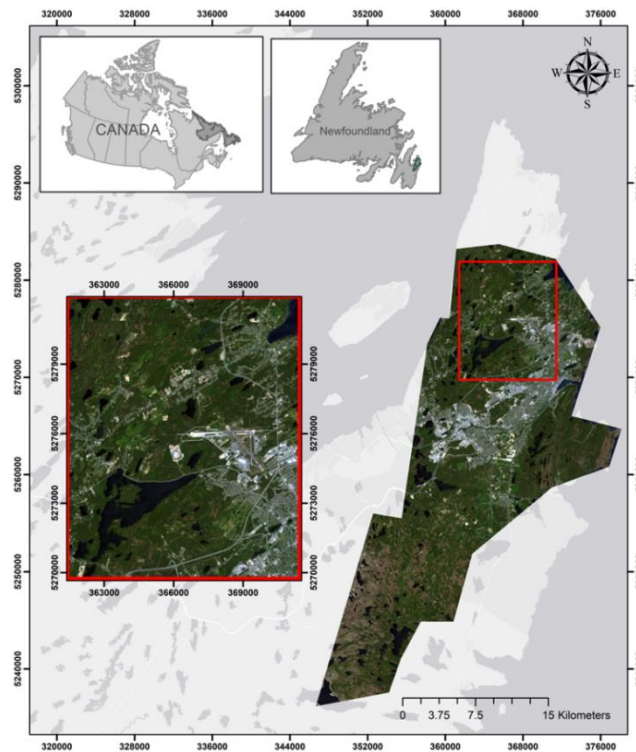
Figure 6.7. A true color composite of RapidEye optical imagery (bands 3, 2, and 1) acquired on 18 June, 2015, illustrating the geographic location of the study area. The red rectangle, the so-called test-zone, was selected to display the classified maps obtained from different approaches. Note that the training samples within the rectangle were excluded during the training stage for deep Convolutional Neural Networks (CNNs).

Land cover in the study area comprises a wide variety of wetland classes categorized by the Canadian Wetland Classification System (CWCS), including bog, fen, marsh, swamp, and shallow water [1]. Wetlands are characterized as complex species with high intra-class variance and low inter-class variance. Additionally, these classes are extremely different from typical objects found in the ImageNet dataset. Such a diverse ecological ecosystem is an ideal setting in which the efficiency and robustness of the state-of-the-art classification algorithms in a comprehensive and comparative study may be examined. Other land-cover classes found in the study area include urban, upland, and deep water classes. Figure 6.8 illustrates ground photo examples of land cover classes in this study.

(a)	(b)	(c)	(d)
(e)	(f)	(g)	(h)
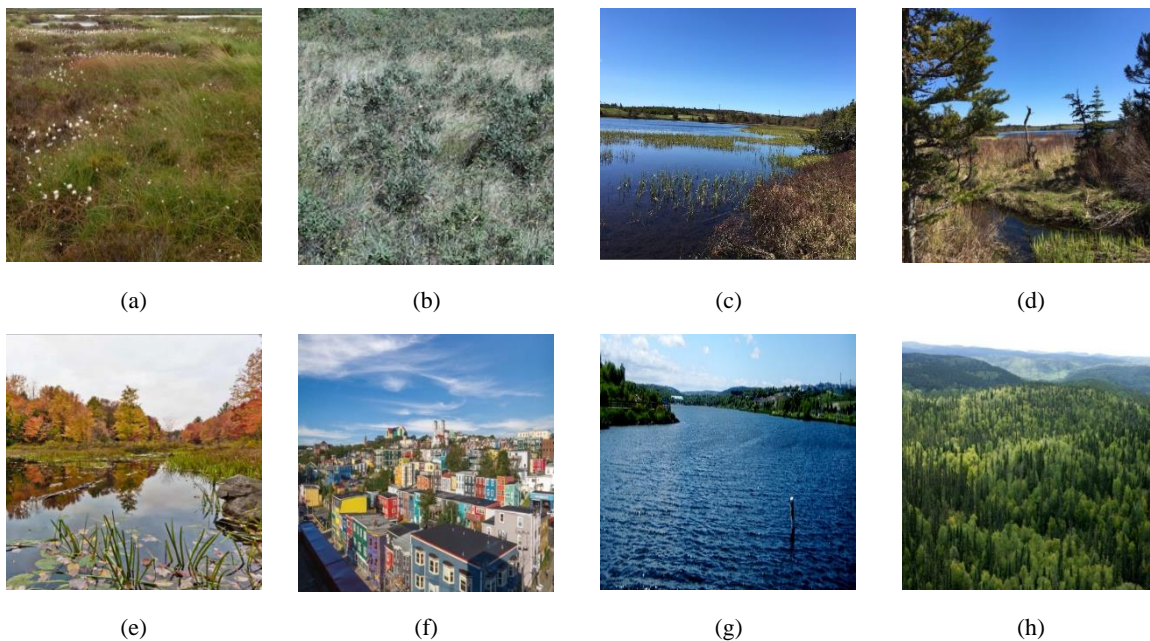
Figure 6.8. Ground reference photos showing land cover classes in the study area: (a) Bog; (b) fen; (c) marsh; (d) swamp; (e) shallow water; (f) urban; (g) deep water; and (h) upland.

Two level 3A multispectral RapidEye images with a spatial resolution of five meters, acquired on 18 June and 22 October 2015, were used for classification in this study. This imagery has five

spectral bands, namely blue (440–510 nm), green (520–590 nm), red (630–685 nm), red edge (690–730 nm), and near-infrared (760–850 nm).

6.2.4. Training, Validation, and Testing Data

Field data were acquired for 257 ground sites in the summer and fall of 2015, 2016, and 2017 by collecting Global Positioning System (GPS) points at each site. For reference data preparation, polygons were sorted by size and alternately assigned to testing and training groups. This resulted in both the testing and training groups containing equal numbers of small and large wetland polygons to allow for similar pixel counts and to account for the high variation of intra-wetland size.

Importantly, five tiles of RapidEye optical images were mosaicked to cover the whole study region. The training polygons within the red rectangle (i.e., one RapidEye tile; see Figure 6.7), the so-called test-zone, were removed for the training of deep CNNs. In particular, all patches within the test-zone were only used for testing (i.e., accuracy assessment) of CNNs. Of the training sample data, 80% and 20% were used for training and validation, respectively. Notably, both training and validation were carried out using the first RapidEye image (18 June, 2015); however, the testing was applied only to the second RapidEye image (22 October, 2015), within the test-zone (see Figure 6.7, the red rectangle), to perform the robust classification accuracy assessment.

Accordingly, the training and testing samples were obtained from independent polygons from distinct geographic regions using satellite imagery acquired at different times. This procedure prevents information leaking from the testing dataset to the model by employing two spatially and geographically independent samples for training and testing.

6.2.5. Experiment Setup

A multispectral satellite image in three dimensions is represented as m × n × h, a 3D tensor, where m and n indicate the height and width of the image, respectively, and h corresponds to the number of channels. On the other hand, convnets require a 3D tensor as input and, accordingly, a patch-based labeling method was used in this study because it inherently aligns with CNNs. Using this approach, the multispectral image was decomposed into patches, which have both spectral and spatial information for a given pixel, and a class label is assigned to the center of each patch [34].

An optimal patch size was determined using a trial-and-error procedure, by taking into account a spatial resolution of 5 m for the input image and the contextual relationship of the objects [35]. In particular, different patch sizes of 5, 10, 15, 20, 25, 30, 35, and 40 were examined, and the patch size of 30 was found to be the optimal value that extracts local spatial correlation within a given neighborhood and contains sufficient information to generate a specific distribution for each object in the image. Thus, we obtained 3D tensors with dimensions of either $30 \times 30 \times 5$ (when using 5 multispectral bands) or $30 \times 30 \times 3$ (when using 3 multispectral bands), which have both spatial and spectral information at a given location.

In the patch-based CNN, a particular class label is assigned to the given patch when a small rectangle in the center of that patch completely covers a single object. In this study, the training polygons were not rectangular, causing challenges during labeling when a patch contains more than one class. Accordingly, within a given patch size of 30×30, if an 8×8 rectangle covered only a single class (e.g., bog), then the label of this patch was assigned to that class (bog). Conversely, when this small rectangular window covered more than one class (e.g., both bog and fen), this patch was removed and excluded from further processing. Thus, the selected patches for

the training of convnets covered more than 50% of the object of interest and overcame the problem of edges that arise from multiple objects within a single patch.

The convnets used in this study include VGG16, VGG19, InceptionV3, Xception, DenseNet121, ResNet50, and InceptionResNetV2. The parameters of the original deep architecture were maintained during both fine-tuning and full-training. However, a learning rate of 0.01 and a decay rate of 10^{-4} were selected for full-training and fine-tuning experiments. The number of iterations was set to be 30,000 and 100,000 for fine-tuning and full-training, respectively. Cross-entropy and Stochastic Gradient Descent (SGD) were selected as the loss function and the optimization algorithm, respectively, during processing. As mentioned earlier, a patch size of 30 was selected and the images were resized to 224×224 for VGG16, VGG19, DenseNet121, and ResNet50, as well as to 299×299 for InceptionV3, Xception, and InceptionResNetV2. All these experiments were implemented using Google's library TensorFlow [36]. Table 6.1 presents the parameter settings and the characteristics of the deep convnets examined in this study.

In terms of computational complexity, the full-training strategy was more time intensive relative to the fine-tuning. This is because, in the former, the network must be trained from scratch, wherein weights and biases are randomly initialized and, accordingly, more time and resources are required for the model to be convergent. Table 6.1 (last column) represents the processing time when full-training of five bands (from scratch) was carried out. In order to determine the most accurate processing time, each network was fed by 800 images (100 images for each class) and the training time was measured. This procedure was repeated ten times and the average processing time for each network is presented in Table 6.1.

All experiments were carried out on an Intel CPU i7 4790 k machine with 3.6 GHz of clock and 32 GB RAM memory. A Nvidia GeForce GTX 1080 Ti GPU with 11 GB of memory under CUDA version 8.0 was also used in this study.

Table 6.1. The characteristics of deep convnets examined in this study.

ConvNet Models	Parameters (millions)	Depth	Processing Time [*] (s)
VGG16	138	23	18
VGG19	144	26	21
InceptionV3	24	159	10
ResNet50	26	168	12
Xception	23	126	16
InceptionResNetV2	56	572	19
DenseNet121	8	121	14

[*] Note: The processing time was calculated for training of 800 images (100 images for each class).

6.2.6. Evaluation Metrices

Three metrics, namely overall accuracy, Kappa coefficient, and F1-score, were used to quantitatively evaluate the performance of different classifiers. Overall accuracy represents the amount of correctly classified area for the whole image and is calculated by dividing the number of correctly classified pixels by the total number of pixels in the confusion matrix. The Kappa coefficient determines the degree of agreement between the reference data and the classified map. F1-score is a quantitative metric useful for imbalanced training data, and it measures the balance between precision and recall. Precision, also known as the positive predictive value, illustrates how many detected pixels for each category are true. Recall, also known as sensitivity, indicates how many actual pixels in each category are detected [37]. Accordingly, F1-score is formulated as follows:

$$F1 - score \ = \ 2 \ \times \frac{Precision \ \times Recall}{Precision + Recall} \qquad (6.1)$$

$$\text{Precision} = \frac{\text{True positives}}{\text{True positives} + \text{False positives}} \quad\quad (6.2)$$

$$R\text{ecall} = \frac{\text{True positives}}{\text{True positives} + \text{False negatives}} \quad\quad (6.3)$$

6.3. Results and Discussion

In this study, fine-tuning was employed for pre-existing, well-known convnets, which were trained based on the ImageNet dataset. Figure 6.9 demonstrates the validation and training accuracy and loss in the case of fine-tuning of convnets using the three selected bands of RapidEye imagery.
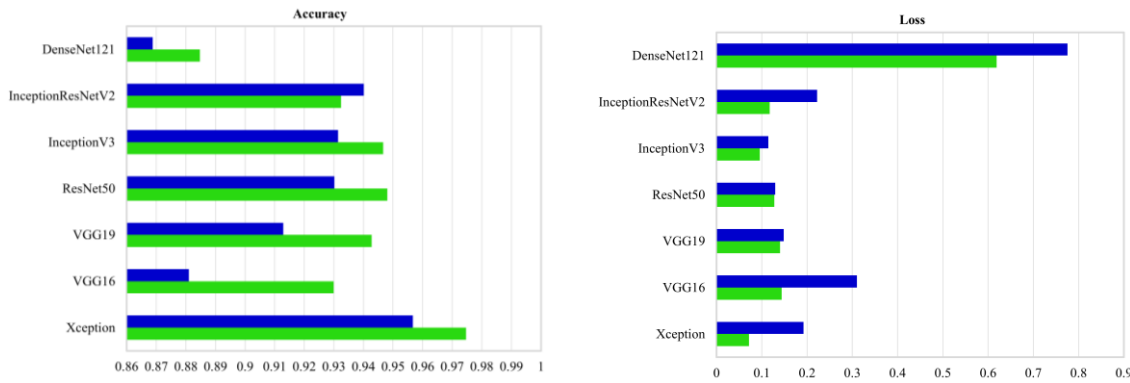
Figure 6.9. Comparing well-known convnets in terms of training and validation accuracy and loss when fine-tuning of three bands (i.e., Green, Red, and near-infrared (NIR)) was employed for complex wetland mapping.

As shown, DenseNet121 has the lowest validation accuracy, followed by VGG16. Conversely, the Xception network has the highest validation accuracy, followed by InceptionResNetV2. The two convnets, namely InceptionV3 and ResNet50, show relatively equal validation accuracies. Figure 6.10 shows the validation and training accuracy and loss in the case of training convnets from scratch when three bands of RapidEye imagery were employed.

Figure 6.10. Comparing well-known convnets in terms of training and validation accuracy and loss when networks were trained from scratch using three bands (i.e., Green, Red, and NIR) for complex wetland mapping.

As shown, all convnets, excluding DensNet121, perform very well for wetland classification when validation accuracies are compared. In particular, three convnets, including InceptionResNetV2, Xception, and VGG19, have higher training and validation accuracies relative to the other well-known convnets. Conversely, DenseNet121 has the lowest validation accuracy, suggesting that this network is less suitable for complex land cover mapping relative to the other convnets. Figure 6.11 shows the validation and training accuracy and loss in the case of training convnets from scratch when five bands of RapidEye imagery were employed.

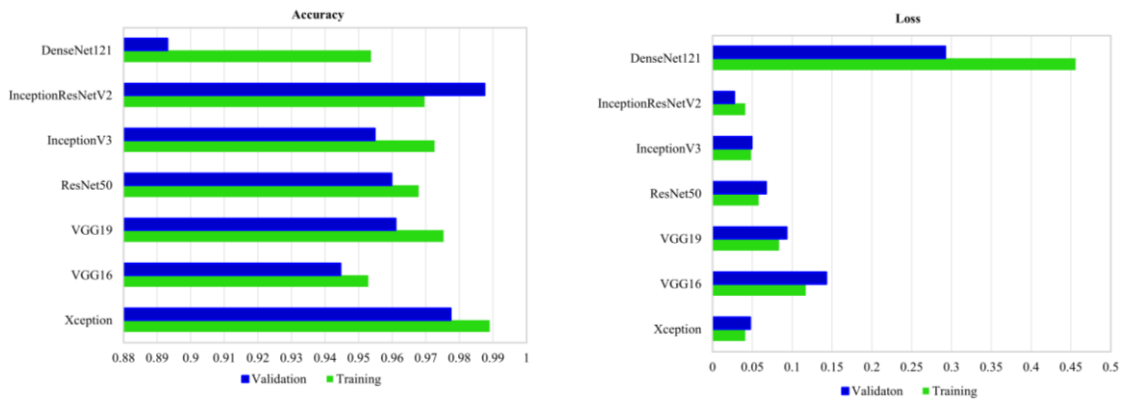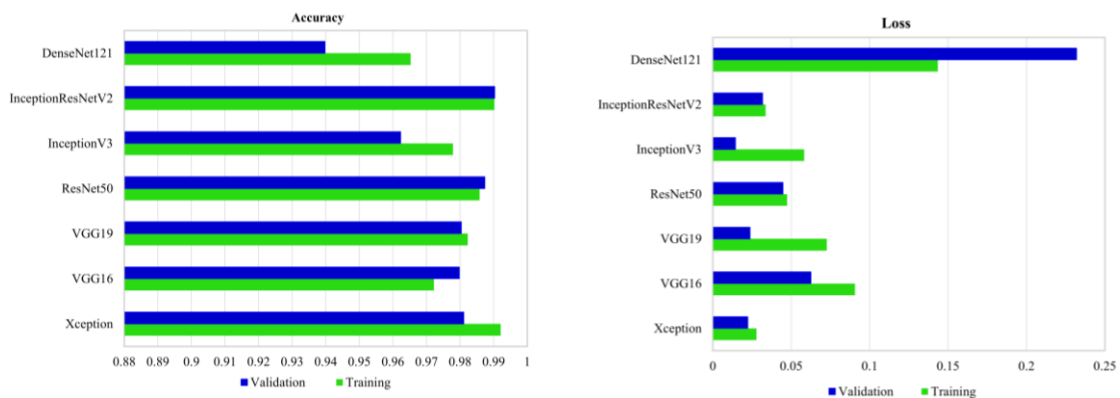Figure 6.11. Comparing well-known convnets in terms of training and validation accuracy and loss when networks were trained from scratch using five bands for complex wetland mapping.

245

The effects of increasing the number of bands are readily apparent by comparing Figures 6.10 and 6.11. Specifically, an increase in the number of bands improves classification accuracy in all cases. For example, the validation accuracy for DenseNet121 was lower than 90% when only three bands were employed. However, by increasing the number of bands, the validation accuracy reached to 94% for DenseNet121. InceptionResNetV2 again exhibited the highest validation accuracy, followed by ResNet50, Xception, and VGG19. Thus, the results indicate the significance of incorporating more spectral information for the classification of spectrally similar wetland classes (see Figures 6.10 and 6.11).

One of the most interesting aspects of the results obtained in this study is that the full-training strategy had better classification results relative to fine-tuning in all cases. Previous studies reported the superiority of fine-tuning relative to full-training for classification of very high resolution aerial imagery, although full-training was found to be more accurate relative to fine-tuning for classification of multi-spectral satellite data [38]. In particular, Nogueira et al. (2017) evaluated the efficiency of fine-tuning and full-training strategies of some well-known deep CNNs (e.g., AlexNet and GoogLeNet) for classification of three well-known datasets, including UCMerced land-use [39], RS19 dataset [40], and Brazilian Coffee Scenes [41]. The fine-tuning strategy yielded a higher accuracy for the first two datasets, likely due to their similarity with the ImageNet dataset, which was originally used for training deep CNNs. However, the full-training strategy had similar [22] or better results [38] relative to the fine-tuning for the Brazilian Coffee Scenes. This is because the latter dataset is multi-spectral (SPOT), containing finer and more homogeneous textures, wherein the patterns visually overlap substantially and, importantly, differ from the objects commonly found within the ImageNet dataset [22]. The results obtained from the latter dataset are similar to those found in our study. In particular, there is a significant difference

between the original training datasets of these convnets and our dataset. Fine-tuning is an optimal solution when the edges and local structures within the dataset of interest are similar to those for which the networks were trained. However, the texture, color, edges, and local structures of the typical objects found in the ImageNet dataset differ from the objects found in the wetland classes. Moreover, our dataset is intrinsically different from the ImageNet dataset used for pre-training. In particular, our dataset has five spectral bands, namely red, green, blue, red-edge, and near-infrared, all of which are essential for classifying spectrally similar wetland classes. However, the ImageNet dataset has only the red, green, and blue bands [38]. This could explain the differences between validation accuracies obtained in the case of full-training and fine-tuning (see Figures 6.9 and 6.10). Nevertheless, the results obtained from fine-tuning are still very promising, taking into account the complexity of wetland classes and the high classification accuracy obtained in most cases. In particular, an average validation accuracy of greater than 86% was achieved in all cases (see Figure 6.9), suggesting the generalizability and versatility of pre-trained deep convnets for the classification of various land cover types. It is also worth noting that fine-tuning was employed on the top three layers of convnets in this study. However, the results could be different upon including more layers in the fine-tuning procedure.

Having obtained higher accuracies via full-training of five bands, the classification results obtained from this strategy were selected for further analysis. These classification results were also compared with the results obtained from two conventional machine learning tools (i.e., SVM and RF). For this purpose, a total number of eight features were used as input features for both the SVM and RF classifiers. These features were Normalized Difference Vegetation Index (NDVI), Normalized Difference Water Index (NDWI), Red-edge Normalized Difference Vegetation Index (ReNDVI), and all the original spectral bands of the RapidEye image. Table 6.2 represents the

overall accuracy, Kappa coefficient, and F1-score using different CNNs (full-training of five bands), RF, and SVM for wetland classification in this study.

Table 6.2. Overall accuracies (%), Kappa coefficients, and F1-score (%) for wetland classification using different deep convnets (full-training of five bands), Random Forest (RF), and Support Vector Machine (SVM).

Methods	Overall Accuracy	Kappa Coefficient	F1
SVM	74.89	0.68	53.58
RF	76.08	0.70	58.87
DenseNet121	84.78	0.80	72.61
InceptionV3	86.14	0.82	75.09
VGG16	87.77	0.84	78.13
VGG19	90.94	0.88	84.20
Xception	93.57	0.92	89.55
ResNet50	94.81	0.93	91.39
InceptionResNetV2	96.17	0.95	93.66

As seen in Table 6.2, SVM and RF have the lowest classification accuracies and F1-scores relative to all deep convnets in this study. Among deep convnets, InceptionResNetV2 has the highest classification accuracy, 96.17%, as well as the highest F1-score, 93.66%, followed by ResNet50 and Xception with overall accuracies of 94.81% and 93.57%, as well as F1-scores of 91.39% and 89.55%, respectively. Conversely, DenseNet121 and InceptionV3 have the lowest overall accuracies, 84.78% and 86.14%, as well as F1-scores, 72.61% and 75.09%, respectively. VGG19 was found to be more accurate than VGG16 by about 3% (OA), presumably due to the deeper structure of the former convnet. These results are in general agreement with [42], which reported the superiority of ResNet relative to GoogLeNet (Inception), VGG16, and VGG19 for the classification of four public remote sensing datasets (e.g., UCM, WHU-RS19). InceptionResNetV2 benefits from integrating two well-known deep convnets, Inception and ResNet, which positively contribute to the most accurate result in this study. This also suggests that the extracted features from different convnets are supplementary and improve the model's

classification efficiency. The results demonstrated that deeper networks (e.g., InceptionResNetV2) have a greater efficiency in extracting varying degrees of abstraction and representation within the hierarchical learning scheme [43]. In particular, they are more efficient in separating the input space into more detailed regions, owing to their deeper architecture, that contributes to a better separation of complex wetland classes.

As shown in Figure 6.12, all deep networks were successful in classifying non-wetland classes, including urban, deep water, and upland classes, with an accuracy greater than 94% in all cases. SVM and RF also correctly classified the non-wetland classes with an accuracy exceeding 96% in most cases (excluding upland). Interestingly, all deep networks correctly classified the urban class with an accuracy of 100%, suggesting the robustness of the deep learning features for classification of complex human-made structures (e.g., buildings and roads). This observation fits well with [13]. However, the accuracy of the urban class did not exceed 97% when either RF or SVM was employed.
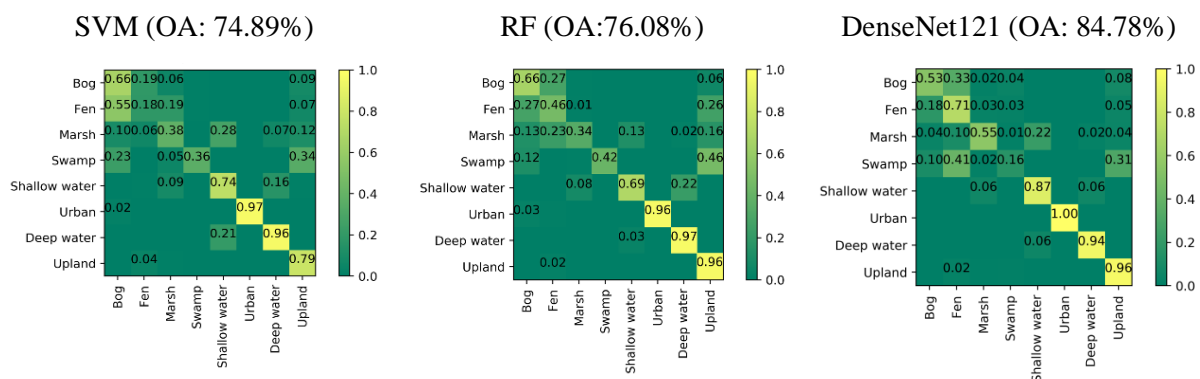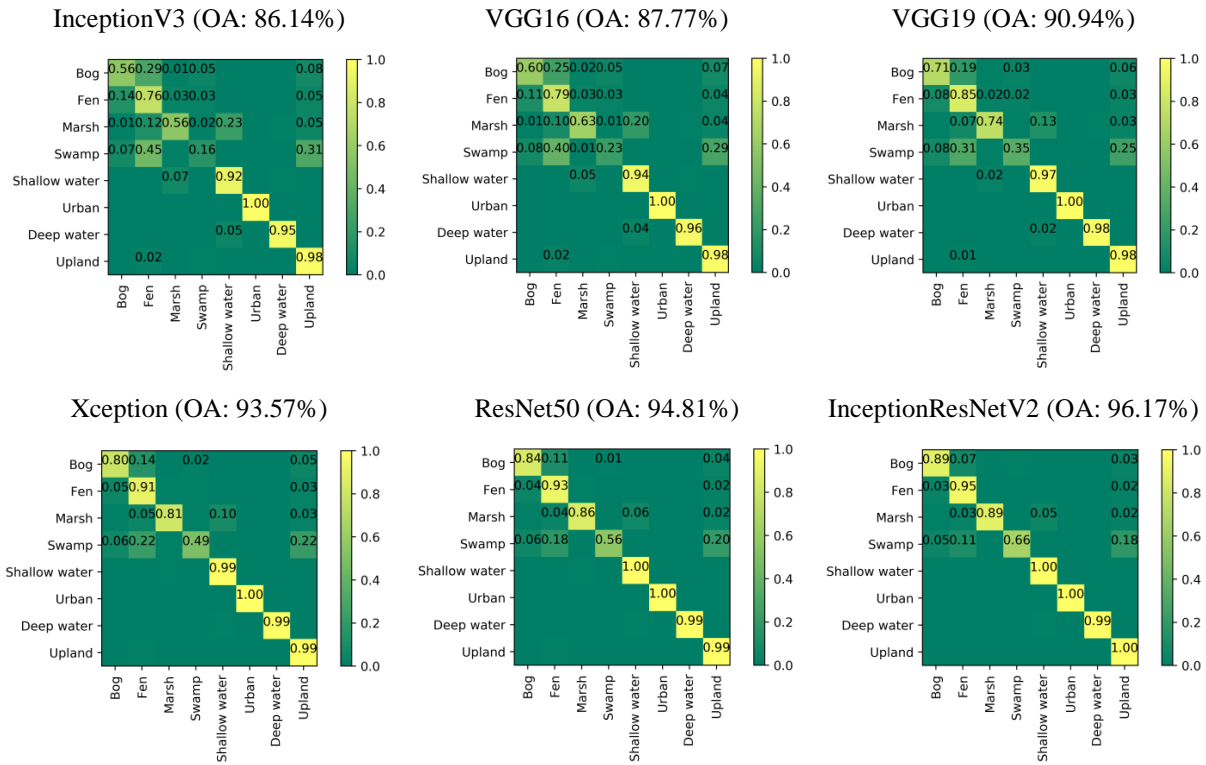
Figure 6.12. Normalized confusion matrix of the wetland classification for different networks in this study (full-training of five optical bands), Random Forest (RF), and Support Vector Machine (SVM).

The confusion matrices demonstrate that, by using the last three networks, a significant improvement was achieved in the accuracy of both overall and individual classes. In particular, InceptionResNetV2 correctly classified non-wetland classes with an accuracy of 99% for deep water and 100% for both urban and upland classes. ResNet50 and Xception were also successful in distinguishing non-wetland classes with an accuracy of 100% for urban and 99% for both deep water and upland. One possible explanation for why the highest accuracies were obtained for these classes is the availability of larger amounts of training samples for non-wetland classes relative to wetland classes.

Although RF and SVM, as well as the convnets, performed very well in distinguishing non-wetland classes, the difference in accuracy between the two groups (i.e., conventional classifiers versus deep networks) was significant for wetland classes. This was particularly true for the last

three convnets compared to SVM and RF. Specifically, the three networks of InceptionResNetV2, ResNet50, and Xception were successful in classifying all wetland classes with accuracies exceeding 80%, excluding the swamp wetland. This contrasts with the results obtained from SVM and RF, wherein the accuracies were lower than 74% for all wetland classes. Overall, the swamp wetland had the lowest accuracy among all classes using the deep convnets. As the effectiveness of these networks largely depends on the numbers of the training samples, the lowest accuracy of the swamp wetland could be attributable to the low availability of training samples for this class.

A large degree of confusion was observed between herbaceous wetlands, namely marsh, bog, and fen (especially between bog and fen), when DenseNet121, InceptionV3, and VGG16 were employed. The largest confusion between bog and fen is possibly due to the very similar visual features of these classes (see Figure 6.8). These two classes are both peatland dominated with different species of Sphagnum in bogs and Graminoid in fens. According to field biologist reports, these two classes were adjacent successional classes with a heterogeneous nature and were hardly distinguished from each other during the in-situ field data collection.

Overall, confusion was more pronounced among the first four deep networks, whereas it was significantly reduced when the last three networks were employed (see Figure 6.12). This suggests that the last three networks and, especially, InceptionResNetV2, are superior for distinguishing confusing wetland classes relative to the other convnets. For example, the classes of bog and fen were correctly classified with accuracies of greater than 89% when InceptionResNetV2 was used. Both Xception and ResNet50 were also found to successfully classify these two classes with accuracies of higher than 80%. Overall, the wetland classification accuracies obtained from these three networks were strongly positive for several spectrally and spatially similar wetland classes (e.g., bog, fen, and marsh) and demonstrate a large number of correctly classified pixels.

Cropped images of the classified maps obtained from SVM, RF, DenseNet121, and InceptionResNetV2 are depicted in Figure 6.13. As shown, the classified maps obtained from convnets better resemble the real ground features. Both classified maps, obtained from convnets (Figure 6.13d,e) show a detailed distribution of all land cover classes; however, the classified map obtained from InceptionResNetV2 (Figure 6.13e) is more accurate when it is compared with optical imagery (Figure 6.13a). For example, in the classified map obtained from DenseNet121, the fen class was misclassified as bog and upland classes in some cases (Figure 6.13d). This, too, occurred between shallow water and deep water; however, this was not the case when InceptionResNetV2 was employed. In particular, most land cover classes obtained from InceptionResNetV2 are accurate representations of ground features. This conclusion was based on the confusion matrix (see Figure 6.12) and further supported by a comparison between the classified map and the optical data (Figure 6.13a, e).
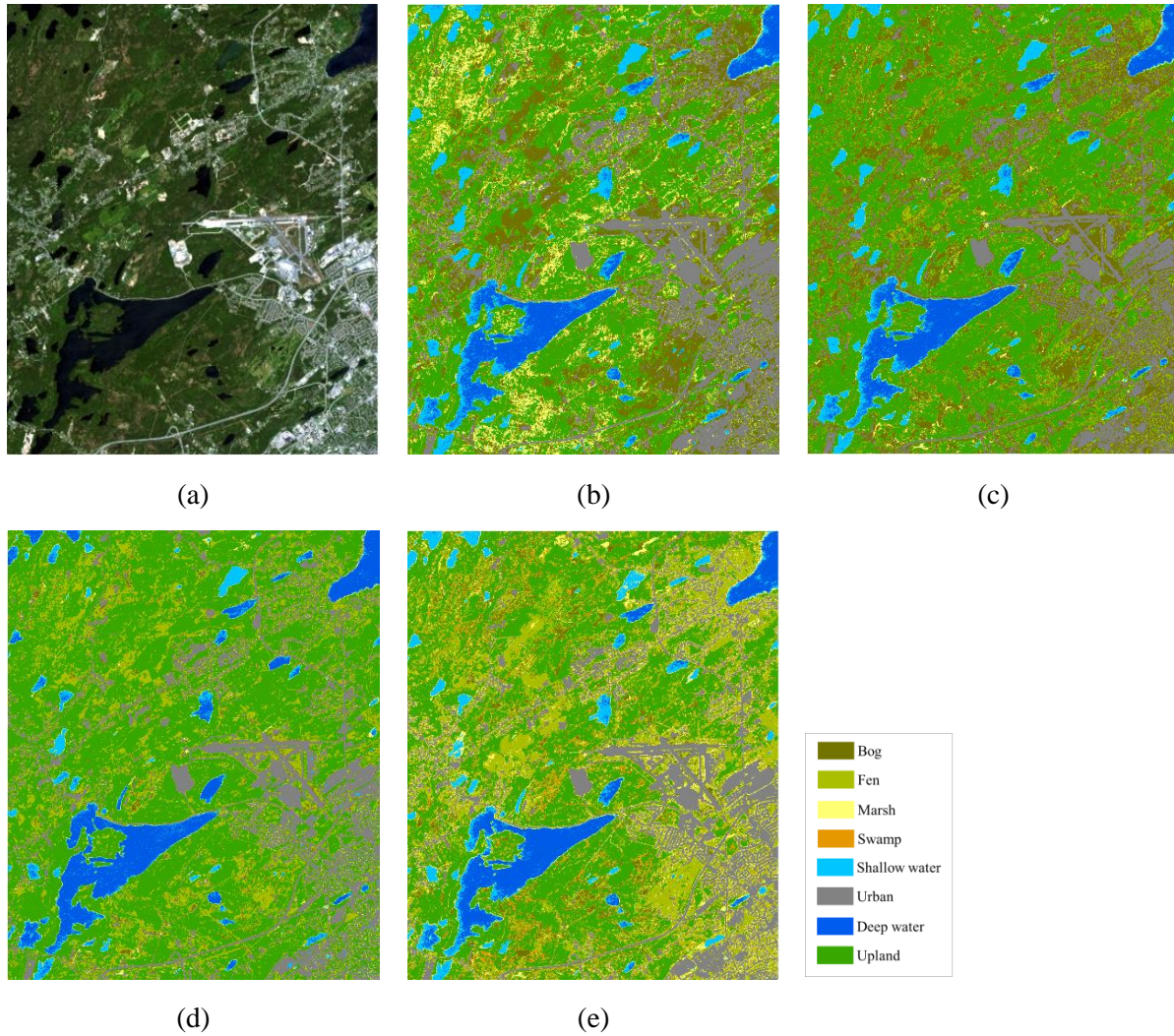
Figure 6.13. (a) True color composite of RapidEye optical imagery (bands 3, 2, and 1). A crop of the classified maps obtained from (b) SVM, (c) RF, (d) DenseNet121, and (e) InceptionResNetV2.

Figure 6.14 shows two-dimensional features extracted from the last layer of the InceptionResNetV2 (a) and DenseNet121 (b) using the two-dimensional t-SNE algorithm [44]. The features from InceptionResNetV2 demonstrate a clear semantic clustering. In particular, most classes are clearly separated from each other; however, the feature clusters of bog and fen show some degree of confusion. Conversely, the features from DenseNet121 only generate a few visible clusters (e.g., upland and urban), while other features corresponding to wetland classes overlap with each other, suggesting a large degree of confusion.

(a)	(b)
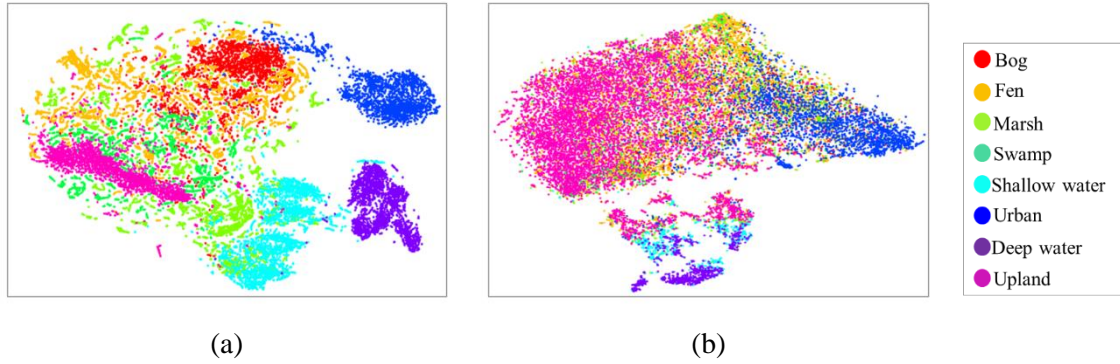
Figure 6.14. A 2-D feature visualization of global image representation of the wetland classes using the t-SNE algorithm for the last layer of (a) InceptionResNetV2 and (b) DenseNet121. Each color illustrates a different class in the dataset.

6.4. Conclusion

Wetlands are characterized by complex land cover with high intra-class variability and low inter-class disparity, posing several challenges to conventional machine learning tools in classification tasks. To date, the discrimination of such complex land cover classes using conventional classifiers heavily relies on a large number of hand-crafted features incorporated into the classification scheme. In this research, we used state-of-the-art deep learning tools, deep Convolutional Neural Networks, to classify such a heterogeneous environment to address the problem of extracting a large number of hand-crafted features. Two different strategies of employing pre-existing convnets were investigated: Full-training and fine-tuning. The potential of the most well-known deep convnets, currently employed for several computer vision tasks, including DenseNet121, InceptionV3, VGG16, VGG19, Xception, ResNet50, and InceptionResNetV2, was examined in a comprehensive and elaborate framework using multispectral RapidEye optical data for wetland classification.

The results of this study revealed that the incorporation of high-level features learned by a hierarchical deep framework is very efficient for the classification of complex wetland classes.

254

Specifically, the results illustrate that the full-training of pre-existing convnets using five bands is more accurate than both full-training and fine-tuning using three bands, suggesting that the extra multispectral bands provide complementary information. In this study, InceptionResNetV2 consistently outperformed all other convnets for the classification of wetland and non-wetland classes with a state-of-the-art overall classification accuracy of about 96%, followed by ResNet50 and Xception, with accuracies of about 94% and 93%, respectively. The impressive performance of InceptionResNetV2 suggests that an integration of the Inception and ResNet modules is an effective architecture for complex land cover mapping using multispectral remote sensing images. The individual class accuracy illustrated that confusion occurred between wetland classes (herbaceous wetlands), although it was less pronounced when InceptionResNetV2, ResNet50, and Xception were employed. The swamp wetland had the lowest accuracy in all cases, potentially because the lowest number of training samples was available for this class. It is also worth noting that all deep convnets were very successful in classifying non-wetland classes in this study.

The results of this study demonstrate the potential for the full exploitation of pre-existing deep convnets for the classification of multispectral remote sensing data, which are significantly different than large datasets (e.g., ImageNet) currently employed in computer vision. Given the similarity of wetland classes across Canada, the deep trained networks in this study provide valuable baseline information and tools, and will substantially contribute to the success of wetland mapping in this country using state-of-the-art remote sensing data.

6.5. References

[1]   R. W. Tiner, M. W. Lang, and V. V Klemas, *Remote sensing of wetlands: applications and advances*. CRC Press, 2015.

[2]   M. Mahdianpari, B. Salehi, F. Mohammadimanesh, and M. Motagh, "Random forest wetland classification using ALOS-2 L-band, RADARSAT-2 C-band, and TerraSAR-X imagery," *ISPRS J. Photogramm. Remote Sens.*, vol. 130, 2017.

[3]   T. L. Evans and M. Costa, "Landcover classification of the Lower Nhecolândia subregion of the Brazilian Pantanal Wetlands using ALOS/PALSAR, RADARSAT-2 and ENVISAT/ASAR imagery," *Remote Sens. Environ.*, vol. 128, pp. 118–137, 2013.

[4]   F. Mohammadimanesh, B. Salehi, M. Mahdianpari, B. Brisco, and M. Motagh, "Multi-temporal, multi-frequency, and multi-polarization coherence and SAR backscatter analysis of wetlands," *ISPRS J. Photogramm. Remote Sens.*, vol. 142, pp. 78–93, 2018.

[5]   E. Adam, O. Mutanga, and D. Rugege, "Multispectral and hyperspectral remote sensing for identification and mapping of wetland vegetation: a review," *Wetl. Ecol. Manag.*, vol. 18, no. 3, pp. 281–296, 2010.

[6]   M. Rezaee, M. Mahdianpari, Y. Zhang, and B. Salehi, "Deep Convolutional Neural Network for Complex Wetland Classification Using Optical Remote Sensing Imagery," *IEEE J. Sel. Top. Appl. Earth Obs. Remote Sens.*, 2018.

[7]   M. Mahdianpari *et al.*, "Fisher Linear Discriminant Analysis of coherency matrix for wetland classification using PolSAR imagery," *Remote Sens. Environ.*, vol. 206, 2018.

[8]   T. Blaschke, "Object based image analysis for remote sensing," *ISPRS J. Photogramm. Remote Sens.*, vol. 65, no. 1, pp. 2–16, 2010.

[9]   W. Zhao and S. Du, "Learning multiscale and deep representations for classifying remotely sensed imagery," *ISPRS J. Photogramm. Remote Sens.*, vol. 113, pp. 155–165, 2016.

[10]   Q. Jackson and D. A. Landgrebe, "Adaptive Bayesian contextual classification based on Markov random fields," *IEEE Trans. Geosci. Remote Sens.*, vol. 40, no. 11, pp. 2454–2463, 2002.

[11]   Y. Zhong, J. Zhao, and L. Zhang, "A hybrid object-oriented conditional random field classification framework for high spatial resolution remote sensing imagery," *IEEE Trans. Geosci. Remote Sens.*, vol. 52, no. 11, pp. 7023–7037, 2014.

[12]   G. Camps-Valls, L. Gomez-Chova, J. Muñoz-Marí, J. Vila-Francés, and J. Calpe-Maravilla, "Composite kernels for hyperspectral image classification," *IEEE Geosci. Remote Sens. Lett.*, vol. 3, no. 1, pp. 93–97, 2006.

[13]   F. Chollet, *Deep learning with python*. Manning Publications Co., 2017.

[14]   Y. LeCun, Y. Bengio, and G. Hinton, "Deep learning," *Nature*, vol. 521, no. 7553, p. 436, 2015.

[15] J. E. Ball, D. T. Anderson, and C. S. Chan, "Comprehensive survey of deep learning in remote sensing: theories, tools, and challenges for the community," *J. Appl. Remote Sens.*, vol. 11, no. 4, p. 42609, 2017.

[16] G. E. Hinton, S. Osindero, and Y.-W. Teh, "A fast learning algorithm for deep belief nets," *Neural Comput.*, vol. 18, no. 7, pp. 1527–1554, 2006.

[17] P. Vincent, H. Larochelle, I. Lajoie, Y. Bengio, and P.-A. Manzagol, "Stacked denoising autoencoders: Learning useful representations in a deep network with a local denoising criterion," *J. Mach. Learn. Res.*, vol. 11, no. Dec, pp. 3371–3408, 2010.

[18] A. Krizhevsky, I. Sutskever, and G. E. Hinton, "Imagenet classification with deep convolutional neural networks," in *Advances in neural information processing systems*, 2012, pp. 1097–1105.

[19] C. Szegedy *et al.*, "Going deeper with convolutions," 2015.

[20] D. Marmanis, K. Schindler, J. D. Wegner, S. Galliani, M. Datcu, and U. Stilla, "Classification with an edge: improving semantic image segmentation with boundary detection," *ISPRS J. Photogramm. Remote Sens.*, vol. 135, pp. 158–172, 2018.

[21] X. Chen, S. Xiang, C.-L. Liu, and C.-H. Pan, "Vehicle detection in satellite images by hybrid deep convolutional neural networks," *IEEE Geosci. Remote Sens. Lett.*, vol. 11, no. 10, pp. 1797–1801, 2014.

[22] K. Nogueira, O. A. B. Penatti, and J. A. dos Santos, "Towards better exploiting convolutional neural networks for remote sensing scene classification," *Pattern Recognit.*, vol. 61, pp. 539–556, 2017.

[23] Y. LeCun, L. Bottou, Y. Bengio, and P. Haffner, "Gradient-based learning applied to document recognition," *Proc. IEEE*, vol. 86, no. 11, pp. 2278–2324, 1998.

[24] J. Deng, W. Dong, R. Socher, L.-J. Li, K. Li, and L. Fei-Fei, "Imagenet: A large-scale hierarchical image database," in *Computer Vision and Pattern Recognition, 2009. CVPR 2009. IEEE Conference on*, 2009, pp. 248–255.

[25] K. Simonyan and A. Zisserman, "Very deep convolutional networks for large-scale image recognition," *arXiv Prepr. arXiv1409.1556*, 2014.

[26] K. He, X. Zhang, S. Ren, and J. Sun, "Deep residual learning for image recognition," in *Proceedings of the IEEE conference on computer vision and pattern recognition*, 2016, pp. 770–778.

[27] F. Chollet, "Xception: Deep learning with depthwise separable convolutions," *arXiv Prepr.*, 2016.

[28] F. Hu, G.-S. Xia, J. Hu, and L. Zhang, "Transferring deep convolutional neural networks for the scene classification of high-resolution remote sensing imagery," *Remote Sens.*, vol. 7, no. 11, pp. 14680–14707, 2015.

[29] G. E. Hinton and R. R. Salakhutdinov, "Reducing the dimensionality of data with neural networks," *Science (80-.).*, vol. 313, no. 5786, pp. 504–507, 2006.

[30] V. Nair and G. E. Hinton, "Rectified linear units improve restricted boltzmann machines," in *Proceedings of the 27th international conference on machine learning (ICML-10)*, 2010, pp. 807–814.

[31] L. Sifre and S. Mallat, "Rotation, scaling and deformation invariant scattering for texture discrimination," in *Computer Vision and Pattern Recognition (CVPR), 2013 IEEE Conference on*, 2013, pp. 1233–1240.

[32] C. Szegedy, S. Ioffe, V. Vanhoucke, and A. A. Alemi, "Inception-v4, inception-resnet and the impact of residual connections on learning.," in *AAAI*, 2017, vol. 4, p. 12.

[33] G. Huang, Z. Liu, K. Q. Weinberger, and L. van der Maaten, "Densely connected convolutional networks," in *Proceedings of the IEEE conference on computer vision and pattern recognition*, 2017, vol. 1, no. 2, p. 3.

[34] K. Makantasis, K. Karantzalos, A. Doulamis, and N. Doulamis, "Deep supervised learning for hyperspectral data classification through convolutional neural networks," in *Geoscience and Remote Sensing Symposium (IGARSS), 2015 IEEE International*, 2015, pp. 4959–4962.

[35] C. Zhang *et al.*, "A hybrid MLP-CNN classifier for very fine resolution remotely sensed image classification," *ISPRS J. Photogramm. Remote Sens.*, 2017.

[36] M. Abadi *et al.*, "Tensorflow: Large-scale machine learning on heterogeneous distributed systems," *arXiv Prepr. arXiv1603.04467*, 2016.

[37] Y. Liu, B. Fan, L. Wang, J. Bai, S. Xiang, and C. Pan, "Semantic labeling in very high resolution images via a self-cascaded convolutional neural network," *ISPRS J. Photogramm. Remote Sens.*, vol. 145, pp. 78–95, 2018.

[38] M. Castelluccio, G. Poggi, C. Sansone, and L. Verdoliva, "Land use classification in remote sensing images by convolutional neural networks," *arXiv Prepr. arXiv1508.00092*, 2015.

[39] Y. Yang and S. Newsam, "Bag-of-visual-words and spatial extensions for land-use classification," in *Proceedings of the 18th SIGSPATIAL international conference on advances in geographic information systems*, 2010, pp. 270–279.

[40] G.-S. Xia, W. Yang, J. Delon, Y. Gousseau, H. Sun, and H. Maître, "Structural high-resolution satellite image indexing," in *ISPRS TC VII Symposium-100 Years ISPRS*, 2010, vol. 38, pp. 298–303.

[41] O. A. B. Penatti, K. Nogueira, and J. A. Dos Santos, "Do deep features generalize from everyday objects to remote sensing and aerial scenes domains?," in *Proceedings of the IEEE conference on computer vision and pattern recognition workshops*, 2015, pp. 44–51.

[42] W. Han, R. Feng, L. Wang, and Y. Cheng, "A semi-supervised generative framework with deep learning features for high-resolution remote sensing image scene classification," *ISPRS J. Photogramm. Remote Sens.*, 2017.

[43]   Y. Chen, Z. Lin, X. Zhao, G. Wang, and Y. Gu, "Deep learning-based classification of hyperspectral data," *IEEE J. Sel. Top. Appl. earth Obs. Remote Sens.*, vol. 7, no. 6, pp. 2094–2107, 2014.

[44]   L. van der Maaten and G. Hinton, "Visualizing data using t-SNE," *J. Mach. Learn. Res.*, vol. 9, no. Nov, pp. 2579–2605, 2008.

Chapter 7. Large-scale wetland mapping using fusion of PolSAR and optical imagery[6]

Preface

A version of this manuscript has been published in the *Remote Sensing Journal*. I am a primary author of this manuscript along with the co-authors, Bahram Salehi, Fariba Mohammadimanesh, Saeid Homayouni, and Eric Gill. I designed and conceptualized the study. I developed the model and performed all experiments and tests. I wrote the paper and revised it based on comments from all co-authors. I also revised the paper according to the reviewers' comments. The co-author, Fariba Mohammadimanesh, helped in performing the experiments and analyzing the results and contributed to revising the manuscript. All co-authors provided editorial input and scientific insights to further improve the paper. They also reviewed and commented on the manuscript.

---

[6] Mahdianpari, M., Salehi, B., Mohammadimanesh, F., Homayouni, S. and Gill, E., 2019. The First Wetland Inventory Map of Newfoundland at a Spatial Resolution of 10 m Using Sentinel-1 and Sentinel-2 Data on the Google Earth Engine Cloud Computing Platform. *Remote Sensing*, *11*(1), p.43.

Abstract

Wetlands are one of the most important ecosystems that provide a desirable habitat for a great variety of flora and fauna. Wetland mapping and modeling using Earth Observation (EO) data are essential for natural resource management at both regional and national levels. However, accurate wetland mapping is challenging, especially on a large scale, given their heterogeneous and fragmented landscape, as well as the spectral similarity of differing wetland classes. Currently, precise, consistent, and comprehensive wetland inventories on a national- or provincial-scale are lacking globally, with most studies focused on the generation of local-scale maps from limited remote sensing data. Leveraging the Google Earth Engine (GEE) computational power and the availability of high spatial resolution remote sensing data collected by Copernicus Sentinels, this study introduces the first detailed, provincial-scale wetland inventory map of one of the richest Canadian provinces in terms of wetland extent. In particular, multi-year summer Synthetic Aperture Radar (SAR) Sentinel-1 and optical Sentinel-2 data composites were used to identify the spatial distribution of five wetland and three non-wetland classes on the Island of Newfoundland, covering an approximate area of 106,000 km^2. The classification results were evaluated using both pixel-based and object-based random forest (RF) classifications implemented on the GEE platform. The results revealed the superiority of the object-based approach relative to the pixel-based classification for wetland mapping. Although the classification using multi-year optical data was more accurate compared to that of SAR, the inclusion of both types of data significantly improved the classification accuracies of wetland classes. In particular, an overall accuracy of 88.37% and a Kappa coefficient of 0.85 were achieved with the multi-year summer SAR/optical composite using an object-based RF classification, wherein all wetland and non-wetland classes were correctly identified with accuracies beyond 70% and 90%, respectively. The results suggest a paradigm-shift from standard static products and approaches toward generating more dynamic,

on-demand, large-scale wetland coverage maps through advanced cloud computing resources that simplify access to and processing of the "Geo Big Data." In addition, the resulting ever-demanding inventory map of Newfoundland is of great interest to and can be used by many stakeholders, including federal and provincial governments, municipalities, NGOs, and environmental consultants to name a few.

7.1. Introduction

Wetlands cover between 3% and 8% of the Earth's land surface [1]. They are one of the most important contributors to global greenhouse gas reduction and climate change mitigation, and they greatly affect biodiversity and hydrological connectivity [2]. Wetland ecosystem services include flood- and storm-damage protection, water-quality improvement and renovation, aquatic and plant-biomass productivity, shoreline stabilization, plant collection, and contamination retention [3]. However, wetlands are being drastically converted to non-wetland habitats due to both anthropogenic activities, such as intensive agricultural and industrial development, urbanization, reservoir construction, and water diversion, as well as natural processes, such as rising sea levels, thawing of permafrost, changing in precipitation patterns, and drought [1].

Despite the vast expanse and benefits of wetlands, there is a lack of comprehensive wetland inventories in most countries due to the expense of conducting nation-wide mapping and the highly dynamic, remote nature of wetland ecosystems [4]. These issues result in fragmented, partial, or outdated wetland inventories in most countries worldwide, and some have no inventory available at all [5]. Although North America and some parts of Western Europe have some of the most comprehensive wetland inventories, these are also incomplete and have considerable limitations related to the resolution and type of data, as well as to developed methods [6]. These differences make these existing inventories incomparable [1] and highlight the significance of long-term comprehensive wetland monitoring systems to identify conservation priorities and sustainable management strategies for these valuable ecosystems.

Over the past two decades, wetland mapping has gained recognition thanks to the availability of remote sensing tools and data. However, accurate wetland mapping using remote sensing data, especially on a large scale, has long proven challenging. For example, input data should be

unaffected/less affected by clouds, haze, and other disturbances to obtain an acceptable classification result [4]. Such input data can be generated by compositing a large volume of satellite images collected during a specific time period. This is of particular concern for distinguishing backscattering/spectrally similar classes (e.g., wetland), wherein discrimination is challenging using a single image. Historically, the cost of acquiring multi-temporal remote sensing data precluded such large-scale land cover (e.g., wetland) mapping [7]. Although Landsat sensors have been collecting Earth Observation (EO) data at frequent intervals since the mid-1980s [8], open-access to its entire archive has occurred since 2008 [7]. This is of great benefit for land cover mapping on a large scale. However, much of this archived data has been underutilized to date. This is because collecting, storing, processing, and manipulating multi-temporal remote sensing data that cover a large geographic area over three decades are infeasible using conventional image processing software on workstation PC-based systems [9]. This is known as the "Geo Big Data" problem and it demands new technologies and resources capable of handling such a large volume of satellite imagery from the data science perspective [10].

Most recently, the growing availability of large-volume open-access remote sensing data and the development of advanced machine learning tools have been integrated with recent implementations of powerful cloud computing resources. This offers new opportunities for broader sets of applications at new spatial and temporal scales in the geospatial sciences and addresses the limitation of existing methods and products [11]. Specifically, the advent of powerful cloud computing resources, such as NASA Earth Exchange, Amazon's Web Services, Microsoft's Azure, and Google cloud platform has addressed these Geo Big Data problems. For example, Google Earth Engine (GEE) is an open-access, cloud-based platform for parallel processing of petabyte-scale data [12]. It hosts a vast pool of satellite imagery and geospatial datasets, and allows

264

web-based algorithm development and results visualization in a reasonable processing time [13]–[15]. In addition to its computing and storage capacity, a number of well-known machine learning algorithms have been implemented, allowing batch processing using JavaScript on a dedicated application programming interface (API) [16].

Notably, the development of advanced machine learning tools further contributes to handling large multi-temporal remote sensing data [17]. This is because traditional classifiers, such as maximum likelihood, insufficiently manipulate complicated, high-dimensional remote sensing data. Furthermore, they assume that input data are normally distributed, which may not be the case [18]. However, advanced machine learning tools, such as Decision Tree (DT), Support Vector Machine (SVM), and Random Forest (RF), are independent of input data distribution and can handle large volumes of remote sensing data. Previous studies have demonstrated that both RF [19] and SVM [20] outperformed DT for classifying remote sensing data. RF and SVM have also relatively equal strength in terms of classification accuracies [21]. However, RF is much easier to execute relative to SVM, given that the latter approach requires the adjustment of a large number of parameters [20]. RF is also insensitive to noise and overtraining [22] and has shown high classification accuracies in various wetland studies [18].

Over the past three years, several studies have investigated the potential of cloud-computing resources using advanced machine learning tools for processing/classifying the Geo Big Data in a variety of applications. These include global surface water mapping [23], global forest-cover change mapping [24], and cropland mapping [25], as well as studies focusing on land- and vegetation-cover changes on a smaller scale [26], [27]. They demonstrated the feasibility of characterizing the elements of the Earth surface at a national and global scale through advanced cloud computing platforms.

Newfoundland and Labrador (NL), a home for a great variety of flora and fauna, is one of the richest provinces in terms of wetlands and biodiversity in Canada. Most recently, the significant value of these ecosystems has been recognized by the Wetland Mapping and Monitoring System (WMMS) project, launched in 2015. Accordingly, a few local wetland maps, each covering approximately 700 km^2 of the province, were produced. For example, Mahdianpari et al. (2017) introduced a hierarchical object-based classification scheme for discriminating wetland classes in the most easterly part of NL, the Avalon Peninsula, using Synthetic Aperture Radar (SAR) observations obtained from ALOS-2, RADARSAT-2, and TerraSAR-X imagery [18]. Later, Mahdianpari et al. (2018) proposed the modified coherency matrix obtained from quad-pol RADARSAT-2 imagery to improve wetland classification accuracy. They evaluated the efficiency of the proposed method in three pilot sites across NL, each of which covers 700 km^2 [28]. Most recently, Mohammadimanesh et al. (2018) investigated the potential of interferometric coherence for wetland classification, as well as the synergy of coherence with SAR polarimetry and intensity features for wetland mapping in a relatively small area in NL (the Avalon Peninsula) [28]. These local-scale wetland maps exhibit the spatial distribution patterns and the characteristics of wetland species (e.g., dominant wetland type). However, such small-scale maps have been produced by incorporating different data sources, standards, and methods, making them of limited use for rigorous wetland monitoring at the provincial, national, and global scales.

Importantly, precise, comprehensive, provincial-level wetland inventories that map small to large wetland classes can significantly aid conservation strategies, support sustainable management, and facilitate progress toward national/global scale wetland inventories [29]. Fortunately, new opportunities for large-scale wetland mapping are obtained from the Copernicus programs by the European Space Agency (ESA) [30]. In particular, concurrent availability of 12-days SAR

Sentinel-1 and 10-days optical Sentinel-2 (multi-spectral instrument, MSI) sensors provides an unprecedented opportunity to collect high spatial resolution data for global wetland mapping. The main purpose of these Sentinel Missions is to provide full, free, and open access data to facilitate the global monitoring of the environment and to offer new opportunities to the scientific community [31]. This highlights the substantial role of Sentinel observations for large-scale land surface mapping. Accordingly, the synergistic use of Sentinel-1 and Sentinel-2 EO data offers new avenues to be explored in different applications, especially for mapping phenomena with highly dynamic natures (e.g., wetland).

Notably, the inclusion of SAR data for land and wetland mapping is of great significance for monitoring areas with nearly permanent cloud-cover. This is because SAR signals are independent of solar radiation and the day/night condition, making them superior for monitoring geographic regions with dominant cloudy and rainy weather, such as Newfoundland, Canada. Nevertheless, multi-source satellite data are advantageous in terms of classification accuracy relative to the accuracy achieved by a single source of data [32]. This is because optical sensors are sensitive to the reflective and spectral characteristics of ground targets [33], [34], whereas SAR sensors are sensitive to their structural, textural, and dielectric characteristics [35]. Thus, a synergistic use of two types of data offers complementary information, which may be lacking when utilizing one source of data [36]. Several studies have also highlighted the great potential of fusing optical and SAR data for wetland classification [23].

This study aims to develop a multi-temporal classification approach based on open-access remote sensing data and tools to map wetland classes as well as the other land cover types with high accuracy, here piloting this approach for wetland mapping in Canada. Specifically, the main objectives of this study were to: (1) Leverage open access SAR and optical images obtained from

267

Sentinel-1 and Sentinel-2 sensors for the classification of wetland complexes; (2) assess the capability of the Google Earth Engine cloud computing platform to generate custom land cover maps, which are sufficient in discriminating wetland classes as standard land cover products; (3) compare the efficiency of both pixel-based and object-based random forest classification; and (4) produce the first provincial-scale, fine resolution (i.e., 10 m) wetland inventory map in Canada. The results of this study demonstrate a paradigm-shift from standard static products and approaches toward generating more dynamic, on-demand, large-scale wetland coverage maps through advanced cloud computing resources that simplify access to and processing of a large volume of satellite imagery. Given the similarity of wetland classes across the country, the developed methodology can be scaled-up to map wetlands at the national-scale.

7.2. Materials and Methods

7.2.1. Study Area

The study area is the Island of Newfoundland, covering an approximate area of 106,000 km^2, located within the Atlantic sub-region of Canada (Figure 7.1). According to the Ecological Stratification Workings Group of Canada, "each part of the province is characterized by distinctive regional ecological factors, including climatic, physiography, vegetation, soil, water, fauna, and land use" [37].
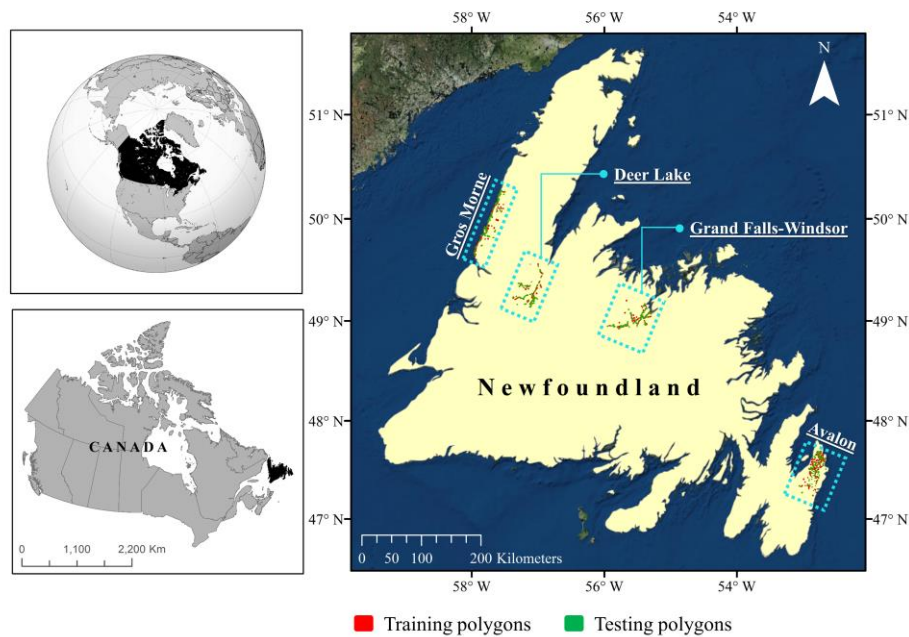
Figure 7.1. The geographic location of the study area with distribution of the training and testing polygons across four pilot sites on the Island of Newfoundland.

In general, the Island of Newfoundland has a cool summer and a humid continental climate, which is greatly affected by the Atlantic Ocean [38]. Black spruce forests that dominate the central area, and balsam fir forests that dominate the western, northern, and eastern areas, are common on the island [37]. Based on geography, the Island of Newfoundland can be divided into three zones, namely the southern, middle, and northern boreal regions, and each is characterized by various ecoregions [39]. For example, the southern boreal zone contains the Avalon forest, Southwestern Newfoundland, Maritime Barrens, and South Avalon-Burin Oceanic Barrens ecoregions. St. John's, the capital city, is located at the extreme eastern portion of the island, in the Maritime Barren ecoregion, and is the foggiest, windiest, and cloudiest Canadian city.

All wetland classes characterized by the Canadian Wetland Classification System (CWCS), namely bog, fen, marsh, swamp, and shallow-water [1], are found throughout the island. However, bog and fen are the most dominant classes relative to the occurrence of swamp, marsh, and

shallow-water. This is attributed to the island climate, which facilitates peatland formation (i.e., extensive agglomeration of partially-decomposed organic peat under the surface). Other land cover classes are upland, deep-water, and urban/bare land. The urban and bare land classes, both having either an impervious surface or exposed soil [40], include bare land, roads, and building facilities and, thus, are merged into one single class in the final classification map.

Four pilot sites, which are representative of regional variation in terms of both landscape and vegetation, were selected across the island for in-situ data collection (see Figure 7.1). The first pilot site is the Avalon area, located in the south-east of the island in the Maritime Barren ecoregion, which experiences an oceanic climate of foggy, cool summers, and relatively mild winters. The second and third pilot sites are Grand Falls-Windsor, located in the north-central area of the island, and Deer Lake, located in the northern portion of the island. Both fall within the Central Newfoundland ecoregion and experience a continental climate of cool summers and cold winters. The final pilot site is Gros Morne, located on the extreme west coast of the island, in the Northern Peninsula ecoregion, and this site experiences a maritime-type climate with cool summers and mild winters [40].

7.2.2. Reference Data

In-situ data were collected via an extensive field survey of the sites mentioned above in the summers and falls of 2015, 2016 and 2017. Using visual interpretation of high resolution Google Earth imagery, as well as the CWCS definition of wetlands, potential and accessible wetland sites were flagged across the island. Accessibility via public roads, the public or private ownership of lands, and prior knowledge of the area were also taken into account for site visitation. In-situ data were collected to cover a wide range of wetland and non-wetland classes with a broad spatial distribution across NL. One or more Global Positioning System (GPS) points, depending on the

size of each wetland, along with the location's name and date were recorded. Several digital photographs and ancillary notes (e.g., dominant vegetation and hydrology) were also recorded to aid in preparing the training samples. During the first year of data collection (i.e., 2015), no limitation was set on the size of the wetland, and this resulted in the production of several small-size classified polygons. To move forward with a larger size, wetlands of size >1 ha (where possible) were selected during the years 2016 and 2017. Notably, a total of 1200 wetland and non-wetland sites were visited during in-situ data collection at the Avalon, Grand Falls-Windsor, Deer Lake, and Gros Morne pilot sites over three years. Such in-situ data collection over a wide range of wetland classes across NL captured the variability of wetlands and aided in developing robust wetland training samples. Figure 7.1 depicts the distribution of the training and testing polygons across the Island.

Recorded GPS points were then imported into ArcMap 10.3.1 and polygons illustrating classified delineated wetlands were generated using a visual analysis of 50 cm resolution orthophotographs and 5 m resolution RapidEye imagery. Next, polygons were sorted based on their size and alternately assigned to either training or testing groups. Thus, the training and testing polygons were obtained from independent samples to ensure robust accuracy assessment. This alternative assignment also ensured that both the training (~50%) and testing (~50%) polygons had equal numbers of small and large polygons, allowing similar pixel counts and taking into account the large variation of intra-wetland size. Table 7.1 presents the number of training and testing polygons for each class.

Table 7.1. Number of training and testing polygons in this study.

Class	Training Polygons	Testing Polygons
bog	92	91
fen	93	92
marsh	75	75
swamp	78	79
shallow-water	55	56
deep-water	17	16
upland	92	92
urban/bare land	99	98
total	601	599

7.2.3. Satellite Data, Pre-Processing, and Feature Extraction

7.2.3.1. SAR Imagery

A total of 247 and 525 C-band Level-1 Ground Range Detected (GRD) Sentinel-1 SAR images in ascending and descending orbits, respectively, were used in this study. This imagery was acquired during the interval between June and August of 2016, 2017 and 2018 using the Interferometric Wide (IW) swath mode with a pixel spacing of 10 m and a swath of 250 km with average incidence angles varying between 30° and 45°. As a general rule, Sentinel-1 collects dual- (HH/HV) or single- (HH) polarized data over Polar Regions (i.e., sea ice zones) and dual- (VV/VH) or single- (VV) polarized data over all other zones. However, in this study, we took advantage of being close to the Polar regions and thus, both HH/HV and VV/VH data were available in our study region. Accordingly, of 247 SAR ascending observations (VV/VH), 12, 120 and 115 images were collected in 2016, 2017 and 2018, respectively. Additionally, of 525 descending observations

(HH/HV), 111, 260, and 154 images were acquired in 2016, 2017 and 2018, respectively. Figure 7.2 illustrates the number of SAR observations over the summer of the aforementioned years.
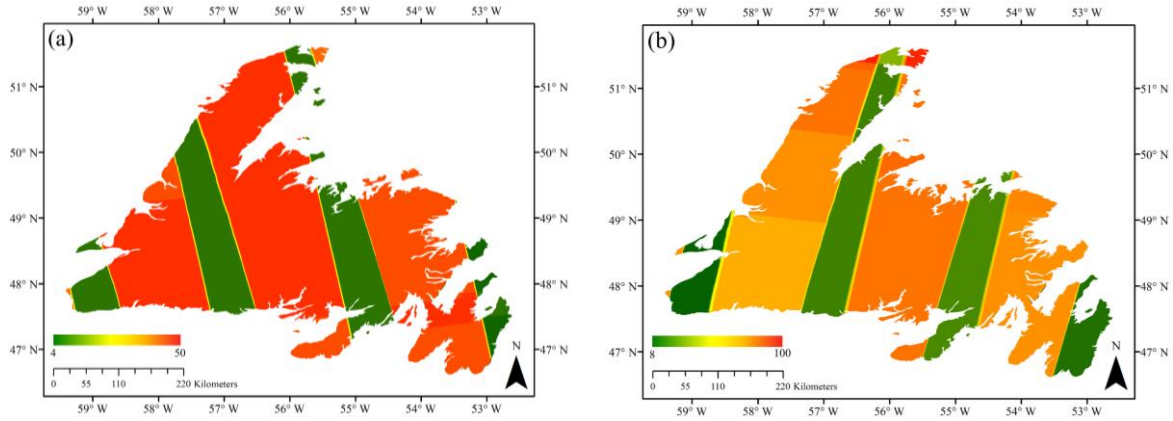

Figure 7.2. The total number of (a) ascending Synthetic Aperture Radar (SAR) observations (VV/VH) and (b) descending SAR observations (HH/HV) during summers of 2016, 2017 and 2018. The color bar represents the number of collected images.

Sentinel-1 GRD data were accessed through GEE. We applied the following pre-processing steps, including updating orbit metadata, GRD border noise removal, thermal noise removal, radiometric calibration (i.e., backscatter intensity), and terrain correction (i.e., orthorectification) [41]. These steps resulted in generating the geo-coded backscatter intensity images. Notably, this is similar to the pre-processing steps implemented in the ESA's SNAP Sentinel-1 toolbox. The unitless backscatter intensity images were then converted into normalized backscattering coefficient (σ^0) values in dB (i.e., the standard unit for SAR backscattering representation). Further pre-processing steps, including incidence angle correction [42] and speckle reduction (i.e., 7×7 adaptive sigma Lee filter in this study) [43], were also carried out on the GEE platform.

Following the procedure described above, σ^0_{VV}, σ^0_{VH}, σ^0_{HH}, and σ^0_{HV} (i.e., backscatter coefficient images) were extracted. Notably, σ^0_{VV} observations are sensitive to soil moisture and are able to distinguish flooded from non-flooded vegetation [44], as well as various types of herbaceous

wetland classes (low, sparsely vegetated areas) [45]. This is particularly true for vegetation in the early stages of growing when plants have begun to grow in terms of height, but have not yet developed their canopy [44]. σ_{VH}^0 observations can also be useful for monitoring wetland herbaceous vegetation. This is because cross-polarized observations are produced by volume scattering within the vegetation canopy and have a higher sensitivity to vegetation structures [46]. σ_{HH}^0 is an ideal SAR observation for wetland mapping due to its sensitivity to double-bounce scattering over flooded vegetation [47]. Furthermore, σ_{HH}^0 is less sensitive to the surface roughness compared to σ_{VV}^0, making the former advantageous for discriminating water and non-water classes. In addition to SAR backscatter coefficient images, a number of other polarimetric features were also extracted and used in this study. Table 7.2 represents polarimetric features extracted from the dual-pol VV/VH and HH/HV Sentinel-1 images employed in this study. Figure 7.3a illustrates the span feature, extracted from HH/HV data, for the Island of Newfoundland.

Table 7.2. A description of extracted features from SAR and optical imagery.

| Data	Feature Description	Formula
Sentinel-1	vertically transmitted, vertically received SAR backscattering coefficient	σ_{VV}^0
	vertically transmitted, horizontally received SAR backscattering coefficient	σ_{VH}^0
	horizontally transmitted, horizontally received SAR backscattering coefficient	σ_{HH}^0
	horizontally transmitted, vertically received SAR backscattering coefficient	σ_{HV}^0
	Span or total scattering power	$\lvert S_{VV}\rvert^2 + \lvert S_{VH}\rvert^2 \,,\, \lvert S_{HH}\rvert^2 + \lvert S_{HV}\rvert^2$
	difference between co- and cross-polarized observations	$\lvert S_{VV}\rvert^2 - \lvert S_{VH}\rvert^2 \,,\, \lvert S_{HH}\rvert^2 - \lvert S_{HV}\rvert^2$
	ratio	$\dfrac{\lvert S_{VV}\rvert^2}{\lvert S_{VH}\rvert^2} \,,\, \dfrac{\lvert S_{HH}\rvert^2}{\lvert S_{HV}\rvert^2}$
Sentinel-2	spectral bands 2 (blue), 3 (green), 4 (red) and 8 (NIR)	B_2, B_3, B_4, B_8
	the normalized difference vegetation index (NDVI)	$\dfrac{B_8 - B_4}{B_8 + B_4}$
	the normalized difference water index (NDWI)	$\dfrac{B_3 - B_8}{B_3 + B_8}$
	modified soil-adjusted vegetation index 2 (MSAVI2)	$\dfrac{2B_8 + 1 - \sqrt{(2B_8 + 1)^2 - 8(B_8 - B_4)}}{2}$
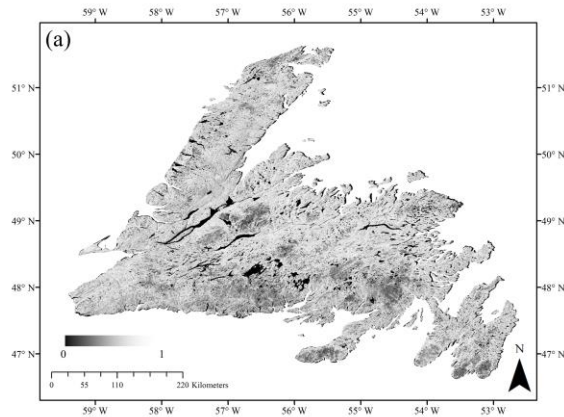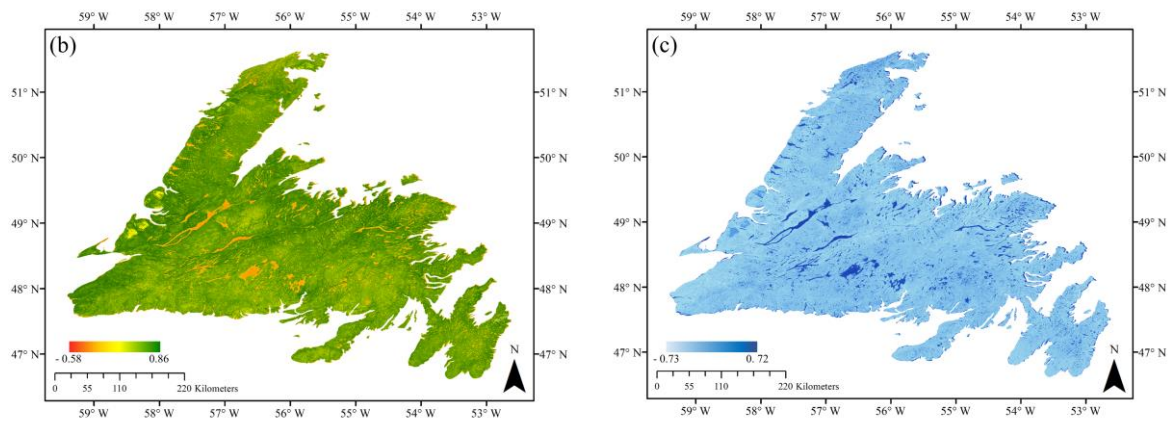
Figure 7.3. Three examples of extracted features for land cover classification in this study. The multi-year summer composite of (a) span feature extracted from HH/HV Sentinel-1 data, (b) normalized difference vegetation index (NDVI), and (c) normalized difference water index (NDWI) features extracted from Sentinel-2 data.

7.2.3.2. Optical Imagery

Creating a 10 m cloud-free Sentinel-2 composition for the Island of Newfoundland over a short period of time (e.g., one month) is a challenging task due to chronic cloud cover. Accordingly, the Sentinel-2 composite was created for three-months between June and August, during the leaf-on season for 2016, 2017 and 2018. This time period was selected since it provided the most cloud-free data and allowed for maximum wall-to-wall data coverage. Furthermore, explicit wetland phenological information could be preserved by compositing data acquired during this time period. Accordingly, monthly composite and multi-year summer composite were used to obtain cloud-free or near-cloud-free wall-to-wall coverage.

 Both Sentinel-2A and Sentinel-2B Level-1C data were used in this study. There were a total of 343, 563 and 1345 images in the summer of 2016, 2017 and 2018, respectively. The spatial distribution of all Sentinel-2 observations during the summers of 2016, 2017 and 2018 are illustrated in Figure 4a. Notably, a number of these observations were affected by cloud coverage.

Figure 7.4b depicts the percentage of cloud cover distribution during these time periods. To mitigate the limitation that arises due to cloud cover, we applied a selection criteria to cloud percentage (<20%) when producing our cloud-free composite. Next, the QA60 bitmask band (a quality flag band) provided in the metadata was used to detect and mask out clouds and cirrus. Sentinel-2 has 13 spectral bands at various spatial resolutions, including four bands at 10 m, six at 20 m, and three bands at 60 m spatial resolution. For this study, only blue (0.490 µm), green (0.560 µm), red (0.665 µm), and near-infrared (NIR, 0.842 µm) bands were used. This is because the optical indices selected in this study are based on the above mentioned optical bands (see Table 7.2) and, furthermore, all these bands are at a spatial resolution of 10 m.
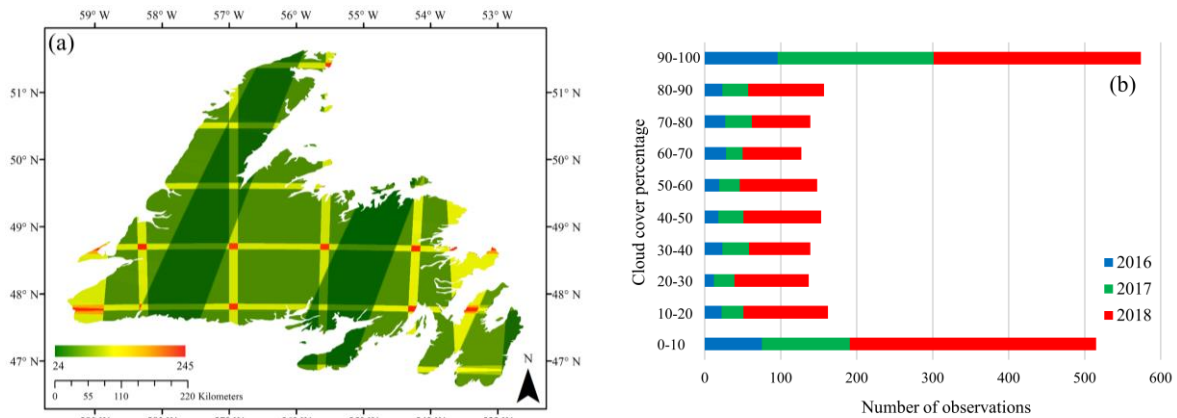
Figure 7.4. (a) Spatial distribution of Sentinel-2 observations (total observations) during summers of 2016, 2017 and 2018 and (b) the number of observations affected by varying degrees of cloud cover (%) in the study area for each summer.

In addition to optical bands (2, 3, 4 and 8), NDVI, NDWI and MSAVI2 indices were also extracted (see Table 7.2). NDVI is one of the most well-known and commonly used vegetation indices for the characterization of vegetation phenology (seasonal and inter-annual changes). Using the ratioing operation (see Table 7.2), NDVI decreases several multiplicative noises, such as sun illumination differences, cloud shadows, as well as some atmospheric attenuation and topographic

variations, within various bands of multispectral satellite images [48]. NDVI is sensitive to photosynthetically active biomasses and can discriminate vegetation/non-vegetation, as well as wetland/non-wetland classes. NDWI is also useful, since it is sensitive to open water and can discriminate water from land. Notably, NDWI can be extracted using different bands of multispectral data [49], such as green and shortwave infrared (SWIR) [50], red and SWIR [51], as well as green and NIR [52]. Although some studies reported the superiority of SWIR for extracting the water index due to its lower sensitivity to the sub-pixel non-water component [49], we used the original NDWI index proposed by [52] in this study. This is because it should provide accurate results at our target resolution and, moreover, it uses green and NIR bands of Sentinel-2 data, both of which are at a 10 m spatial resolution. Finally, MSAVI2 was used because it addresses the limitations of NDVI in areas with a high degree of exposed soil surface. Figure 7.3b,c demonstrates the multi-year summer composite of NDVI and NDWI features extracted from Sentinel-2 optical imagery.

7.2.4. Multi-Year Monthly and Summer Composite

Although several studies have used the Landsat archive to generate nearly-cloud-free Landsat composites of a large area (e.g., [53]–[55]), to the best of our knowledge, such an investigation has not yet been thoroughly examined for Sentinel-2 data. This is unfortunate since the latter data offer both improved temporal and spatial resolution relative to Landsat imagery, making them advantageous for producing high resolution land cover maps on a large scale. For example, Roy et al. (2010) produced monthly, seasonally, and yearly composites using maximum NDVI and brightness temperature obtained from Landsat data for the conterminous United States [55]. Recent studies also used different compositing approaches, such as seasonally [53] and yearly [54] composites obtained from Landsat data in their analysis.

In this study, two different types of image composites were generated: Multi-year monthly and summer composites. Due to the prevailing cloudy and rainy weather conditions in the study area, it was impossible to collect sufficient cloud-free optical data to generate a full-coverage monthly composite of Sentinel-2 data for classification purposes. However, we produced the monthly composite (optical) for spectral signature analysis to identify the month during which the most semantic information of wetland classes could be obtained. A multi-year summer composite was produced to capture explicit phenological information appropriate for wetland mapping. As suggested by recent research [56], the multi-year spring composite is advantageous for wetland mapping in the Canada's boreal regions. This is because such time-series data capture within-year surface variation. However, in this study, the multi-year summer composite was used given that the leaf-on season begins in late spring/early summer on the Island of Newfoundland.

Leveraging the GEE composite function, 10 m wall-to-wall, cloud-free composites of Sentinel-2 imagery, comprising original optical bands (2, 3, 4 and 8), NDVI, NDWI, and MSAVI2 indices, across the Island of Newfoundland were produced. SAR features, including σ_{VV}^0, σ_{VH}^0, σ_{HH}^0, σ_{HV}^0, span, ratio, and difference between co- and cross-polarized SAR features (see Table 7.2), were also stacked using GEE's array-based computational approach. Specifically, each monthly and summer season group of images were stacked into a single median composite on a per-pixel, per band basis.

7.2.5. Separability Between Wetland Classes

In this study, the separability between wetland classes was determined both qualitatively, using box-and-whiskers plots, and quantitatively, using Jeffries–Matusita (JM) distance. The JM distance indicates the average distance between the density function of two classes [57]. It uses both the first order (mean) and second order (variance) statistical variables from the samples and

has been illustrated to be an efficient separability measure for remote sensing data [58], [59]. Given

normal distribution assumptions, the JM distance between two classes is represented as

$$JM = 2\left(1 - e^{-B}\right) \tag{7.1}$$

where B is the Bhattacharyya (BH) distance given by

$$B = \frac{1}{8}\left(\mu_i - \mu_j\right)^T \left(\frac{\Sigma_i + \Sigma_j}{2}\right)^{-1} \left(\mu_i - \mu_j\right) + \frac{1}{2}\ln\left(\frac{\left|(\Sigma_i + \Sigma_j)/2\right|}{\sqrt{|\Sigma_i||\Sigma_j|}}\right) \tag{7.2}$$

where μ_i and Σ_i are the mean and covariance matrix of class i and μ_j and Σ_j are the mean and

covariance matrix of class j. The JM distance varies between 0 and 2, with values that approach 2

demonstrating a greater average distance between two classes. In this study, the separability

analysis was limited to extracted features from optical data. This is because a detailed

backscattering analysis of wetland classes using multi-frequency SAR data, including X-, C-, and

L-band, has been presented in our previous study [18].

7.2.6. Classification Scheme

7.2.6.1. Random Forest

In this study, the random forest (RF) algorithm was used for both pixel-based and object-based

wetland classifications. RF is a non-parametric classifier, comprised of a group of tree classifiers,

and is able to handle high dimensional remote sensing data. It is also more robust compared to the

DT algorithm and easier to execute relative to SVM. RF uses bootstrap aggregating (bagging) to

produce an ensemble of decision trees by using a random sample from the given training data, and

determines the best splitting of the nodes by minimizing the correlation between trees. Assigning

a label to each pixel is based on the majority vote of trees. RF can be tuned by adjusting two input

parameters [60], namely the number of trees (*Ntree*), which is generated by randomly selecting samples from the training data, and the number of variables (*Mtry*), which is used for tree node splitting. In this study, these parameters were selected based on (a) direction from previous studies and (b) a trial-and-error approach. Specifically, *Mtry* was assessed for the following values (when *Ntree* was adjusted to 500): (a) One third of the total number of input features; (b) the square root of the total number of input features; (c) half of the total number of input features; (d) two thirds of the total number of input features; and (e) the total number of input features. This resulted in marginal or no influence on the classification accuracies. Accordingly, the square root of the total number of variables was selected for *Mtry*, as suggested by [27]. Next, by adjusting the optimal value for *Mtry*, the parameter *Ntree* was assessed for the following values: (a) 100; (b) 200; (c) 300; (d) 400; (e) 500; and (f) 600. A value of 400 was then found to be appropriate in this study, as error rates for all classification models were constant beyond this point. The 601 training polygons in different categories were used to train the RF classifier on the GEE platforms (see Table 7.1).

7.2.6.2. Simple Non-Iterative Clustering (SNIC) Superpixel Segmentation

Conventional pixel-based classification algorithms rely on the exclusive use of the spectral/backscattering value of each pixel in their classification scheme. This results in "salt and pepper" noise in the final classification map, especially when high-resolution images are employed [61]. An object-based algorithm, however, can mitigate the problem that arises during such image processing by taking into account the contextual information within a given imaging neighborhood [62]. Image segmentation divides an image into regions or objects based on the specific parameters (e.g., geometric features and scaled topological relation). In this study, simple non-iterative clustering (SNIC) algorithm was selected for superpixel segmentation (i.e., object-based) analysis

[62]. The algorithm starts by initializing centroid pixels on a regular grid in the image. Next, the dependency of each pixel relative to the centroid is determined using its distance in the five-dimensional space of color and spatial coordinates. In particular, the distance integrates normalized spatial and color distances to produce effective, compact and approximately uniform superpixels. Notably, there is a trade-off between compactness and boundary continuity, wherein larger compactness values result in more compact superpixels and, thus, poor boundary continuity. SNIC uses a priority queue, 4- or 8-connected candidate pixels to the currently growing superpixel cluster, to select the next pixels to join the cluster. The candidate pixel is selected based on the smallest distance from the centroid. The algorithm takes advantage of both priority queue and online averaging to evolve the centroid once each new pixel is added to the given cluster. Accordingly, SNIC is superior relative to similar clustering algorithms (e.g., Simple Linear Iterative Clustering) in terms of both memory and processing time. This is attributed to the introduction of connectivity (4- or 8-connected pixels) that results in computing fewer distances during centroid evolution [62].

7.2.6.3. Evaluation Indices

Four evaluation indices, including overall accuracy (OA), Kappa coefficient, producer accuracy, and user accuracy were measured using the 599 testing polygons held back for validation purposes (see Table 7.1). Overall accuracy determines the overall efficiency of the algorithm and can be measured by dividing the total number of correctly-labeled samples by the total number of the testing samples. The Kappa coefficient indicates the degree of agreement between the ground truth data and the predicted values. Producer's accuracy represents the probability that a reference sample is correctly identified in the classification map. User's accuracy indicates the probability

282

that a classified pixel in the land cover classification map accurately represents that category on the ground [63].

Additionally, the McNemar test [64] was employed to determine the statistically significant differences between various classification scenarios in this study. Particularly, the main goals were to determine: (1) Whether a statistically significant difference exists between pixel-based and object-based classifications based on either SAR or optical data; and (2) whether a statistically significant difference exists between object-based classifications using only one type of data (SAR or optical data) and an integration of two types of data (SAR and optical data). The McNemar test is non-parametric and is based on the classification confusion matrix. The test is based on a chi-square (χ^2) distribution with one degree of freedom [65], [66] and assumes the number of correctly and incorrectly identified pixels are equal for both classification scenarios [64],

$$\chi^2 = \frac{(f_{12} - f_{21})^2}{f_{12} + f_{21}} \tag{7.3}$$

where f_{12} and f_{21} represent the number of pixels that were correctly identified by one classifier as compared to the number of pixels that the other method incorrectly identified, respectively.

7.2.7. Processing Platform

The GEE cloud computing platform was used for both the pixel-based and superpixel RF classification in this study. Both Sentinel-1 and Sentinel-2 data hosted within the GEE platform were used to construct composite images. The zonal boundaries and the reference polygons were imported into GEE using Google fusion tables. A JavaScript API in the GEE code editor was used for pre-processing, feature extraction, and classification in this study. Accordingly, we generated

10 m spatial resolution wetland maps of Newfoundland for our multi-year seasonal composites of optical, SAR, and integration of both types of data using pixel-based and object-based approaches.

7.3. Results

7.3.1. Spectral Analysis of Wetland Classes Using Optical Data

To examine the discrimination capabilities of different spectral bands and vegetation indices, spectral analysis was performed for all wetland classes. Figures 7.5, 7.6 and 7.7 illustrate the statistical distribution of reflectance, NDVI, NDWI, and MSAVI2 values for the multi-year monthly composites of June, July, and August, respectively, using box-and-whisker plots.
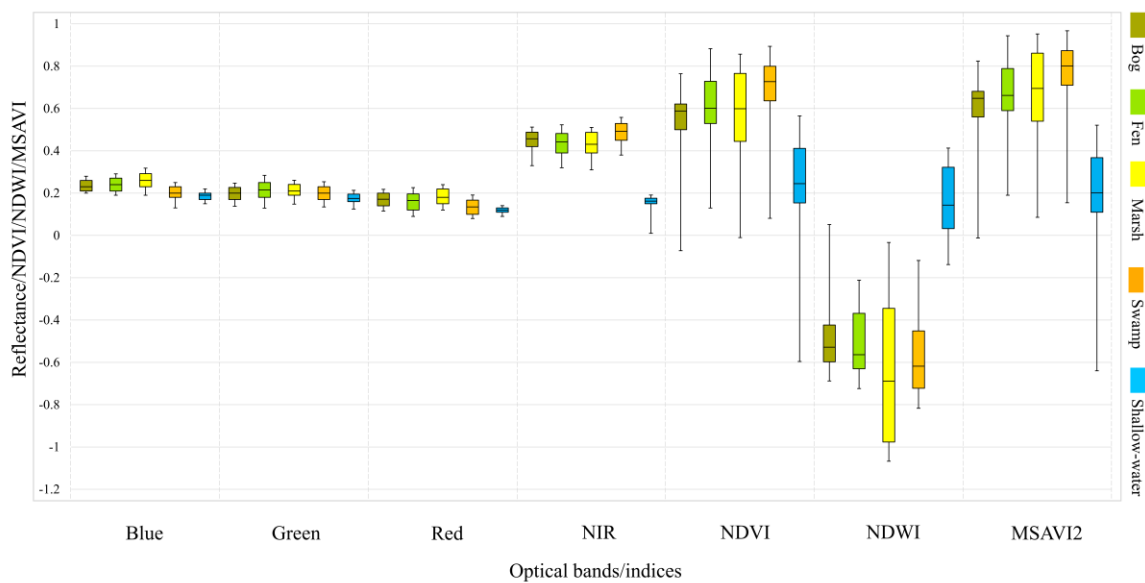

Figure 7.5. Box-and-whisker plot of the multi-year June composite illustrating the distribution of reflectance, NDVI, NDWI, and MSAVI2 for wetland classes obtained using pixel values extracted from training datasets. Note that black, horizontal bars within boxes illustrate median values, boxes demonstrate the lower and upper quartiles, and whiskers extend to minimum and maximum values.

As shown, all visible bands poorly distinguish spectrally similar wetland classes, especially the bog, fen, and marsh classes. The shallow-water class, however, can be separated from other classes

using the red band in August (see Figure 7.7). Among the original bands, NIR represents clear advantages when discriminating the shallow-water from other classes (see Figures 7.5, 7.6 and 7.7), but is not more advantageous for classifying herbaceous wetland classes. Overall, vegetation indices are superior when separating wetland classes compared to the original bands.
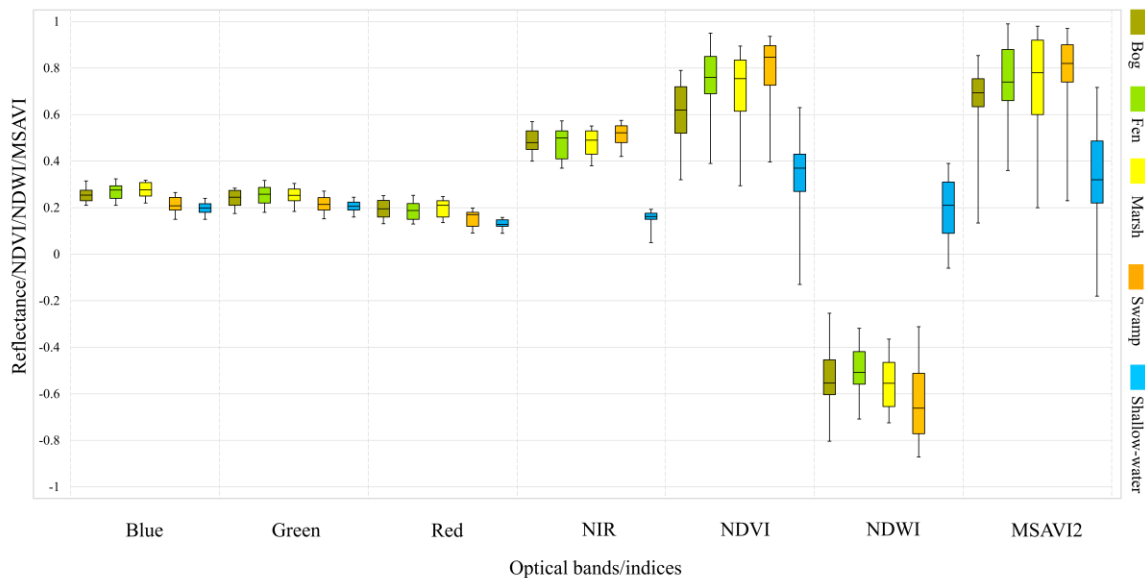

Figure 7.6. Box-and-whisker plot of the multi-year July composite illustrating the distribution of reflectance, NDVI, NDWI, and MSAVI2 for wetland classes obtained using pixel values extracted from training datasets.

As illustrated in Figures 7.5, 7.6 and 7.7, the shallow-water class is easily distinguishable from other classes using all vegetation indices. The swamp and bog classes are also separable using the NDVI index from all three months. Although both NDVI and MSAVI2 are unable to discriminate herbaceous wetland classes using the June composite, the classes of bog and fen are distinguishable using the NDVI index obtained from the July and August composites.
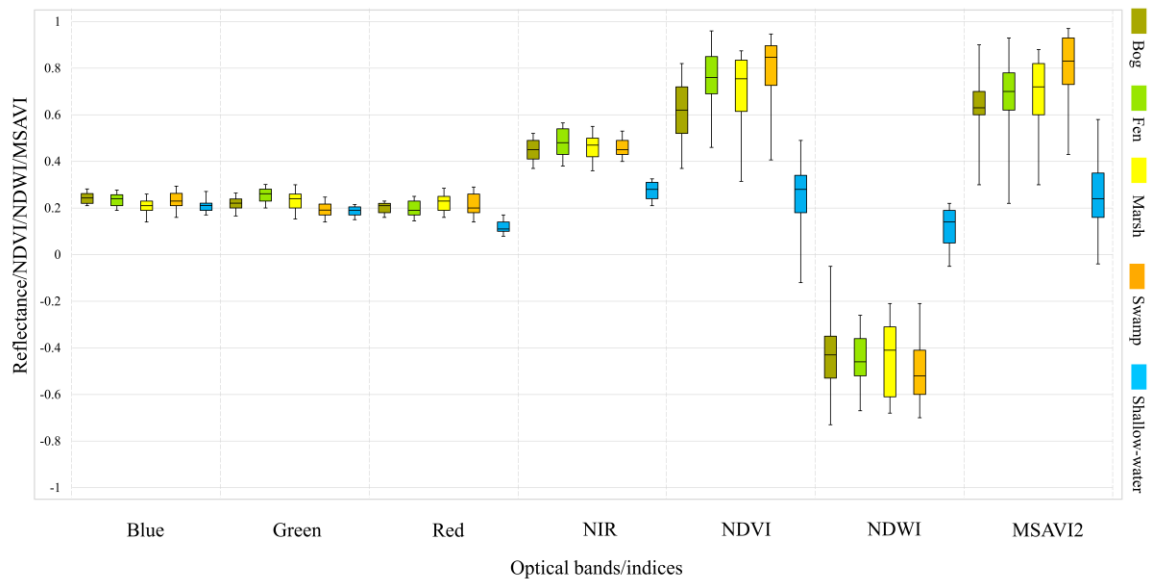
Figure 7.7. Box-and-whisker plot of the multi-year August composite illustrating the distribution of reflectance, NDVI, NDWI, and MSAVI2 for wetland classes obtained using pixel values extracted from training datasets.

The mean JM distances obtained from the multi-year summer composite for wetland classes are represented in Table 7.3.

Table 7.3. Jeffries–Matusita (JM) distances between pairs of wetland classes from the multi-year summer composite for extracted optical features in this study.

Optical features	d_1	d_2	d_3	d_4	d_5	d_6	d_7	d_8	d_9	d_{10}
blue	0.002	0.204	0.470	1.153	0.232	0.299	1.218	0.520	1.498	0.380
green	0.002	0.331	0.391	0.971	0.372	0.418	1.410	0.412	1.183	0.470
red	0.108	0.567	0.570	1.495	0.546	0.640	1.103	0.634	1.391	0.517
NIR	0.205	0.573	0.515	1.395	0.364	0.612	1.052	0.649	1.175	1.776
NDVI	0.703	0.590	0.820	1.644	0.586	0.438	1.809	0.495	1.783	1.938
NDWI	0.268	0.449	0.511	1.979	0.643	0.519	1.792	0.760	1.814	1.993
MSAVI2	0.358	0.509	0.595	1.763	0.367	0.313	1.745	0.427	1.560	1.931
all	1.098	1.497	1.561	1.999	1.429	1.441	1.999	1.614	1.805	1.999

Note: d_1: Bog/Fen, d_2: Bog/Marsh, d_3: Bog/ Swamp, d_4: Bog/Shallow-water, d_5: Fen/Marsh, d_6: Fen/Swamp, d_7: Fen/Shallow-water, d_8: Marsh/Swamp, d_9: Marsh/Shallow-water, and d_{10}: Swamp/Shallow-water.

According to the JM distance, shallow-water is the most separable class from other wetland classes. In general, all wetland classes, excluding shallow-water, are hardly distinguishable from each other using single optical feature and, in particular, bog and fen are the least separable classes.

However, the synergistic use of all features considerably increases the separability between wetland classes, with JM values exceeding 1.4 in most cases; however, bog and fen remain hardly discernible in this case.

7.3.2. Classification

The overall accuracies (OA) and Kappa coefficients of different classification scenarios are presented in Table 7.4. Overall, the classification results using optical imagery were more advantageous relative to SAR imagery. As illustrated, the optical imagery resulted in approximately 4% improvements in both the pixel-based and object-based approaches. Furthermore, object-based classifications were found to be superior to pixel-based classifications using optical (~6.5% improvement) and SAR (~6% improvements) imagery in comparative cases. It is worth noting that the accuracy assessment in this study was carried out using the testing polygons well distributed across the whole study region.

Table 7.4. Overall accuracies and Kappa coefficients obtained from different classification scenarios in this study.

Classification	Data composite	Scenario	Overall accuracy (%)	Kappa coefficient
pixel-based	SAR	S1	73.12	0.68
	Optic	S2	77.16	0.72
	SAR	S3	79.14	0.74
object-based	Optic	S4	83.79	0.80
	SAR + optic	S5	88.37	0.85

The McNemar test revealed that the difference between the accuracies of pixel-based and object-based classifications was statistically significant when either SAR ($p = 0.023$) or optical ($p = 0.012$) data were compared (see Table 7.5). There was also a statistically very significant difference between object-based classifications using SAR vs. SAR/optical data ($p = 0.0001$) and optical vs SAR/optical data ($p = 0.008$).

Table 7.5. The results of McNemar test for different classification scenarios in this study.

Scenarios	χ^2	*p*-value
S1 vs. S3	5.21	0.023
S2 vs. S4	6.27	0.012
S3 vs. S5	9.27	0.0001
S4 vs. S5	7.06	0.008

Figure 7.8 demonstrates the classification maps using SAR and optical multi-year summer composites for Newfoundland obtained from pixel- and object-based RF classifications. They illustrate the distribution of land cover classes, including both wetland and non-wetland classes, identifiable at a 10 m spatial resolution. In general, the classified maps indicate fine separation of all land cover units, including bog and fen, shallow- and deep-water, and swamp and upland, as well as other land cover types.
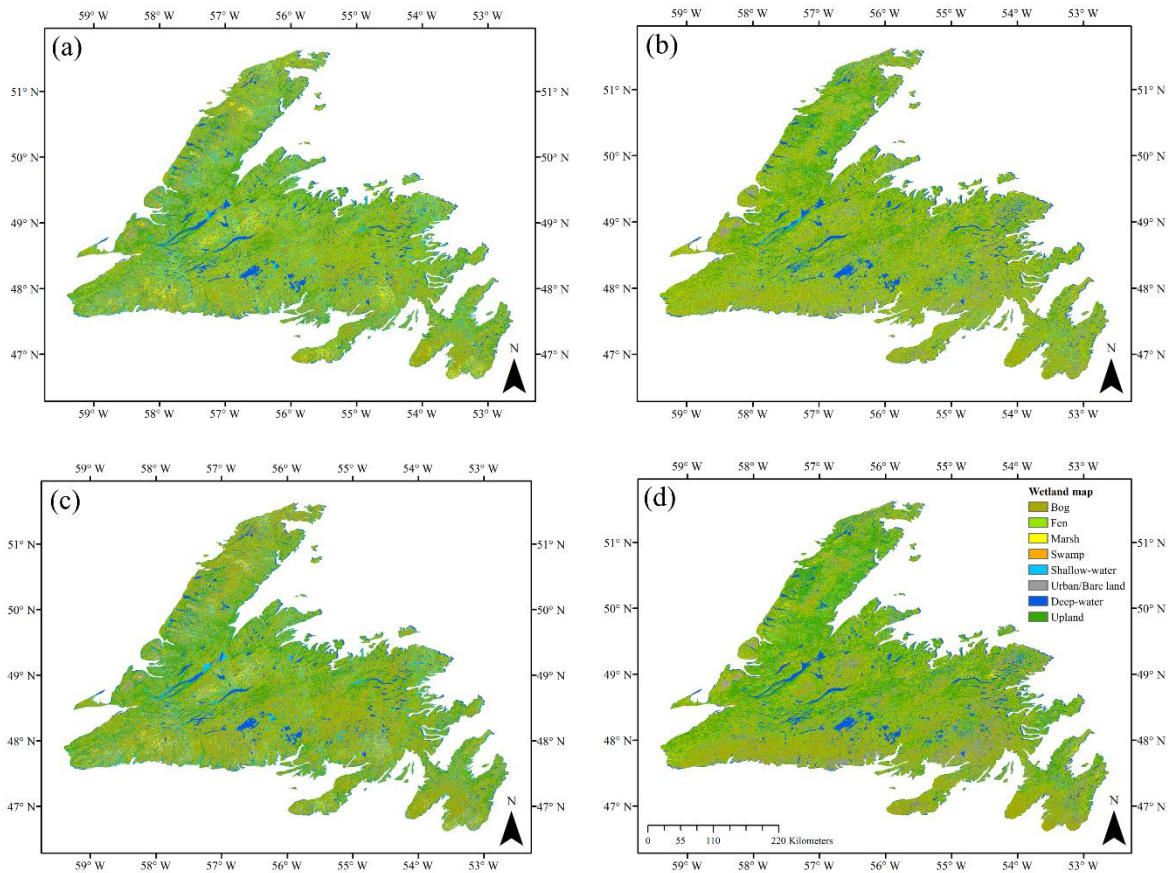
Figure 7.8. The land cover maps of Newfoundland obtained from different classification scenarios, including (a) S1, (b) S2, (c) S3 and (d) S4 in this study.

Figure 7.9 depicts the confusion matrices obtained from different methods, wherein the diagonal elements are the producer's accuracies. The user's accuracies of land cover classes using different classification scenarios are also demonstrated in Figure 7.10. Overall, the classification of wetlands have lower accuracies compared to those of the non-wetland classes. In particular, the classification of swamp has the lowest producer's and user's accuracies among wetland (and all) classes in this study. In contrast, the classification accuracies of bog and shallow-water are higher (both user's and producer's accuracies) than the other wetland classes.
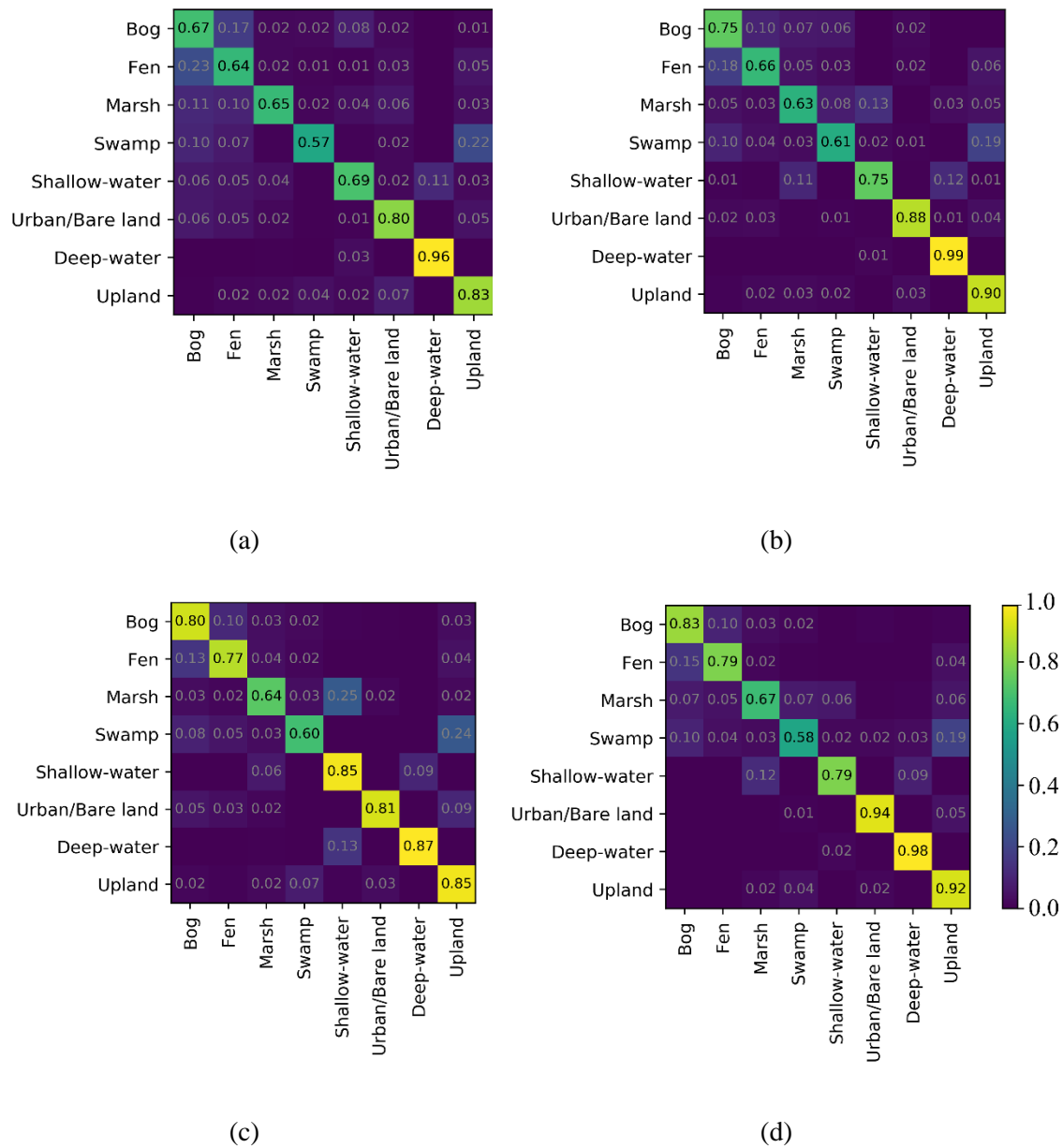
Figure 7.9. The confusion matrices obtained from different classification scenarios, including (a) S1, (b) S2, (c) S3 and (d) S4 in this study.

Notably, all methods successfully classified the non-wetland classes with producer's accuracies beyond 80%. Among the first four scenarios, the object-based classification using optical imagery (i.e., S4) was the most successful approach for classifying the non-wetland classes, with producer's

and user's accuracies exceeding 90% and 80%, respectively. The wetland classes were also

identified with high accuracies in most cases (e.g., bog, fen, and shallow-water) in S4.
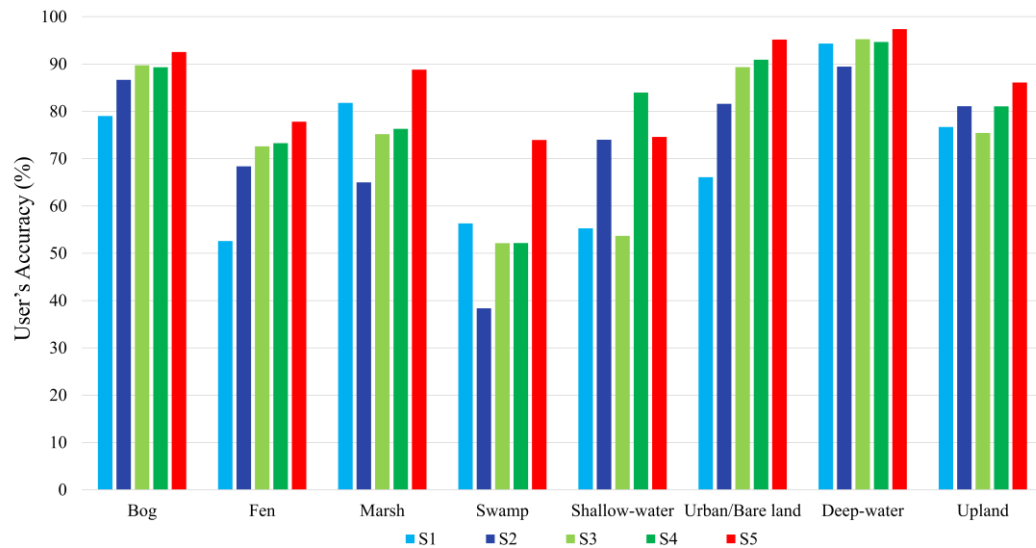

Figure 7.10. The user's accuracies for various land cover classes in different classification
scenarios in this study.

The object-based approach, due to its higher accuracies, was selected for the final classification

scheme in this study, wherein the multi-year summer SAR and optical composites were integrated
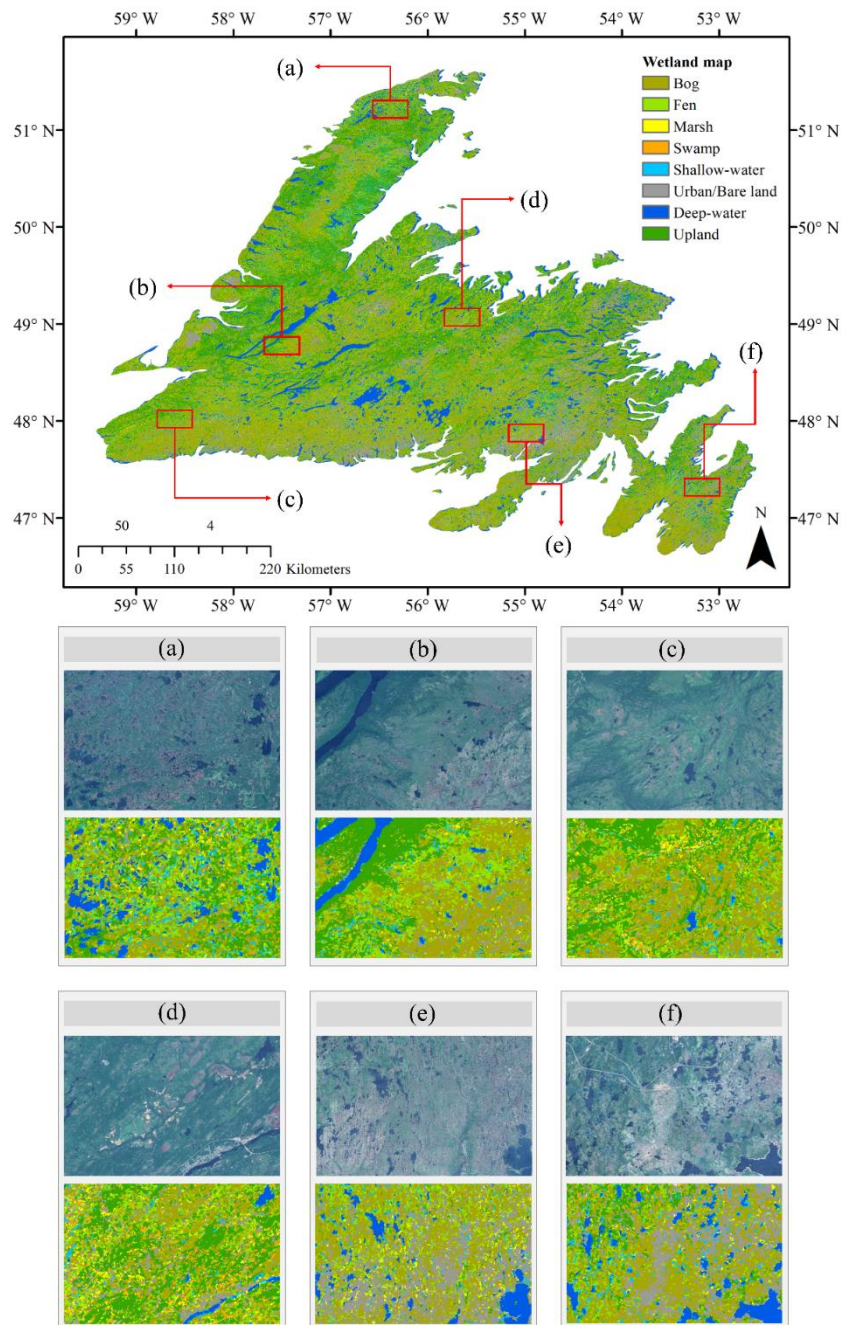
(see Figure 7.11).

Figure 7.11. The final land cover map for the Island of Newfoundland obtained from the object-based Random Forest (RF) classification using the multi-year summer SAR/optical composite. An overall accuracy of 88.37% and a Kappa coefficient of 0.85 were achieved. A total of six insets and their corresponding optical images (i.e., Sentinel-2) were also illustrated to appreciate some of the classification details.

The final land cover map is noiseless and accurately represents the distribution of all land cover classes on a large scale. As shown, the classes of bog and upland are the most prevalent wetland and non-wetland classes, respectively, in the study area. These observations agree well both with field notes recorded by biologists during the in-situ data collection and with visual analysis of aerial and satellite imagery. Figure 7.11 also illustrates several insets from the final land cover map in this study. The visual interpretation of the final classified map by ecological experts demonstrated that most land cover classes were correctly distinguished across the study area. For example, ecological experts noted that bogs appear as a reddish color in optical imagery (true color composite). As shown in Figure 7.11, most bog wetlands are accurately identified in all zoomed areas. Furthermore, small water bodies (e.g., small ponds) and the perimeter of deep water bodies are correctly mapped belonging to the shallow-water class. The upland and urban/bare land classes were also correctly distinguished.

The confusion matrix for the final classification map is illustrated in Figure 7.12. Despite the presence of confusion among wetland classes, the results obtained from the multi-year SAR/optical composite were extremely positive, taking into account the complexity of distinguishing similar wetland classes. As shown in Figure 7.12, all non-wetland classes and shallow-water were correctly identified with producer's accuracies beyond 90%. The most similar wetland classes, namely bog and fen, were classified with producer's accuracies exceeding 80%. The other two wetland classes were also correctly identified with a producer's accuracy of 78% for marsh and 70% for swamp.
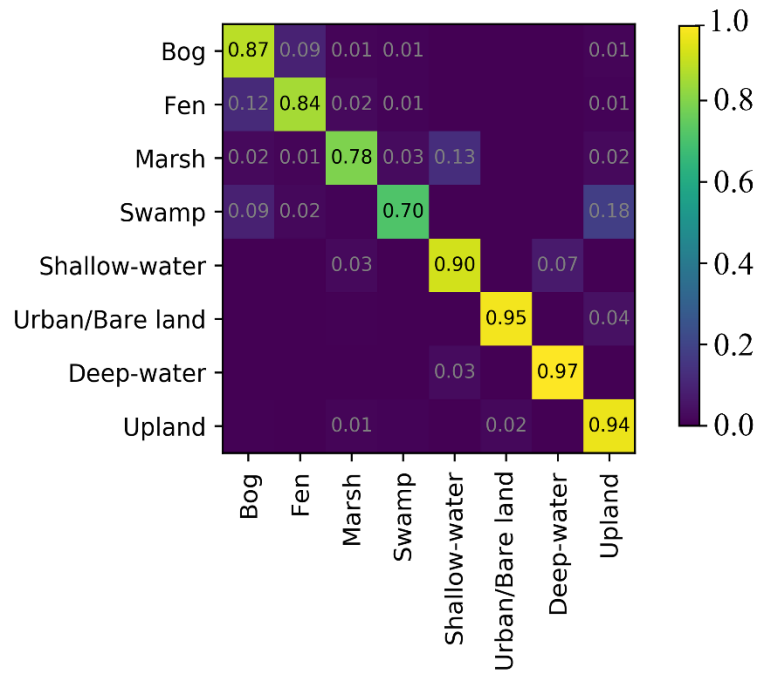
Figure 7.12. The confusion matrix for the final classification map obtained from the object-based
RF classification using the multi-year summer SAR/optical composite (OA: 88.37%, K: 0.85).

7.4. Discussion

In general, the results of the spectral analysis demonstrated the superiority of the NIR band
compared to the visible bands (i.e., blue, green, and red) for distinguishing various wetland classes.
This was particularly true for shallow-water, which was easily separable using NIR. This is logical,
given that water and vegetation exhibit strong absorption and reflection, respectively, in this region
of the electromagnetic spectrum. NDVI was found to be the most useful vegetation index. This
finding is potentially explained by the high sensitivity of NDVI to photosynthetically active
biomasses [48]. Furthermore, the results of the spectral analysis of wetland classes indicated that
class separability using the NDVI index is maximized in July, which corresponds to the peak
growing season in Newfoundland. According to the box-and-whisker plots and the JM distances,
the spectral similarities of wetland classes are slightly concerning, as they revealed the difficulties
in distinguishing similar wetland classes using a single optical feature, which is in agreement with

a previous study [43]. However, the inclusion of all optical features significantly increased the separability between wetland classes.

As shown in Figure 7.9, confusion errors occurred among all classes, especially those of wetlands using the pixel-based classification approach. Notably, the highest confusion was found between the swamp and upland classes in some cases. The upland class is characterized by dry forested land, and swamps are specified as woody (forested) wetland. This results in similarities in both the visual appearance and spectral/backscattering signatures for these classes. With regard to SAR signatures, for example, the dominant scattering mechanism for both classes is volume scattering, especially when the water table is low in swamp [67], which contributes to the misclassification between the two. This is of particular concern when shorter wavelengths (e.g., C-band) are employed, given their shallower penetration depth relative to that of longer wavelengths (e.g., L-band).

Confusion was also common among the herbaceous wetland classes, namely bog, fen, and marsh. This is attributable to the heterogeneity of the landscape in the study area. As field notes suggest, the herbaceous wetland classes were found adjacent to each other without clear cut borders, making them hardly distinguishable. This is particularly severe for bog and fen, since both have very similar ecological and visual characteristics. For example, both are characterized by peatlands, dominated by ecologically similar vegetation types of *Sphagnum* in bogs and *Graminoid* in fens.

Another consideration when interpreting the classification accuracies for different wetland classes is the availability of the training samples/polygons for the supervised classification. As shown in Table 7.1, for example, bogs have a larger number of training polygons compared to the swamp

class. This is because NL has a moist and cool climate [38], which contributes to extensive peatland formation. Accordingly, bog and fen were potentially the most visited wetland classes during in-situ data collection. This resulted in the collection of a larger number of training samples/polygons for these classes. On the other hand, the swamp class is usually found in physically smaller areas relative to those of other classes; for example, in transition zones between wetland and other land cover classes. As such, they may have been dispersed and mixed with other land cover classes, making them difficult to distinguish by the classifier.

Comparison of the classification accuracies using optical and SAR images (i.e., S1 vs. S2 and S3 vs. S4) indicated, according to all evaluation indices in this study, the superiority of the former relative to the latter for wetland mapping in most cases. This suggests that the phenological variations in vegetative productivity captured by optical indices (e.g., NDVI), as well as the contrast between water and non-water classes captured by the NDWI index are more efficient for wetland mapping in our study area than the extracted features from dual-polarimetric SAR data. This finding is consistent with the results of a recent study [11] that employed optical, SAR, and topographic data for predicting the probability of wetland occurrence in Alberta, Canada, using the GEE platform. However, it should be acknowledged that the lower success of SAR compared to optical data is, at least, partially related to the fact that the Sentinel-1 sensor does not collect full-polarimetric data at the present time. This hinders the application of advanced polarimetric decomposition methods that demand full-polarimetric data. Several studies highlighted the great potential of polarimetric decomposition methods for identifying similar wetland classes by characterizing their various scattering mechanisms using such advanced approaches [47].

Despite the superiority of optical data relative to SAR, the highest classification accuracy was obtained by integrating multi-year summer composites of SAR and optical imagery using the

object-based approach (see Table 7.4(S5)). In particular, this classification scenario demonstrates an improvement of about 9% and 4.5% in overall accuracy compared to the object-based classification using the multi-year summer SAR and optical composites, respectively. This is because optical and SAR data are based on range and angular measurements and collect information about the chemical and physical characteristics of wetland vegetation, respectively [68]; thus, the inclusion of both types of observations enhances the discrimination of backscattering/spectrally similar wetland classes [36]. Accordingly, it was concluded that the multi-year summer SAR/optical composite is very useful for improving overall classification accuracy by capturing chemical, biophysical, structural, and phenological variations of herbaceous and woody wetland classes. This was later reaffirmed via the confusion matrix (see Figure 7.12) of the final classification map, wherein confusion decreased compared to classifications based on either SAR or optical data (see Figure 7.9). Furthermore, the McNemar test indicated that there was a very statistically significant difference ($p < 0.05$) for object-based classifications using SAR vs optical/SAR (S3 vs. S5) and optical vs optical/SAR (S4 vs. S5) models (see Table 7.5).

Notably, the multi-year summer SAR/optical composite improved the producer's accuracies of marsh and swamp classes. Specifically, the inclusion of SAR and optical data improved the producer's accuracies of marsh in the final classification map by about 14% and 11% compared to the object-based classification using SAR and optical imagery on their own, respectively. This, too, occurred to a lesser degree for swamp, wherein the producer's accuracies improved in the final classified map by about 12% and 10% compared to those of object-based classified maps using optical and SAR imagery, respectively. The accuracies for other wetland classes, namely bog and fen, were also improved by about 4% and 5%, respectively, in this case relative to the object-based classification using the multi-year optical composite.

Despite significant improvements in the producer's accuracies for some wetland classes (e.g., marsh and swamp) using the SAR/optical data composite, marginal to no improvements were obtained in this case for the non-wetland classes compared to classification based only on optical data. In particular, the use of SAR data does not offer substantial gains beyond the use of optical imagery for distinguishing typical land cover classes, such as urban and deep-water, nor does it present any clear disadvantages. Nevertheless, combining both types of observations addresses the limitation that arises due to the inclement weather in geographic regions with near-permanent cloud cover, such as Newfoundland. Therefore, the results reveal the importance of incorporating multi-temporal optical/SAR data for classification of backscattering/spectrally similar land cover classes, such as wetland complexes. Accordingly, given the complementary advantages of SAR and optical imagery, the inclusion of both types of data still offers a potential avenue for further research in land cover mapping on a large scale.

The results demonstrate the superiority of object-based classification compared to the pixel-based approach in this study. This is particularly true when SAR imagery was employed, as the producer's accuracies for all wetland classes were lower than 70% (see Figure 7.9a). Despite applying speckle reduction, speckle noise can remain, and this affects the classification accuracy during such processing. In contrast to the pixel-based approach, object-based classification benefits from both backscattering/spectral information, as well as contextual information within a given neighborhood. This further enhances semantic land cover information and is very useful for the classification of SAR imagery.

As noted in a previous study [69], the image mosaicking technique over a long time-period may increase classification errors in areas of high inter-annual change, causing a signal of seasonality to be overlooked. Although this image mosaicking technique is essential for addressing the

298

limitation of frequent cloud cover for land cover mapping using optical remote sensing data across a broad spatial scale, this was mitigated in this study to a feasible extent. In particular, to diminish the effects of multi-seasonal observations, the mosaicked image in this study was produced from the multi-year summer composite rather than the multi-year, multi-seasonal composite. The effectiveness of using such multi-year seasonal (e.g., either spring or summer) composites has been previously highlighted, given the potential of such data to capture surface condition variations beneficial for wetland mapping [56]. The overall high accuracy of this technique obtained in this study further corroborates the value of such an approach for mapping wetlands at the provincial-level.

Although the classification accuracies obtained from our previous studies were slightly better in some cases (e.g., [18]), our previous studies involve more time and resources when compared with the current study. For example, our previous study incorporated multi-frequency (X-, C-, and L-bands), multi-polarization (full-polarimetric RADARSAT-2) SAR data to produce local-scale wetland inventories. However, the production of such inventories demanded significant levels of labor, in terms of data preparation, feature extraction, statistical analysis, and classification. Consequently, updating wetland inventories using such methods on a regular basis for a large scale is tedious and expensive. In contrast, the present study relies on open access, regularly updated remotely sensed imagery collected by the Sentinel Missions at a 10 m spatial resolution, which is of great value for provincial- and national-scale wetland inventory maps that can be efficiently and regularly updated.

As mentioned earlier, GEE is an ideal platform that hosts Sentinel-1 and Sentinel-2 data and offers advanced processing functionally. This removes the process of downloading a large number of satellite images, which are already in "analysis ready" formats [30] and, as such, offers significant

built-in time saving aspects [84]. Despite these benefits, limitations with GEE are related to both the lack of atmospherically-corrected Sentinel-2 data within its archive and the parallel method of the atmospheric correction at the time of this research. This may result in uncertainty due to the bidirectional reflectance effects caused by variations in sun, sensor, and surface geometries during satellite acquisitions. Such an atmospheric correction algorithm has been carried out in local applications, such as the estimation of forest aboveground biomass [70], using the Sentinel-2 processing toolbox. Notably, Level-2A Sentinel-2 bottom-of-atmosphere (BOA) data that are atmospherically-corrected are of great value for extracting the most reliable temporal and spatial information, but such data are not yet available within GEE. Recent research, however, reported the potential of including BOA Sentinel-2 data in the near future into the GEE archive [10]. Although the high accuracies of wetland classifications in this study indicated that the effects of C (TOA) reflectance could be negligible, a comparison between TOA and BOA Sentinel-2 data for wetland mapping is suggested for future research.

In the near future, the addition of more machine learning tools and EO data to the GEE API and data catalog, respectively, will further simplify information extraction and data processing. For example, the availability of deep learning approaches through the potential inclusion of TensorFlow in the GEE platform will offer unprecedented opportunities for several remote sensing tasks [9]. Currently, however, employing state-of-the-art classification algorithms across broad spatial scales requires downloading data for additional local processing tasks and uploading data back to GEE due to the lack of functionality for such processing at present. Downloading such a large amount of remote sensing data is time consuming, given bandwidth limitations, and further, its processing demands a powerful local processing machine. Nevertheless, full exploitation of

300

deep learning methods for mapping wetlands at hierarchical levels requires abundant, high-quality representative training samples.

The approaches presented in this study may be extended to generate a reliable, hierarchical, national-scale Canadian wetland inventory map and are an essential step toward global-scale wetland mapping. However, more challenges are expected when the study area is extended to the national-scale (i.e., Canada) with more cloud cover, more fragmented landscapes, and various dominant wetland classes across the country [71]. Notably, the biggest challenge in producing automated, national-scale wetland inventories is collecting a sufficient amount of high quality training and testing samples to support dependable coding, rapid product delivery, and accurate wetland mapping on large scale. Although using GEE for discriminating wetland and non-wetland samples could be useful, it is currently inefficient for identifying hierarchical wetland ground-truth data. There are also challenges related to inconsistency in terms of wetland definitions at the global-scale that can vary by country (e.g., Canadian Wetland Classification System, New Zealand, and East Africa) [1]. However, given recent advances in cloud computing and big data, these barriers are eroding and new opportunities for more comprehensive and dynamic views of the global extent of wetlands are arising. For example, the integration of Landsat and Sentinel data using the GEE platform will address the limitations of cloud cover and lead to production of more accurate, finer category wetland classification maps, which are of great benefit for hydrological and ecological monitoring of these valuable ecosystems. The results of this study suggest the feasibility of generating provincial-level wetland inventories by leveraging the opportunities offered by cloud-computing resources, such as GEE. The current study will contribute to the production of regular, consistent, provincial-scale wetland inventory maps that can support biodiversity and sustainable management of Newfoundland and Labrador's wetland resources.

7.5. Conclusion

Cloud-based computing resources and open-access EO data have caused a remarkable paradigm-shift in the field of landcover mapping by replacing the production of standard static maps with those that are more dynamic and application-specific thanks to recent advances in geospatial science. Leveraging the computational power of the Google Earth Engine and the availability of high spatial resolution remote sensing data collected by Copernicus Sentinels, the first detailed (category-based), provincial-level wetland inventory map was produced in this study. In particular, multi-year summer Sentinel-1 and Sentinel-2 data were used to map a complex series of small and large, heterogeneous wetlands on the Island of Newfoundland, Canada, covering an approximate area of 106,000 km^2.

Multiple classification scenarios, including those that were pixel- versus object-based, were considered and the discrimination capacities of optical and SAR data composites were compared. The results revealed the superiority of object-based classification relative to the pixel-based approach. Although classification accuracy using the multi-year summer optical composite was found to be more accurate than the multi-year summer SAR composite, the inclusion of both types of data (i.e., SAR and optical) significantly improved the accuracies of wetland classification. An overall classification accuracy of 88.37% was achieved using an object-based RF classification with the multi-year (2016–2018) summer optical/SAR composite, wherein wetland and non-wetland classes were distinguished with accuracies beyond 70% and 90%, respectively.

This study further contributes to the development of Canadian wetland inventories, characterizes the spatial distribution of wetland classes over a previously unmapped area with high spatial resolution, and importantly, augments previous local-scale wetland map products. Given the relatively similar ecological characteristics of wetlands across Canada, future work could extend

this study by examining the value of the presented approach for mapping areas containing wetlands with similar ecological characteristics and potentially those with a greater diversity of wetland classes in other Canadian provinces and elsewhere. Further extension of this study could also focus on exploring the efficiency of a more diverse range of multi-temporal datasets (e.g., the 30 years Landsat dataset) to detect and understand wetland dynamics and trends over time in the province of Newfoundland and Labrador.

7.6. References

[1]   R. W. Tiner, M. W. Lang, and V. V Klemas, *Remote sensing of wetlands: applications and advances*. CRC Press, 2015.

[2]   W. J. Mitsch *et al.*, "Wetlands, carbon, and climate change," *Landsc. Ecol.*, vol. 28, no. 4, pp. 583–597, 2013.

[3]   W. J. Mitsch, "GOSSELINK. JG, 2000. Wetlands." John Wiley and Sons, Inc., New York, New York, USA.

[4]   A. L. Gallant, "The challenges of remote monitoring of wetlands." Multidisciplinary Digital Publishing Institute, 2015.

[5]   M. Maxa and P. Bolstad, "Mapping northern wetlands with high resolution satellite images and LiDAR," *Wetlands*, vol. 29, no. 1, p. 248, 2009.

[6]   M. Lang, L. L. Bourgeau-Chavez, R. W. Tiner, and V. V Klemas, "Advances in remotely sensed data and techniques for wetland mapping and monitoring," *Remote Sens. Wetl. Appl. Adv. Ralph, WT, Megan, WL, Victor, VK, Eds*, pp. 79–118, 2015.

[7]   M. A. Wulder, J. G. Masek, W. B. Cohen, T. R. Loveland, and C. E. Woodcock, "Opening the archive: How free data has enabled the science and monitoring promise of Landsat," *Remote Sens. Environ.*, vol. 122, pp. 2–10, 2012.

[8]   T. Whiteside and R. Bartolo, "Mapping aquatic vegetation in a tropical wetland using high spatial resolution multispectral satellite imagery," *Remote Sens.*, vol. 7, no. 9, pp. 11664–11694, 2015.

[9]   P. Teluguntla *et al.*, "A 30-m landsat-derived cropland extent product of Australia and China using random forest machine learning algorithm on Google Earth Engine cloud computing platform," *ISPRS J. Photogramm. Remote Sens.*, vol. 144, pp. 325–340, 2018.

[10]   A. Shelestov, M. Lavreniuk, N. Kussul, A. Novikov, and S. Skakun, "Exploring Google earth engine platform for Big Data Processing: Classification of multi-temporal satellite imagery for crop mapping," *Front. Earth Sci.*, vol. 5, p. 17, 2017.

[11]   J. Hird, E. DeLancey, G. McDermid, and J. Kariyeva, "Google Earth Engine, open-access satellite data, and machine learning in support of large-area probabilistic wetland mapping," *Remote Sens.*, vol. 9, no. 12, p. 1315, 2017.

[12]   N. Gorelick, M. Hancher, M. Dixon, S. Ilyushchenko, D. Thau, and R. Moore, "Google Earth Engine: Planetary-scale geospatial analysis for everyone," *Remote Sens. Environ.*, vol. 202, pp. 18–27, 2017.

[13]   N. Sazib, I. Mladenova, and J. Bolten, "Leveraging the Google Earth Engine for Drought Assessment Using Global Soil Moisture Data," *Remote Sens.*, vol. 10, no. 8, p. 1265, 2018.

[14]   R. Aguilar, R. Zurita-Milla, E. Izquierdo-Verdiguier, and R. A De By, "A cloud-based multi-temporal ensemble classifier to map smallholder farming systems," *Remote Sens.*, vol. 10, no. 5, p. 729, 2018.

[15] F. de Lucia Lobo, P. W. M. Souza-Filho, E. M. L. de Moraes Novo, F. M. Carlos, and C. C. F. Barbosa, "Mapping Mining Areas in the Brazilian Amazon Using MSI/Sentinel-2 Imagery (2017)."

[16] L. Kumar and O. Mutanga, "Google Earth Engine Applications Since Inception: Usage, Trends, and Potential," *Remote Sens.*, vol. 10, no. 10, p. 1509, 2018.

[17] B. Waske, M. Fauvel, J. A. Benediktsson, and J. Chanussot, "Machine learning techniques in remote sensing data analysis," *Kernel methods Remote Sens. data Anal.*, pp. 3–24, 2009.

[18] M. Mahdianpari, B. Salehi, F. Mohammadimanesh, and M. Motagh, "Random forest wetland classification using ALOS-2 L-band, RADARSAT-2 C-band, and TerraSAR-X imagery," *ISPRS J. Photogramm. Remote Sens.*, vol. 130, 2017.

[19] P. Thanh Noi and M. Kappas, "Comparison of random forest, k-nearest neighbor, and support vector machine classifiers for land cover classification using Sentinel-2 imagery," *Sensors*, vol. 18, no. 1, p. 18, 2018.

[20] P. O. Gislason, J. A. Benediktsson, and J. R. Sveinsson, "Random forests for land cover classification," *Pattern Recognit. Lett.*, vol. 27, no. 4, pp. 294–300, 2006.

[21] V. F. Rodriguez-Galiano, B. Ghimire, J. Rogan, M. Chica-Olmo, and J. P. Rigol-Sanchez, "An assessment of the effectiveness of a random forest classifier for land-cover classification," *ISPRS J. Photogramm. Remote Sens.*, vol. 67, pp. 93–104, 2012.

[22] A. Whyte, K. P. Ferentinos, and G. P. Petropoulos, "A new synergistic approach for monitoring wetlands using Sentinels-1 and 2 data with object-based machine learning algorithms," *Environ. Model. Softw.*, vol. 104, pp. 40–54, 2018.

[23] M. C. Hansen *et al.*, "High-resolution global maps of 21st-century forest cover change," *Science (80-.).*, vol. 342, no. 6160, pp. 850–853, 2013.

[24] J. Xiong *et al.*, "Automated cropland mapping of continental Africa using Google Earth Engine cloud computing," *ISPRS J. Photogramm. Remote Sens.*, vol. 126, pp. 225–244, 2017.

[25] Y. Tsai, D. Stow, H. Chen, R. Lewison, L. An, and L. Shi, "Mapping Vegetation and Land Use Types in Fanjingshan National Nature Reserve Using Google Earth Engine," *Remote Sens.*, vol. 10, no. 6, p. 927, 2018.

[26] H. Huang *et al.*, "Mapping major land cover dynamics in Beijing using all Landsat images in Google Earth Engine," *Remote Sens. Environ.*, vol. 202, pp. 166–176, 2017.

[27] M. Mahdianpari *et al.*, "Fisher Linear Discriminant Analysis of coherency matrix for wetland classification using PolSAR imagery," *Remote Sens. Environ.*, vol. 206, 2018.

[28] F. Mohammadimanesh, B. Salehi, M. Mahdianpari, M. Motagh, and B. Brisco, "An efficient feature optimization for wetland mapping by synergistic use of SAR intensity, interferometry, and polarimetry data," *Int. J. Appl. earth Obs. Geoinf.*, vol. 73, pp. 450–462, 2018.

[29] R. d'Andrimont, G. Lemoine, and M. van der Velde, "Targeted Grassland Monitoring at Parcel Level Using Sentinels, Street-Level Images and Field Observations," *Remote Sens.*, vol. 10, no. 8,

p. 1300, 2018.

[30] J. Aschbacher and M. P. Milagro-Pérez, "The European Earth monitoring (GMES) programme: Status and perspectives," *Remote Sens. Environ.*, vol. 120, pp. 3–8, 2012.

[31] J.-R. B. Bwangoy, M. C. Hansen, D. P. Roy, G. De Grandi, and C. O. Justice, "Wetland mapping in the Congo Basin using optical and radar remotely sensed data and derived topographical indices," *Remote Sens. Environ.*, vol. 114, no. 1, pp. 73–86, 2010.

[32] M. Mahdianpari, B. Salehi, M. Rezaee, F. Mohammadimanesh, and Y. Zhang, "Very deep convolutional neural networks for complex land cover mapping using multispectral remote sensing imagery," *Remote Sens.*, vol. 10, no. 7, p. 1119, 2018.

[33] M. Rezaee, M. Mahdianpari, Y. Zhang, and B. Salehi, "Deep Convolutional Neural Network for Complex Wetland Classification Using Optical Remote Sensing Imagery," *IEEE J. Sel. Top. Appl. Earth Obs. Remote Sens.*, 2018.

[34] D. Amarsaikhan *et al.*, "Comparison of multisource image fusion methods and land cover classification," *Int. J. Remote Sens.*, vol. 33, no. 8, pp. 2532–2550, 2012.

[35] S. van Beijma, A. Comber, and A. Lamb, "Random forest classification of salt marsh vegetation habitats using quad-polarimetric airborne SAR, elevation and optical RS data," *Remote Sens. Environ.*, vol. 149, pp. 118–129, 2014.

[36] J. Zhang, "Multi-source remote sensing data fusion: status and trends," *Int. J. Image Data Fusion*, vol. 1, no. 1, pp. 5–24, 2010.

[37] E. S. W. G. (Canada), C. for Land, B. R. R. (Canada), and C. S. of the E. Directorate, *A national ecological framework for Canada*. Centre for Land and Biological Resources Research; Hull, Quebec: State of …, 1996.

[38] R. South, *Biogeography and Ecology of the Island of Newfoundland*, vol. 48. Springer Science & Business Media, 1983.

[39] X. Zhang, B. Wu, G. Ponce-Campos, M. Zhang, S. Chang, and F. Tian, "Mapping up-to-date paddy rice extent at 10 m resolution in China through the integration of optical and synthetic aperture radar images," *Remote Sens.*, vol. 10, no. 8, p. 1200, 2018.

[40] I. B. Marshall, C. A. S. Smith, and C. J. Selby, "A national framework for monitoring and reporting on environmental sustainability in Canada," in *Global to Local: Ecological Land Classification*, Springer, 1996, pp. 25–38.

[41] Y. Gauthier, M. Bernier, and J.-P. Fortin, "Aspect and incidence angle sensitivity in ERS-1 SAR data," *Int. J. Remote Sens.*, vol. 19, no. 10, pp. 2001–2006, 1998.

[42] J.-S. Lee, J.-H. Wen, T. L. Ainsworth, K.-S. Chen, and A. J. Chen, "Improved sigma filter for speckle filtering of SAR imagery," *IEEE Trans. Geosci. Remote Sens.*, vol. 47, no. 1, pp. 202–213, 2009.

[43] F. Mohammadimanesh, B. Salehi, M. Mahdianpari, B. Brisco, and M. Motagh, "Multi-temporal,

multi-frequency, and multi-polarization coherence and SAR backscatter analysis of wetlands," *ISPRS J. Photogramm. Remote Sens.*, vol. 142, pp. 78–93, 2018.

[44]   N. Baghdadi, M. Bernier, R. Gauthier, and I. Neeson, "Evaluation of C-band SAR data for wetlands mapping," *Int. J. Remote Sens.*, vol. 22, no. 1, pp. 71–88, 2001.

[45]   S. C. Steele-Dunne, H. McNairn, A. Monsivais-Huertero, J. Judge, P.-W. Liu, and K. Papathanassiou, "Radar remote sensing of agricultural canopies: A review," *IEEE J. Sel. Top. Appl. Earth Obs. Remote Sens.*, vol. 10, no. 5, pp. 2249–2273, 2017.

[46]   L. F. de Almeida Furtado, T. S. F. Silva, and E. M. L. de Moraes Novo, "Dual-season and full-polarimetric C band SAR assessment for vegetation mapping in the Amazon várzea wetlands," *Remote Sens. Environ.*, vol. 174, pp. 212–222, 2016.

[47]   J. R. Jensen and K. Lulla, "Introductory digital image processing: a remote sensing perspective," 1987.

[48]   L. Ji, L. Zhang, and B. Wylie, "Analysis of dynamic thresholds for the normalized difference water index," *Photogramm. Eng. Remote Sens.*, vol. 75, no. 11, pp. 1307–1317, 2009.

[49]   H. Xu, "Modification of normalised difference water index (NDWI) to enhance open water features in remotely sensed imagery," *Int. J. Remote Sens.*, vol. 27, no. 14, pp. 3025–3033, 2006.

[50]   A. S. Rogers and M. S. Kearney, "Reducing signature variability in unmixing coastal marsh Thematic Mapper scenes using spectral indices," *Int. J. Remote Sens.*, vol. 25, no. 12, pp. 2317–2335, 2004.

[51]   S. K. McFeeters, "The use of the Normalized Difference Water Index (NDWI) in the delineation of open water features," *Int. J. Remote Sens.*, vol. 17, no. 7, pp. 1425–1432, 1996.

[52]   N. Flood, "Seasonal composite Landsat TM/ETM+ images using the medoid (a multi-dimensional median)," *Remote Sens.*, vol. 5, no. 12, pp. 6481–6500, 2013.

[53]   P. Griffiths, S. van der Linden, T. Kuemmerle, and P. Hostert, "A pixel-based Landsat compositing algorithm for large area land cover mapping," *IEEE J. Sel. Top. Appl. Earth Obs. Remote Sens.*, vol. 6, no. 5, pp. 2088–2101, 2013.

[54]   D. P. Roy *et al.*, "Web-enabled Landsat Data (WELD): Landsat ETM+ composited mosaics of the conterminous United States," *Remote Sens. Environ.*, vol. 114, no. 1, pp. 35–49, 2010.

[55]   M. Wulder *et al.*, "A National Assessment of Wetland Status and Trends for Canada's Forested Ecosystems Using 33 Years of Earth Observation Satellite Data," *Remote Sens.*, vol. 10, no. 10, p. 1623, 2018.

[56]   P. H. Swain and S. M. Davis, "Remote sensing: the quantitative approach," *IEEE Trans. Pattern Anal. Mach. Intell.*, no. 6, pp. 713–714, 1981.

[57]   S. Padma and S. Sanjeevi, "Jeffries Matusita based mixed-measure for improved spectral matching in hyperspectral image analysis," *Int. J. Appl. earth Obs. Geoinf.*, vol. 32, pp. 138–151, 2014.

[58]   K. S. Schmidt and A. K. Skidmore, "Spectral discrimination of vegetation types in a coastal

wetland," *Remote Sens. Environ.*, vol. 85, no. 1, pp. 92–108, 2003.

[59]   M. Belgiu and L. Drăguţ, "Random forest in remote sensing: A review of applications and future directions," *ISPRS J. Photogramm. Remote Sens.*, vol. 114, pp. 24–31, 2016.

[60]   L. Breiman, "Random forests," *Mach. Learn.*, vol. 45, no. 1, pp. 5–32, 2001.

[61]   U. C. Benz, P. Hofmann, G. Willhauck, I. Lingenfelder, and M. Heynen, "Multi-resolution, object-oriented fuzzy analysis of remote sensing data for GIS-ready information," *ISPRS J. Photogramm. Remote Sens.*, vol. 58, no. 3–4, pp. 239–258, 2004.

[62]   R. Achanta and S. Süsstrunk, "Superpixels and polygons using simple non-iterative clustering," in *Computer Vision and Pattern Recognition (CVPR), 2017 IEEE Conference on*, 2017, pp. 4895–4904.

[63]   R. G. Congalton, "A review of assessing the accuracy of classifications of remotely sensed data," *Remote Sens. Environ.*, vol. 37, no. 1, pp. 35–46, 1991.

[64]   Q. McNemar, "Note on the sampling error of the difference between correlated proportions or percentages," *Psychometrika*, vol. 12, no. 2, pp. 153–157, 1947.

[65]   J. de Leeuw, H. Jia, L. Yang, X. Liu, K. Schmidt, and A. K. Skidmore, "Comparing accuracy assessments to infer superiority of image classification methods," *Int. J. Remote Sens.*, vol. 27, no. 1, pp. 223–232, 2006.

[66]   L. Dingle Robertson and D. J. King, "Comparison of pixel-and object-based classification in land cover change mapping," *Int. J. Remote Sens.*, vol. 32, no. 6, pp. 1505–1529, 2011.

[67]   B. Chen *et al.*, "A mangrove forest map of China in 2015: Analysis of time series Landsat 7/8 and Sentinel-1A imagery in Google Earth Engine cloud computing platform," *ISPRS J. Photogramm. Remote Sens.*, vol. 131, pp. 104–120, 2017.

[68]   L. Kelley, L. Pitcher, and C. Bacon, "Using Google Earth Engine to Map Complex Shade-Grown Coffee Landscapes in Northern Nicaragua," *Remote Sens.*, vol. 10, no. 6, p. 952, 2018.

[69]   A. Jacobson *et al.*, "A novel approach to mapping land conversion using Google Earth with an application to East Africa," *Environ. Model. Softw.*, vol. 72, pp. 1–9, 2015.

[70]   J. Dong *et al.*, "Mapping paddy rice planting area in northeastern Asia with Landsat 8 images, phenology-based algorithm and Google Earth Engine," *Remote Sens. Environ.*, vol. 185, pp. 142–154, 2016.

[71]   M. A. Wulder, J. C. White, J. G. Masek, J. Dwyer, and D. P. Roy, "Continuity of Landsat observations: Short term considerations," *Remote Sens. Environ.*, vol. 115, no. 2, pp. 747–751, 2011.

Chapter 8. Summary, conclusions, and future outlook

8.1. Summary

This thesis examined the potential of various EO data, including optical (i.e., RapidEye and Sentinel-2) and SAR (i.e., ALOS PALSAR-2, RADARSAT-2, TerraSAR-X, and Sentinel-1) imagery for discriminating Canadian wetland classes, namely bog, fen, marsh, swamp, and shallow-water in Newfoundland and Labrador. This study compared the advantages and disadvantages of the aforementioned EO data and the extracted features from such data for distinguishing similar wetland classes. Various new techniques were introduced to improve and contribute to the methodologies developed in the existing literature for land cover and, in particular, wetland mapping.

 The importance of employing an efficient speckle reduction method was discussed based on the literature review and was later supported by proposing a new speckle reduction technique for PolSAR data. The study also demonstrated the significance of a hierarchical classification scheme for discriminating complex land cover units. This is a paradigm shift that benefits from a dynamic classification design based on the complexity and similarity of land cover (wetland) classes, rather than on a single stream processing chain, which is better suited for the classification of typical land cover classes. The proposed approach achieved a competitive classification accuracy using single source EO data (i.e., only SAR images).

This thesis also illustrated the strengths of the proposed feature weighting of PolSAR data in enhancing semantic land cover information. The proposed method considered both the statistical and physical characteristics of PolSAR data and resulted in significant improvements in overall classification results, as compared to those classifications based on typical PolSAR features. The

investigation of extracted features from simulated compact polarimetric SAR data revealed their ability to distinguish wetland classes with similar backscattering signatures.

The study also demonstrated that, compared to conventional machine learning tools, such as RF and SVM, deep CNNs were advantageous for the classification of complex land cover ecosystems. This is because the latter approaches attained significantly higher classification accuracies and removed the tedious process of feature engineering design. Finally, the production of the first provincial-scale wetland inventory map of NL revealed a paradigm-shift from standard static products and approaches toward generating more dynamic, on-demand, large-scale wetland coverage maps through advanced cloud computing resources that simplify access to and processing of "Geo Big Data".

8.2. Conclusion

Given both the economical and environmental benefits of wetlands [1], there have been significant efforts for wetland mapping and monitoring using remote sensing imagery worldwide [2]–[7]. In particular, the production of updated wetland inventory maps are of particular interest for monitoring changes and for sustainable management of these productive ecosystems [8]. This dissertation represents an advancement toward the cost-effective production of operational wetland inventory maps using advanced remote sensing tools and data. This results in several developed methodologies for wetland classification and beyond [9]–[14], as well as the production of several small-scale maps and, importantly, a provincial-scale wetland inventory map of Newfoundland and Labrador [15]. The specific conclusions of this study are described below.

8.2.1. PolSAR image processing: speckle reduction

A new speckle reduction method was proposed and its effectiveness was evaluated at two stages: de-speckled images and classification results [9]. The proposed de-speckling method was

advantageous compared to several well-known methods, including Frost [16], Kuan [17], enhanced Lee [18], and SARBM3D [19]. Hence, it was concluded that both contextual and pixel-wised analysis in a Gaussian Markov Random Field (GMRF) based on a Bayesian framework are useful for PolSAR image de-speckling. To the best of the author's knowledge, the effect of PolSAR image de-speckling on the accuracy of wetland classification was first investigated in this research. The results of this study revealed that speckle reduction is a crucial pre-processing step for PolSAR image applications.

8.2.2. Wetland classification using PolSAR imagery

In this thesis, two new methodologies were developed for wetland classification using data collected from SAR sensors, and the capabilities of the proposed methods were compared with those of conventional algorithms [11], [12]. The hierarchical classification algorithm proposed in Chapter 3 demonstrated that some wetland classes are easier to distinguish compared to others. For example, the shallow-water class was discriminable using only SAR backscattering analysis, as it had the lowest SAR responses compared to other wetland classes. Hence, it was concluded that the discrimination of this class does not require the exploitation of advanced polarimetric decomposition methods. In contrast, herbaceous wetland classes (e.g., bog, fen, and marsh) were found to be difficult to distinguish based only on SAR backscattering analysis and the discrimination of these classes requires the use of polarimetric decompositions. In Chapter 3, features were extracted from single-pol TerraSAR-X, dual-pol ALOS PALSAR-2, and full-pol RADARSAT-2 imagery. Overall, features extracted from full-polarimetry data were found to be better for discrimination of similar wetland classes. A total of 44 polarimetric features, including features from covariance and coherency matrices, the Cloude-Pottier [20], Freeman-Durden [21], Touzi [22], and Yamaguchi [23] decompositions, as well as Kennaugh matrix elements were

extracted from dual- and full-pol data and were incorporated into the final classification scheme. The variable importance analysis of RF revealed the superiority of extracted features from the Kennaugh matrix element, Yamaguchi, and Freeman-Durden decompositions for wetland mapping.

Furthermore, to enhance the discrimination capability of the input data prior to their incorporation into the classification scheme, a new PolSAR feature, the modified coherency matrix, was proposed [12]. The proposed feature was developed based on both the physical and statistical characteristics of PolSAR data and was applied to full polarimetric RADARSAT-2 image. This is an adaptive feature weighting, as it increases the contribution of the most discriminant features and decreases that of the least separable features by assigning them higher and lower weights, respectively. The experimental results illustrated the superiority of the proposed approach compared to other well-known PolSAR features for wetland classification. Notably, the feature pair selected in Chapter 3 demonstrated a higher classification accuracy compared to Chapter 4 in the last classification scenarios of both studies for the Avalon study area. This may be attributed to the contribution of L-band data with deeper penetration depth in the former study, as compared to that of the latter, for which only C-band data were used.

In addition to the developed methodologies of wetland mapping using currently operating SAR missions, we examined the transferability of existing methods to data to be collected by the upcoming RADARSAT Constellation Mission (RCM) [10]. Several features were extracted from simulated CP SAR data and their discrimination capabilities were compared with those of full- and dual-polarimetrtic data. The experimental results confirmed the potential of data collected from CP for wetland classification. Furthermore, the increased temporal frequency of image

acquisitions and large swath coverage of RCM further enhance its capability for operational applications [24].

Overall, Chapters 3, 4, and 5 present novel approaches for classifying wetland classes and improve our understanding for mapping these productive ecosystems using SAR and PolSAR data.

8.2.3. Deep Convolutional Neural Network (CNN) for wetland classification

In this thesis, very deep CNNs were adopted for the classification of multi-spectral RapidEye optical imagery for the first time. One of the limitations of these deep CNNs for remote sensing applications is that they were originally designed to handle three input bands. This was addressed in this research by developing a pipeline in Python capable of handling data with more than three input bands [13]. Seven state-of-the-art deep CNNs, namely DenseNet121 [25], InceptionV3 [26], VGG16, VGG19 [27], Xception [28], ResNet50 [29], and InceptionResNetV2, were adopted for the classification of wetland complexes. Two strategies were carried out for training these deep CNNs: fine-tuning of pre-trained networks using three input bands and full-training using three- and five-input bands. The experimental results revealed the full-training of five input bands was advantageous relative to other approaches, thus confirming the significance of the developed technique (i.e., adoption of five input bands) for discriminating similar wetland classes.

8.2.4. Wetland classification on large scales

The intent of this part of research was to illustrate the capability of cloud-based computing resources, such as Google Earth Engine (GEE), and the significance of open access Earth Observation (EO) data, such as Sentinel-1 and Sentinel-2, for generating custom, on demand, large-scale land cover maps. Leveraging the GEE computational power and large pool of open access optical and SAR data collected by the Copernicus Sentinels, we produced wetland inventory maps of Newfoundland and Labrador and the other Canadian provinces (i.e., Alberta, British

313

Columbia, and Ontario) at a spatial resolution of 10 m. The classification maps were produced using optical, SAR, and the integration of both types of data. The highest classification accuracy was attained by compositing multi-source (optical and SAR) EO data. This is because the SAR signal is responsive to geometrical and physical characteristics of targets, whereas optical data are responsive to chemical and molecular characteristics of targets. Thus, the integration of both types of data was advantageous for discriminating wetland classes with similar backscatter and spectral signatures. The developed algorithm in GEE for processing Geo Big data clearly demonstrated the ability to discriminate wetland classes with various sizes accurately at a large scale ($\sim$500,531km^2). The resulting ever-in-demand inventory map of the Atlantic provinces is of great interest to and can be used by many stakeholders, including federal and provincial governments, municipalities, NGOs, and environmental consultants.

8.3. Future outlook

Remote sensing data have long proven to be effective for wetland mapping and monitoring [2], [3], [30], yet some limitations remain. These challenges include the backscattering/spectrally similar signature of wetland classes, insufficient classification accuracy of wetland classes, and limitations of wetland mapping on large scales. While most of these limitations are addressed in this dissertation, some recommendations for future research are given in the following.

All methods proposed in this thesis have been tested and applied to wetland classification (see Chapters 2, 3, and 4). However, more extensive testing is required to further confirm the potential of these developed algorithms in other applications. In addition to examining the capability of these methods for other wetlands globally, they have potential for classifying other complex land cover ecosystems, such as sea ice and crop classifications. This will further move these proposed methods from the research stage to the operational stage. Our comparison between data collected

by multi-frequency SAR sensors for wetland mapping could also be further improved (Chapter 3). In particular, we used single-pol TerraSAR-X, dual-pol ALOS-2, and full-pol RADARSAT-2 data, as these data were available at the time of this research. Although full-pol TerraSAR-X data are not yet available, a comparison and utilization of full-pol ALOS-2 and RADARSAT-2 offer a potential avenue for future research. Furthermore, the classification results obtained from simulated CP SAR data in this study can be validated when real CP SAR data are available by RCM.

As mentioned earlier, the proposed coherency matrix was developed based on the physical and statistical characteristics of PolSAR data. For the statistical component, a Fisher Linear Discriminant Analysis (FLDA) was considered, whereas an H/α Wishart classification was used for physical interpretation of PolSAR data [31]. Alternative approaches, such as the physical interpretation of extracted features from Freeman-Durden [21] and Touzi [22] decompositions, could also be explored. The results of such an investigation may further deepen our knowledge of polarimetric decomposition techniques for wetland characterization.

Most wetland studies have focused on the production of small-scale (regional) wetland inventory maps [3], [32], [33]. Although these small-scale wetland inventories are useful, they are obtained by applying different methodologies and incorporating various types of data, making them incomparable and inconsistent [1]. This study clearly demonstrated the capability of cloud computing resources and open access EO data for wetland mapping and monitoring [15]. Such investigations in other Canadian provinces, as well as at the national scale (Canada wide), should be increased. However, collecting country wide ground truth data with sufficient accuracy will be essential for such an investigation. Accordingly, to produce a comprehensive national-scale wetland inventory map, efforts to collect accurate ground truth data in other provinces should be

315

initiated or continued. This necessitates the incorporation of several government and non-government organizations. Importantly, Landsat sensors have been collecting frequent EO data for over 30 years. These time series of EO data along with powerful cloud computing resources offer unprecedented opportunities for wetland change detection at provincial and national scales.

Wetland classification using EO data has shown promising results in several studies (e.g., [2], [34]–[37]) with varying degrees of accuracy, depending on the type of data and applied techniques. In this study, the integration of multi-sensor SAR (Chapter 3) and multi-source optical and SAR (Chapter 7) data was found to be useful. This suggests that the inclusion of various source of EO data is promising and should be further examined in the future. This may include data collected by SAR, optical, and Light Detection and Ranging (Lidar) sensors. In addition to the expected improvement in overall classification accuracy by employing such a multi-sensor, multi-source approach, as in this thesis, it also addresses the limitations of single source (or type) of data. For example, the integration of optical and SAR data not only increases the sensitivity to the various characteristics of ground targets but addresses the limitations that may arise due to chronic cloud cover upon the exclusive use of optical data. Furthermore, lower ground feature detectability within SAR data due to the presence of speckle noise may also be addressed using this technique.

Another area for future research is consideration of the scale effect. It is beneficial to examine the level of required spatial and spectral resolutions for particular applications. Higher spatial resolution data provide much detail of wetland classes, but is both cost- and resource-intensive. However, such detailed information may not be mandatory in some applications, such as wetland boundary identification and the temporal trends of wetlands. Thus, the most appropriate data resolution should be determined based on specific research objectives and questions.

Finally, wetland studies incorporating a multidisciplinary approach should be undertaken, as geography, ecology, environmental science, and remote sensing are capable of mapping and managing wetlands from different perspectives [38]. Given the high variability and diversity of wetlands worldwide, a clear management strategy is lacking in most cases, although such a strategy is necessary for the restoration and effective protection of wetlands. Thus, the synergistic use of remote sensing for wetland mapping, along with advanced technologies for wetland conservation and restoration and managing wetland ecological processes is one broad area to explore in future research. All of these avenues for future research are possible because of the techniques and results presented in this dissertation.

8.4. References

[1]   R. W. Tiner, M. W. Lang, and V. V Klemas, *Remote sensing of wetlands: applications and advances*. CRC press, 2015.

[2]   T. L. Evans and M. Costa, "Landcover classification of the Lower Nhecolândia subregion of the Brazilian Pantanal Wetlands using ALOS/PALSAR, RADARSAT-2 and ENVISAT/ASAR imagery," *Remote Sens. Environ.*, vol. 128, pp. 118–137, 2013.

[3]   S. van Beijma, A. Comber, and A. Lamb, "Random forest classification of salt marsh vegetation habitats using quad-polarimetric airborne SAR, elevation and optical RS data," *Remote Sens. Environ.*, vol. 149, pp. 118–129, 2014.

[4]   L. F. de Almeida Furtado, T. S. F. Silva, and E. M. L. de Moraes Novo, "Dual-season and full-polarimetric C band SAR assessment for vegetation mapping in the Amazon várzea wetlands," *Remote Sens. Environ.*, vol. 174, pp. 212–222, 2016.

[5]   C. Wohlfart, K. Winkler, A. Wendleder, and A. Roth, "TerraSAR-X and Wetlands: A Review," *Remote Sens.*, vol. 10, no. 6, p. 916, 2018.

[6]   P. Kandus *et al.*, "Remote sensing of wetlands in South America: Status and challenges," *Int. J. Remote Sens.*, vol. 39, no. 4, pp. 993–1016, 2018.

[7]   M. L. Zoffoli, P. Kandus, N. Madanes, and D. H. Calvo, "Seasonal and interannual analysis of wetlands in South America using NOAA-AVHRR NDVI time series: the case of the Parana Delta Region," *Landsc. Ecol.*, vol. 23, no. 7, pp. 833–848, 2008.

[8]   W. J. Mitsch *et al.*, "Wetlands, carbon, and climate change," *Landsc. Ecol.*, vol. 28, no. 4, pp. 583–597, 2013.

[9]   M. Mahdianpari, B. Salehi, and F. Mohammadimanesh, "The Effect of PolSAR Image De-speckling on Wetland Classification: Introducing a New Adaptive Method," *Can. J. Remote Sens.*, vol. 43, no. 5, 2017.

[10]   M. Mahdianpari, B. Salehi, F. Mohammadimanesh, and B. Brisco, "An Assessment of Simulated Compact Polarimetric SAR Data for Wetland Classification Using Random Forest Algorithm," *Can. J. Remote Sens.*, vol. 43, no. 5, 2017.

[11]   M. Mahdianpari, B. Salehi, F. Mohammadimanesh, and M. Motagh, "Random forest wetland classification using ALOS-2 L-band, RADARSAT-2 C-band, and TerraSAR-X imagery," *ISPRS J. Photogramm. Remote Sens.*, vol. 130, 2017.

[12]   M. Mahdianpari *et al.*, "Fisher Linear Discriminant Analysis of coherency matrix for wetland classification using PolSAR imagery," *Remote Sens. Environ.*, vol. 206, pp. 300–317, 2018.

[13]   M. Mahdianpari, B. Salehi, M. Rezaee, F. Mohammadimanesh, and Y. Zhang, "Very Deep Convolutional Neural Networks for Complex Land Cover Mapping Using Multispectral Remote Sensing Imagery," *Remote Sens.*, vol. 10, no. 7, p. 1119, 2018.

[14]   M. Rezaee, M. Mahdianpari, Y. Zhang, and B. Salehi, "Deep Convolutional Neural Network for

Complex Wetland Classification Using Optical Remote Sensing Imagery," *IEEE J. Sel. Top. Appl. Earth Obs. Remote Sens.*, no. 99, 2018.

[15] M. Mahdianpari, B. Salehi, F. Mohammadimanesh, S. Homayouni, and E. Gill, "The First Wetland Inventory Map of Newfoundland at a Spatial Resolution of 10 m Using Sentinel-1 and Sentinel-2 Data on the Google Earth Engine Cloud Computing Platform," *Remote Sens.*, vol. 11, no. 1, p. 43, 2019.

[16] V. S. Frost, J. A. Stiles, K. S. Shanmugan, and J. C. Holtzman, "A model for radar images and its application to adaptive digital filtering of multiplicative noise," *IEEE Trans. Pattern Anal. Mach. Intell.*, no. 2, pp. 157–166, 1982.

[17] D. T. Kuan, A. A. Sawchuk, T. C. Strand, and P. Chavel, "Adaptive noise smoothing filter for images with signal-dependent noise," *IEEE Trans. Pattern Anal. Mach. Intell.*, no. 2, pp. 165–177, 1985.

[18] J.-S. Lee, J.-H. Wen, T. L. Ainsworth, K.-S. Chen, and A. J. Chen, "Improved sigma filter for speckle filtering of SAR imagery," *IEEE Trans. Geosci. Remote Sens.*, vol. 47, no. 1, pp. 202–213, 2009.

[19] S. Parrilli, M. Poderico, C. V. Angelino, and L. Verdoliva, "A nonlocal SAR image denoising algorithm based on LLMMSE wavelet shrinkage," *IEEE Trans. Geosci. Remote Sens.*, vol. 50, no. 2, pp. 606–616, 2012.

[20] S. R. Cloude and E. Pottier, "An entropy based classification scheme for land applications of polarimetric SAR," *IEEE Trans. Geosci. Remote Sens.*, vol. 35, no. 1, pp. 68–78, 1997.

[21] A. Freeman and S. L. Durden, "A three-component scattering model for polarimetric SAR data," *IEEE Trans. Geosci. Remote Sens.*, vol. 36, no. 3, pp. 963–973, 1998.

[22] R. Touzi, "Target scattering decomposition in terms of roll-invariant target parameters," *IEEE Trans. Geosci. Remote Sens.*, vol. 45, no. 1, pp. 73–84, 2007.

[23] Y. Yamaguchi, T. Moriyama, M. Ishido, and H. Yamada, "Four-component scattering model for polarimetric SAR image decomposition," *IEEE Trans. Geosci. Remote Sens.*, vol. 43, no. 8, pp. 1699–1706, 2005.

[24] F. J. Charbonneau *et al.*, "Compact polarimetry overview and applications assessment," *Can. J. Remote Sens.*, vol. 36, no. sup2, pp. S298–S315, 2010.

[25] G. Huang, Z. Liu, L. Van Der Maaten, and K. Q. Weinberger, "Densely Connected Convolutional Networks.," in *CVPR*, 2017, vol. 1, no. 2, p. 3.

[26] C. Szegedy *et al.*, "Going deeper with convolutions," in *Proceedings of the IEEE conference on computer vision and pattern recognition*, 2015, pp. 1–9.

[27] K. Simonyan and A. Zisserman, "Very deep convolutional networks for large-scale image recognition," *arXiv Prepr. arXiv1409.1556*, 2014.

[28] F. Chollet, "Xception: Deep learning with depthwise separable convolutions," *arXiv Prepr.*, pp.

1610–2357, 2017.

[29] K. He, X. Zhang, S. Ren, and J. Sun, "Deep residual learning for image recognition," in *Proceedings of the IEEE conference on computer vision and pattern recognition*, 2016, pp. 770–778.

[30] E. S. Kasischke and L. L. Bourgeau-Chavez, "Monitoring South Florida wetlands using ERS-1 SAR imagery," *Photogramm. Eng. Remote Sensing*, vol. 63, no. 3, pp. 281–291, 1997.

[31] J.-S. Lee, M. R. Grunes, T. L. Ainsworth, L.-J. Du, D. L. Schuler, and S. R. Cloude, "Unsupervised classification using polarimetric decomposition and the complex Wishart classifier," *IEEE Trans. Geosci. Remote Sens.*, vol. 37, no. 5, pp. 2249–2258, 1999.

[32] K. Millard and M. Richardson, "On the importance of training data sample selection in random forest image classification: A case study in peatland ecosystem mapping," *Remote Sens.*, vol. 7, no. 7, pp. 8489–8515, 2015.

[33] L. Dingle Robertson, D. J. King, and C. Davies, "Object-based image analysis of optical and radar variables for wetland evaluation," *Int. J. Remote Sens.*, vol. 36, no. 23, pp. 5811–5841, 2015.

[34] J. N. Hird, E. R. DeLancey, G. J. McDermid, and J. Kariyeva, "Google Earth Engine, open-access satellite data, and machine learning in support of large-area probabilistic wetland mapping," *Remote Sens.*, vol. 9, no. 12, p. 1315, 2017.

[35] M. W. Lang, E. S. Kasischke, S. D. Prince, and K. W. Pittman, "Assessment of C-band synthetic aperture radar data for mapping and monitoring Coastal Plain forested wetlands in the Mid-Atlantic Region, USA," *Remote Sens. Environ.*, vol. 112, no. 11, pp. 4120–4130, 2008.

[36] L. L. Hess, J. M. Melack, and D. S. Simonett, "Radar detection of flooding beneath the forest canopy: a review," *Int. J. Remote Sens.*, vol. 11, no. 7, pp. 1313–1325, 1990.

[37] F. M. Henderson and A. J. Lewis, "Radar detection of wetland ecosystems: a review," *Int. J. Remote Sens.*, vol. 29, no. 20, pp. 5809–5835, 2008.

[38] W. Meng *et al.*, "Status of wetlands in China: A review of extent, degradation, issues and recommendations for improvement," *Ocean Coast. Manag.*, vol. 146, pp. 50–59, 2017.

Appendix. Canadian wetland inventory map

Abstract

Detailed information on the spatial distribution of wetland classes is crucial for sustainable management and resource assessment. Furthermore, annually updated wetland inventories are of particular importance given that wetlands comprise a dynamic, rather than permanent, land condition. As such, satellite-derived wetland maps are greatly beneficial, as they capture a synoptic and multi-temporal view of landscapes. Currently, accurate, comprehensive, categorical-based, and repeatable wetland inventory on large-scale is in high demand. This is a challenging task given wetlands' heterogeneous and fragmented landscape, the spectral similarity of differing wetland classes, and limitations related to processing large volumes of data, accessing cloud computing resources, and collecting adequate reference samples over such large-scale landscapes. Leveraging state-of-the-art remote sensing data and tools, this study produces a detail categorical-based wetland inventory map of Canada using new opportunities offered by high resolution open access Earth Observation (EO) data and powerful cloud computing resources. In particular, a high resolution 10-m wetland inventory map of Canada, covering an approximate area of one billion hectares, is generated using multi-year (2016-2018), multi-source (Sentinel-1 and Sentinel-2) EO data and a large volume of reference samples within an object-based random forest classification scheme on the Google Earth Engine cloud computing platform. The whole country is classified with an overall accuracy approaching 80% with individual accuracies varying from 74% to 84 % in different provinces, depending on available resources (i.e., ground truth data and intensity of EO data). The resulting nation-wide wetland inventory map illustrates that 19% of Canada's land area is covered by wetlands, most of which are peatlands dominate in the northern ecozones. This represents a general increase of wetland extents in Canada (~6%) relative to past studies potentially

reflecting recent climate change. Importantly, the resulting ever-demanding wetland inventory map of Canada provides unprecedented details on the extent and status, spatial distribution, and landscape pattern of wetlands and, thus, is useful for many stakeholders, including federal and provincial governments, municipalities, NGOs, and environmental consultants.

A.1. Introduction

Wetlands are optimum natural ecosystems offering a variety of environmental functions, such as flood and storm mitigation, coastal and wildlife protection, sediment retention and stabilization, carbon sequestration, and soil and water conservation [1], [2]. According to Warner and Rubec (1997) wetlands are defined as "land that is saturated with water long enough to promote wetland or aquatic processes as indicated by poorly drained soils, hydrophytic vegetation, and various kinds of biological activity which are adapted to a wet environment".

Recently, significant effort has been put toward the reclamation of wetlands to fulfill human needs (e.g., feeding livestock and agricultural activities). Importantly, the economical and environmental values of wetland ecosystems were recognized after a century of wetland reclamation in American society by government wildlife biologists in the 1950s [2]. Since the recognition of the value of wetlands either as a resource or as an important ecosystem for biological and ecological production [4], federal, provincial, and territorial government have voiced their commitments and interests for monitoring environmental changes and developing sustainable strategies for wetland preservation in Canada [5]. Several conservation strategies were also initiated globally. For example, the Ramsar Convention on Wetlands, held since 1971, is among the most well-known initiatives, wherein the main purpose is "the conservation and wise use of wetlands globally" [6], [7]. As of January 2013, 163 nations, including Canada, have joined the convention and indicated their commitments to wetland protection globally. The Ramsar Convention's proposed framework for wetland inventory provides wetland management strategies, including the use of in-situ field measurements and remote sensing data [8].

Wetlands occupy approximately 14% of the total land surface of Canada, which is about 25% of the globally documented wetlands [9]. Wetlands in Canada can be broadly categorized into organic

wetlands, or peatlands, formed by the agglomeration of hydrophilic vegetation, and mineral wetlands, which are developed in saturated areas and contain little or no peat [9]. Peatlands are efficient energy balance systems, as they stored a large amount of energy within their lower layers [10]. Generally, the characteristics of wetlands significantly vary in space and time depending on climatic and physiographic conditions. As such, much effort has been devoted to designing an acceptable wetland classification system reflecting such diversity [4]. Accordingly, the Canadian National Wetland Working Group devised a classification system comprising three hierarchical levels, namely class, form, and type, by incorporating the characteristics of soil, water and vegetation. In particular, the Canadian Wetland Classification system (CWCS) includes five broad wetland classes, namely bog, fen, marsh, swamp, and shallow water, defined based on the overall genetic origin and properties of wetlands, 49 wetland forms defined based on surface morphology and pattern, and several wetland types defined based on vegetation physiognomy [9].

Despite the existence of such a widely accepted classification system and vast expanses of wetlands in Canada, the extent and distribution of Canadian wetlands have not yet been determined with an acceptable degree of precision based on the CWCS definition. Although various estimates are available based on local- and regional-scale wetland inventories across Canada using advanced techniques [11]–[15], these local inventories are incomplete, partial, outdated, and are not intercomparable due to the incorporation of different data and methodologies and in terms of wetland definition.

Baseline information on the large-scale spatial distribution of wetlands is critical for monitoring these productive ecosystems, obtaining information on their historic status and trends, and acquiring accurate inputs for carbon budget, habitat, biodiversity, and resource management strategies [16]. Production of nationally synoptic baseline information is of particular concern in

countries such as Canada, which contains such a significant portion of the world's wetlands. However, wetland mapping on a large scale has long proven challenging given the expense of conducting nation-wide mapping and the highly dynamic and remote nature of wetland ecosystems. Specifically, long term monitoring of wetlands across Canada requires extensive field work and sustainable human involvement and financial investment [17]. In this context, the data obtained using remote sensing tools offer unprecedented opportunities for production of large-scale wetland inventories. Historically, the cost of acquiring such data precluded such operational application on large scales, particularly in geographic regions with chronic cloud cover. Although the U.S. Geological Survey (USGS) has made its entire 30 m Landsat archive publicly accessible since 2008 [18], collecting, storing, and processing of such a time series of remotely sensed imagery covering three decades on a large scale are challenging using conventional image processing software.

Dealing with the "geo big data" problem requires new technologies and resources that enable us to seamlessly extract accurate, high-level information with less user interaction [19]. In particular, to produce national-scale wetland and, in general, land cover maps, input data should be less affected by clouds, haze, shadow, and other disturbances. This can be obtained by compositing a time series of remotely sensed imagery over a large scale during a specific time period [20]. Generating such image composites and executing advanced classification algorithms on large scales demand a massive data storage capacity and high computational efficiency. Until very recently, only a limited number of research institutions and very specialized individuals were privileged to access such advanced resources [21]. Fortunately, new opportunities for the production of national-scale wetland inventories have emerged through the recent development of new powerful cloud-based computational frameworks, such as Google Earth Engine (GEE), the

325

availability of high-quality, open-access Earth Observation (EO) data by USGS, NOAA, and the European Space Agency (ESA), and advances in machine learning tools [22]. In particular, GEE is a cloud-based platform that contains a large repository of open access, ready-to-use geospatial datasets within its data catalog and offers intrinsically parallel computation services. This allows the manipulation of petabyte-scale archives of remotely sensed data, enabling computing, parallel processing, and the visualization of results through its built-in application programming interface (API) [23].

Currently, Canada lacks a national wetland monitoring system [5]. Accordingly, a nation-wide wetland inventory map of Canada with the capability to be updated on an annual basis using a cost-effective approach is of increasing interest for natural resource managers and policy makers, as it provides opportunities for monitoring, conserving, and restoring wetlands. However, the main challenges of wetland mapping on a large scale include the: (1) heterogeneity of wetland landscapes in Canada, wherein clear-cut borders between classes are lacking; (2) spectral similarity of wetland vegetation classes; (3) large seasonal and annual fluctuation both temporally and spatially; and (4) inconsistent wetland vegetation patterns across the country, necessitating the existence of accurate, intensive ground-truth data. Notably, most of these limitations have been addressed to a feasible extent for the production of regional-scale wetland inventories by several recent studies either through enhancing semantic land cover information using a variety of high resolution, advanced EO data [14] or proposing new classification schemes appropriate for wetland characterization [24]. Wulder et al. (2018) first demonstrated the capability of 30-m Landsat time series data to produce wetland extent maps over Canada's forested ecosystems, but for only treed and non-treed wetland classes, rather than wetland types based on the definition of CWCS.

Given the above discussion, the overarching goal of this research was to address the current limitations of Canadian wetland mapping by leveraging the capabilities of recent cloud-based computing resources and open-access high resolution EO data. In particular, the synergistic use of open access 12-days Synthetic Aperture Radar (SAR) Sentinel-1 and 10-days optical Sentinel-2 Multi-Spectral Instrument (MSI) were considered in this study, as the spatial, temporal, and backscatter/spectral specification of these data are highly suitable for addressing the above mentioned limitations of wetland mapping. Incorporating multi-source EO data further enhanced our ability to discriminate backscattering/spectrally similar wetland classes, as complementary land cover information exists within this data. This is because while optical data are responsive to the chemical and molecular structure of vegetation, SAR is sensitive to the geometric and physical structure of vegetation. Furthermore, SAR is sensitive to the flooding status of vegetation, capable of monitoring seasonal and annual fluctuation within wetland ecosystem [25]. It is also unaffected by cloud cover and day/night conditions, which are additional benefits of such data for mapping wetlands in Canada. Importantly, the present research built upon the knowledge gained from our previous work and further extends our recent study, wherein the first provincial-scale wetland inventory map of Canada was produced [19]. In the present study, the study area was expanded to include the whole country (Canada-wide) and this led to the production of the first detailed (categorical-based) Canada wetland inventory map at a spatial resolution of 10-m with extensive ground truth data using state-of-the-art remote sensing tools and data.

A.2. Methods

A.2.1. Study area

Canada is a vast country, covering an approximate area of one billion hectares [26] and is comprising 18 terrestrial ecozones, as defined by Environment and Climate Change Canada (see

). Ecozones are representative of discrete systems with relatively similar geologic, climatic, landform, water, soil, and vegetation patterns [27].
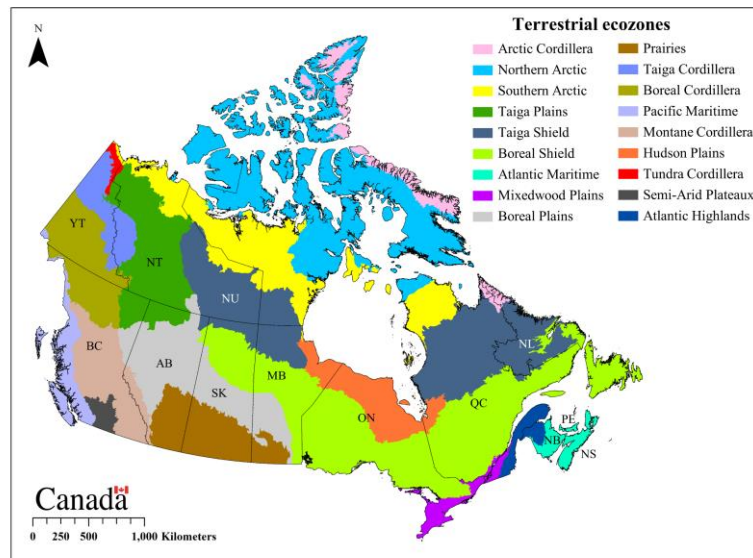
Figure. A.1. Map of terrestrial ecozones in Canada with the distribution of reference samples in different Canadian provinces (AB: Alberta, BC: British Columbia, MB: Manitoba, NB: New Brunswick, NL: Newfoundland and Labrador, NS: Nova Scotia, NT: Northwest Territories, NU: Nunavut, ON: Ontario, PE: Prince Edward Island, QC: Quebec, SK: Saskatchewan, YT: Yukon).

Climates vary from cool temperate to cold arctic with coastal areas affected by oceanic weather. Overall, a north-south temperature and an east-west precipitation gradient affect both the distribution and development of wetlands across Canadian ecozones, wherein both temperature and precipitation decrease toward the south and west, respectively [28]. Particularly, the northern parts of Canada are highly seasonal, experience extensive snowfall during winter and have short summers. Coastal regions are generally warmer and have longer growing seasons. Central regions of Canada experience a continental climate with long, cold winters and hot summers.

According to Glooschenko et al. (1993), 14% of the land area of Canada is unevenly covered by wetlands, 88% of which is peatland. Cool and moist climates, which are the optimum conditions for peatland formation, account for development of the major wetlands in the boreal and subarctic regions of Canada. Low, poorly drained regions that were previously covered by glacial lakes are also suitable areas for wetland development. According to Environment and Climate Change Canada, the Boreal Shield, Hudson Plains, and Boreal Plains ecozones respectively contain 25%, 21%, and 18% of Canada's wetlands. In contrast, mountainous regions of the Arctic Cordillera ($<$ 0.5%) and Montane Cordillera ($<$ 2%) are covered with very low proportions of wetlands. Notably, much of Canada's wetlands are affected by permafrost. Overall, time, water chemistry, hydrology, the characteristics of terrain, and sedimentological processes affect wetland development [28].

According to the CWCS, wetlands can be categorized into five main classes, namely bog, fen, marsh, swamp, and shallow water. These wetland classes were considered in this study and their characteristics are presented in Table A.1.

Table A.1. The characteristic of Canadian wetland classes according to the CWCS [9], [28].

Wetland classes	General characteristics	Hydrological systems[*]/characteristics of water	Water table	Soil [29]	Dominant vegetation
Bog	Peatland	Ombrogenous/ acidy and low in nutrients	At or slightly below the surface	Fibrisols, Mesisols, and Organic Cryosols	*Sphagnum* mosses with tree, shrub or treeless vegetation cover and ericaceous shrubs
Fen	Peatland	Minerogenous/ nutrient-rich	At or above the surface, fluctuating water table	Mesisols, Humisols, and Organic Cryosols	*Graminoid* vegetation, sedges, grasses, reeds, and brown mosses with some shrub cover
Marsh	Mineral wetlands	Minerogenous/ nutrient-rich	Periodically inundated by standing or slowly moving water	Humisols, Mesisols, and Gleysols	Emergent non-woody plants such as rushes, reeds, reed-grasses, and sedges.
Swamp	Peatland and mineral wetland	Minerogenous/ nutrient-rich	At or below the surface	Mesisols, Humisols, and Gleysols	A dense tree cover of coniferous or deciduous species and by tall shrubs, herbs, and mosses
Shallow water	Mineral wetland characterized by fresh to saline water bodies less than 2 m deep in mid-summer	N/A	Semi-permanent to permanent standing or flowing water	N/A	Submerged and floating aquatic plant forms

*Note that direct precipitation is the source of water in ombrogeneous wetlands, while minerogenous wetlands receive water and mineral element from groundwater or littoral sources in addition to atmospheric sources.
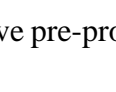
In addition to wetland classes, other land cover classes are also present in the study area. For example, 65% of Canada's land area is covered by forested ecosystems [30]. Extensive agricultural activities are also common in several Canadian provinces (e.g., Manitoba). As such, other land cover classes were also considered in the production of the final wetland inventory map of Canada. These included cropland, forest, grassland/herbs, and urban/bare land. It is worth noting that these four non-wetland classes were obtained by aggregating other relevant classes to better align with the purpose of this study. For example, the forest class included three dominant forested land cover types in Canada, namely broadleaf, coniferous, and mixedwood. Similarly, cropland contained

various types of crop classes, all of which were integrated into a single class in the final product. The two classes of grassland and pasture were also merged into the single class of grassland/herbs due to their relatively similar characteristics. Finally, the urban and bare land classes, both of which are characterized by either an impervious surface or exposed soil, comprising bare land, rocks, roads, and building facilities, were combined into one single class in the final classification map.

A.2.2. Reference sample repository

Reference samples for training and accuracy assessment were collected from a variety of reliable sources. In-situ samples obtained from field campaigns are a prerequisite for developing a classification algorithm. Although it is assumed these data are reliable, small sample size, sampling bias, and inconsistent labelling systems affect their quality, especially on large-scales [31]. In this study, reference samples were provided from various partners/collaborators for all Canadian provinces (see Table A.2).

Table A.2. Number of reference samples in different Canadian provinces.

Province		Bog	Fen	Marsh	Swamp	Water	Urban/ Bare land	Forest	Herbs/ Grassland	Cropland	Total
	BC	88	40	58	76	49	73	127	81	67	659
	AB	91	87	65	83	57	93	120	92	104	792
	SK	93	85	49	56	71	92	99	76	81	702
	MB	108	90	51	54	78	119	108	67	122	797
	ON	102	113	69	101	74	98	98	96	111	862
	QC	101	98	66	82	82	81	110	79	94	793
	NB	83	89	77	93	76	100	103	87	108	816
	NS	56	75	75	41	36	37	78	74	49	521
	PEI	-	-	-	-	41	29	74	68	84	296
	NL	141	167	146	151	39	149	133	113	33	1072
	YT	72	84	55	65	47	85	124	93	-	625
	NT	66	56	29	28	51	98	89	61	-	478
	NU	54	73	18	27	68	123	70	58	-	491

Extensive pre-processing was carried out on the reference data to ensure data quality. Furthermore, there was inconsistency in terms of described systems for wetland classes and, as such, data were

re-labelled into a consistent format following the definition of wetland classes based on the CWCS when necessary.

Reference samples for wetland classes were obtained in all provinces but those for non-wetland classes were not consistently available. For provinces where reference data for non-wetland classes were not available from our collaborators, the preparation of reference samples was carried out by visual interpretation of high-resolution Google Earth imagery, aerial photography, and annual crop inventories of Canadian provinces. Notably, Agriculture and Agri-Food Canada (AAFC) produces Canada's Annual Space-Based Crop Inventories using multi-source EO data (optical and SAR) and ground-based measurements with accuracies exceeding 85% [32]. As mentioned earlier, these sources were only used for the preparation of reference data for non-wetland classes if required.

Table A.2 represents the number of reference samples for wetland and non-wetland classes in different Canadian provinces. It should be noted that significant effort was devoted to incorporate only homogeneous reference polygons with sizes of 1 to 6 ha. Upon the completion of our reference repository, these samples were sorted based on their size and alternatively assigned to either training (50%) or testing (50%) groups. The training samples were used to create knowledge and train the classifier, wherein 20% of the 50% were used for validation and the remaining 30% were used for accuracy assessment. As shown in Table A.2, the availability of such reference data over a wide range of wetland and non-wetland classes in all Canadian provinces allowed us to capture variability across wetlands and provided the opportunity to produce a robust and comprehensive wetland training dataset.

A.2.3. Data composites at 10-m spatial resolution

Concurrent availability of EO data offered through the Copernicus programs by the European Space Agency (ESA; [33], [34]), as well as petabyte-scale storage capacity and the large-scale

computing capability of GEE [23], provide an unprecedented opportunity for large-scale wetland mapping with high temporal and spatial resolution. In this study, high spatial resolution SAR Sentinel-1 and Sentinel-2 A/B multispectral instrument (MSI) data were used for wetland mapping in Canada for the first time. All these data were accessed through the GEE data catalogue and processed within the GEE platform. Figure A.2 illustrates the number of Sentinel-1 and Sentinel-2 scenes used in this study for each Canadian province.
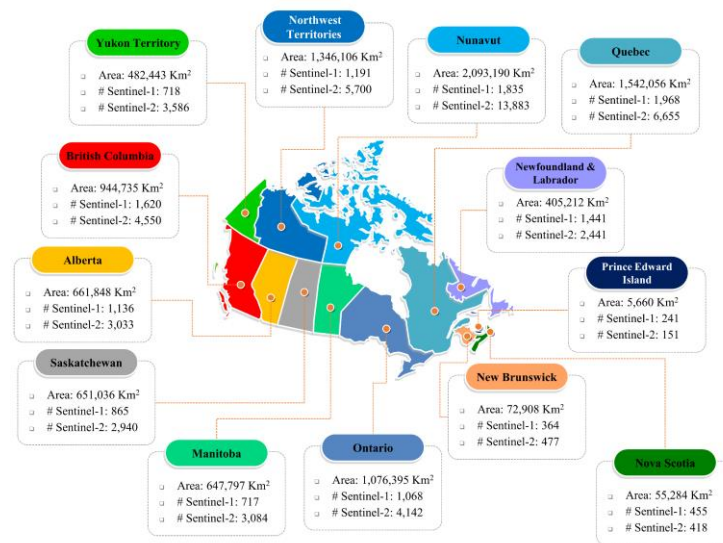
Figure A.2. Number of Sentinel-1 and Sentinel-2 scenes in each Canadian province used for wetland classification in this study.

A.2.3.1. Sentinel-1 images

A total of 13,519 C-band Level-1 Ground Range Detected (GRD) Sentinel-1 SAR images were accessed through GEE and used in this study. This imagery was collected in the Interferometric Wide (IW) swath mode with a resolution of 10 m and a swath width of 250 km between June and August of 2016, 2017, and 2018. Of the 13,519 images, 10,277 and 3,242 were collected with VV-VH and HH-HV polarizations, respectively. The greater availability of VV-VH data is because HH-HV data were only available for the northern parts of Canada. This is due to the general

principle that Sentinel-1 collects single- (HH) or dual- (HH-HV) polarized data over sea ice zones and single- (VV) or dual- (VV-VH) polarized data over all other observation zones (e.g., lands) (https://sentinel.esa.int/web/sentinel/missions/sentinel-1/observation-scenario). The spatial distribution of all available Sentinel-1 observations is depicted in Figure A.3.
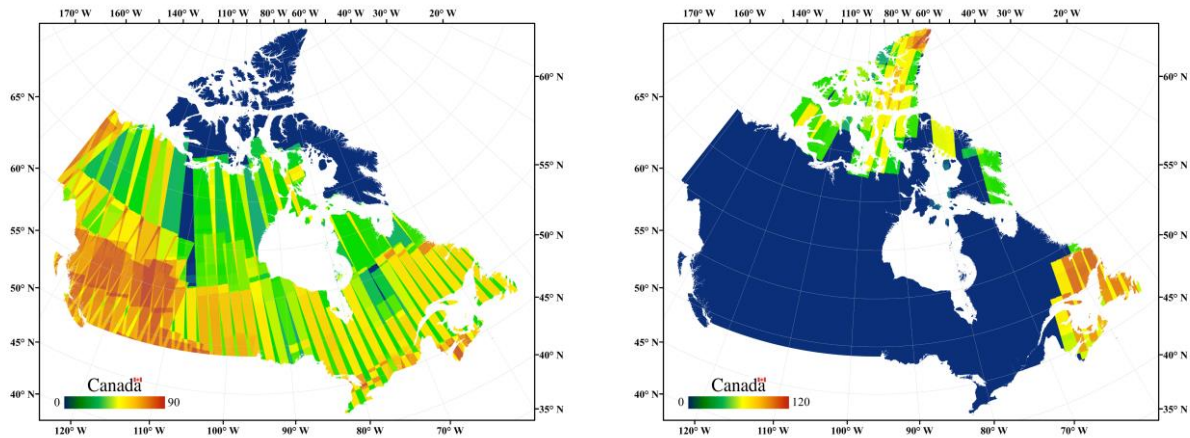
Figure A.3. The total number of (a) ascending SAR observations (VV/VH) and (b) descending SAR observations (HH/HV) during the summers of 2016, 2017, and 2018 in Canada. The color bar represents the number of collected images.

Sentinel-1 GRD data in GEE are already subjected to several preprocessing steps. These include thermal noise removal, radiometric calibration, and terrain correction, resuling in the production of geo-coded SAR backscattering coefficient (σ^0) images in dB (https://developers.google.com/earth-engine/sentinel1). An adaptive sigma Lee filter with a pixel size of 7x7 was then employed to suppress the effect of speckle noise and increase the number of looks prior to further image processing of the SAR data [35]. Further speckle noise reduction was accomplished by producing the multi-year seasonal median composite. In this study, SAR backscattering coefficient images and a number of polarimetric features were extracted from dual-polarized HH-HV and VV-VH data (see Table A.3).

Table A.3. A description of features extracted in this study.

	Feature description	Formula
Sentinel-1	Vertically transmitted, vertically received SAR backscattering coefficient	σ_{VV}^0
	Vertically transmitted, horizontally received SAR backscattering coefficient	σ_{VH}^0
	Horizontally transmitted, horizontally received SAR backscattering coefficient	σ_{HH}^0
	Horizontally transmitted, vertically received SAR backscattering coefficient	σ_{HV}^0
	Span or total scattering power	$\|S_{VV}\|^2 + \|S_{VH}\|^2 , \|S_{HH}\|^2 + \|S_{HV}\|^2$
	Ratio	$\dfrac{\|S_{VV}\|^2}{\|S_{VH}\|^2} , \dfrac{\|S_{HH}\|^2}{\|S_{HV}\|^2}$
Sentinel-2	Spectral bands 2 (blue), 3 (green), 4 (red), and 8 (NIR)	B_2, B_3, B_4, B_8
	The normalized difference vegetation index (NDVI)	$\dfrac{B_8 - B_4}{B_8 + B_4}$

Specifically, σ_{VV}^0 observations are useful for discriminating herbaceous wetland classes, especially in cases of sparse canopy closure [36]. σ_{HV}^0 observations are sensitive to the structure of vegetation, are produced by volume scattering within the vegetation canopy, and can contribute to discriminating wetland vegetation classes [37]. Given its high sensitivity to the flooding status of vegetation [38], σ_{HH}^0 is the most favorable SAR observation for wetland mapping. All extracted SAR features, including σ_{VV}^0, σ_{VH}^0, σ_{HH}^0, σ_{HV}^0, span, and ratio, were stacked to produce a seasonal Sentinel-1 data composite using the GEE's array-based computational approach. Next, the images from multiple years (2016-2018) were combined.

A.2.3.2. Sentinel-2 images

Despite the Sentinel-2 10-day revisit cycle, creating a 10-m cloud-free Sentinel-2 composite for Canada over a short period of time is challenging due to chronic cloud cover. To address this limitation, tri-monthly composites, extending from June to August, were considered to produce cloud-free wall-to-wall coverage. This is an optimum period for wetland vegetation studies in Canada, as explicit wetland phenological information is preserved at this time and a larger number of cloud-free optical data are available.

Both Sentinel-2A and Sentinel-2B Level-1C reflectance data, the standard Sentinel-2 archive in GEE, were used in this study. A total of 211,926 Sentinel-2 images from the summers of 2016, 2017, and 2018 were queried from the GEE data pool. However, some of these observations were contaminated with cloud coverage and were not useful. Accordingly, a selection criterion was applied to remove observations with cloud percentage greater than 20%, after which remained a total of 51,060 Sentinel-2 observations for use in this study. Next, the 'QA60' bitmask band (a quality flag band) available in the metadata was used to detect and mask out remaining clouds and cirrus. Figure A.4 illustrates that the spatial distribution of these clear observation vary unevenly across Canada.
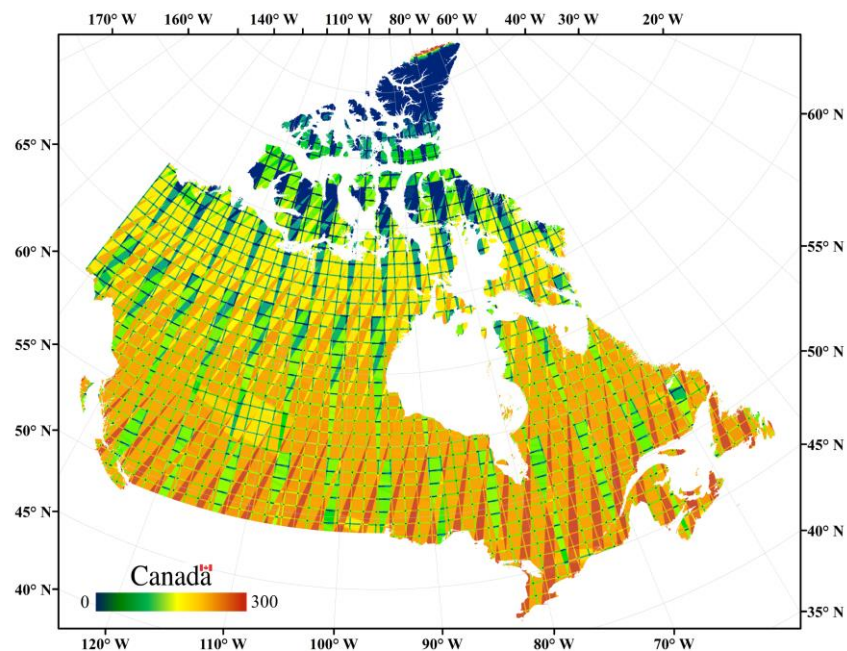
Figure A.4. The spatial distribution of Sentinel-2 data with cloud cover of less than 20% in the summers of 2016, 2017, and 2018 over Canada.

For each period (June to August 2016, 2017, and 2018), five bands, namely blue, green, red, NIR, and a normalized difference vegetation index (NDVI; [39]) band were considered. Figure A.5

337

illustrates the NDVI feature extracted from Sentinel-2 data used as an input feature for wetland classification.
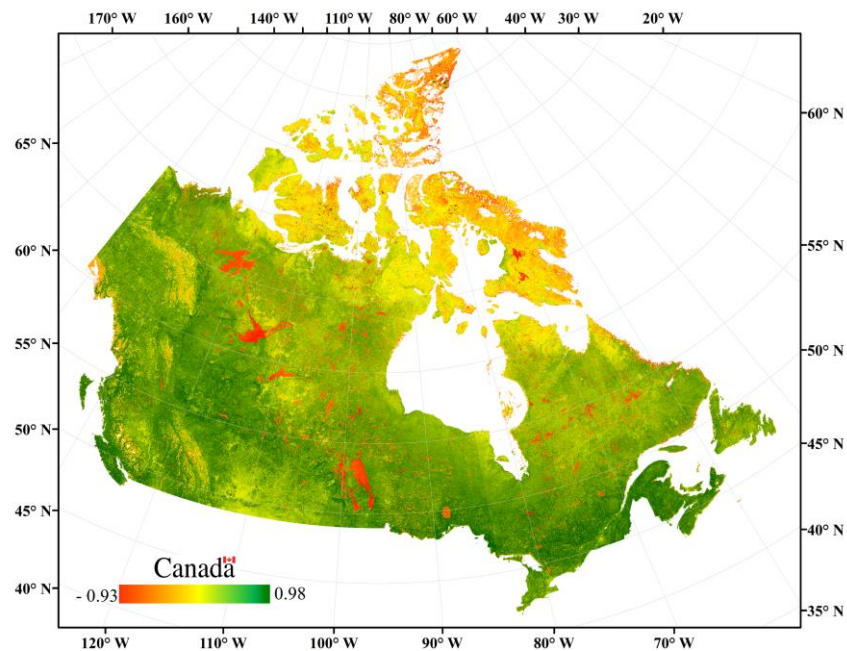

Figure A.5. NDVI feature extracted from Sentinel-2 data.

Each seasonal group of images were stacked into a single median composite on a per-pixel, per-band basis, comprising four spectral bands and NDVI, by leveraging the GEE composite function. Notably, Sentinel-2 data from multiple years (2016-2018) were used to enhance the likelihood of pure cloud-free pixels over Canada (see Figure A.6).

Sentinel-1

σ_{VV}^0

σ_{VH}^0

$|\sigma_{VV}^0|^2 + |\sigma_{VH}^0|^2$

$|\sigma_{VV}^0|^2 / |\sigma_{VH}^0|^2$

σ_{HH}^0

σ_{HV}^0

$|\sigma_{HH}^0|^2 + |\sigma_{HV}^0|^2$

$|\sigma_{HH}^0|^2 / |\sigma_{HV}^0|^2$

Sentinel-2

Blue band (492 nm)
Green band (560 nm)
Red band (665 nm)
NIR band (833 nm)
NDVI
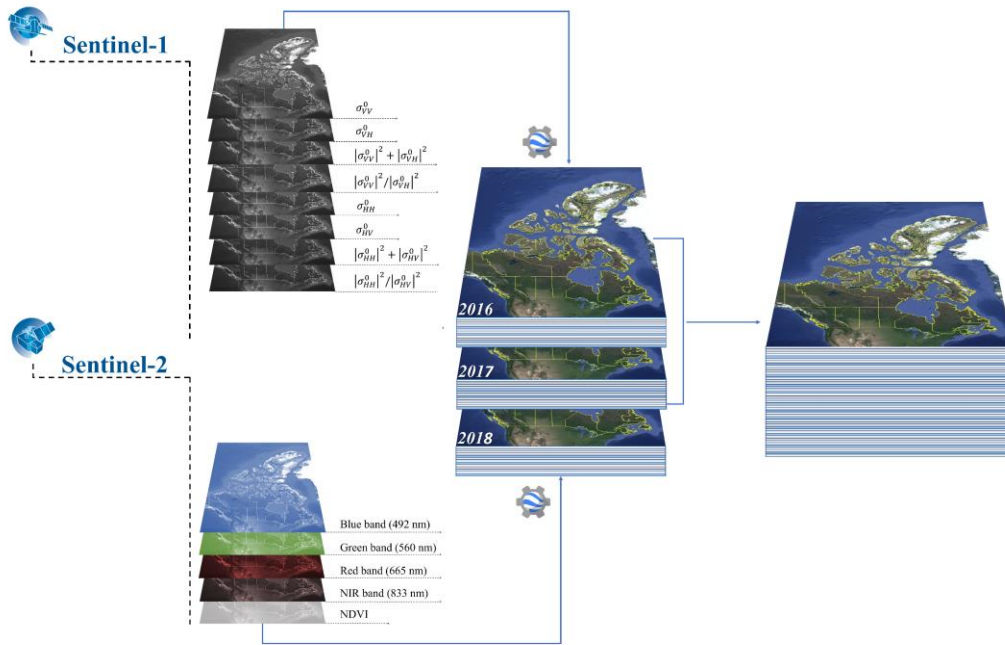
2016
2017
2018

Figure A.6. 10-m data-cube of Canada composited for three time-periods using 2016-2018 Sentinel-1 and Sentinel-2 data. For each period eight Sentinel-1 features and five Sentinel-2 features were composited.

A.2.4. Classification scheme

An object-based image analysis (OBIA) framework was developed for this study. This approach is advantageous compared to the conventional pixel-based classification that relies on the exclusive use of SAR backscattering/spectral information within its classification scheme, resulting in "salt and pepper" noise [40]. This problem, however, is addressed by employing an OBIA technique that takes into account contextual information within a given neighborhood [41].

For OBIA, a simple non-iterative clustering (SNIC) algorithm was selected for superpixel (i.e., small clusters of connected pixels) segmentation [42]. SNIC is advantageous compared to similar approaches, such as simple linear iterative clustering (SLIC), as it is non-iterative, memory efficient, fast, and incorporates the connectivity between pixels once the algorithm is initiated. The

algorithm starts by centering pixels on a regular grid in the image. The dependency of each pixel to a centroid of interest is determined using a distance in the five-dimensional space of color and spatial coordinates. The algorithm adopts a priority queue of 4- or 8-connected pixels to a currently growing superpixel cluster to determine the next candidate pixel to be added to the cluster. This candidate pixel is selected based on the smallest distance from the centroid. A detailed explanation of the SNIC algorithm is beyond the scope of this paper; however, we refer the reader to the original paper [42] for further explanation.

Random forest (RF), which has demonstrated promising results for the classification of remote sensing data [14], [43], [44], was selected for image classification in this study. RF is a non-parametric classifier and is superior compared to other well-known machine learning algorithms, such as the decision tree (DT; Chan and Paelinckx, 2008) in terms of classifier performance and is easily adjustable compared to support vector machine (SVM; [45]). RF uses bootstrap aggregating (a bagging approach) to generate an ensemble of decision trees using a random sample from the given training data and specifies the best splitting of the nodes by minimizing the correlation between the trees. Each pixel is then labeled based on the majority vote of trees [46]. A complete description of the RF algorithm and its advantages for classification of remotely sensed data is presented by Belgiu and Drăguţ (2016).

The RF algorithm is adjustable using two input parameters, namely the number of tress (*Ntree*) and the number of variables (*Mtry*). These parameters were adjusted based on our previous studies of wetland mapping (e.g., [19], [24]) and a trial-and-error procedure, as commonly described in the literature. Accordingly, a total number of 500 trees were selected for *Ntree* and the square root of the number of variables was selected for *Mtry*, as suggested by Breiman (2001).

Initially, the RF classifier was built using 50% of the training samples within the GEE platform. Visual assessment of the classification map was carried out through a comparison with Google Earth images and aerial photos (provided by collaborators and partners) where available. To determine user, producer, and overall accuracy in each Canadian province, an accuracy assessment was carried out using 20% of the testing samples (validation data). Training data were added if these evaluation indices were lower than 70% for a given province. In view of the complexity of wetland classification in Canada, this procedure was repeated 5 times, until the target accuracies for each province were met. The remaining 30% of testing samples were used for further independent accuracy assessment [48].

A.2.5. Accuracy assessment

Accuracy assessment is a key element when producing land cover maps using remotely sensed imagery [49]. This demands high quality testing samples at suitable spatial and temporal scales obtained through standard methods. In this study, reference samples were available from each Canadian province. As such, approximately 50% of reference samples were selected for training, 30% for testing, and 20% for validation purposes as described in detail in section 2.2. The overall accuracy and Kappa coefficient were measured for each province as well as for Canada as a whole.

The areas identified as wetlands in this study were compared with available, valid wetland inventory maps in Canada, including [5], [28], and [50]. Notably, these studies reported only the general distribution of wetlands and did not produce Canada wetland maps based on the definition of the CWCS. Where possible, we compared the resulting classification map in this study visually and statistically. For example, the first study reported the distribution of wetlands in 18 Canadian ecozones and approximately 13% of Canada is covered by wetlands, although the accuracies of the wetland maps in different Canadian ecozones vary. The accuracy was greater than 90% in the

Hudson Plains ecoregion, whereas it reached only 70% in several northern ecozones (e.g., the Northern and Southern Arctic), for example. Following Environment and Climate Change Canada (2016), we report the distribution of wetlands classes in different Canadian ecozones for comparative purposes.

A.3. Results

Figure A.7 demonstrates the first detailed categorically-based Canada-wide wetland inventory map at a spatial resolution of 10 m using the object-based RF classification.
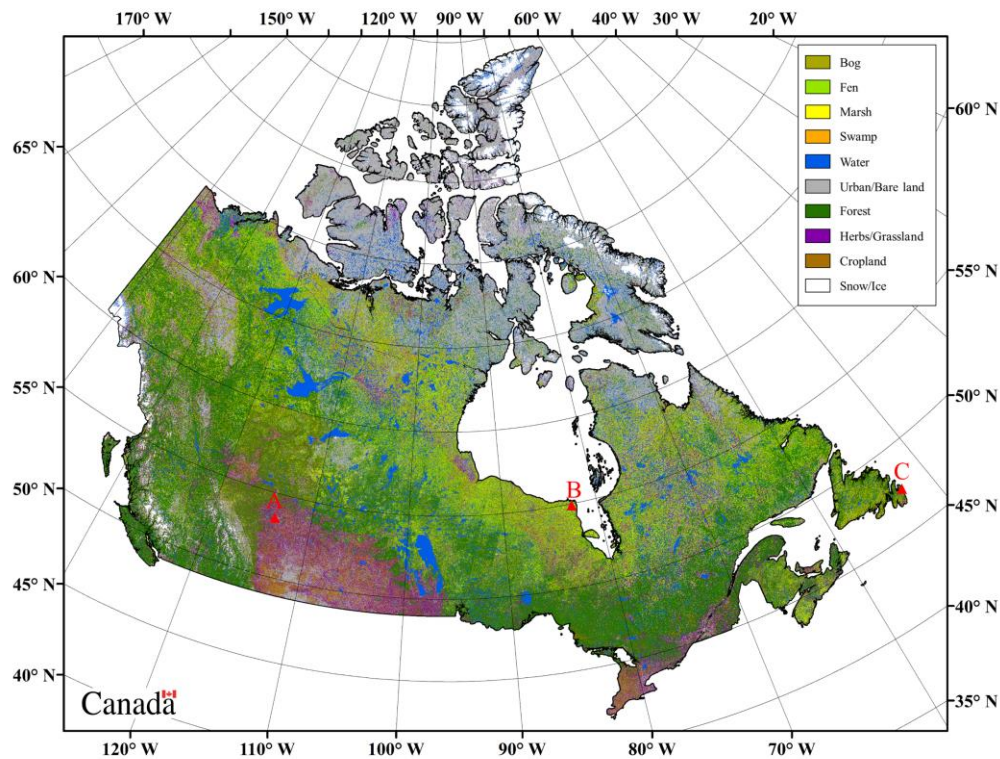

Figure A.7. The first Canada-wide wetland inventory map with a spatial resolution of 10 m obtained from an object-based RF classification using multi-year optical/SAR composite data.

The accuracy of our Canada-wide wetland inventory map was evaluated using independent reference samples. As reference data were available from each Canadian province, overall

accuracies and Kappa coefficients were also measured separately for different provinces (see Table A.4).

Table A.4. Overall accuracies (OA) and Kappa coefficients (K) for wetland classification in different Canadian provinces.

Province	OA	K	Province	OA	K
BC	77.43	0.73	NS	80.88	0.76
AB	82.55	0.80	PEI	75.29	0.71
SK	80.74	0.76	NL	83.67	0.81
MB	81.36	0.77	YT	74.81	0.70
ON	82.17	0.79	NT	78.05	0.75
QC	76.21	0.73	NU	74.32	0.69
NB	77.91	0.74	CA	78.88	0.75

As shown, overall accuracies exceed 74% in all Canadian provinces, with the lowest (~74%) and highest (~84%) accuracies obtained in NU and NL, respectively. The high overall accuracy in NL is partially due to the availability of a larger number of high quality, spatially distributed training samples. This is of special importance for classification of spectrally similar wetland classes. On the other hand, the lowest accuracy of NU could be potentially due to the limited availability of Sentinel-2 data in this region (see Figure A.4), as these areas experience higher cloud cover and snow, even in summers, compared to the other Canadian provinces and territories. Overall, the accuracies for several wetland dominated provinces (e.g., ON, NL, and AB) are promising and exceed 80%. The whole country was classified with an accuracy of approximately 79%. This

implies the high level of confidence in discriminating wetland classes according to the definition of CWCS (detailed wetland classes). Generally, the overall accuracy increases with the increasing level of generalization [51].

As shown in Figure A.7, the two classes of bog and fen (peatlands) are the most dominant wetland classes in Canada, whereas marsh and swamp are barely classified. This is in agreement with past studies [28], which reported that peatlands cover 88% of Canada's wetlands. Our study also identified the forest class as the most dominant of the non-wetland classes. This also agrees well with the results of previous studies, such as [26], and [30], who reported that 65% of Canada's land area is covered by forested ecosystems.

Overall, there is a correlation between the classification map in this study and results of previous studies. For example, our classification map illustrates that wetlands cover a large portion of Northern Ontario. This corroborates the results of previous studies (e.g., [28]), which reported that wetlands cover 33% of land area in Ontario. Likewise, the classification map in this study is visually comparable with Wulder et al. (2018) who demonstrated the annual changes in wetland extents in Canada's forested ecozone between 1984 and 2016 using Landsat data. To appreciate some of the classification details, three insets from the final land cover map were selected (see Figure A.8) for further investigation.
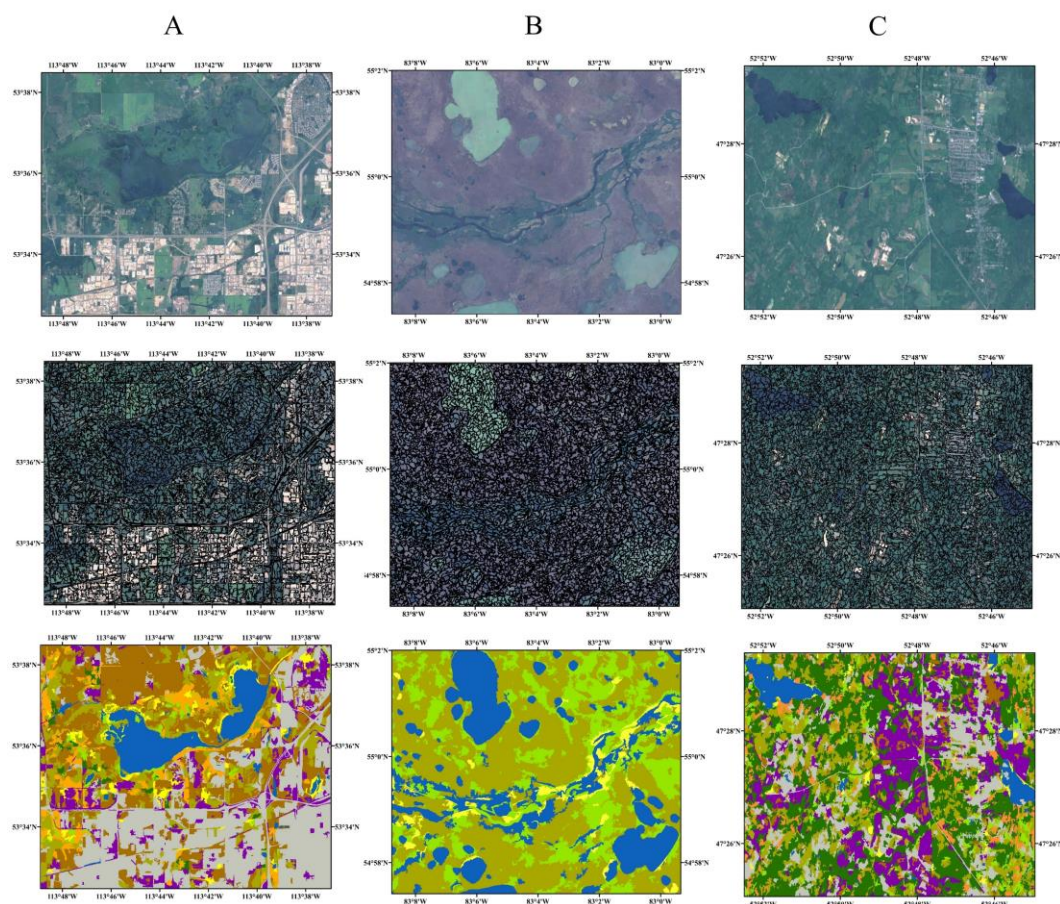
Figure A.8. Three insets of the final Canada wide wetland inventory map selected from various Canada ecozones, including (A) Prairies, (B) Hudson Plains, and (C) Boreal Shield ecozones. (Top panel) The Sentinel-2 MSI color composite images, (middle panel) the object-based SNIC image segmentation results, and (bottom panel) the classification results.

The visual interpretation of the final classification map by ecological and remote sensing experts demonstrated that most land cover classes were correctly identified across the study area. For example, the dominance of the urban class (gray color) in the southern part of the first (A) inset in Figure A.8 was accurately distinguished. The water class was also correctly identified in all three images. Furthermore, according to biological experts, bogs usually appear with reddish color in optical imagery (true color composite), and most bog wetlands were accurately identified in Figure A.8 (B). Table A.5 presents the distribution of wetland classes in different Canadian ecozones.

Table A.5. The distribution of wetlands classes in different Canadian ecozones obtained in this study. Classes of bog, fen, marsh, swamp, and shallow water are represented as forest green, light green, yellow, orange, and blue, respectively.

Ecoregion	Wetland area	Ecoregion	Wetland area
Arctic Cordillera	17,650 km²	Prairies	23,269 km²
Northern Arctic	79,065 km²	Taiga Cordillera	6,682 km²
Southern Arctic	97,448 km²	Boreal Cordillera	13,908 km²
Taiga Plains	255,276 km²	Pacific Maritime	2,371 km²
Taiga Shield	358,051 km²	Montane Cordillera	74,109 km²
Boreal Shield	470,588 km²	Hudson Plains	292,109 km²
Atlantic Maritime	8,128 km²	Tundra Cordillera	5,495 km²
Mixedwood Plains	4,723 km²	Semi-Arid Plateaux	1,192 km²
Boreal Plains	202,455 km²	Atlantic Highlands	2,792 km²

According to Table A.5, wetlands in the Boreal Shield, Taiga Shield, and Hudson Plains (an area centered in northern Ontario extending into northeastern Manitoba and western Quebec) cover approximately 24%, 18%, and 15% of Canadian wetlands, respectively. This is in relative agreement with the results of the Canadian wetland extent reported by Environment and Climate Change Canada (2016), as they also found wetlands were dominate in both the Boreal Shield (25%) and Hudson Plains (21%). However, the classification map in the present study also found the prevalence of wetlands in the Taiga Shield Canada ecozone (18%), which is slightly higher than that reported in a previous study [50]. We believe that wetland distribution was underestimated in this ecozone in the aforementioned study, particularly in the Taiga Shield eastern area. This is also supported by the fact that the accuracy of wetland classification was relatively low (up to 70%) in this region [50]. Furthermore, Wulder et al. (2018) reported an large increase in the extent of wetlands in the eastern part of the Taiga Shield ecozone between 1984 and 2016, which further supports the results of our classification map in this area. In contrast, wetland extent is lowest in the most mountainous ecozones, including Arctic Cordillera, Taiga Cordillera, Boreal Cordillera, and Pacific Maritime, each containing less than 1% of Canada's wetlands. Again, this is in agreement with distribution of wetlands reported in Environment and Climate Change Canada (2016).

Another novel component of our Canada-wide wetland inventory framework is the class-based wetland binary masks (see Figure A.9), which offer a unique source of information about the distribution of wetland classes in Canada.
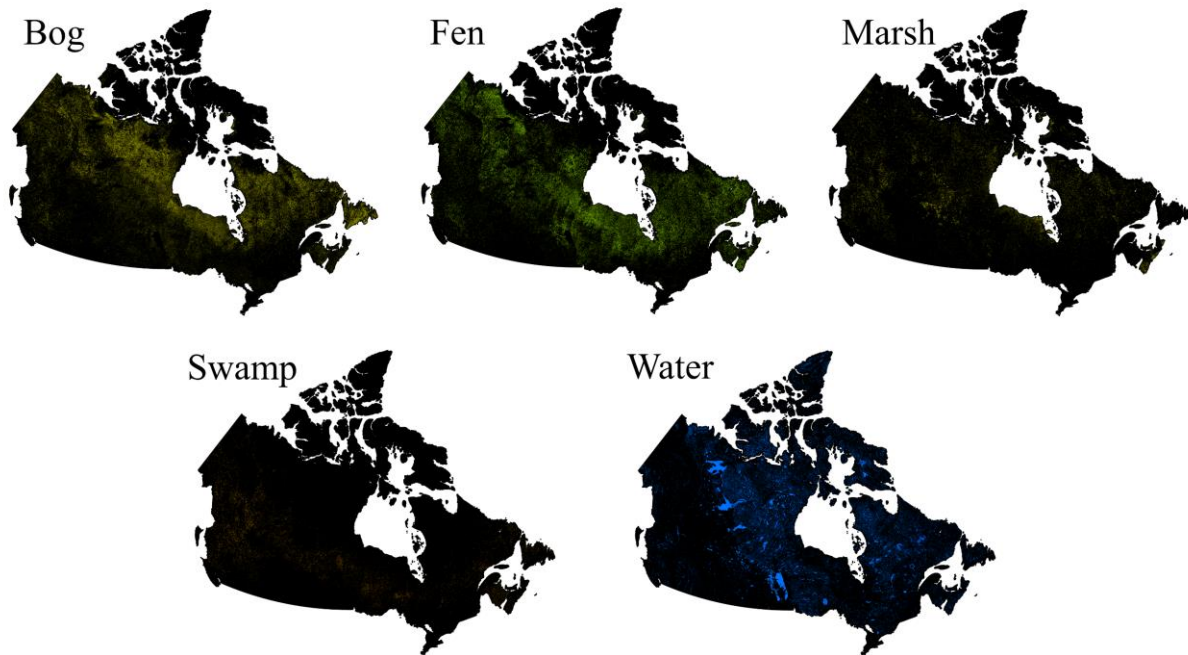
Figure A.9. Binary masks of wetland classes in different Canada's ecozones. The dominancy of peatland classes in the northern ecozones is clearly visible.

These maps are of special interest for several applications demanding generalized land cover information and, in particular, wetland information for modeling and reporting purposes [16]. Figure A.9 further confirms that the bog and fen wetland classes are the most prevalent in Canada, whereas marsh and swamp are less common. Furthermore, these peatland classes are generally distributed in the northern part of the country, especially in the Taiga Shield and Hudson Plains ecozones, and they are the most affected by permafrost. Swamps, however, are mostly isolated wetlands found in the southern regions of the boreal forest, particularly in the Boreal Plains ecozone. Our classification map also successfully distinguished several small water bodies. However, it is worth noting that the water and shallow water classes were merged into a single water class in the final product, as shallow water reference data were unavailable from several provinces.

Finally, to move forward with the more generalized land cover classes in Canada, we produced 10 m binary masks of the wetland and forest classes (see Figure A.10). As shown, wetlands and forests are most prevalent in the northern and southern Canadian ecozones, respectively.
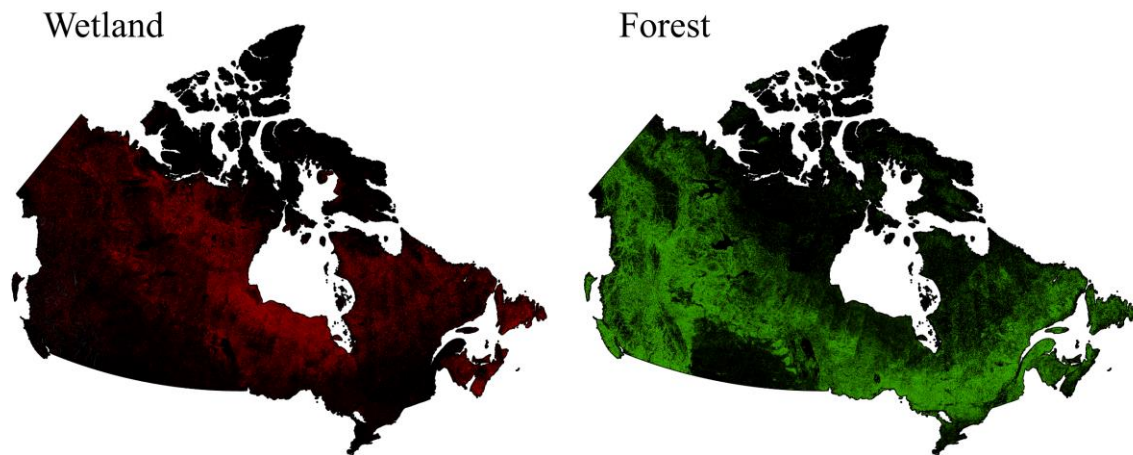

Figure A.10. The 10 m wetland and forest binary masks of Canada. The wetland binary mask was generated by merging all wetland-related classes.

A.4. Discussion

Accurate mapping of complex and heterogeneous wetland landscapes is greatly beneficial for understanding dynamic land cover changes in wetland-dominated regions, such as Canada. Importantly, up-to-date maps of the location and extent of wetlands are essential for conservation and restoration of these valuable ecosystems. The recent development of open-access, high temporal and spatial resolution remotely sensed data provides the unique opportunity to accurately map wetlands on previously infeasible temporal and spatial scales. These advanced products are advantageous compared to traditional approaches based on interoperation of aerial photography,

as they be can updated annually and cover a much larger scale. To date, given the low capacity of typical local processing machines, most remote sensing studies have focused on the generation of small-scale wetland inventories [52]–[54]. Leveraging the capability of GEE, we produced the first categorically detailed, Canada-wide wetland inventory map using open access, regularly updated remotely sensed imagery collected by the Sentinel Missions at a 10 m spatial resolution. Importantly, we determined how wetland distribution varies among Canadian ecozones, which is of interest for monitoring ecosystem services that change from region to region.

The resulting wetland inventory map in this study provides information on the trends and status of Canadian wetlands using standard remote sensing tools and data at the national scale. This map was produced through the synergistic use of complimentary optical and SAR data to take advantage of both types of observations in a broad-scale investigation, as suggested by a recent study [5]. Furthermore, the spatial distribution of Sentinel-2 data (cloud cover $< 20\%$) over Canada (see Figure A.4) further affirms the necessity of incorporating SAR data for such large-scale monitoring, as the density of cloud free observations significantly varies from region to region. However, the inclusion of multi-source data addressed this limitation and offered a rich archive of high temporal and spatial resolution EO data, further making multi-source approaches advantageous for large scale remote sensing applications in Canada. Nevertheless, future studies also need to incorporate alternative sources of data with higher spatial and temporal resolutions and greater capacities. In particular, SAR data in this study were limited to dual-polarimetric data in all Canada ecozones (see Figure A.3). This hindered the application of advanced polarimetric decomposition techniques, which are of great value for discriminating wetland classes with similar backscattering signatures. Accordingly, Canada's upcoming RADARSAT Constellation Mission (RCM), with the capability to collect sub-weekly SAR data in various polarization modes, offers

potential avenues for future research of large-scale wetland mapping. Likewise, airborne LiDAR data, although expensive and difficult to systematically acquire on large scales, can be useful to capture information on wetland drainage systems and the overall structure of wetland landscapes and, as such, may improve the characterization of Canada's wetland ecosystems [5].

The Canada-wide wetland inventory map produced in this study demonstrates that approximately 19% of Canada's land area is covered by wetlands. This represents a 5% and 6% increase in the estimated extent of Canada's wetlands compared to Glooschenko et al. (1993) and Environment and Climate Change Canada (2016), respectively. However, it should be noted that wetlands are highly dynamic landscapes and may significantly vary on seasonal, annual, and decadal bases, as they are water-dependent ecosystems and therefore are greatly affected by melting snow, changing precipitation patterns, thawing permafrost, and changing groundwater flows, for example. Furthermore, these aforementioned studies are relatively old and determine the extent of wetlands in Canada by incorporating data from various sources. For example, the Environment and Climate Change Canada (2016) wetland extent map illustrates wetland distribution around the year 2000 using data obtained from 2000 to 2014. Nevertheless, the distribution of wetlands in this study agrees with that of Wulder et al. (2018), who reported wetlands cover approximately 18% of Canada's forested ecozones during the interval of 1984 to 2016. The higher extent of Canada's wetlands obtained in our study, particularly in the northern ecozones, suggests that thawing permafrost, and melting ice and snow contribute to increasing water levels and wetland extension. This increase in wetland distribution in the northern ecozones (e.g., Taiga Shield) is also supported by reports of extensive permafrost thaw and wetland expansion as a result of climate change [55]. Likewise, although wetlands in mountainous ecozones (e.g., Boreal and Taiga Cordillera) cover a small portion of Canada's wetlands, our study found a general increase in their extent compared

to past studies (Environment and Climate Change Canada, 2016), our results are in agreement with the most recent research [5].

It is also possible to increase the accuracy of our Canada-wide wetland inventory map. The greatest challenge to developing this national-scale wetland inventory map was collecting sufficient, reliable training samples to ensure reliable coding and the production of an accurate final product. Thus, a certain class in a particular ecozone may have a low accuracy not because of the uncertainty in the classification algorithm, but rather due to the poor quality of the reference data. Although several studies have collected training data from pre-existing, reliable land cover maps, such an approach is not ideal given the intrinsic errors that could propagate to the final land cover map. Notably, training data for all wetland classes in all Canadian provinces and territories were obtained from collaborators/partners; however, training data for non-wetland classes were acquired through the interpretation of high-resolution imagery and the AAFC annual crop inventory map. This could affect the accuracy of the final product in some regions. Overall, larger and higher quality reference training and testing samples from all presented land cover classes in different Canadian ecozones will improve the accuracy and ensure the robustness of the classification algorithm. Although costly, such field campaigns remain a necessary element to enrich and validate models for large-scale applications.

Several studies have highlighted the superiority of multi-temporal remote sensing data for land cover classification compared to single-date images [56]. This is of particular importance for characterizing wetland classes with highly dynamic natures [19], [38]. In the present study, multi-temporal, multi-source EO data were incorporated into the classification scheme to enhance semantic land cover information. Another strategy for incorporating temporal data for wetland characterization could be determining wetland changes using large multi-temporal remote sensing

data, which are of special interest for ecosystem services in various Canadian ecozones. This is possible through the availability of multi-decadal open-access Landsat data, yet such data may provide insufficient details for distinguishing small land cover classes, such as wetlands or regions subject to agricultural activities, demanding higher spatial resolution imagery. As more open-access, high temporal and spatial resolution data collected by Copernicus Sentinels are added to the GEE data catalogue, these barriers are eroding and new opportunities for fine-scale land (wetland) cover mapping are arising.

The approaches presented in this study are transferable to other large-scale wetland ecosystems, adaptable to sufficient, appropriate ecological training data, and are also suitable for other land cover ecosystems beyond wetlands for a range of user needs and focus domains. The baseline information obtained from such spatially explicit, regional trends in Canada's wetland map provides a useful context for determining the causes of wetland changes and for improving our understanding of the mechanisms behind wetland dynamics. The resulting 10 m Canada-wide wetland inventory map derived from multiple sources using an advanced remote sensing tool is an essential starting point toward the production of global-scale wetland inventory maps. However, more challenges are expected for upscaling to global maps, such as collecting reliable ground-truth data, inconsistencies in terms of wetland definitions, and more cloud cover issues. Despite these barriers, the realization of a global-scale wetland inventory should be feasible given recent advances in the geospatial sciences.

A.5. Conclusion

Leveraging the computational power of Google Earth Engine and a large pool of high temporal and spatial resolution satellite imagery collected by Copernicus Sentinels, we have generated Canada's first detail categorically-based wetland inventory map at a spatial resolution of 10 m,

covering an approximate area of one billion hectares, yet within a reasonable time using GEE. In particular, this map was produced by training a random forest classifier in an object-based framework using multi-year summer composites of Sentinel-1 and Sentinel-2 data.

The 10 m Canada wetland inventory mapped a complex series of small and large, heterogeneous wetland classes, along with other dominant land cover classes (e.g., forest) accurately. Notably, the whole country was classified with accuracy approaching 80%, with accuracies varying from 74% to 84% in different Canadian provinces and territories. The resulting Canada-wide wetland inventory map illustrated that wetlands cover approximately 19% of Canada's land area. The results demonstrated that the Boreal Shield, Taiga Shield, and Hudson Plains comprise much of Canada's wetlands, whereas wetlands are least common in mountainous ecozones. Bogs and fens were found to be the most dominant wetland classes in Canada, especially in the northern ecozones. The results also identified further expansion of wetlands in Canada's northern ecoszones, potentially as a consequence of climate change.

This study transforms low-level information of Canada's wetland status into categorically detailed wetland maps, complements the previously produced national-scale Canada wetland map from circa 2000, and characterizes the spatial distribution of wetland classes over a previously unmapped area with high spatial resolution. Interesting opportunities to continually contribute to the classification map presented herein are also available through the launch of new satellites, such as RCM, that aim to provide high resolution coverage on a sub-weekly basis. Thanks to recent advances in geospatial science, a remarkable paradigm-shift in the field of land cover mapping is expected in the near future, wherein the production of standard static maps will be replaced with those that are more dynamic and application-specific. Such detailed and large-scale maps of

wetlands, for example, offer the opportunity to more closely monitor these dynamic ecosystems

and will contribute to studies in several fields.

A.6. References

[1]   W. J. Mitsch *et al.*, "Wetlands, carbon, and climate change," *Landsc. Ecol.*, vol. 28, no. 4, pp. 583–597, 2013.

[2]   R. W. Tiner, M. W. Lang, and V. V Klemas, *Remote sensing of wetlands: applications and advances*. CRC Press, 2015.

[3]   B. G. Warner and C. D. A. Rubec, "The Canadian wetland classification system," *Wetl. Res. Centre, Univ. Waterloo, Waterloo, Ontario*, 1997.

[4]   S. C. Zoltai and F. C. Pollett, *Wetlands in Canada, their classification, distribution, and use*. Elsevier Scientific, 1983.

[5]   M. Wulder *et al.*, "A National Assessment of Wetland Status and Trends for Canada's Forested Ecosystems Using 33 Years of Earth Observation Satellite Data," *Remote Sens.*, vol. 10, no. 10, p. 1623, 2018.

[6]   R. C. Gardner and N. C. Davidson, "The ramsar convention," in *Wetlands*, Springer, 2011, pp. 189–203.

[7]   F. Mohammadimanesh, B. Salehi, M. Mahdianpari, B. Brisco, and E. Gill, "Full and Simulated Compact Polarimetry SAR Responses to Canadian Wetlands: Separability Analysis and Classification," *Remote Sens.*, vol. 11, no. 5, p. 516, 2019.

[8]   R. A. Fournier, M. Grenier, A. Lavoie, and R. Hélie, "Towards a strategy to implement the Canadian Wetland Inventory using satellite remote sensing," *Can. J. Remote Sens.*, vol. 33, no. sup1, pp. S1–S16, 2007.

[9]   N. W. W. Group, "The Canadian wetland classification system." Edited by, 1997.

[10]   D. F. Whigham, D. Dykyjová, and S. Hejný, "Wetlands of the world: Inventory, ecology and management Volume I Africa, Australia, Canada and Greenland, Mediterranean, Mexico, Papua New Guinea, South Asia, Tropical South America, United States," 1993.

[11]   L. Dingle Robertson, D. J. King, and C. Davies, "Object-based image analysis of optical and radar variables for wetland evaluation," *Int. J. Remote Sens.*, vol. 36, no. 23, pp. 5811–5841, 2015.

[12]   K. Millard and M. Richardson, "Wetland mapping with LiDAR derivatives, SAR polarimetric decompositions, and LiDAR–SAR fusion using a random forest classifier," *Can. J. Remote Sens.*, vol. 39, no. 4, pp. 290–307, 2013.

[13]   R. Jahncke, B. Leblon, P. Bush, and A. LaRocque, "Mapping wetlands in Nova Scotia with multi-beam RADARSAT-2 Polarimetric SAR, optical satellite imagery, and Lidar data," *Int. J. Appl. earth Obs. Geoinf.*, vol. 68, pp. 139–156, 2018.

[14]   M. Mahdianpari, B. Salehi, F. Mohammadimanesh, and M. Motagh, "Random forest wetland classification using ALOS-2 L-band, RADARSAT-2 C-band, and TerraSAR-X imagery," *ISPRS J. Photogramm. Remote Sens.*, vol. 130, pp. 13–31, 2017.

[15]   B. Brisco, K. Li, B. Tedford, F. Charbonneau, S. Yun, and K. Murnaghan, "Compact polarimetry

assessment for rice and wetland mapping," *Int. J. Remote Sens.*, vol. 34, no. 6, pp. 1949–1964, 2013.

[16]   T. Hermosilla, M. A. Wulder, J. C. White, N. C. Coops, and G. W. Hobart, "Disturbance-informed annual land cover classification maps of Canada's forested ecosystems for a 29-year Landsat time series," *Can. J. Remote Sens.*, vol. 44, no. 1, pp. 67–87, 2018.

[17]   R. A. Van Dam, C. Camilleri, and C. M. Finlayson, "The potential of rapid assessment techniques as early warning indicators of wetland degradation: a review," *Environ. Toxicol. Water Qual. An Int. J.*, vol. 13, no. 4, pp. 297–312, 1998.

[18]   C. E. Woodcock *et al.*, "Free access to Landsat imagery," *Science (80-.).*, vol. 320, no. 5879, p. 1011, 2008.

[19]   M. Mahdianpari, B. Salehi, F. Mohammadimanesh, S. Homayouni, and E. Gill, "The First Wetland Inventory Map of Newfoundland at a Spatial Resolution of 10 m Using Sentinel-1 and Sentinel-2 Data on the Google Earth Engine Cloud Computing Platform," *Remote Sens.*, vol. 11, no. 1, p. 43, 2019.

[20]   W. Lück and A. Van Niekerk, "Evaluation of a rule-based compositing technique for Landsat-5 TM and Landsat-7 ETM+ images," *Int. J. Appl. Earth Obs. Geoinf.*, vol. 47, pp. 1–14, 2016.

[21]   G. Azzari and D. B. Lobell, "Landsat-based classification in the cloud: An opportunity for a paradigm shift in land cover monitoring," *Remote Sens. Environ.*, vol. 202, pp. 64–74, 2017.

[22]   G. Azzari, M. Jain, and D. B. Lobell, "Towards fine resolution global maps of crop yields: Testing multiple methods and satellites in three countries," *Remote Sens. Environ.*, vol. 202, pp. 129–141, 2017.

[23]   N. Gorelick, M. Hancher, M. Dixon, S. Ilyushchenko, D. Thau, and R. Moore, "Google Earth Engine: Planetary-scale geospatial analysis for everyone," *Remote Sens. Environ.*, vol. 202, pp. 18–27, 2017.

[24]   F. Mohammadimanesh, B. Salehi, M. Mahdianpari, M. Motagh, and B. Brisco, "An efficient feature optimization for wetland mapping by synergistic use of SAR intensity, interferometry, and polarimetry data," *Int. J. Appl. earth Obs. Geoinf.*, vol. 73, pp. 450–462, 2018.

[25]   B. Brisco, "Mapping and monitoring surface water and wetlands with synthetic aperture radar," *Remote Sens. Wetl. Appl. Adv.*, pp. 119–136, 2015.

[26]   J. C. White, M. A. Wulder, T. Hermosilla, N. C. Coops, and G. W. Hobart, "A nationwide annual characterization of 25 years of forest disturbance and recovery for Canada using Landsat time series," *Remote Sens. Environ.*, vol. 194, pp. 303–321, 2017.

[27]   L. Directorate, "Terrestrial ecozones of Canada," *Ecol. L. Classif. no*, vol. 19, 1986.

[28]   W. A. Glooschenko, C. Tarnocai, S. Zoltai, and V. Glooschenko, "Wetlands of Canada and Greenland," in *Wetlands of the world: Inventory, ecology and management Volume I*, Springer, 1993, pp. 415–514.

[29]   C. S. S. Committee, *The Canadian system of soil classification*. Research Branch, Canada

Department of Agriculture, 1978.

[30] M. A. Wulder *et al.*, "Monitoring Canada's forests. Part 1: Completion of the EOSD land cover project," *Can. J. Remote Sens.*, vol. 34, no. 6, pp. 549–562, 2008.

[31] G. M. Foody, "Assessing the accuracy of land cover change with imperfect ground reference data," *Remote Sens. Environ.*, vol. 114, no. 10, pp. 2271–2285, 2010.

[32] T. Fisette *et al.*, "AAFC annual crop inventory," in *Agro-Geoinformatics (Agro-Geoinformatics), 2013 Second International Conference on*, 2013, pp. 270–274.

[33] R. Torres *et al.*, "GMES Sentinel-1 mission," *Remote Sens. Environ.*, vol. 120, pp. 9–24, 2012.

[34] M. Drusch *et al.*, "Sentinel-2: ESA's optical high-resolution mission for GMES operational services," *Remote Sens. Environ.*, vol. 120, pp. 25–36, 2012.

[35] J.-S. Lee, J.-H. Wen, T. L. Ainsworth, K.-S. Chen, and A. J. Chen, "Improved sigma filter for speckle filtering of SAR imagery," *IEEE Trans. Geosci. Remote Sens.*, vol. 47, no. 1, pp. 202–213, 2009.

[36] C. C. Schmullius and D. L. Evans, "Synthetic aperture radar (SAR) frequency and polarization requirements for applications in ecology, geology, hydrology, and oceanography: a tabular status quo after SIR-C/X-SAR," *Oceanogr. Lit. Rev.*, vol. 3, no. 45, p. 574, 1998.

[37] F. M. Henderson and A. J. Lewis, "Radar detection of wetland ecosystems: a review," *Int. J. Remote Sens.*, vol. 29, no. 20, pp. 5809–5835, 2008.

[38] F. Mohammadimanesh, B. Salehi, M. Mahdianpari, B. Brisco, and M. Motagh, "Multi-temporal, multi-frequency, and multi-polarization coherence and SAR backscatter analysis of wetlands," *ISPRS J. Photogramm. Remote Sens.*, vol. 142, pp. 78–93, 2018.

[39] F. J. Kriegler, W. A. Malila, R. F. Nalepka, and W. Richardson, "Preprocessing transformations and their effects on multispectral recognition," in *Remote sensing of environment, VI*, 1969, p. 97.

[40] U. C. Benz, P. Hofmann, G. Willhauck, I. Lingenfelder, and M. Heynen, "Multi-resolution, object-oriented fuzzy analysis of remote sensing data for GIS-ready information," *ISPRS J. Photogramm. Remote Sens.*, vol. 58, no. 3–4, pp. 239–258, 2004.

[41] T. Blaschke, "Object based image analysis for remote sensing," *ISPRS J. Photogramm. Remote Sens.*, vol. 65, no. 1, pp. 2–16, 2010.

[42] R. Achanta and S. Süsstrunk, "Superpixels and polygons using simple non-iterative clustering," in *Computer Vision and Pattern Recognition (CVPR), 2017 IEEE Conference on*, 2017, pp. 4895–4904.

[43] J. C.-W. Chan and D. Paelinckx, "Evaluation of Random Forest and Adaboost tree-based ensemble classification and spectral band selection for ecotope mapping using airborne hyperspectral imagery," *Remote Sens. Environ.*, vol. 112, no. 6, pp. 2999–3011, 2008.

[44] S. van Beijma, A. Comber, and A. Lamb, "Random forest classification of salt marsh vegetation habitats using quad-polarimetric airborne SAR, elevation and optical RS data," *Remote Sens.*

Environ., vol. 149, pp. 118–129, 2014.

[45] C. Pelletier, S. Valero, J. Inglada, N. Champion, and G. Dedieu, "Assessing the robustness of Random Forests to map land cover with high resolution satellite image time series over large areas," *Remote Sens. Environ.*, vol. 187, pp. 156–168, 2016.

[46] L. Breiman, "Random forests," *Mach. Learn.*, vol. 45, no. 1, pp. 5–32, 2001.

[47] M. Belgiu and L. Drăguţ, "Random forest in remote sensing: A review of applications and future directions," *ISPRS J. Photogramm. Remote Sens.*, vol. 114, pp. 24–31, 2016.

[48] R. G. Congalton, "A review of assessing the accuracy of classifications of remotely sensed data," *Remote Sens. Environ.*, vol. 37, no. 1, pp. 35–46, 1991.

[49] R. G. Congalton and K. Green, *Assessing the accuracy of remotely sensed data: principles and practices*. CRC press, 2008.

[50] Environment and Climate Change Canada, "Canadian Environmental Sustainability Indicators: Extent of Canada's Wetlandsle," QC, 2016.

[51] T. K. Remmel, F. Csillag, S. Mitchell, and M. A. Wulder, "Integration of forest inventory and satellite imagery:: a Canadian status assessment and research issues," *For. Ecol. Manage.*, vol. 207, no. 3, pp. 405–428, 2005.

[52] M. Mahdianpari, B. Salehi, F. Mohammadimanesh, and M. Motagh, "Random forest wetland classification using ALOS-2 L-band, RADARSAT-2 C-band, and TerraSAR-X imagery," *ISPRS J. Photogramm. Remote Sens.*, vol. 130, 2017.

[53] K. Millard and M. Richardson, "On the importance of training data sample selection in random forest image classification: A case study in peatland ecosystem mapping," *Remote Sens.*, vol. 7, no. 7, pp. 8489–8515, 2015.

[54] L. D. Robertson, D. J. King, and C. Davies, "Assessing land cover change and anthropogenic disturbance in wetlands using vegetation fractions derived from Landsat 5 TM imagery (1984–2010)," *Wetlands*, vol. 35, no. 6, pp. 1077–1091, 2015.

[55] C. Brekke and A. H. S. Solberg, "Oil spill detection by satellite remote sensing," *Remote Sens. Environ.*, vol. 95, no. 1, pp. 1–13, 2005.

[56] C. Gómez, J. C. White, and M. A. Wulder, "Optical remotely sensed time series data for land cover classification: A review," *ISPRS J. Photogramm. Remote Sens.*, vol. 116, pp. 55–72, 2016.